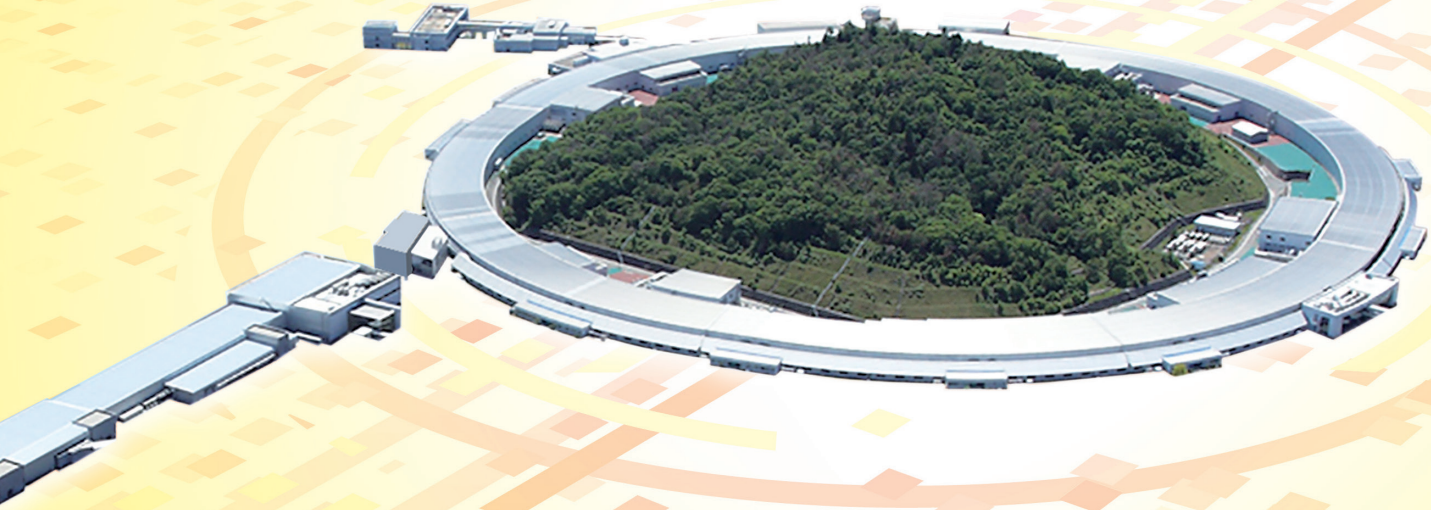

Research Frontiers 2024

SPring-8
SACLA

ISSN 2760-2877
SPring-8 Document D2025-010

SPring-8/SACLA Research Frontiers 2024

CONTENTS

Physical Science

Chemical Science

Earth & Planetary Science

Industrial Applications

Accelerators & Beamlines Frontiers 102

SPring-8

New Apparatus, Upgrades & Methodology

SACLA

Facility Status 114

SPring-8

SACLA

SPring-8/SACLA

Note: The principal publication(s) concerning each article is indicated with all author's names in italics in the list of references.

PREFACE

We are pleased to announce the release of SPring-8/SACLA Research Frontiers 2024, now available exclusively online. This marks the first issue not published in print.

JASRI's mission is to support users and ensure transparent and fair selection of experimental proposals as the user promotion organization for SPring-8 and SACLA, registered with the Ministry of Education, Culture, Sports, Science and Technology of Japan (MEXT). Another key mission of JASRI is to manage SPring-8 and SACLA, which are owned by RIKEN. In this role, JASRI works closely with RIKEN to operate and manage both facilities, located on the same campus. The synergy between these world-class facilities continues to drive groundbreaking scientific achievements.

In 2024, SPring-8 welcomed over 15,000 users who carried out more than 2,000 experiments. Currently, SPring-8 users publish over 1,100 research papers each year, while SACLA users publish approximately 100 research papers annually.

Notably, several SPring-8 and SACLA users were awarded prestigious prizes in 2024 for their achievements in science and technology. Among them, Professor Isao Tanaka (Kyoto University) was awarded the Medal with Purple Ribbon in the fall of 2024 for his contributions to new theory and technological innovation in the pioneering research field of "Quantum Materials Design." Professor Toru Wakihara (University of Tokyo) received the Ceramic Society of Japan Academic Award for his contributions to the application of ceramic processing to zeolite science through PDF analysis at SPring-8. Professor Hitoki Yoneda (The University of Electro-Communications) received the Photonics and Quantum Electronics Achievement Award from the Japan Society of Applied Physics (JSAP) for his contributions to the realization of the shortest wavelength (0.15 nm) X-ray atomic laser.

This volume also includes two comprehensive review articles. The first, by Professor Hiroshi Sawa (Nagoya Industrial Science Research Institute), introduces his group's ultra-precise valence electron density analysis. They successfully extracted only valence electron density (VED) within a crystal using their developed core-differential Fourier synthesis (CDFS) method. The second review, by Dr. Takeshi Morikawa (Toyota Central R&D Labs.), describes his group's recent advances in artificial photosynthesis using solid-state semiconductors and molecular metal complexes. The team performed angle-resolved HAXPES and *operando* XAS at SPring-8, as well as femtosecond time-resolved X-ray absorption near-edge structure (TR-XANES) at SACLA, to investigate and improve the structure and function of the artificial photosynthetic systems.

The main part of this volume features research highlights from users of SPring-8 and SACLA, presenting the essence of their results across various fields such as Life Science, Physical Science, Chemical Science, Earth & Planetary Science, and Industrial Applications. Additionally, the second part contains principal activity reports on SPring-8/SACLA facilities, provided in the Accelerators & Beamlines Frontiers and Facility Status sections.

I am very grateful to the many authors and experts who contributed their papers to this volume. Special thanks are due to Dr. Toyohiko Kinoshita, Ms. Marcia Obuti-Daté and the members of the editorial board for their continuous efforts.

Y. Amemiya

Yoshiyuki Amemiya
President
Japan Synchrotron Radiation Research Institute (JASRI)

Editor's Note

This is the 2024 issue of SPring-8/SACLA Research Frontiers, presents the outstanding scientific outcomes from SPring-8 and SACLA in 2023 and 2024. Each year, the best scientific achievements are selected from among more than 1,000 papers published at SPring-8 or SACLA. Time-resolved serial femtosecond protein crystallography using SACLA shows high activity, and research on a variety of functional materials aimed at achieving the sustainable development goals (SDGs) is ongoing. Research on spintronic devices and battery electrode materials is also thriving.

Starting with this issue, SPring-8/SACLA Research Frontiers is available exclusively in digital format. Previous issues were distributed in both print and online formats.

This issue features 47 articles and two review articles. One of the reviews was written by Professor Hiroshi Sawa (Nagoya Industrial Science Research Institute), who discusses ultra-precision valence electron density (VED) analysis. The VED was successfully extracted using high-performance X-ray diffraction, primarily at BL02B1, and the core-differential Fourier synthesis (CDFS) method. Visualization of 3*d* orbitals for several representative examples is presented. A recent activity report from his group is also included in this issue. The other review is contributed by Dr. Takeshi Morikawa (Toyota Central R&D Labs., Inc.). It is well known that industrial users account for approximately 20% of all SPring-8 users, with Toyota being one of the most active. They use various analysis techniques available at SPring-8 and SACLA. Dr. Morikawa introduces one of the key results from ongoing research on artificial photosynthesis.

SPring-8/SACLA Research Frontiers is composed primarily of two sections. The first, "Scientific Frontiers," presents the scientific results. The second provides additional information on the hard and soft infrastructures that support scientific research. Although some important parameters, such as the operation time, are included in the second section, other comprehensive and up-to-date statistical data on the operation of SPring-8 and SACLA can be found on our website: http://www.spring8.or.jp/en/about_us/spring8data/.
The full text of SPring-8/SACLA Research Frontiers is available at:
http://www.spring8.or.jp/en/news_publications/publications/research_frontiers/.
For the list of publications by SPring-8 users and staff, please visit our publication database:
http://www.spring8.or.jp/en/science/publication_database/.

On behalf of all the editors, I would like to express our sincere gratitude to those who recommended excellent research results for inclusion in this issue, as well as the users and staff of SPring-8, who contributed their reports.

Toyohiko Kinoshita
Japan Synchrotron Radiation Research Institute (JASRI)

Editorial Board

Scientific Frontiers

Review Article

Ultra-precision valence electron density analysis: Unlocking quantum parameters with synchrotron X-ray diffraction

1. Introduction

Advances in synchrotron X-ray radiation has enabled previously challenging or impossible measurements, allowing refinement of numerous experimental techniques. This review explores the capabilities of X-ray diffraction, a fundamental application of synchrotron radiation.

Structural-property research elucidates physical properties through crystallographic information. While referencing crystal structures is standard in solid-state physics, recent advances in material synthesis have allowed precise structural control. Improved measurement techniques have also revealed unique physical phenomena that cannot be fully explained by conventional crystallographic data alone.

Band structure calculations are the primary approach used to understand physical properties and predict material behavior when accurate crystal structure data are available. However, for strongly correlated electron materials, where competing interactions exist, band calculations alone fail to capture the essential physics. First-principles calculations have expanded this approach, but inherent approximations and scalability issues sometimes yield contradictory results, particularly in time evolution via molecular dynamics and electronically excited states.

Experimental elucidation of electronic states thus remains crucial. While spectroscopic methods using synchrotron radiation have advanced [1,2], diffraction experiments still focus on powder diffraction and microcrystal analysis. High-precision single-crystal X-ray diffraction remains an underdeveloped approach in Japan. To address this, we introduced "ultra-precision analysis," which allows successful determination of quantum parameters from valence electron density (VED). This method enables experimental analysis even in high-temperature metastable states, paving the way for further advancements.

2. Investigating chemical bonding

Using the core-differential Fourier synthesis (CDFS) method, we successfully extracted only the VED within a crystal, which directly contributes to its physical properties. This method uses single-crystal X-ray diffraction data obtained from synchrotron radiation. A key advantage of our approach is that it does not require a quantum mechanical model, making it applicable to any single crystal approximately ten micrometers in size. The details of the analytical method have been described previously [3,4]. However, before delving into these specifics, we first introduce fundamental concepts of hybrid orbitals and chemical bonding, as described in textbooks, after which we explain high-resolution electronic orbital visualization and its physical implications to demonstrate the utility of our approach.

To investigate the σ-bonding in carbon–carbon interactions, we examined the glycine molecule, one of the simplest amino acids [5]. Figure 1(a) presents its structural formula alongside a conceptual representation of the surrounding electron cloud. The electron cloud's spatial distribution is described using the same conceptual framework as that for the bonding electron density in a hydrogen molecule. Figure 1(b) displays the experimentally obtained the VED distribution of crystalline glycine. Rather than having a smooth distribution, the VED is markedly inhomogeneous and discrete across the entire molecule. The cross-sectional view of the electron density (Fig. 1(c)) reveals distinct toroidal nodes (regions devoid of electron clouds) around carbon atoms C1 and C2, along with a significantly reduced electron density at the midpoint of the C1–C2 bond, where bonding orbitals are expected.

This seemingly counterintuitive pattern can be more clearly interpreted when considering that *sp* hybrid orbitals are formed by a combination of 2*s* and 2*p* orbitals. Unlike 1*s* orbitals, 2*s* orbitals, which possess a spherical distribution, exhibit nodal structures in the radial direction, resulting in a dual-shell configuration. This characteristic arises from the phase properties of the 2*s* orbital wave function. By experimentally identifying structural features of VED distributions, the wave functions that contribute to bond formation can be determined.

The experimentally obtained VED distribution aligned remarkably well with the results from long-range corrected-density functional theory. This agreement enabled distinction of orbital components within the

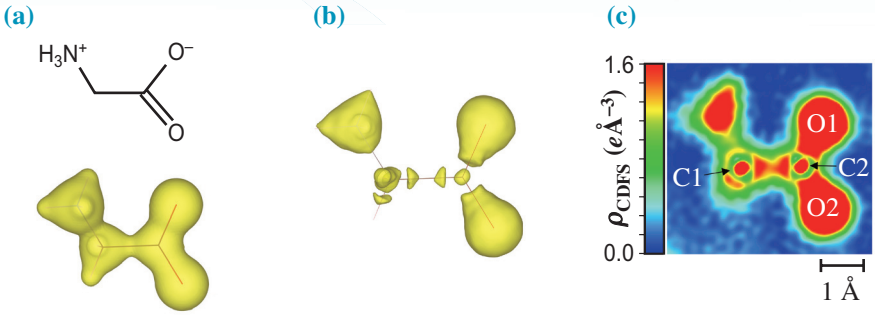

Fig. 1. Glycine: **(a)** chemical structure and an electron distribution model diagram drawn using the VESTA, **(b)** experimentally obtained valence electron density distribution, **(c)** cross-sectional view of the valence electron density.

VED by integrating experimental results with theoretical calculations. Consequently, we successfully visualized the distinctions between single and double bonds in chemical structures and captured the representation of π-electrons positioned above and below the plane of six-membered rings. This finding suggested the potential for directly applying molecular orbital concepts to molecular design in the field of chemistry.

3. Concepts of the core differential Fourier analysis method

To extract only the VED from diffraction data, we fully exploited the characteristics of atomic electron density distributions. As shown in Fig. 2, the atomic scattering factor for X-rays depends on the magnitude of the scattering vector, expressed as $\sin\theta/\lambda$, where λ is the X-ray wavelength and θ is the scattering angle. In conventional structural analysis, atomic scattering factors, based on the total electron density distribution of atoms, are used (black line). However, quantum mechanical computational methods enable the separation of contributions from inner-shell electrons (blue line) and valence electrons (orange line). Since inner-shell electrons are spatially confined, their contribution remains smooth, even at high scattering angles. In contrast, valence electrons exhibit a more extended spatial distribution and predominantly contribute to the low $\sin\theta/\lambda$ region. An important point is that the scattering factor of inner-shell electrons and the total atomic scattering factor almost overlap in the high-angle region.

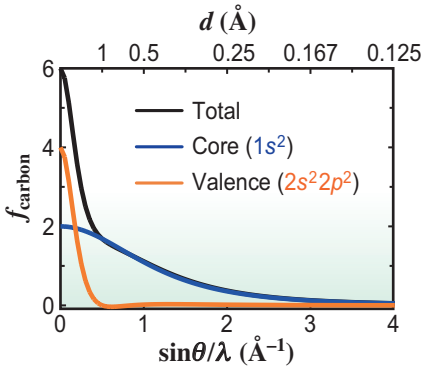

Fig. 2. Atomic scattering factor of carbon. The black line represents total electrons, the blue line corresponds to core-shell electrons ($1s^2$), and the orange line represents the valence electron components ($2s^22p^2$). The horizontal axis indicates the magnitude of the scattering vector, calculated from the X-ray wavelength (λ) and the scattering angle (θ).

Therefore, precise atomic positions can be determined using only high-angle X-ray diffraction data, which requires high-energy synchrotron X-rays. Based on this distribution, subtracting the contribution of the inner-shell electron density from the total X-ray diffraction measurements isolates the VED. The mathematical formulation of this process is detailed in Ref. [4], and a conceptual illustration is provided in Fig. 3. Consequently, to determine precise atomic positions (phase factors), refining the structure by using only high-angle X-ray diffraction data is sufficient. This principle underscores the advantage of high-energy X-rays for precise structural analysis, which is one of the key benefits of synchrotron X-rays.

Since VED information is crucial for understanding chemical bonding and physical properties, a fraction—approximately one-tenth to one-hundredth—of the total electron count of the chemical formula must be extracted. In terms of diffraction intensity, this corresponds to the square of these ratios. Consequently, stringent experimental constraints are imposed on the dynamic range, statistical precision, and spatial resolution of the diffraction intensities. If any of these conditions are not met, the reliability of the obtained information is severely compromised. High-quality synchrotron radiation X-rays, as quantum beams, play a crucial role in satisfying these stringent requirements. Further details on the beamline are described elsewhere [6].

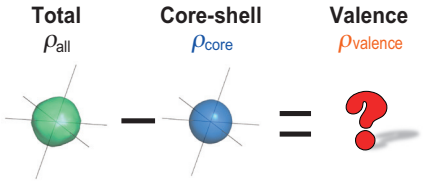

Fig. 3. Conceptual diagram of extracting only the valence electron density. Note that the total electron density distribution cannot be directly observed.

4. Observing 3*d* orbitals of transition metal at even higher resolution

By analyzing electron density using the CDFS method, we successfully observed σ bonds and double-bond states directly in small organic molecular crystals, demonstrating both the mechanism and reliability of this method. Nevertheless, extracting information that directly contributes to physical properties—such as the orbital degrees of freedom in transition metal oxides within strongly correlated electron systems—demands even higher spatial

resolution. Therefore, we attempted to observe the anisotropic 3*d* orbitals of a transition metal ion.

The target material for this study was the perovskite-type oxide $YTiO_3$, which has been extensively investigated as a standard material for orbital observation experiments since the 1970s (Fig. 4(a)). $YTiO_3$ is a Mott insulator in which the magnetic Ti^{3+} ion possesses 19 electrons, of which 18 inner-shell electrons form an overall isotropic spherical distribution and contribute minimally to its physical properties. The physical properties of the system are primarily governed by a single valence electron occupying the Ti 3*d* orbital. Due to the presence of a single electron in a doubly degenerate t_{2g} orbital, orbital degrees of freedom exist, and theoretical predictions suggest that electron correlation induces an antiferro-orbital ordered state (i.e., electrons at adjacent sites occupy different orbitals), resulting in ferromagnetism through the Kugel–Khomskii interaction.

Numerous experimental and theoretical studies have predicted the orbital state and the butterfly-shaped VED distribution, as shown in Fig. 4(b). The experimental details have been described previously [4]. Figure 4(c) presents the results of the CDFS analysis. The VED localized at the center of the TiO_6 octahedron clearly exhibits the butterfly-like shape of the 3*d* orbital, as depicted in quantum mechanics textbooks. This confirms the successful extraction of the VED distribution corresponding to the 3*d* orbital wave function without assuming any quantum mechanical model. Extracting quantum parameters of the 3*d* orbital from this anisotropic VED distribution yielded qualitative agreement with previous experimental and theoretical calculations, demonstrating that the quantum parameters of the Ti^{3+}: $3d^1$ orbital can be directly determined from the VED.

The relationship between the spatial resolution of the obtained diffraction data and the VED should also be considered. Figure 5 illustrates how the VED (cross-sectional view) changes with variation of the maximum scattering parameter $(\sin\theta/\lambda)_{max}$ used in the CDFS analysis. The X-ray diffraction data used for the CDFS analysis were identical in all aspects, except for the resolution. Figure 5(c), obtained using diffraction data with $(\sin\theta/\lambda)_{max}$ = 2.0 Å^{-1}, clearly reveals the anisotropy of the 3*d* orbital. However, the resolution of an X-ray diffraction apparatus using characteristic laboratory-based X-rays (Mo *K*α: λ = 0.71 Å) is limited to approximately $(\sin\theta/\lambda)_{max}$ ≈ 1.32 Å^{-1} (d_{min} ≈ 0.38 Å), preventing observation of orbital anisotropy. As previously mentioned, valence electron information is primarily contained in low-angle scattering intensities, but high-angle diffraction intensities are essential for accurately capturing the spatial anisotropy of VED.

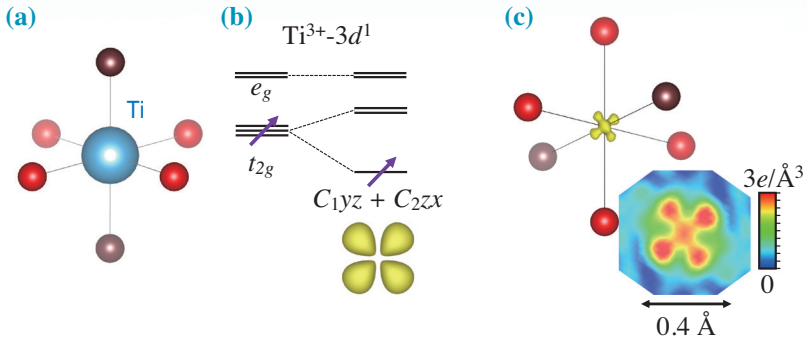

Fig. 4. **(a)** TiO_6 octahedron, **(b)** electron configuration of Ti^{3+}. Orbital degrees of freedom are lost due to both the distortion of the TiO_6 octahedron and electron correlation. **(c)** Experimentally obtained valence electron density distribution of Ti^{3+} [2].

5. Observing degenerate 3*d* orbitals

As noted earlier, several studies have reported the direct observation of orbital-ordered states. However, there remains a significant lack of research on the electron density observation of systems with orbital degrees of freedom, which are expected to exhibit strong responses to external fields. This study aims to investigate electron orbitals in which multiple electrons are localized within degenerate orbital states, without charge degrees of freedom, due to strong electron correlation.

The material investigated in this study, FeV_2O_4, has a spinel-type structure consisting of FeO_4 tetrahedra and VO_6 octahedra. In its high-temperature phase, it crystallizes in a cubic system with space group $Fd\bar{3}m$ (No. 227), exhibiting high symmetry. The formal valence states are Fe^{2+} and V^{3+}, corresponding to six and two 3*d* electrons, respectively. Due to the presence of geometric frustration in electronic correlations,

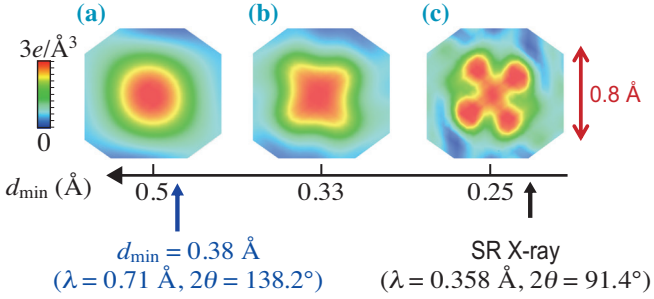

Fig. 5. Valence electron density distribution of Ti^{3+} with varying resolution. The same diffraction data were used for the CDFS analysis.

the spin, orbital, and lattice degrees of freedom are intricately intertwined, resulting in three structural and magnetic phase transitions upon cooling. Although various theoretical predictions have been made regarding the ground state, as discussed below, misinterpretations of the state with orbital degrees of freedom have hindered a full understanding.

For VO_6 octahedra at the V site in the cubic phase above 140 K, if a perfect octahedron is assumed, crystal field theory (O_h symmetry) predicts that the 3*d* orbitals would split into triply degenerate t_{2g} orbitals ($|yz\rangle$, $|zx\rangle$, $|xy\rangle$) and doubly degenerate e_g orbitals. The two 3*d* electrons of V^{3+} occupy the stabilized t_{2g} orbitals, preserving orbital degrees of freedom and leading to an expected $3d^2$ electron distribution (Fig. 6(a)). In the ground state, the system adopts tetragonal symmetry, and theoretical predictions suggest that a Jahn–Teller distortion along a specific axis would stabilize the electronic state, resulting in an orbital-ordered state.

However, the experimentally observed VED distribution of V^{3+} (Fig. 6(b)) exhibits pronounced anisotropy, indicating that the observed state is not a degenerate orbital state. This discrepancy arises because the VO_6 octahedra in the unit cell are not perfect octahedra. The site symmetry of V is $\bar{3}m$, possessing only a single, three-fold, improper rotation axis. Consequently, from a symmetry perspective, the octahedra are allowed to distort along the three-fold axis. Examination of the VO_6 octahedra within the unit cell confirms that they elongate along the $\langle 111 \rangle$ direction.

Under such D_{3d} distortion, the t_{2g} orbitals split into a doubly degenerate state and a singly occupied orbital. The quantization axis aligns with $\langle 111 \rangle$, uniquely determining the wave function of the singly occupied orbital, as shown in Fig. 6(c). The twofold degenerate orbitals remain undetermined, except for the condition that the three orbitals, including ϕ_1, must be mutually orthogonal. Consequently, even under D_{3d} distortion, the system retains orbital degeneracy.

The obtained VED distribution can be remarkably well explained by a model in which electrons probabilistically occupy ϕ_1 and the doubly degenerate orbitals. Further details are provided in the literature; however, this study represents the first direct observation clarifying how degenerate orbital electronic states manifest experimentally [7]. The theoretical predictions of the orbital ordering transition represent a typical case where the failure to account for the existence of ϕ_1 prevented reaching the correct conclusion.

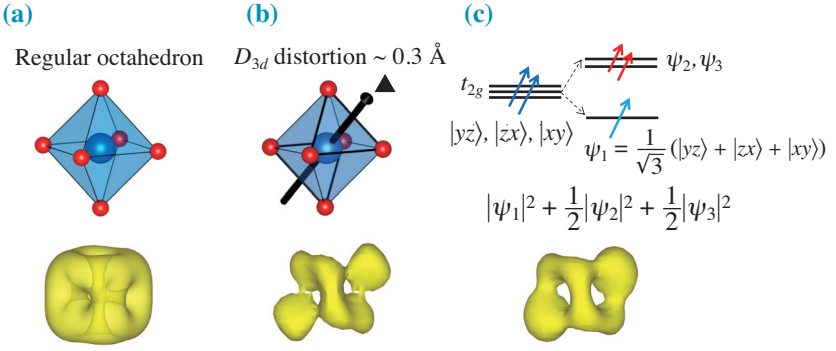

Fig. 6. Spinel structure FeV_2O_4 in the cubic phase $Fd\bar{3}m$: 3*d* orbital state of V^{3+} ($3d^2$: $S = 1$) in VO_6. **(a)** In the case of a regular octahedron, the 3*d* orbitals would be a cubic shape (simulation). **(b)** The VO_6 octahedron with D_{3d} distortion and an experimentally obtained valence electron density distribution. **(c)** Simulation results are estimated using quantum mechanical calculations with hydrogen-like wave functions.

6. Conclusion

As demonstrated above, this study introduced ultra-high-precision VED analysis using synchrotron radiation. Single-crystal diffraction experiments typically require various corrections, such as anisotropic absorption correction, multiple scattering, simultaneous reflection, and extinction effects. However, in practice, systematic errors arising from measurement conditions and detector characteristics often present more significant challenges. We successfully established a new analytical technique by using thorough adjustments and validations in collaboration with the facility staff. Our study demonstrated that by leveraging a high-quality X-ray source at SPring-8, qualitatively distinct analyses beyond conventional laboratory-based experiments can be achieved. As facilities and instrumentation continue to advance, the cutting-edge techniques described here may soon become standard methodologies. Furthermore, we are actively collaborating with synchrotron facilities to extend this VED observation method to operando measurements, accommodating multi-extreme conditions and external field responses.

Hiroshi Sawa†

Dept. Applied Physics, Nagoya University

Email: hiroshi.sawa@nagoya-u.jp

† Present address:
Nagoya Industrial Science Research Institute

References

[1] J. Itatani *et al.*: Nature **432** (2004) 213.
[2] H. Hafiz *et al.*: Nature **594** (2021) 213.
[3] S. Kitou *et al.*: Phys. Rev. Lett. **119** (2017) 065701.
[4] S. Kitou *et al.*: Phys. Rev. Res. **2** (2020) 033503.
[5] T. Hara *et al.*: J. Am. Chem. Soc. **146** (2024) 23825.
[6] K. Sugimoto *et al.*: AIP Conf. Proc. **1234** (2010) 887.
[7] T. Manjo *et al.*: Mater. Adv. **3** (2022) 3192.

Review Article

Artificial photosynthesis utilizing solid semiconductors and molecular metal complexes

1. Introduction

Since the establishment of SPring-8, researchers at Toyota Central R&D Labs. have extensively utilized it for the analysis of materials and devices for automotive technology, such as catalysts for exhaust gas purification and environmental cleanup, energy-storage batteries, and fuel cells. We express our sincere gratitude for this. Among these technical targets, this review highlights recent results on artificial photosynthesis, promoted as research ahead of time. This technology is expected to contribute to a sustainable society in the future, and the structural characteristics and dynamic behaviors of materials and devices obtained at SPring-8 and SACLA are valuable for progress in this research field.

Artificial photosynthesis is an uphill reaction technology that stores solar energy as chemical bond energy in small molecules by directly synthesizing organic compounds from carbon dioxide (CO_2) and water (H_2O) under mild conditions, such as a near ambient temperature and pressure under sunlight irradiation (Fig. 1). This technology involves a CO_2 reduction reaction (CO_2RR), which uses electrons and protons extracted from H_2O molecules via an oxidation reaction. We do not need to synthesize sugars as in natural photosynthesis, and prefer to obtain chemical raw materials, fuels, and other substances necessary for human society. To date, particulate photocatalysts, photoelectrodes, and photovoltaic (PV)-powered catalyst electrodes have been studied worldwide. However, CO_2 molecules are end products of the combustion of various organic compounds and are highly stable under ambient conditions, making it difficult to achieve a highly efficient CO_2RR.

Recently, however, our research group demonstrated that the solar-to-chemical energy conversion efficiencies have reached 4–20% at electrode scales ranging from 1 cm^2 to 1 m^2 for generating molecules smaller than sugars [1,2]. From the viewpoint of electrical energy conversion, the efficiencies of these systems exceeded 70%. Based on these demonstrations, novel visible-light-absorbing semiconductors, metal complex catalysts for the CO_2RR, and inorganic catalysts for water oxidation are required at the present stage. This review presents results obtained at SPring-8 BL33XU, BL47XU, as well as SACLA BL3 to understand the functions of these high-value materials in improving artificial photosynthetic systems.

2. Practical approach to artificial photosynthetic system for CO_2RR

Many studies have applied solid semiconductors or molecular metal complexes as photocatalysts under light irradiation in artificial photosynthetic systems. The catalytic reaction rate of these semiconductors can be enhanced by the surface loading of inorganic co-catalysts. The development of this technology relies on understanding the physical properties of individual materials for light absorption, charge separation, electron transfer, and catalytic reactions. Combining these materials without substantial energy loss is essential to achieving high conversion efficiency in the entire system. A new approach has recently emerged to realize solar-driven CO_2RR, that is, hybrid photosystems of solid semiconductors and molecular metal complex catalysts, which combine the functions of light absorption and charge separation of the semiconductors with the catalytic

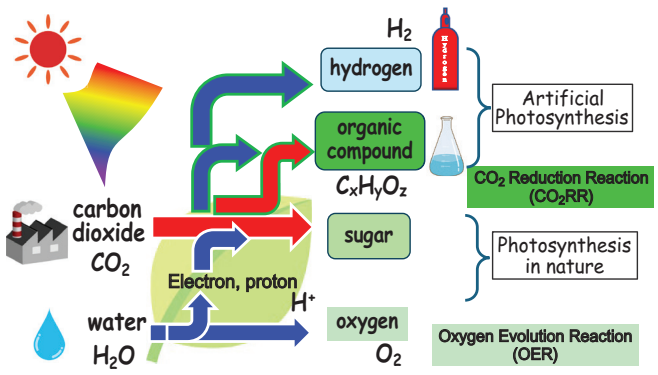

Fig. 1. Simplified schematic illustration of photosynthesis in plants and artificial photosynthesis. Conversion of CO_2 and H_2O to organic compounds under sunlight is the target.

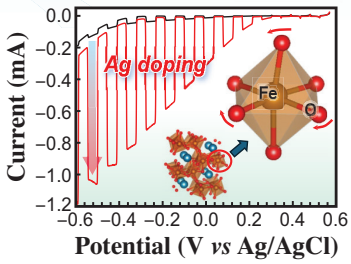

Fig. 2. Current–potential curves measured in O_2-saturated aqueous K_2SO_4 solution under chopped Xe-lamp light irradiation for Ag-doped $CaFe_2O_4$ photocathode. Inset shows crystal structure of $CaFe_2O_4$ and Fe–O octahedra.

functions of the metal complexes in a complementary manner. After demonstrating the high energy efficiencies and product selectivity mentioned in the introduction, the facilities and measurement technology at SPring-8 and SACLA are powerful tools for clarifying the structural and electronic aspects of new materials for application to artificial photosynthetic system platforms. The case studies are presented in this article.

3. Structural analyses of semiconductor and inorganic co-catalysts

The valence states of Cu and Ag co-catalysts for CO_2RR, supported on UV-responsive oxide semiconductor photocatalysts such as Nb_3O_8 nanosheets, particulate $SrTiO_3$:Al, Ga_2O_3, and $CaTiO_3$, have been investigated using X-ray absorption near edge structure (XANES) analysis at SPring-8 [3–5]. The local structure of the oxide semiconductor is also examined. This information supports our understanding of the photocatalytic reactions. Hybrid photosystems composed of semiconductors and molecular catalysts drive the CO_2RR with high efficiency under visible-light irradiation [6]. In $CaFe_2O_4$, which absorbs visible light with wavelengths shorter than 650 nm, Ag doping significantly enhances the photoelectrochemical reaction current. This improvement is attributed to the increased mobility of photoexcited carriers. Combined XANES analysis and Fourier transform of k^2-weighted extended X-ray absorption fine structure (FT-EXAFS), and X-ray diffraction (XRD) analyses suggested that the increased carrier mobility may originate from an improvement in the symmetry of the initially distorted Fe-centered octahedral coordination surrounded by six oxygen atoms in the orthorhombic crystal (Fig. 2) [7].

4. Band bending by angular-resolved HAXPES

In semiconductor photoelectrodes, band bending in the semiconductor, which extends from the bulk to the surface, is a critical factor for electron transfer from the semiconductor to the co-catalyst. Electronic interactions between the semiconductor surface and co-catalysts also play a vital role in determining the activity of the co-catalysts. Angular-resolved hard X-ray photoelectron spectroscopy (AR-HAXPES) is a valuable technique for investigating them by varying the take-off angle (θ_{toff}) of the detector.

Figure 3 displays AR-HAXPES spectra for the Ti $2p_{3/2}$ and Ta $3d_{5/2}$ core-state photoemissions of TiO_2 and N-doped Ta_2O_5 films, which exhibit n-type and p-type conduction, respectively [8]. N-Ta_2O_5 is the semiconductor used in the world's first demonstration of visible-light-driven photocatalytic CO_2RR in a hybrid photosystem [9]. The bare TiO_2 films exhibited similar spectral shapes at θ_{toff} of 65° (bulk phase; maximum analysis depth d of ~31 nm) and 10° (surface; d ~6 nm), with no significant shifts. However, the peak position of Ti $2p_{3/2}$ in bare TiO_2 (Fig. 3(a)) shifted negatively by 0.25 eV toward the surface upon loading a nanoscale Pt catalyst (Pt/TiO_2) (Fig. 3(b)). In contrast, for bare N-Ta_2O_5, the peak

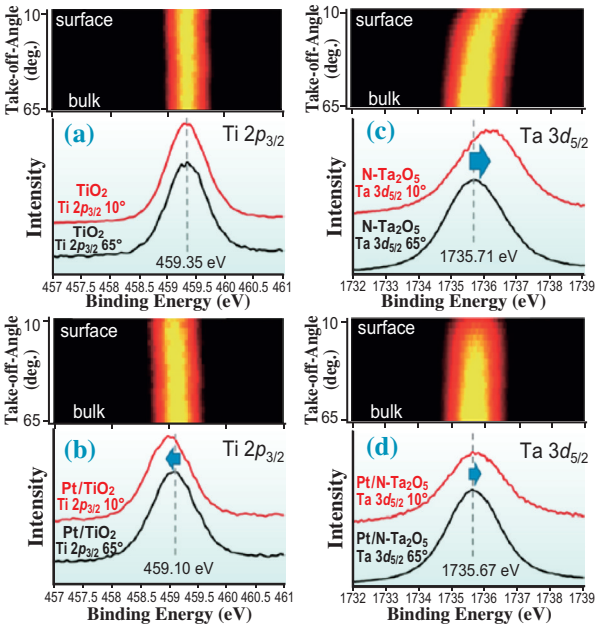

Fig.3. Series of Ti $2p_{3/2}$ spectra measured on **(a)** TiO_2 and **(b)** Pt/TiO_2 using angular-resolved HAXPES [θ_{toff}s 10° (red line) and 65° (black line)]. The upper panel represents a single shot of Ti $2p_{3/2}$ peaks from a 2D image for θ_{toff}s from 10° to 65°. Series of Ta $3d_{5/2}$ spectra measured on **(c)** N-Ta_2O_5 and **(d)** Pt/N-Ta_2O_5 by angular-resolved HAXPES (θ_{toff} of 10° and 65°). The upper panel is a single shot of Ta $3d_{5/2}$ peaks from a 2D image of θ_{toff}s from 10° to 65°. [8]

at θ_{toff} of 10° (surface; d ~5 nm) shifted by 0.40 eV toward a higher binding energy compared to that at θ_{toff} of 65° (bulk phase; d ~24 nm), indicating a significant downward band bending toward the surface (Fig. 3(c)). This 0.40 eV band bending was drastically reduced to 0.05 eV upon Pt surface loading (Fig. 3(d)), suggesting a stronger electrostatic interaction between Pt and N-Ta_2O_5. A similar trend was observed for metallic Rh and Au nanoparticles, and these interaction differences significantly affected the properties of the semiconductor photoelectrodes.

In contrast, surface linkages with molecular Ru and Re complex catalysts, in which metal ions are coordinated with bipyridine ligands, exhibited a minor effect on band bending [6]. These results indicate that the metal complexes have minimal influence on the electronic state of the semiconductor surface. However, an FT-IR spectroscopy investigation demonstrated that TiO_2 withdrew electrons from the Ru center of the complex at the CO_2RR site, whereas N-Ta_2O_5 did not. These results indicate that the CO_2RR activity at the Ru complex could be significantly altered when attached to TiO_2. These findings provide valuable insights into the design of nanoscale metal and metal complex catalysts for applications in semiconductor-based photosystems.

5. *Operando* XAS

A prominent trend in catalysis research is *operando* XAFS analysis, which allows for real-time analysis of catalysts under actual operating conditions, offering insights into their catalytic behavior. This requires specially designed reactors tailored to the physical form of the catalyst and specific operational parameters. These factors include the flow rates of the aqueous solution and gaseous CO_2, as well as the application of light and electrical energy. Once an optimized setup is established, *operando* XAFS serves as a powerful tool for investigating structural transformations during catalytic CO_2RR and the oxygen evolution reaction (OER) by water oxidation.

Our research demonstrated that the performance of electrocatalytic CO_2RR in aqueous solutions was significantly improved when using Mn, Co, and Re complex catalysts, which was attributed to the synergistic effect with K^+ and the carbon support. In particular, for the Co tetrapyridinoporphyrazine complex catalyst ([Co(PyPc)]), *operando* XANES confirmed that K^+ is essential for maintaining catalyst stability during operation, although detailed structural analysis was not possible due to the small amount of catalyst (Fig. 4) [10]. In a membrane electrode assembly (MEA) setup, the overpotential for CO_2RR was significantly reduced, enabling [Co(PyPc)] to effectively generate CO at an exceptionally low cell voltage of 1.9 V, achieving a reaction current density of 100 mA/cm^2. The turnover number, that is, the molar ratio of the produced CO to [Co(PyPc)], reached 3,800,000.

In another case study, *operando* XANES of a Br-bridged dinuclear Cu molecular electrocatalyst, facilitating the production of ethanol, ethylene, and propanol, confirmed the stability of the Cu(I) state during the CO_2RR [11].

The development of water-oxidation catalysts is also essential. Catalysts composed of earth-abundant elements are necessary to construct artificial photosynthesis systems in an environmentally sustainable manner. One example is an electrode composed of Ni-doped β-FeOOH(Cl) hyperfine nanorods coated with Fe-incorporated Ni hydroxide (β-FeOOH:Ni/Ni(OH)$_2$:Fe), with an average size of ϕ5 × 16 nm. The nanorods are synthesized at ambient temperature and normal pressure (β-FeOOH:Ni/Ni(OH)$_2$), and post-treatment at 200°C in KOH facilitates the diffusion of Fe and Ni between the core β-FeOOH:Ni and the surface amorphous Ni(OH)$_2$:Fe, resulting in a low overpotential for the electrochemical OER (Fig. 5(a)) [12]. *Operando* XANES and EXAFS were conducted in a CO_2-saturated pH 6.9 solution were conducted at the open-circuit potential (OC), where the OER did not occur. Along with XRD and Mössbauer spectroscopy, lattice distortion in the core β-FeOOH:Ni and the formation of short-range-ordered β-Ni(OH)$_2$:Fe were confirmed. Furthermore, under aqueous OER conditions (+1.6 V *vs* RHE), Fe *K*-edge spectra revealed a shortening of the Fe–Fe distance in the core β-FeOOH:Ni, while Ni *K*-edge spectra indicated a transition of short-range-ordered β-Ni(OH)$_2$:Fe toward β-NiOOH:Fe at the nanorod surface (Figs. 5(b,c)). The structural transformation was reversible and corresponded to an applied electrical bias. The dynamic change in structure responding to the electrical bias is a key factor in the enhanced OER activity compared to the as-synthesized β-FeOOH:Ni/Ni(OH)$_2$.

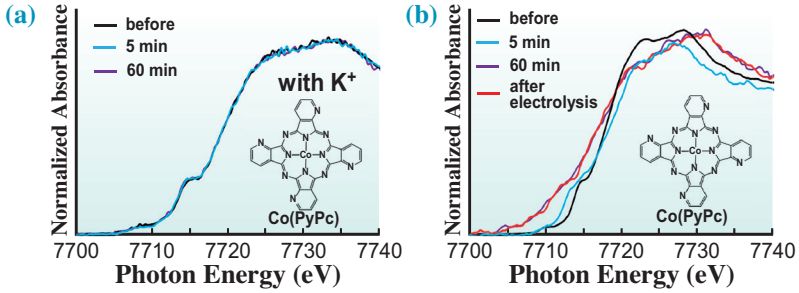

Fig. 4. *In situ* XANES spectra of molecular Co-catalyst with and without K salt. Spectra of (**a**) [Co(PyPc)] + K/carbon and (**b**) [Co(PyPc)]/carbon electrodes are measured at –1.4 V (*vs* Ag/AgCl) in CO_2-saturated aqueous solution [before electrolysis (black), 5-min electrolysis (blue), 60-min electrolysis (purple), and after electrolysis (red)].

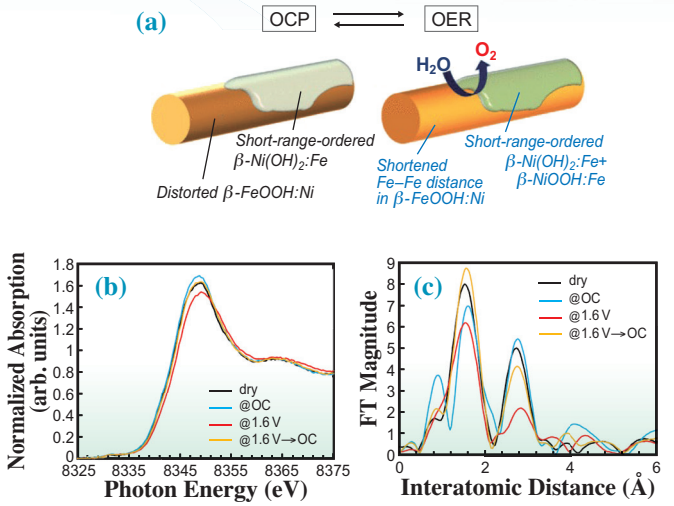

Fig. 5. *Operando* XAFS spectra acquired during the OER over the β-Fe/Ni electrode in aqueous KBB solution. **(a)** Ni *K*-edge XANES and **(b)** Ni *K*-edge EXAFS spectra. Conditions are (—) in air (dry), (—) in the solution without an electrical bias (OC), (—) in the solution under OER conditions of +1.6 V *vs* RHE, and (—) at OC after the OER.

6. Photoexcited electron transfer in an iridium complex photocatalysts measured at SACLA

Intersystem crossing (ISC) from the singlet excited state (^{1}MLCT) to the triplet excited state (^{3}MLCT) in photoexciton is a well-known ultrafast process. With the advancements in X-ray free electron lasers (XFELs), transient X-ray spectra can be recorded at a time resolution of less than 100 fs. Femtosecond time-resolved X-ray absorption near-edge structure (TR-XANES) spectroscopy was employed to investigate the visible-light excitation dynamics of mononuclear iridium(III) terpyridine (tpy) 2-phenylpyridine (ppy) ([Ir(tpy)(ppy)Cl]$^+$), a photocatalyst for CO_2RR. ISC was observed, revealing that the photoexcited MLCT had a lifetime of 114 fs. Theoretical calculations successfully reproduced the TR-XANES spectral changes in the molecule, directly capturing the rapid structural transformation around the Ir atom associated with ISC to the hot triplet state (Fig. 6). In contrast, subsequent relaxation to the lowest triplet state via internal conversion was not detected, suggesting that this process primarily occurs at ligands such as tpy rather than around the Ir center [13].

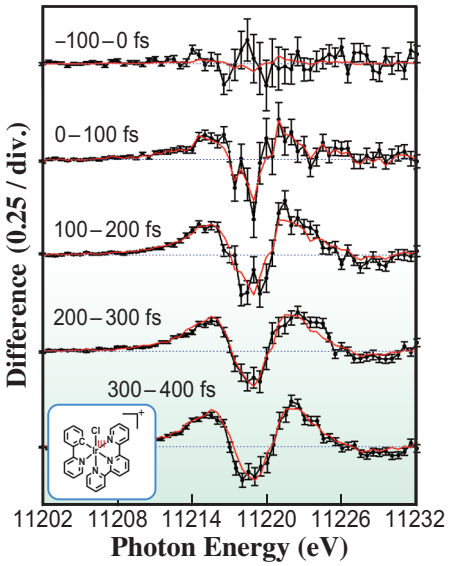

Fig. 6. Femtosecond TR-XANES spectra of [Ir(tpy)(ppy)Cl]$^+$ in acetonitrile.

7. Summary

Continuous research is necessary for artificial photosynthesis to reach a stage at which it can be regarded as a practical technology for future energy carrier production and environmental conservation. To this end, the analyses of key component materials related to light absorption, charge separation, catalytic functions, and their combinations at SPring-8 and SACLA are indispensable. Furthermore, expanding the application of these techniques and developing new methodologies for measurements under device conditions are anticipated.

Takeshi Morikawa

Toyota Central R&D Labs., Inc.

Email: morikawa@mosk.tytlabs.co.jp

References

[1] T. Arai *et al.*: Energy Environ. Sci. **8** (2015) 1998.
[2] N. Kato *et al.*: ACS Sustainable Chem. Eng. **9** (2021) 16031.
[3] G. Yin *et al.*: ACS Nano **9** (2015) 2111.
[4] S. Wang *et al.*: Sustainable Chem. Eng. **9** (2021) 9327.
[5] H. Qiu *et al.*: ACS Catal. **13** (2023) 3618.
[6] T. Morikawa *et al.*: Acc. Chem. Res. **55** (2022) 933.
[7] K. Sekizawa *et al.*: ACS Appl. Mater. Interfaces **6** (2014) 10969.
[8] S. Sato *et al.*: SPring-8 Research Frontiers 2018 (2019) 11.
[9] S. Sato *et al.*: Angew. Chem. Int. Ed. **49** (2010) 5101.
[10] S. Sato *et al.*: Sci. Adv. **9** (2023) eadh9986.
[11] N. Sakamoto *et al.*: Nat. Catal. **7** (2024) 574.
[12] T. M. Suzuki *et al.*: ACS App. Energy Mater. **7** (2024) 9689.
[13] K. Yamanaka *et al.*: J. Photochem. Photobiol. A Chem. **435** (2023) 114267.

Time-resolved crystallography of ultrafast light driven DNA repair by photolyases

Photolyase is an enzyme that repairs DNA lesions caused by ultraviolet (UV) exposure, such as cyclobutane pyrimidine dimers (CPDs), in which the C5 and C6 carbons of one pyrimidine base covalently bond with the C5' and C6' carbons of an adjacent base [1] (Fig. 1). The catalytic process of CPD photolyases involves multiple redox reactions. The enzyme is first activated through the photoreduction of its coenzyme, flavin adenine dinucleotide (FAD), from its oxidized form (FAD_{ox}) to its reduced form ($FADH^-$) [2]. This photoreduction process requires two single-electron transfer steps, mediated by an electron transfer chain that includes three tryptophan residues.

We employed time-resolved serial femtosecond crystallography (TR-SFX) to elucidate the structural mechanism underlying the photoreduction processes in the *Methanosarcina mazei* class II CPD photolyase (*Mm*CPDII) [3]. Our analysis revealed an Asn/Arg-Asp redox sensor triad that regulates FAD rehybridization and protonation. Additionally, we observed buckling and twisting of the isoalloxazine ring of the coenzyme FAD, occurring within the submicrosecond regime following the light-triggered electron transfer step [3]. This TR-SFX investigation of the photoreduction process provided a foundation for studying the main function of the *Mm*CPDII photolyase—the repair of CPD lesions. We further elucidated the dynamic structural mechanisms of DNA repair through time-resolved crystallographic analyses conducted at the X-ray free electron laser (XFEL) facilities, SACLA **BL2** and SwissFEL Alvra.

Crystals of enzyme-DNA complexes in the pre-reaction state were grown under dark and anaerobic conditions by mixing reduced photolyase with damaged DNA [4,5]. Blue light, which triggers the reaction, was applied to the crystals, followed by XFEL irradiation at time intervals ranging from picoseconds to sub-milliseconds, to capture diffraction patterns [5]. By analyzing tens of thousands of diffraction images, we reconstructed the three-dimensional structures of the enzyme and DNA during the repair process as a series of snapshots.

Two series of TR-SFX experiments were conducted: one from picoseconds (ps) to nanoseconds (ns), and the other from nanoseconds to microseconds (μs) [5]. The CPD repair begins at 100 ps, with Arg256 (R256) becoming dynamic and moving to stabilize the CPD. This suggests the initiation of the forward electron transfer from the $FADH^-$ to the CPD (Figs. 2 and 3). By 650 picoseconds (ps), the C5–C5' bond of the CPD is predominantly split, and by 1 ns, the C6–C6' bond is also split (Fig. 3). During the following 500 ns, R256, a five-water cluster (5WC), and the $FADH^-$ coenzyme gradually return to their respective resting-state conformations. The repaired thymine bases remain within the active site during this time and begin to reanneal with the dsDNA in the microsecond range. The structures captured at 200 μs show the coexistence of a back-flipping intermediate and the reannealed product, prior to their final release from the enzyme (Fig. 3).

Overall, our results reveal the atomic mechanism by which DNA photolyases repair DNA in real time. The time-resolved intermediate structures illustrate a sequential process involving the ordered cleavage of covalent bonds, the opening of the cyclobutane ring, and the release of repaired pyrimidine bases from the enzyme, ultimately restoring the DNA double helix. DNA damage disrupts replication and transcription, leading to cellular consequences such as cell death, mutations, and carcinogenesis. This study enhances our understanding of DNA repair processes that mitigate damage linked to diseases, and is expected to accelerate the rational design of artificial enzymes and drugs using sequential structural information.

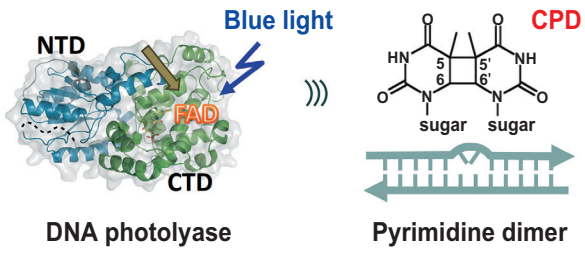

Fig. 1. Light-driven enzymatic catalysis of DNA repair by DNA photolyase. The FAD cofactor, located within the conserved folded structure of photolyase, should be fully reduced through photoreduction by the same blue light, prior to the DNA repair reaction.

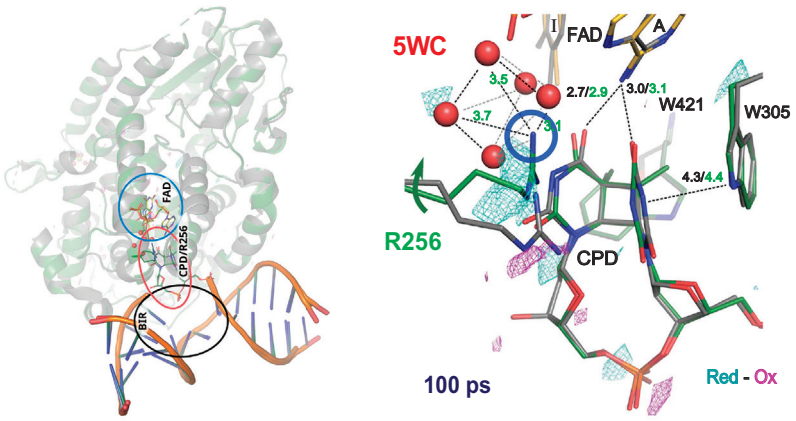

Fig. 2. *Mm*CPDII structure complexed with damaged DNA. The left panel shows the global structure, highlighting the overall fold, with the bound DNA backbone in orange. The right panel focuses on the 5WC/R256 locus in the active site at 100 ps. Interactions between the CPD; FAD and active-site residues R256, W305, and W421; and the 5WC that exclusively appears in the dark state (gray) are also depicted. In the presence of the 5WC, R256 undergoes a conformational change, with its guanidinium moiety forming the final vertex of the bipyramidal 5WC. Selected interatomic distances are indicated by dashed lines, with corresponding values in angstroms labeled nearby. [5]

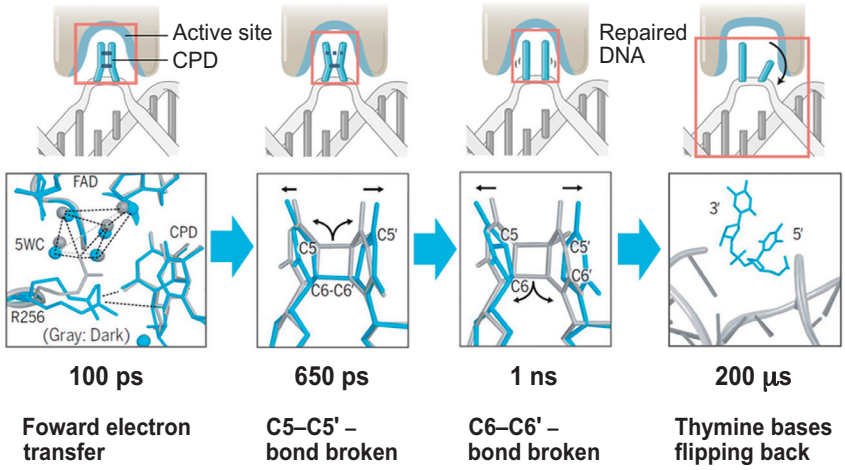

Fig. 3. Intermediates in photolyase-mediated DNA repair. The reaction is initiated by an electron transfer from the FAD cofactor embedded within the enzyme to the CPD. DNA repair by photolyase begins 100 ps after blue light irradiation. The C5–C5' bond is cleaved 650 ps after the reaction starts, followed by the cleavage of the C6–C6' bond 1 ns later. The repaired pyrimidine bases then rotate sequentially and exit the enzyme's active site, ultimately restoring the DNA double-helix structure. This last process takes approximately 200 µs, a relatively long time, and represents the rate-limiting step in the sequential enzymatic reaction. [5]

Y. Bessho[a,b,*], M. Maestre-Reyna[a,c], L.-O. Essen[d] and M.-D. Tsai[a]

[a] Institute of Biological Chemistry, Academia Sinica, Taiwan
[b] RIKEN SPring-8 Center
[c] Dept. Chemistry, National Taiwan University, Taiwan
[d] Dept. Chemistry, Philipps University Marburg, Germany

*Email: bessho@spring8.or.jp

References

[1] A. Sancar: Angew. Chem. Int. Ed. (Nobel Lecture) **55** (2016) 8502.
[2] K. Brettel and M. Byrdin: Curr. Opin. Struct. Biol. **20** (2010) 693.
[3] M. Maestre-Reyna *et al.*: Nat. Chem. **14** (2022) 677.
[4] M. Maestre-Reyna *et al.*: IUCrJ **5** (2018) 608.
[5] *M. Maestre-Reyna, P.-H. Wang, E. Nango, Y. Hosokawa, M. Saft, A. Furrer, C.-H. Yang, E. P. G. N. Putu, W.-J. Wu, H.-J. Emmerich, N. Caramello, S. Franz-Badur, C. Yang, S. Engilberge, M. Wranik, H. L. Glover, T. Weinert, H.-Y. Wu, C.-C. Lee, W.-C. Huang, K.-F. Huang, Y.-K. Chang, J.-H. Liao, J.-H. Weng, W. Gad, C.-W. Chang, A. H. Pang, K.-C. Yang, W.-T. Lin, Y.-C. Chang, D. Gashi, E. Beale, D. Ozerov, K. Nass, G. Knopp, P. J. M. Johnson, C. Cirelli, C. Milne, C. Bacellar, M. Sugahara, S. Owada, Y. Joti, A. Yamashita, R. Tanaka, T. Tanaka, F. Luo, K. Tono, W. Zarzycka, P. Müller, M. A. Alahmad, F. Bezold, V. Fuchs, P. Gnau, S. Kiontke, L. Korf, V. Reithofer, C. J. Rosner, E. M. Seiler, M. Watad, L. Werel, R. Spadaccini, J. Yamamoto, S. Iwata, D. Zhong, J. Standfuss, A. Royant, Y. Bessho, L.-O. Essen, M.-D. Tsai: Science **382** (2023) eadd7795.*

Time-resolved protein crystallography – Structural changes of the catalyst for water oxidation captured by XFEL

Photosynthetic water oxidation is catalyzed by a Mn_4CaO_5 cluster, which is bound to photosystem II (PSII), a huge membrane protein complex (Figs. 1(a,b)) [1]. Through this reaction, two molecules of water are split into four electrons, four protons, with the concomitant generation of one dioxygen, using the light energy from the sun. This reaction is important because it converts light energy to biologically useful chemical energy and generates molecular oxygen, both of which are indispensable for sustaining almost all life forms on the earth. This reaction proceeds through the so-called S-state cycle (Fig. 1(c)), in which the Mn_4CaO_5 cluster undergoes state transitions upon absorption of photons in the sequence of $S_1 \rightarrow S_2 \rightarrow S_3 \rightarrow (S_4) \rightarrow S_0$. The structure of the dark-stable S_1 state, as well as those of the meta-stable S_2, S_3 states, have been solved [2,3], and some time-resolved studies have also been conducted [4]. However, the full time-resolved structural changes of the S_2 and S_3 states have not yet been elucidated.

Using the X-ray free electron laser (XFEL) at SACLA **BL2**, we conducted pump-probe serial femtosecond X-ray crystallography (SFX) experiments of PSII microcrystals at room temperature at delay times of 20 ns, 200 ns, 1 μs, 30 μs, 200 μs, and 5 ms after either one (1F) or two (2F) flashes, corresponding to the $S_1 \rightarrow S_2$ and $S_2 \rightarrow S_3$ transitions, respectively [5]. We calculated difference *Fourier* maps between those after light illumination and before illumination ($F_{o\,(\text{after pump})} - F_{o\,(\text{before pump})}$), which sensitively detect maps of areas where structural changes have occurred. In this way, we are able to detect transient structural changes of the catalyst during the formation of the S_2 and S_3 states.

While we observed many structural changes following either 1F or 2F illumination, including both the electron acceptor and donor sides of PSII [5], we will focus these changes on the electron donor side and around the Mn_4CaO_5 cluster here. At 200 ns following 1F, P680, a chlorophyll *a* molecule of the reaction center of PSII, showed some positive density at its Mg ion, reflecting the charge separation event after light illumination (Fig. 2(a)). Accompanying this, an electron is donated to P680 through Y_Z, a Try residue of D1-Y161, from the Mn_4CaO_5 cluster. D1-F186, a residue lying between Y_Z and P680, is shifted toward P680 together with Y_Z and D1-Q165 (Fig. 2(a)), reflecting the electron donation from Y_Z to P680 at this time range. D1-H190, which forms a short, low-barrier H-bond with Y_Z in the S_1 state, moved away from Y_Z,

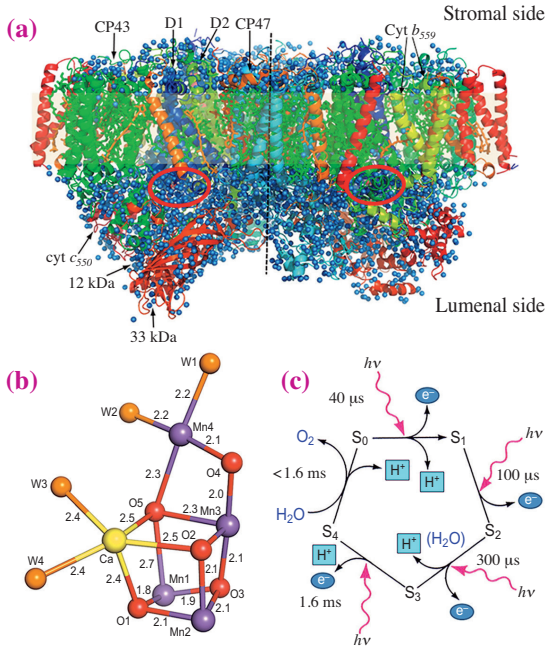

Fig. 1. Structure of PSII and the S-state model of water oxidation. **(a)** Structure of a PSII dimer with a side view of the membrane. The area highlighted in weak yellow in the middle is the trans-membrane area, and a dashed line divides two monomers. The areas encircled with red lines are the site where the Mn_4CaO_5 cluster is bound. **(b)** Structure of the Mn_4CaO_5 cluster, with distances indicated in Å. **(c)** Kok cycle (S-state model) for water oxidation.

making the H-bond between Y_Z 'normal' (Figs. 2(b,c)). These structural changes disappeared gradually following time progression, indicating that the structure returned to its original state after electron donation (Fig. 2). The structural changes following 2F are more or less the same as those following 1F in this area, but they appeared later and smaller than those following 1F, indicating some loss of efficiency as well as the time required to donate the second electron than donating one electron.

In the Mn_4CaO_5 cluster and its immediate environment, a number of difference densities appeared after either 1F or 2F (Fig. 3), indicating large structural changes during the $S_1 \rightarrow S_2$ and $S_2 \rightarrow S_3$ transitions. At 200 ns following 1F, Mn1–Mn3 were found to be unstable (Fig. 3(a)), which corresponds to the electron donation from the Mn_4CaO_5 cluster to P680. After the meta-stable S_2 is formed (5 ms after 1F), these Mn ions mostly become stable again; instead, Mn4 slightly shifted its position, corresponding to the stable donation of an electron from Mn4 to P680. At this time, W16, a water molecule that participates

in the H-bond network in the O4-channel, has disappeared, and W10 is largely displaced. In addition, D1-E189, a unique carboxylate ligand that is bound to Mn1 in a monodentate way and thus has the freedom to rotate, rotated its side chain slightly (Fig. 3(a)).

Following 2F, there are also a number of structural changes observed at various time points. Among them, the most remarkable one is that a new water molecule named O6*, appeared near Ca and the side chain of D1-E189 at 1 μs following 2F (Fig. 3(b)). The density for O6* increased at 30–200 μs following 2F, but disappeared completely by 5 ms. Instead, the density for O6 (or Ox), a water molecule previously reported to be inserted into a position close to O5 [2,3], appeared at 200 μs after 2F, and became maximum at 5 ms after 2F (Fig. 3(b)). This indicates that O6* is the precursor for O6, and is translocated to the O6 position during formation of the meta-stable S_3 state. Accompanying these structural changes, Mn1 and Mn4 shifted toward the opposite side, resulting in the elongation of the distance between them which is required for the insertion of O6. D1-E189 also shifted its side chain largely in order for the insertion of O6. Finally, O6 is ligated to the Ca ion, making it from 7-coordinated in the S_1 state to 8-coordinated in the S_3 state.

In addition to the above structural changes, we also found a number of structural changes at the channels and H-bond networks in PSII. First, new water molecules are found in the O1-channel following 2F, suggesting that this channel may function to pump water into the reaction site. Second, different movements are found in the Cl-1 channel between 1F and 2F, suggesting that this channel may play different roles in the $S_1 \rightarrow S_2$ and $S_2 \rightarrow S_3$ transitions. Details can be found in the original publication [5].

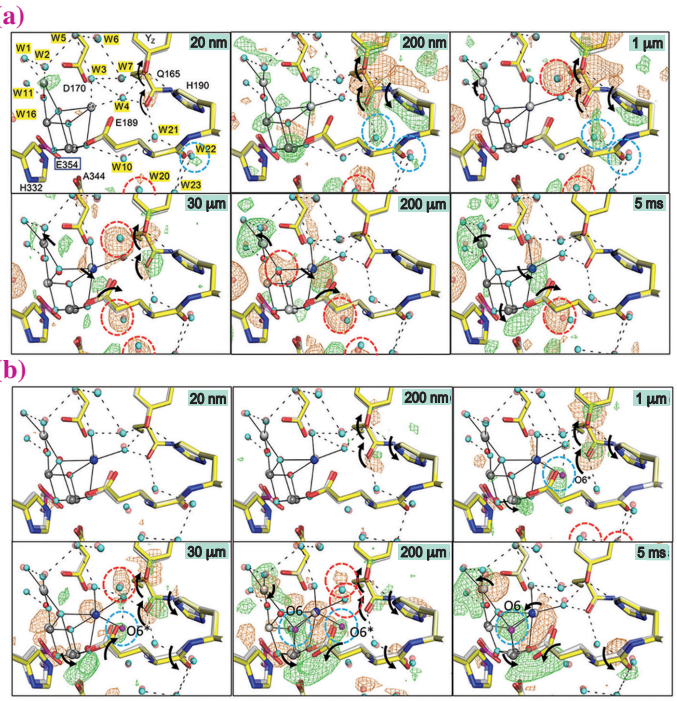

Fig. 3. Structural changes of the Mn_4CaO_5 cluster and its immediate environment following **(a)** 1F or **(b)** 2F. Residue names not encircled in a rectangle are of D1 subunit, whereas that encircled in a rectangle is of the CP43 subunit. Residues or water molecules encircled with red dashed lines indicate their disappearance, and those encircled with cyan dashed lines indicate their appearance.

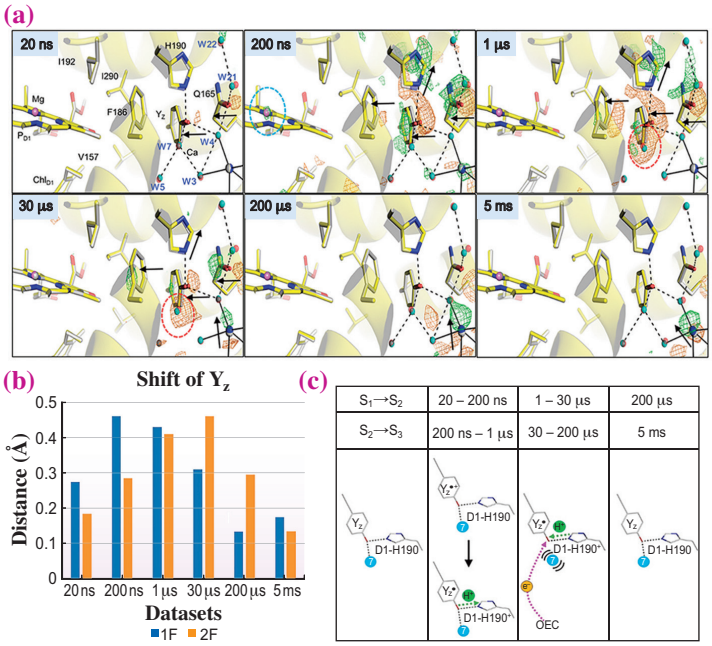

Fig. 2. Structural changes in the Y_Z-P680 area after light excitation. **(a)** Structural changes at various time points after 1F. Green and red meshes represent positive and negative difference densities between 1F-0F, and arrows indicate movements of residues and water molecules. **(b)** Distance changes in the H-bond between D1-H190 and Y_Z after 1F or 2F. **(c)** Schematic of the relationship between D1-H190 and Y_Z after 1F or 2F.

Jian-Ren Shen* and Michihiro Suga

Research Institute for Interdisciplinary Science, Okayama University

*Email: shen@cc.okayama-u.ac.jp

References

[1] Y. Umena *et al.*: Nature **473** (2011) 55.
[2] M. Suga *et al.*: Nature **543** (2017) 131.
[3] M. Suga *et al.*: Science **366** (2019) 334.
[4] A. Bhowmick *et al.*: Nature **617** (2023) 629.
[5] *H. Li, Y. Nakajima, E. Nango, S. Owada, D. Yamada, K. Hashimoto, F. Luo, R. Tanaka, F. Akita, K. Kato, J. Kang, Y. Saitoh, S. Kishi, H. Yu, N. Matsubara, H. Fujii, M. Sugahara, M. Suzuki, T. Masuda, T. Kimura, T. N. Thao, S. Yonekura, L.-J. Yu, T. Tosha, K. Tono, Y. Joti, T. Hatsui, M. Yabashi, M. Kubo, S. Iwata, H. Isobe, K. Yamaguchi, M. Suga and J.-R. Shen: Nature* **626** *(2024) 670.*

Protein crystal as a host to study small molecule reaction by time-resolved serial femtosecond crystallography

Capturing snapshots of dynamic changes in proteins and enzymes is essential for revealing their detailed mechanisms of action in real time. Time-resolved serial femtosecond crystallography (TR-SFX) is a powerful method for determining the real-space structures of dynamic changes in ultrashort intervals [1,2]. For example, the light-driven energy-harvesting mechanism of bacteriorhodopsin was revealed by conformational changes in 13 snapshot structures [2]. Most TR-SFX studies have used natural proteins and enzymes, whereas the use of small molecules is rare. Small molecule crystals diffract well but produce spots that are less numerous compared to biomacromolecules. This makes it challenging to determine the structural and conformational changes induced by SFX. Therefore, new methods, such as small-molecule SFX, are being developed; however, observing their dynamic structural changes is difficult [3,4].

In this context, the development of a new method for studying the dynamics of small molecules is highly important. To this end, we used a host-guest system to study metal complex reactions using light activation. A porous protein crystal was used as the host, and the metal center was fixed to the host as a guest [5]. This avoids the inherent difficulty in determining the structural changes in metal-complex reactions. Microcrystals of hen egg white lysozyme (HEWL) were used as a host and soaked in a photosensitive Mn-carbonyl complex to fix them into the porous solvent channels of the crystals (Fig. 1). The absorption and infrared spectra of the washed microcrystals confirmed the immobilization of the Mn-carbonyl on the crystal. The host-guest system was then applied to SFX at SACLA **BL2** (EH3 and 4b) to determine the structure under dark conditions (Fig. 2(a)). The results revealed the binding of the Mn-carbonyl complex at His15 to three carbon monoxide and two water molecules (Fig. 2(b)).

After confirming the structure of the Mn-carbonyl-bound HEWL, the microcrystals were subjected to TR-SFX at BL2 (EH3 and 4b) with 365 nm pump laser irradiation (Fig. 2(a)). The structures after 10 ns, 100 ns, and 1 μs of photoexcitation were determined (Fig. 2(c)). The difference in density features revealed that after 10 ns of light excitation, the axial CO started to release and was replaced by a water molecule (Fig. 2(c)-i). The process continued up to 1 μs. Subsequently, the 2nd CO ligand located at the equatorial position, was released. When the laser intensity was increased to 40 μJ at 1 μs delay time, the release of the 2nd CO ligand was prominent in the difference density map (Fig. 2(c)-iv). However, a further increase in the delay time to 17 ms hampered the precise assignment of the later-stage intermediates, possibly owing to the increased population of multiple intermediates. Therefore, our method is suitable for studying the early stages of the reactions. Although the CO release reaction from the Mn-carbonyl complex was previously investigated by transient spectroscopic

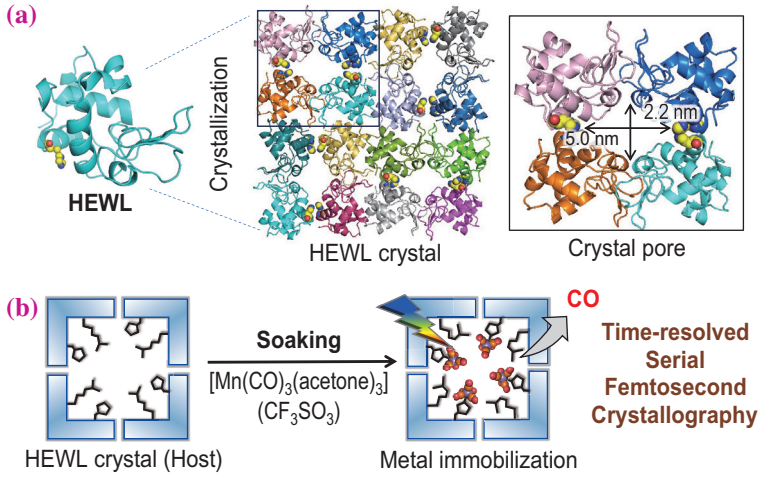

Fig. 1. Porous protein crystal as a host to immobilize small molecules. **(a)** Hen egg white lysozyme (HEWL) crystal and pore structure. **(b)** Schematic representing showing the immobilization of a Mn-carbonyl complex on the HEWL crystal host and light-induced CO release reaction study using the TR-SFX method. [5]

methods, real-time structure determination, particularly observing the release of 2nd CO, was not previously observed.

The experimentally observed intermediate structures were further verified using quantum mechanical/molecular mechanical studies. The observed intermediates followed the lowest-energy paths, in which axial CO was released first, followed the release of equatorial CO. However, the release of 3rd CO or subsequent changes was difficult, as the release of $Mn(CO)(wat)_4$ was found to be more energetically favorable. This explains why we did not observe intermediates in the later stages of the reaction.

Overall, the study demonstrated the potential and scope of applying TR-SFX to small molecule reactions using protein crystals as hosts. Our method avoids the challenges in the structure determination of small molecules. This study opens new possibilities for investigating the chemical reaction mechanisms of small molecules such as metal complexes or organic molecules. In addition, this study will be valuable for the development of artificial metalloenzymes.

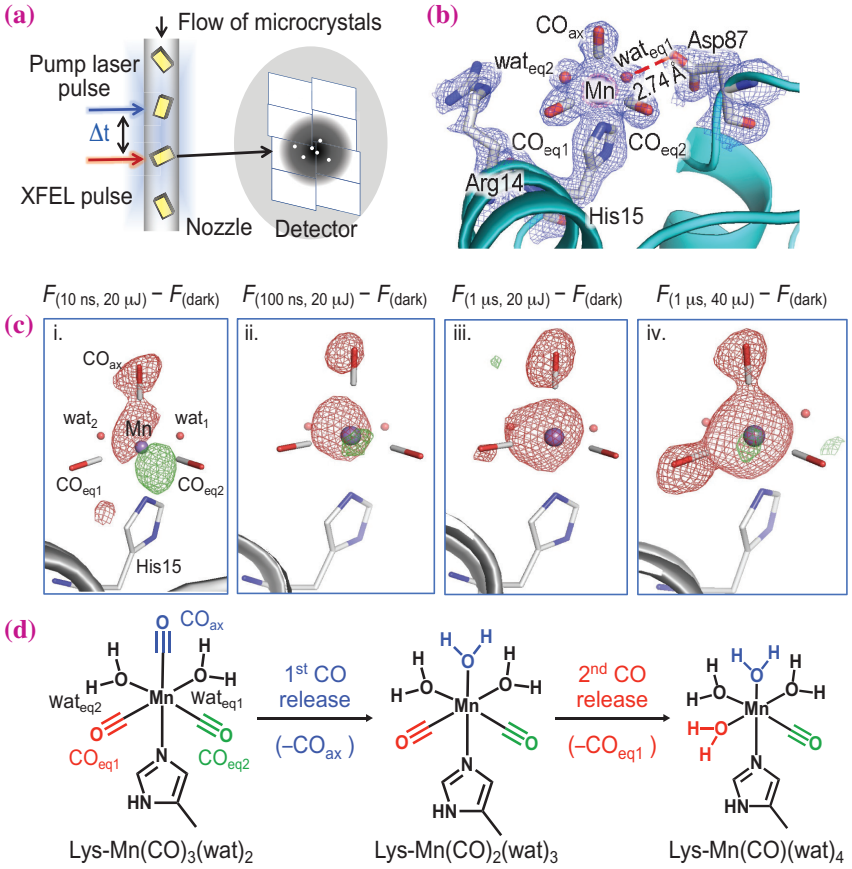

Fig. 2. Porous protein crystal as a host to study small molecule reaction. **(a)** A typical experimental setup to determine time-resolved structures by serial crystallography. **(b)** The dark structure of Mn-carbonyl is bound in the lysozyme crystal. **(c)** Observation of the CO release reaction through time-resolved structures at various delay times after photoexcitation. The difference $|F_o|_{light} - |F_o|_{dark}$ maps at ±3.2 σ (green/red) show the changes in the structures at various delay times after light excitation. **(d)** Schematics of the CO-releasing reaction steps for Mn-carbonyl, based on experimental results. [5]

Basudev Maity[a], Satoshi Abe[b] and Takafumi Ueno[a,*]

[a] School of Life Science and Technology, Institute of Science Tokyo
[b] Department of Biomolecular Chemistry, Kyoto Prefectural University

*Email: ueno.t.bb33@m.isct.ac.jp

References

[1] J. Tenboer *et al.*: Science **346** (2014) 1242.
[2] E. Nango *et al.*: Science **354** (2016) 1552.
[3] E. A. Schriber *et al.*: Nature **601** (2022) 360.
[4] J. Kang *et al.*: Nat. Chem. **16** (2024) 693.
[5] *B. Maity, M. Shoji, F. Luo, T. Nakane, S. Abe, S. Owada, J. Kang, K. Tono, R. Tanaka, T. T. Pham, M. Kojima, Y. Hishikawa, J. Tanaka, J. Tian, M. Nagama, T Suzuki, H. Noya, Y. Nakasuji, A. Asanuma, X. Yao, S. Iwata, Y. Shigeta, E. Nango, T. Ueno: Nat. Commun.* ***15*** *(2024) 5518.*

Key structural differences between green and red fluorescent proteins

Fluorescent proteins (FPs), indispensable tools in recent biological research, are exceptionally unique because their fluorophores are autocatalytically formed from the polypeptide chain. Most FPs discovered in nature are green fluorescent proteins (GFPs), which emit green fluorescence, while a smaller subset, red fluorescent proteins (RFPs), emit red fluorescence. The GFP fluorophore forms through the cyclization of three consecutive amino acids (Xaa-Tyr-Gly), creating an imidazolinone ring, followed by the formation of a double bond between the C_α and C_β atoms of the Tyr residue. This series of reactions requires one molecule of oxygen [1]. In the case of RFP, an additional oxidative step occurs, leading to the formation of an N-acylimine, absent in GFP fluorophores, which extends the π conjugation system in the fluorophore and shifts the absorbance and fluorescence to a longer wavelength (Fig. 1) [2-4]. Therefore, one extra molecule of oxygen is required for the formation of the RFP fluorophore.

There is a high demand for high-performance RFPs for their use in multi-color labeling and their advantage in deep tissue imaging. Converting GFP into RFP through mutagenesis could significantly contribute to developing novel RFPs, but such attempts have so far been unsuccessful. Moreover, the mechanisms by which GFPs and RFPs achieve distinctly different autocatalytic reactions while sharing similar overall structure remain poorly understood.

Our recent study successfully engineered GFPs into red and revealed key structural differences between GFP and RFP [5]. First, we focused on the differences between AzamiGreen (AG), a GFP derived from stony coral, and three representative RFPs—DsRed, eqFP578, and eqFP611. By introducing amino acid residues highly conserved among the three RFPs into AG and combining this with site-directed saturation mutagenesis, we successfully converted this GFP into an RFP (Figs. 2(a,b)). Notably, this novel RFP, named AzamiRed1.0 (AR1.0), exhibited a high fluorescence quantum yield of 0.65, among the highest for RFPs with fluorescence wavelengths exceeding 600 nm. The sequence difference between AG and AR1.0 was only 29 amino acids, making it the closest GFP-RFP pair. We determined the three-dimensional structures of AG and AR1.0 by collecting X-ray diffraction data at SPring-8 **BL41XU** to investigate the mechanisms of forming the distinct GFP and RFP fluorophores.

Strikingly, it was revealed that the multiple mutations introduced in AR1.0 cooperatively contributed to significant rearrangements in the interaction networks around the fluorophore (Figs. 2(c,d)). For example, a new hydrogen bond network formed in AR1.0, extending from the main chain nitrogen of Ala67 through Thr107 and the side chain of Gln105 to the main chain oxygen of Gln60. The hydrogen bond between the Asn65 side chain and the Tyr87 hydroxyl group in AG was absent in AR1.0, where residue 65 was substituted with Ser and residue 87 with Phe. Instead, the Ser65 side chain of AR1.0 formed a hydrogen bond with the hydroxyl group of Tyr116. Additionally, the hydroxyl group of Thr69 in AG formed a hydrogen bond with the guanidino group of Arg66, assisting its interaction with the Glu211 side chain. In AR1.0, however, Arg66 and Thr69 were replaced with Lys and Ile, respectively, leading to a new interaction between Lys66 and Glu144. Due to these structural changes, a cavity absent in AG appeared in AR1.0

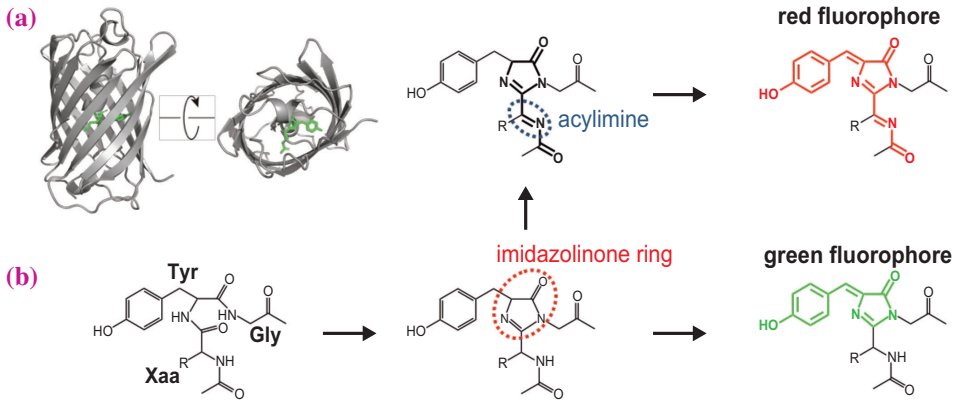

Fig. 1. Fluorophore of fluorescent proteins. **(a)** Structure of a fluorescent protein. **(b)** Proposed scheme of fluorophore formation in GFP and RFP.

near the fluorophore (Figs. 2(e,f)). A similar cavity was also observed in other RFPs. Interestingly, while water molecules occupied this cavity in the AR1.0 structure, glycerol and acetate molecules used for crystallization were found in the cavities of eqFP578 and eqFP611 structures, respectively, indicating that the cavity is accessible from outside the protein. As mentioned above, red fluorophore formation requires one additional molecule of oxygen, which must enter the vicinity of the fluorophore. This cavity would allow the entry of the oxygen molecule necessary for red fluorophore formation, although further verification is needed.

In addition to the cavity, the protonation state of the Tyr63, the core residue of the fluorophore, also seems to be important for the formation of RFP fluorophores. As a result of the M159K mutation in AR1.0, the side chain amino group of Lys159 into close proximity with the phenolic hydroxyl group of the fluorophore, suggesting that the phenolic hydroxyl group of Tyr63 is stabilized in its deprotonated state in AR1.0. When Lys159 in AR1.0 is reverted to Met, a mixture of red and green fluorophores is formed, underscoring the critical role of Tyr63 deprotonation.

AR1.0 formed a homo-tetramer, like its precursor AG. Because monomeric FPs are generally preferred as a fluorescent tag, we constructed a monomeric AR1.0 variant named mARs1. While mARs1 exhibited a reduced quantum yield of 0.26 compared to AR1.0, its fluorescence was sufficiently bright for live cell imaging. When expressed in cells as fusion constructs with various proteins or localization tags, mARs1 localized to expected cellular locations, including mitochondria, Golgi apparatus, lysosomes, actin filaments, and microtubule plus ends, demonstrating its utility for visualizing these structures.

Previously, new RFPs were obtained only by isolating new proteins from nature or modifying existing RFPs. However, isolating new RFPs from nature is challenging, and the limited sequence diversity of existing RFPs constrains the development of high-performance variants. Our study demonstrates that the artificial conversion of GFP to RFP offers a promising alternative approach, significantly enhancing the sequence diversity of RFPs. Additionally, our findings provide structural insights into the mechanisms underlying red fluorophore formation in RFPs.

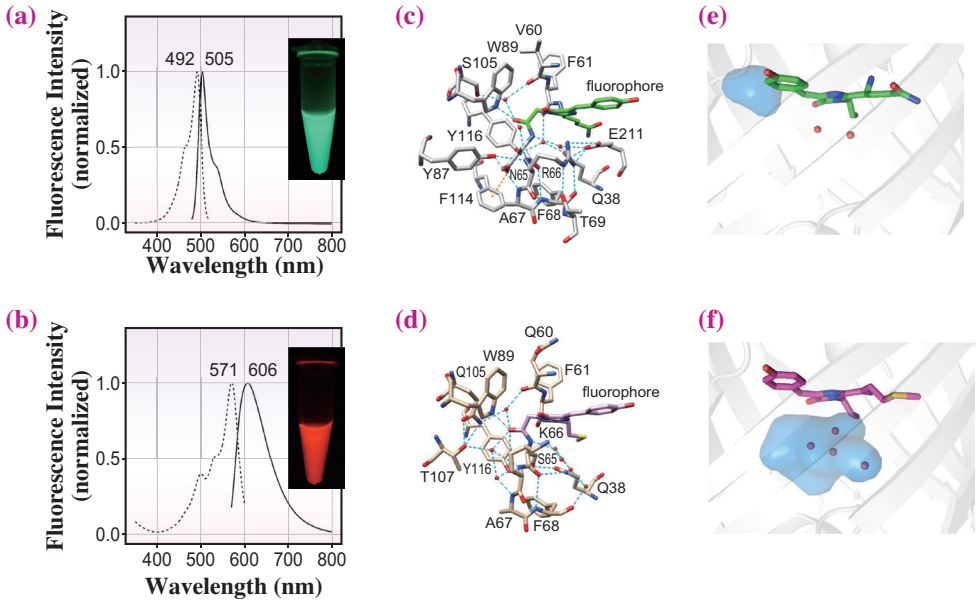

Fig. 2. Spectroscopic and structural difference between AG (upper panels) and AR1.0 (lower panels). **(a,b)** Excitation (dot) and emission (solid) spectra and fluorescence photographs of purified FPs. **(c,d)** Interaction networks near the fluorophore. **(e,f)** Cavities near the fluorophore.

Hiromi Imamura[a,*] and Katsumi Imada[b]

[a] Organization of Research Initiatives, Yamaguchi University
[b] Graduate School of Science, Osaka University

*Email: imamura-h@yamaguchi-u.ac.jp

References

[1] R. Y. Tsien: Annu. Rev. Biochem. **67** (1998) 509.
[2] L. A. Gross *et al.*: Proc. Natl. Acad. Sci. USA **97** (2000) 11990.
[3] S. Pletnev *et al.*: J. Am. Chem. Soc. **132** (2010) 2243.
[4] R. L. Strack *et al.*: J. Am. Chem. Soc. **132** (2010) 8496.
[5] *H. Imamura, S. Otsubo, M. Nishida, N. Takekawa, K. Imada: Proc. Natl. Acad. Sci. USA **120** (2023) e2307687120.*

High-throughput structure determination of an intrinsically disordered protein

Intrinsically disordered proteins (IDPs) are a class of protein with multiple conformations that play an important role in signal transduction *in vivo*. The conformation of IDPs is significantly influenced by their external environment, and exhibits changes through interactions with binding partners. Identifying the determinants that stabilize the atomic-level structure of IDPs is crucial for understanding their biological functions. One promising method for determining the structures of IDPs is crystallizing IDPs fused with a binding partner. However, the versatility of this approach is limited by the challenges in designing robust scaffold crystals that maintain high diffraction quality.

To address these limitations, proteins that spontaneously crystallize in the cells of specific expression hosts were identified. In-cell protein crystallization ensures rapid, small-scale synthesis of crystals with high diffraction quality, which is particularly useful for crystallization screening to optimize crystal design. In this context, the crystallization of the target protein incorporated into in-cell protein crystals is proposed as a scaffold to immobilize the target protein in well-defined pores within the crystal. We have attempted X-ray structure analysis of target proteins using polyhedra crystals (PhCs), known for their high diffraction quality, produced in insect cells following infection with the cytoplasmic polyhedral virus [1]. Previously, we have successfully determined the structure of a ten-amino acid miniprotein, CLN025, fused to a polyhedrin monomer (PhM), resulting in the formation of PhCs in insect cells using SPring-8 **BL32XU** [2]. These findings highlight the potential of PhCs as versatile scaffolds for various proteins. Additionally, a cell-free expression system from wheat germ extract was used to express PhM. The structure of PhC was determined at a high resolution of 1.80 Å from sub-micron crystals obtained at a reaction scale of 100 μL within 24 h (Fig. 1(a)) [3]. This method contrasts with the conventional *in vitro* crystallization systems, which requires 1 L or more cell culture and several months for crystallization trials and optimization.

By utilizing the versatility of PhCs and the rapid structural analysis enabled by cell-free protein crystallization (CFPC), a pipeline for structure determination optimized for IDPs was established by integrating CFPC with the protein structure prediction software Foldit Standalone (Fig. 1(c)). Our goal was to elucidate the structural regulatory mechanism of the IDP region of c-Myc, a transcription factor known to bind to MAX (Fig. 1(b)) [4]. To clarify the structure-fixation factors of the 11-residue fragment within c-Myc (Y402–K412), which serves as a drug-binding site, we conducted X-ray crystal structure analysis of PhC mutants containing the domain swapped with this c-Myc fragment through several cycles of the CFPC screening method [5].

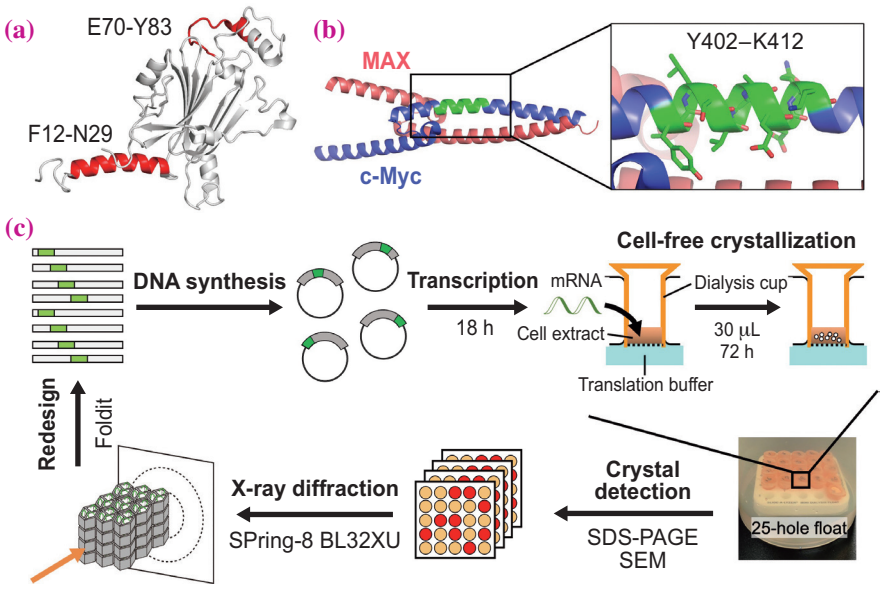

Fig. 1. **(a)** Crystal structure of PhM (PDB ID: 7XWS) and two sites in PhM for swapping with the c-Myc fragment [3]. **(b)** Crystal structure of the c-Myc/MAX complex (PDB ID: 1NKP) [4]. The black box shows the position of Y402–K412, colored green. **(c)** Scheme of high-throughput screening of X-ray crystallography for proteins.

First, six mutant PhCs, in which F12–N29 or E70–Y83 were partially swapped with the c-Myc fragment, predicted to be stably crystallized by Foldit Standalone (Fig. 1(a)). These mutants were rapidly synthesized on a small scale (30 μL) through the CFPC method. The obtained crystals were then subjected to high-resolution structural determination of the IDP region using diffraction data acquisition at SPring-8 BL32XU. In one of the six candidate mutants, the electron density corresponding to the entire length of the c-Myc fragment was successfully observed in the PhC (Fig. 2(a)). The c-Myc fragment in PhC forms a helical structure that is structurally similar to that of the c-Myc/MAX complex (Fig. 2(b)) and the structure predicted by Foldit. Two fragments of c-Myc, directed oppositely in the middle of the N-terminal helical region, interact via hydrophobic interactions involving I403 and V406 and hydrogen bonds at E410 (Fig. 2(c)). This structure was used in further redesigns to identify the key determinants fixing the c-Myc structure. Two additional crystal structures were obtained in which the c-Myc fragments were stepwise replaced with the original PhC sequence. B-factor analysis of these mutants indicated that the lack of the hydrophobic interaction at I403 destabilized the α-helical structure of the c-Myc fragment. In contrast, the lack of hydrogen bonds at E410 did not disrupt the structure.

Finally, this method allowed for the determination of eight crystal structures out of 22 mutants, revealing that interactions of residues I403 and V406 in c-Myc significantly stabilize the α-helical structure. This comprehensive approach enabled the successful determination of the IDP structure and provided insights into the specific residues involved in stabilizing the secondary structure of proteins. These findings underscore the power of our CFPC screening method as a valuable tool for elucidating essential molecular interactions that govern the stability of target proteins.

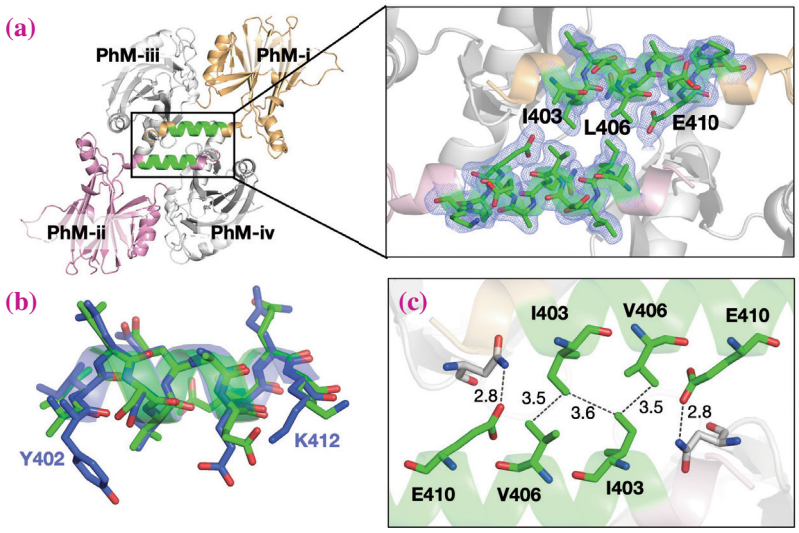

Fig. 2. Crystal structure of the c-Myc fragment fused to PhC. **(a)** Structure of the c-Myc fragment fused PhC tetramer and a close-up view of the c-Myc fragment in PhC. Each monomer in the tetramer is designated PhM-i, PhM-ii, PhM-iii, or PhM-iv. **(b)** Superposed structure of the c-Myc fragment in PhC (green) and the one in c-Myc/MAX (blue) (PDB ID: 1NKP). **(c)** Noncovalent interactions between the c-Myc fragment and surrounding residues in PhC. All fragments of c-Myc and c-Myc/MAX are colored green. The selected $2|F_o|-|F_c|$ electron density maps at 1.0σ are shown in blue. Nitrogen and oxygen atoms are colored blue and red, respectively. The cut-off distances of noncovalent interactions are 3.5 Å and 5.75 Å for hydrogen bonds and hydrophobic interactions, respectively. Hydrophobic interactions of the shortest distance between two residues are shown (c).

Mariko Kojima[a,†], Satoshi Abe[b] and Takafumi Ueno[c,*]

[a] Faculty of Environmental Earth Sci., Hokkaido University
[b] Dept. Biomolecular Chemistry, Kyoto Prefectural University
[c] School of Life Science and Technology, Institute of Science Tokyo

*Email: tueno@bio.titech.ac.jp

[†] Present Address: Tohoku University

References

[1] F. Coulibaly *et al.*: Nature **446** (2007) 97.
[2] M. Kojima *et al.*: Biomater. Sci. **11** (2023) 1350.
[3] S. Abe *et al.*: Sci. Rep. **12** (2022) 16031.
[4] S. K. Nair and S. K. Burley: Cell **112** (2003) 193.
[5] *M. Kojima, S. Abe, T. Furuta, K. Hirata, X. Yao, A. Kobayashi, R. Kobayashi and T. Ueno: PNAS **121** (2024) e2322452121.*

Structural insights into cancer cell-specific recognition by H_2Mab-214, a novel anti-HER2 antibody

Monoclonal antibodies bind to target molecules with high specificity and affinity and are used as therapeutic agents for various diseases. In cancer therapy, antibody drugs typically target proteins that are overexpressed in cancer cells and are significantly more abundant on the surface of cancer cells than on normal cells (Fig. 1). However, such proteins have been extensively studied, making the discovery of novel target molecules increasingly challenging. Moreover, if the target molecule is expressed in normal cells even at relatively low levels, there is a risk of adverse effects.

Human epidermal growth factor receptor 2 (HER2) is a well-known therapeutic target that is overexpressed in several cancers, including breast, gastric, bladder, ovarian, and non-small cell lung cancers [1-3]. Multiple anti-HER2 antibodies, such as trastuzumab (Herceptin®, approved by Food and Drug Administration in 1998), have been developed and are clinically used. However, these antibodies also bind to HER2 on normal cells, causing concerns regarding their cardiotoxic side effects. Recently, we succeeded in obtaining a novel antibody, H_2Mab-214, which specifically binds to HER2 on cancer cells, through the differential screening of numerous hybridomas. In flow cytometry analysis, trastuzumab reacted with breast cancer cells (SK-BR-3), as well as with human mammary epithelial cells (MCF 10A) and human embryonic kidney epithelial cells (HEK293T), whereas H_2Mab-214 showed reactivity only with SK-BR-3 cells [4]. ELISA-based assessments showed that the affinity of H_2Mab-214 for the HER2 ectodomain (HER2ec) is equivalent to that of trastuzumab (K_D values of H_2Mab-214 and trastuzumab are 0.53 and 0.31 nM, respectively), indicating that the cancer selectivity of H_2Mab-214 is not dependent on its affinity for HER2 (or the HER2 expression level).

To elucidate the mechanism underlying the cancer cell-selectivity of H_2Mab-214, we identified the binding site (that is, epitope) of H_2Mab-214 by evaluating its binding to various HER2 fragments. As a result, it was found that the antibody recognizes a sequence of only seven residues, spanning Pro612 to Asp618, in HER2 domain IV. It is well-known that proteins produced by cancer cells often contain sugar chains with abnormal chemical compositions or amino acid mutations that can serve as cancer-specific markers. However, the identified epitope does not exhibit these chemical characteristics, leaving the mechanism by which H_2Mab-214 distinguishes between cancer and normal cells unclear. To investigate further, we conducted a crystallographic analysis. For this, H_2Mab-214 was converted into a small and hyper-crystallizable antibody fragment, Fv-clasp [5]. Crystals of the H_2Mab-214 Fv-clasp were successfully obtained in the presence of an epitope peptide (a synthetic peptide corresponding to HER2 residues 611–618 was used for crystallization). X-ray diffraction data were collected at SPring-8 **BL44XU**, and the complex structure was obtained at a resolution of 1.75 Å (Fig. 2(a)).

Numerous interactions were observed between H_2Mab-214 and the peptide in the crystal structure, reflecting high affinity between the two (Fig. 2(b)). Interestingly, when we compared the conformation of the peptide bound to H_2Mab-214 with that of the corresponding region in the known HER2ec structures, we found that they are entirely different. The epitope peptide bound to H_2Mab-214 adopts a U-shaped conformation, whereas the corresponding region in HER2ec adopts an extended conformation, part of which forms a β-strand (Figs. 2(c) and 2(d)). This finding suggests that H_2Mab-214 recognizes the structurally compromised HER2. However, because our crystal structure represents H_2Mab-214 complexed with the epitope peptide rather than with HER2ec itself, it remains unclear whether H_2Mab-214 actually recognizes misfolded HER2 on the cell surface. To address this, we artificially disrupted the tertiary structure of HER2 on HEK293T cells and investigated antibody binding using flow cytometry. The extracellular region of HER2 contains many disulfide bonds, which contribute to the maintenance

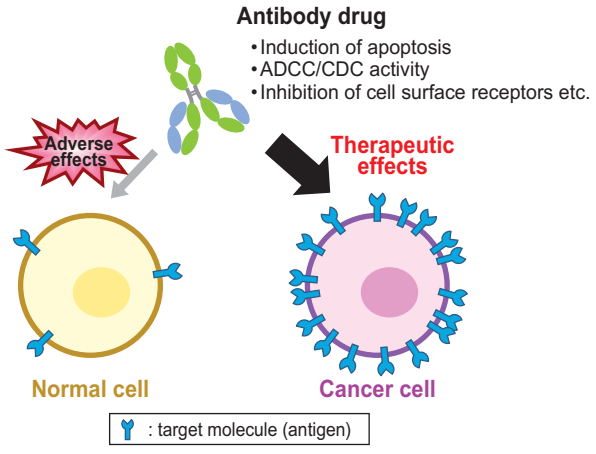

Fig. 1. Conventional strategies for cancer treatment using monoclonal antibodies. ADCC, antibody-dependent cellular cytotoxicity; CDC, complement-dependent cytotoxicity.

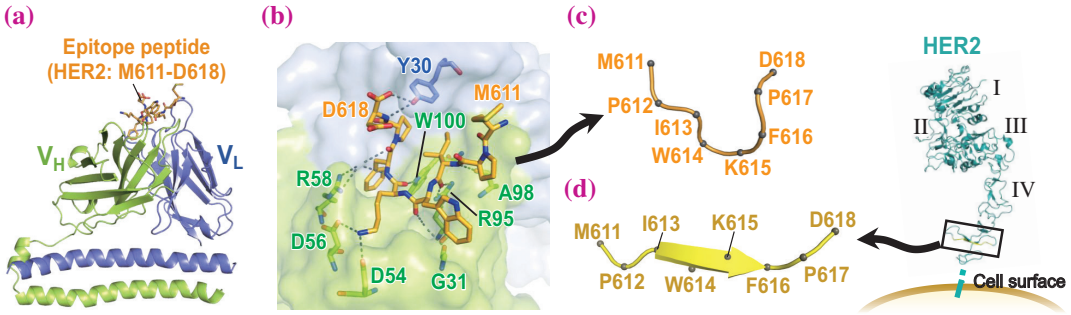

Fig. 2. Crystal structure of H_2Mab-214 in complex with its epitope peptide. **(a)** Overall structure of the H_2Mab-214 Fv-clasp/peptide complex. **(b)** Close-up view of the antigen-binding site of H_2Mab-214. Hydrogen bonding interactions are indicated with dashed lines. **(c,d)** Comparison of the conformation of the epitope peptide bound to H_2Mab-214 with the corresponding region in the HER2ec crystal structure (PDB: 3n85).

of the correct tertiary structure. Therefore, we cultured HEK293T cells in medium containing the reducing agent dithiothreitol (DTT, 1 mM) for 1 h to cleave the disulfide bonds of HER2 on the cell surface. After DTT treatment, trastuzumab binding to cells was nearly abolished, confirming the structural disruption of HER2. In contrast, H_2Mab-214 binding increased significantly after DTT treatment (Fig. 3(a)), indicating that the epitope of H_2Mab-214 was exposed due to structural disruption. Furthermore, when a disulfide bond near the epitope of H_2Mab-214 was specifically broken through mutations, H_2Mab-214 binding increased. This suggests that the H_2Mab-214 epitope region in HER2 is particularly susceptible to structural defects, even with minor destabilization of the surrounding conformation [4].

Our results suggest that locally misfolded HER2 molecules are produced in cancer cells, and that H_2Mab-214 recognizes these molecules to achieve cancer specificity (Fig. 3(b)). Considering the abnormal state of cancer cells, similar local misfolding may occur in other cell surface molecules, which can be a promising target for the development of new cancer-specific antibodies.

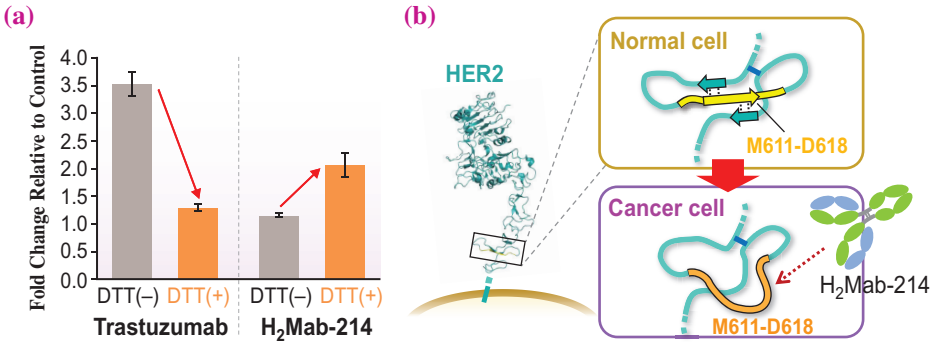

Fig. 3. H_2Mab-214 recognizes misfolded HER2. **(a)** Effects of DTT treatment of HEK293T cells on antibody binding. HEK293T cells were treated with 1 mM DTT for 1 h and stained with trastuzumab or H_2Mab-214, followed by flow cytometric analysis. Results are reported as the fold-change in the median fluorescence intensity compared with the buffer control. Data are presented as the mean ± standard error (SEM) of four independent experiments. **(b)** Proposed model of local structural differences in HER2 between normal and cancer cells.

Takao Arimori

Institute for Protein Research, Osaka University

Email: arimori@protein.osaka-u.ac.jp

References

[1] E. Van Cutsem *et al.*: Gastric Cancer **18** (2015) 476.
[2] D. J. Slamon *et al.*: Science **244** (1989) 707.
[3] P. M. Schneider *et al.*: Cancer Res. **49** (1989) 4968.
[4] *T. Arimori, E. Mihara, H. Suzuki, T. Ohishi, T. Tanaka, M. K. Kaneko, J. Takagi, Y. Kato: Structure **32** (2024) 536.*
[5] T. Arimori *et al.*: Structure **25** (2017) 1611.

Structural characterization of the unique pH-responsive anti-TIGIT therapeutic antibody Ociperlimab

TIGIT has attracted tremendous attention in cancer immunotherapy. As an inhibitory immune checkpoint, TIGIT is expressed on most NK and multiple T cell subsets and exerts inhibitory effects on innate and adaptive immunity by binding to its ligands, PVR (CD155) and nectin-2 [1]. Competitive binding of TIGIT and CD226 (an activating receptor) to PVR has been known as a key mechanism of TIGIT-driven immune suppression, and anti-TIGIT blocking mAbs are presumed to reverse the suppression by inhibiting TIGIT binding to PVR, thereby enhancing T cell or NK cell activity (Fig. 1 and Fig. 2(a)). Several clinical trials are currently evaluating the efficacy of anti-TIGIT mAbs in patients with different types of cancer. Ociperlimab from BeiGene and Tiragolumab from Roche block the TIGIT-PVR interaction and are in clinical development. However, the molecular blockade mechanism of these anti-TIGIT mAbs remains elusive.

We determined the crystal structures of the Ociperlimab_Fab/TIGIT complex and the Tiragolumab_Fab/TIGIT complex at resolutions of 2.4 and 2.0 Å with SPring-8 **BL45XU** beamline, respectively [2]. Competitive binding of Ociperlimab_Fab or Tiragolumab_Fab against PVR was revealed by overlaying Ociperlimab_Fab/TIGIT or the Tiragolumab_Fab/TIGIT complex on the PVR/TIGIT complex (Fig. 1). The binding of TIGIT by Ociperlimab_Fab was dominated by the front CC'C'' β-sheets, which have obvious steric clashes with PVR (Fig. 1 and Fig. 2(d)). The overlapping binding surface of Ociperlimab_Fab and PVR on TIGIT is located near the front CC'C'' β-sheets. Similarly, the binding of TIGIT by Tiragolumab_Fab is also mediated by the front CC'C''DF β-sheets. Moreover, the blockade mechanism of Ociperlimab_Fab relies on the steric hindrance of both the VH and VL domains against PVR to abolish its binding to TIGIT, whereas only the VH domain of Tiragolumab_Fab participated in the steric conflict with PVR to prevent its binding. Ociperlimab and Tiragolumab exhibit distinct binding modes toward TIGIT (Fig. 2(c)). We did not observe any obvious conformational change in TIGIT upon Ociperlimab_Fab or Tiragolumab_Fab binding compared with its apo structure (Fig. 2(b)), as both antibodies mainly bind to the β-sheet of TIGIT with rigid secondary structures (Figs. 2(c,d)). However, Ociperlimab and Tiragolumab have distinct epitopes when binding to TIGIT, implying that the antagonistic mechanism of the two antibodies could be different.

Almost all known pH-responsive antibodies sense pH due to histidine residues. pK_a value of the histidine side chain is about 6. Thus, at pH 6.0 or below, the histidine side chain is mostly protonated whereas at physiological pH 7.4 it is deprotonated. As a result, the histidine side chain could change ionization states due to subtle changes in pH, leading to its net charge varying [3]. In some cases, histidine residues in the epitopes could also contribute to the pH-responsive antibodies as demonstrated by this structural study. Our surface plasmon resonance (SPR) data shows that the binding affinity of Ociperlimab towards TIGIT increased approximately 17-fold when the pH decreased from 7.4 to 6.0, whereas Tiragolumab did not show obvious pH-dependent binding to TIGIT (Fig. 3(c)). This observation is further supported by the fluorescence-activated cell sorting experiment which shows the enhanced binding of Ociperlimab to TIGIT when the pH shifts from 7.4 to 6.0 (Fig. 3(d)). In the Ociperlimab_Fab/TIGIT crystal structure, $Asp103_{HCDR3}$ is well positioned with respect to $His76_{TIGIT}$ at a 2.7 Å distance and forms a strong electrostatic interaction, whereas no favorable architecture surrounding $His76_{TIGIT}$ in Tiragolumab_Fab/TIGIT was observed (Figs. 3(a,b)). Consistent with the critical role of $His76_{TIGIT}$ in Ociperlimab binding, a substantial decrease in the binding affinity

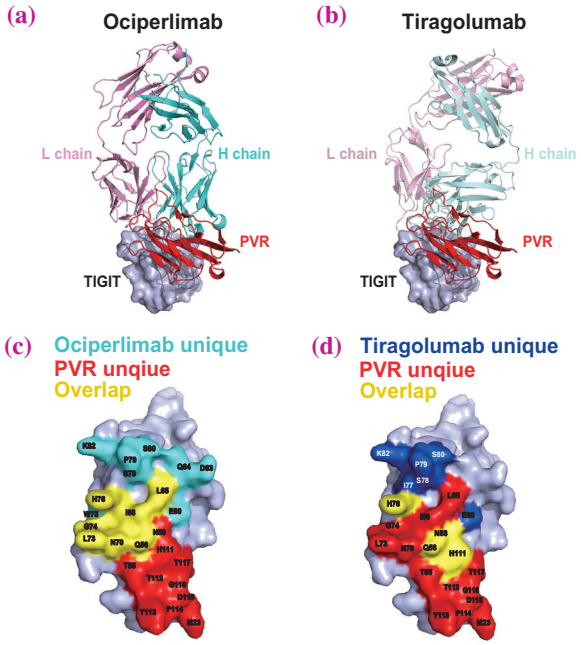

Fig. 1. Competitive binding of Ociperlimab_Fab or Tiragolumab_Fab against PVR for TIGIT. **(a)** Superposition of Ociperlimab_Fab/TIGIT with the PVR/TIGIT (PDB: 3UDW) complex when aligned via TIGIT. **(b)** Superposition of Tiragolumab_Fab/TIGIT with the PVR/TIGIT complex when aligned via TIGIT. **(c)** The binding surface of TIGIT with PVR or Ociperlimab_Fab. **(d)** The binding surface of TIGIT with PVR or Tiragolumab_Fab.

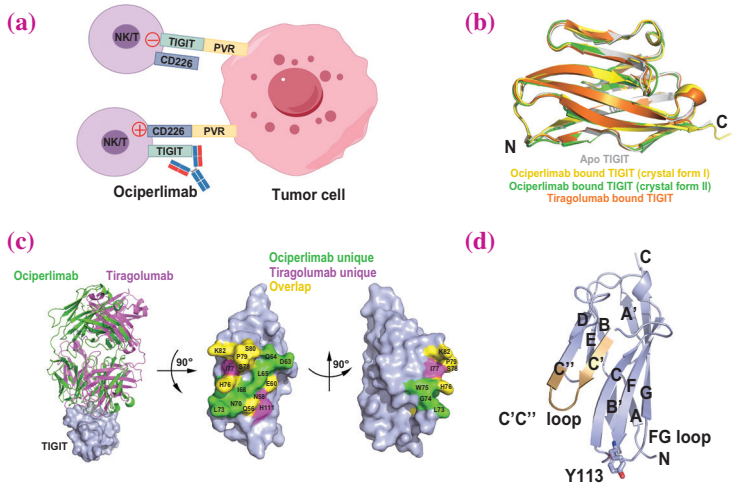

Fig. 2. Mechanisms of action (MOA) of anti-TIGIT therapeutic antibodies. **(a)** A schematic diagram for MOA of anti-TIGIT antibodies. **(b)** Superposition of Fab-bound TIGIT with apo TIGIT (PDB: 3UCR). **(c)** Superposition of Ociperlimab_Fab/TIGIT with the Tiragolumab_Fab/TIGIT complex. **(d)** Structural overview of the TIGIT IgV domain.

of Ociperlimab to H76A$_{TIGIT}$ mutant was observed at pH 6.0, with a nearly 24,303-fold reduction (Fig. 3(c)). Meanwhile, Ociperlimab displayed comparable binding affinities to H76A$_{TIGIT}$ mutant at pH 6.0 and pH 7.4, confirming the critical role of His76$_{TIGIT}$ in mediating this pH-dependent effect for Ociperlimab. These findings clearly demonstrate that His76 of TIGIT is indeed pivotal for the pH-dependent binding characteristics of Ociperlimab. Therefore, Ociperlimab has a stronger binding affinity with TIGIT under acidic pH conditions than physiological conditions, which could be valuable in targeting acidified tumor microenvironment and reducing on-target off-tumor toxicities.

In summary, our structural studies on Ociperlimab and Tiragolumab have revealed the molecular blockade mechanism of these antibodies on TIGIT-driven immune suppression. The Ociperlimab competes with PVR towards TIGIT, which is consistent with previous functional studies by Chen *et al.* [4]. In addition, the pH-responsive property of Ociperlimab, rationalized in our structures, could potentiate the cytotoxicity of immune cells toward cancer cells in the tumor microenvironment. Therefore, the present complex structures should provide useful insights into improving the effectiveness of immunotherapeutic antibody development.

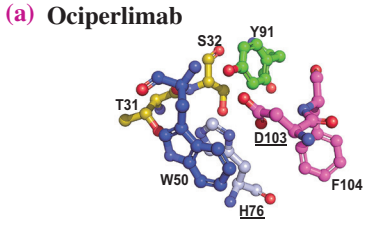

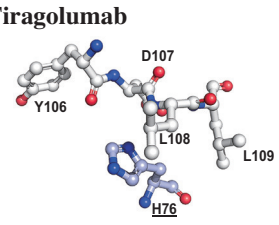

(c)

TIGIT binding kinetics with Ociperlimab under different pHs

Analyte	Kon ($M^{-1}s^{-1}$)	Koff (s^{-1})	Ociperlimab KD (M)
TIGIT (WT) pH 7.4	2.4 E+5	1.27 E−4	5.32 E−10
TIGIT (WT) pH 6.0	2.94 E+6	9.28 E−5	3.16 E−11
TIGIT (H76A) pH 7.4	N.A.	N.A.	9.79 E−7
TIGIT (H76A) pH 6.0	N.A.	N.A.	7.68 E−7

TIGIT binding kinetics with Tiragolumab under different pHs

Analyte	Kon ($M^{-1}s^{-1}$)	Koff (s^{-1})	Tiragolumab KD (M)
TIGIT (WT) pH 7.4	1.75 E+5	1.03 E−4	5.88 E−10
TIGIT (WT) pH 6.0	9.05 E+5	4.60 E−4	5.08 E−10
TIGIT (H76A) pH 7.4	6.81 E+5	1.41 E−4	2.06 E−10
TIGIT (H76A) pH 6.0	7.57 E+5	2.42 E−4	3.20 E−10

(d)

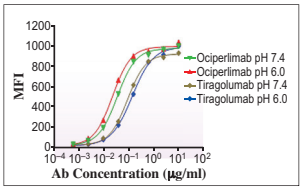

Sample code	Ociperlimab pH 7.4	Ociperlimab pH 6.0	Tiragolumab pH 7.4	Tiragolumab pH 6.0
Top, MFI	972.3	990.3	919.6	988
RV of top (%)	100	102	95	102
EC_{50} (μg/ml)	0.03512	0.02298	0.09067	0.1407
RV of EC_{50} (%)	100	153	100	64
Hillslope	1.16	1.177	1.196	1.047
RV of Hillslope (%)	100	101	103	90
R^2	0.9976	0.998	0.9985	0.9975

Fig. 3. Structural basis of the pH-dependent property of Ociperlimab towards TIGIT. **(a)** The surrounding residues of HIS76$_{TIGIT}$ within Ociperlimab. **(b)** The surrounding residues of HIS76$_{TIGIT}$ within Tiragolumab. **(c)** SPR binding kinetics of the interactions of Ociperlimab or Tiragolumab with TIGIT at different pH values. **(d)** Cell binding affinity measurement on Ociperlimab or Tiragolumab toward TIGIT under different pHs.

Xiangxiang Zhang and Jian Sun*

Dept. Biologics, BeiGene (Beijing) Co., Ltd., China

*Email: jian1.sun@beigene.com

References

[1] X. Yu *et al.*: Nat. Immunol. **10** (2009) 48.
[2] *J. Sun, X. Zhang, L. Xue, L. Cheng, J. Zhang, X. Chen, Z. Shen, K. Li, L. Wang, C. Huang, J. Song: Structure* ***32*** *(2024) 550.*
[3] W. Wei *et al.*: Proteins **90** (2022) 1538.
[4] X. Chen *et al.*: Front. Immunol. **13** (2022) 828319.

Zn-containing immature structure of a Rieske-type iron-sulfur protein

Iron-sulfur clusters are involved in a wide range of biological processes, including enzymatic reactions, photosynthesis, and respiration, as prosthetic groups for various proteins. Iron-sulfur clusters are biosynthesized by protein machinery, such as sulfur mobilization (SUF) and iron-sulfur cluster (ISC) systems [1]. The biosynthesis of iron-sulfur clusters is divided into two main steps: assembly and insertion (Fig. 1(a)). In the assembly step, iron-sulfur cluster assembly is catalyzed by cysteine desulfurases on scaffold proteins. The iron-sulfur clusters are transferred to the final target proteins in the next insertion step with the assistance of molecular chaperones. The bacterial ISC system is similar to the mitochondrial ISC system and the central component proteins are homologous to each other [2]. Although the elucidation of the assembly step has recently progressed [3], the insertion step from scaffold proteins to the target protein remains unclear. Accordingly, the molecular details of iron-sulfur protein maturation remain unclear.

The Rieske protein PetA is a subunit of the bacterial cytochrome bc_1 complex [4]. PetA is composed of a single transmembrane α-helix and one soluble globular domain with a Rieske-type [2Fe–2S] cluster (Fig. 1(b)). In this study [5], the soluble domain of PetA from a photosynthetic bacterium was expressed in *Escherichia coli* cells. In a purification process with size-exclusion chromatography (SEC), PetA was divided into a colorless elution peak of approximately 40 kDa, corresponding to the dimer, and a dark-brown peak of approximately 20 kDa, corresponding to the monomer (Fig. 2(a)). The ultraviolet-visible (UV-vis) absorption spectra indicated that only the monomer fraction contained iron-sulfur clusters. Therefore, the dimer and monomer fractions in the SEC were assigned to the immature and mature forms of PetA, respectively.

The crystals of the two PetA samples were obtained and used for X-ray diffraction (XRD) measurements at SPring-8 **BL41XU**. The immature PetA structure was determined at 1.7 Å resolution, whereas that of [2Fe–2S]-containing mature PetA was determined at 1.8 Å resolution. The structures of both forms were typical of the Rieske subunit of the cytochrome bc_1 complex. In immature PetA, $ZnCl_2$ is found in the cluster-binding site instead of [2Fe–2S] (Fig. 2(b)). The zinc ion is chelated in a tetra-coordination geometry by two cysteine residues (Cys124 and Cys152) and two chloride ions. Only one histidine residue (His155) exhibited a conformational difference in the cluster-binding site (Figs. 2(b,c)), whereas no significant differences were observed between the two structures. This implies that the structure of the cluster-binding site was almost completely constructed prior to the insertion of [2Fe–2S].

To investigate the oligomeric structure of Zn-PetA in solution, a SEC coupled with small-angle X-ray scattering (SEC–SAXS) experiments were performed at SPring-8 **BL38B1** (Fig. 3(a)). An *ab initio* envelope model derived from the SAXS data had the following approximate dimensions: 80 × 40 × 40 $Å^3$ (Fig. 3(b)). The scattering curve calculated from one of the dimers formed in the crystal fit the experimental scattering data better than those of the other dimers in the crystal (Fig. 3(a)). The two protomers in the dimer were related to translational symmetry. In the dimer model, the hydrophobic patch of one protomer interacted with the hydrophobic patch of another protomer. Furthermore, a salt bridge was formed between the two protomers. The residues involved in these interactions were highly conserved in bacterial

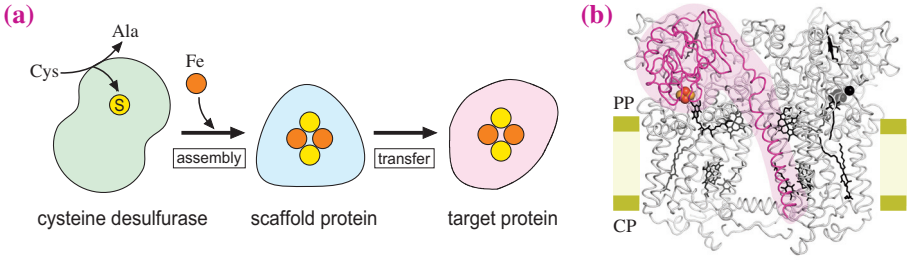

Fig. 1. Biosynthesis of iron-sulfur clusters. (**a**) The ISC system. (**b**) PetA in the cytochrome bc_1 complex of a photosynthetic bacterium [4]. The complex contains two PetA, one of those is colored in magenta. PP: periplasmic side, CP: cytoplasmic side.

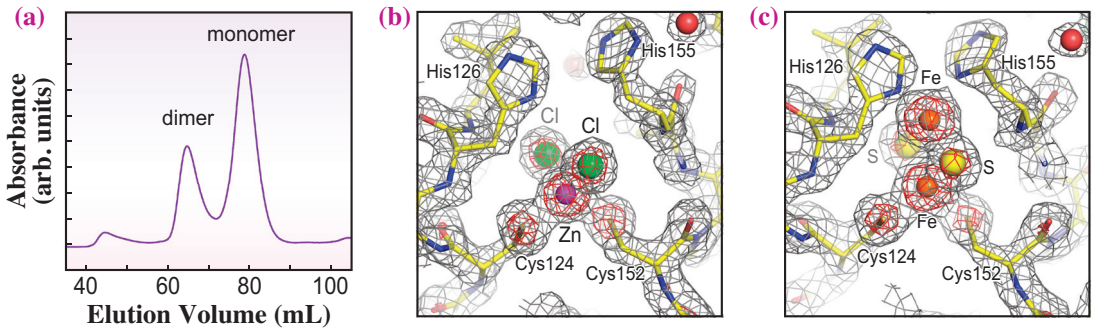

Fig. 2. Structural analyses of PetA. (**a**) The SEC elusion profile monitored at 280 nm. (**b**) Electron density ($2F_{obs} - F_{calc}$) map for the cluster-binding site of Zn-PetA. (**c**) Electron density map for [2Fe–2S]-PetA.

PetA. Thus, such dimer can be formed in bacterial PetA. When structural changes are introduced in the C-terminal region of one protomer, the fit to the envelope are further improved (Fig. 3(b)). These changes can inhibit the formation of salt bridges between the dimer and another protomer. This should explain why they did not form oligomers larger than dimers. Iron-sulfur clusters were confirmed to be reconstituted in Zn-PetA under *in vitro* condition [5]. This indicates that the Zn-containing structure determined in this study is an immature structure that appears before the maturation of iron-sulfur cluster-containing proteins. The dimerization of immature proteins may avoid unfavorable degradation caused by proteases in cells.

In this study, the combination of X-ray crystallography and SAXS analysis revealed the tertiary and quaternary structures of the immature form of a Rieske-type iron-sulfur protein to be accurately elucidated. Further studies should be performed to reveal the insertion process in detail, including the formation of intermediate complexes of the scaffold protein and the target protein.

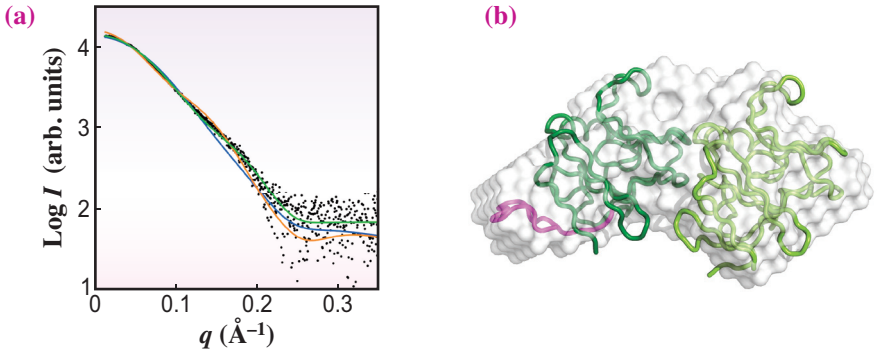

Fig. 3. SAXS analysis for the dimer structure of Zn-PetA. (**a**) The experimental scattering data are shown as black dots, and the calculated curves of three dimer candidates constructed based on the crystal packing are shown in green, orange and blue. (**b**) The *ab initio* envelope model derived from the SAXS data is represented as gray surface. The most plausible dimer model giving the green curve in the (a) is fitted to the envelope. The changed portion of the C-terminus is colored in magenta.

Kazuki Takeda

Department of Chemistry, Kyoto University

Email: ktakeda@kuchem.kyoto-u.ac.jp

References

[1] J. J. Braymer *et al.*: BBA Mol. Cell Res. **1868** (2021) 118863.
[2] C. Baussier *et al.*: Adv. Microb. Physiol. **76** (2020) 1.
[3] B. Srour et *al.*: J. Am. Chem. Soc. **144** (2022) 17496.
[4] L. Esser *et al.*: J. Biol. Chem. **283** (2008) 2846.
[5] *E. Tsutsumi, S. Niwa, R. Takeda, N. Sakamoto, K. Okatsu, S. Fukai, H. Ago, S. Nagao, H. Sekiguchi, K. Takeda: Commun. Chem.* ***6*** *(2023) 190.*

CryoEM and SAXS studies on metastable conformations appearing in cofactor-ligand association and catalysis of glutamate dehydrogenase

Enzymes are indispensable biological macromolecules that play critical roles in maintaining the metabolism in living cells. To grasp the fundamental processes of life from physics and chemistry perspectives, understanding the structure and dynamics of enzymes is crucial. Although enzyme structures have traditionally been determined using X-ray crystallography, this method may restrict conformational dynamics due to the molecular contacts necessary to preserve the crystalline arrangements of the enzymes. In contrast, cryoEM may have the potential of visualizing metastable conformations that arise during the enzymatic reaction cycles. In this study, we investigated the metastable conformations appearing in the enzymatic reaction of glutamate dehydrogenase from *Thermococcus profundus* (GDH) using cryoEM (EM01CT: CRYO ARM 300 (K3)) and small-angle X-ray scattering (SAXS) performed at SPring-8 **BL38B1** [1].

GDH catalyzes the deamination converting glutamate to 2-oxoglutarate and ammonia in the presence of cofactor, nicotinamide dinucleotide phosphate (NADP) (Fig. 1(a)). The reaction kinetics of GDH is described by the ordered bi scheme [1]. GDH is composed of six identical subunits, each with a molecular weight of 46k, and each subunit folds into a cofactor-binding domain (NAD domain) and a hexamer-forming domain (core-domain) [2]. Between the two domains, a large active-site cleft is situated. In the unliganded state, the NAD domain exhibits spontaneous hinge and shear motions controlled predominantly by the association and dissociation of several hydration water molecules located at the depth of the active-site cleft [2-4].

In this study, we focused on the metastable conformations that emerge during the enzymatic reaction of GDH [1]. For cryoEM observation for the initial stage, a GDH-NADP-glutamate solution at 278 K was flash-frozen for 15 s after mixing. For the steady stage, a GDH-NADP-glutamate solution at 293 K was flash-frozen at 3600 s after mixing. For each stage, the consensus map of the GDH hexamer was reconstructed at a resolution range of 2.3–2.2 Å, assuming D3 symmetry in the hexamer (Fig. 1(b)). The consensus maps of both stages displayed compaction from the hexamer structure in the unliganded state. Compaction in the steady stage was confirmed by comparing the SAXS data obtained at BL38B1 with that in the unliganded state (Fig. 1(c)). The radius of gyration of GDH in the steady stage was 42.2 ± 0.1 Å, while that in the unliganded state was 43.2 ± 0.1 Å. The NAD domain regions of the consensus map exhibited disorder, particularly at the tip, suggesting that the NAD domain map was in an ensemble of different metastable conformations.

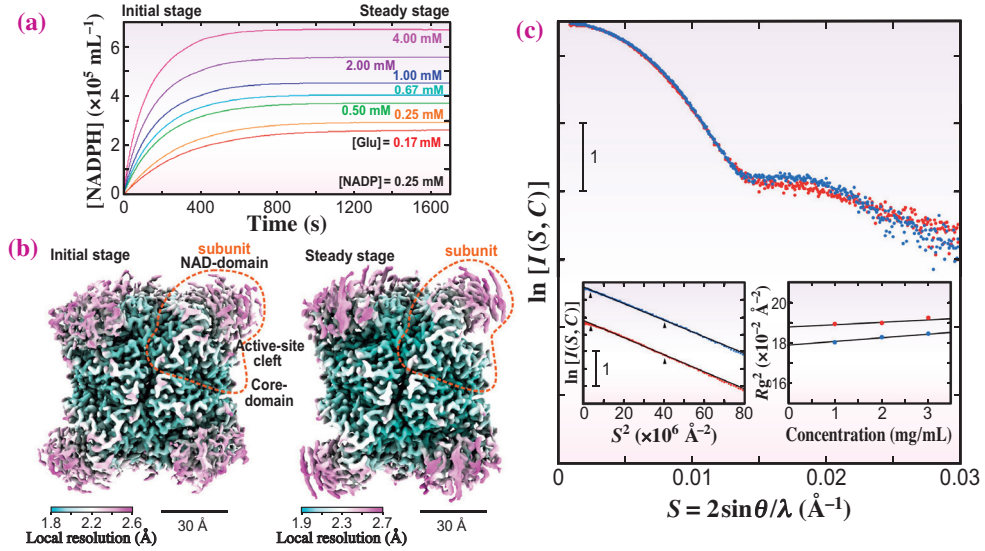

Fig. 1. **(a)** Enzymatic reaction of GDH for 0.17–4.00 mM glutamate in the presence of NADP. The reaction monitored by the concentration of the product NADPH is divided into the initial and steady stages. **(b)** Potential maps of GDH hexamer in initial (left) and steady (right) stages. The maps are shown using the coloring scheme on the local resolution shown at the bottom left in each panel. **(c)** SAXS profiles of GDH (2 mg·mL^{-1}) in the absence (red dots) and in the steady stage (blue dots). The left inset panel is the Guinier plot for SAXS profiles of GDH (1 mg·mL^{-1}). For clarity, the plot for the steady stage was appropriately shifted. The right is the concentration dependencies of the square of the radii of gyration ($Rg^2(C)$).

To separate the metastable conformations, we applied the focused classification protocol to the NAD domain, and revealed four and seven metastable conformations in the initial (Fig. 2) and steady stages, respectively. In each metastable state, a map, interpretable as a cofactor molecule, appeared in the NAD domain. The number of cofactor molecules associated with GDH was consistent with the estimation from the enzyme kinetic analysis for the initial stage.

Among the metastable conformations, the conformations designated as “reaction” had a completely closed active-site cleft and were separated into two states, pre- and post- reaction, with respect to the structure in the reaction pocket. In the pocket of the pre-reaction state, an isolated map assignable to one hydration water molecule used in the deamination reaction appeared near the tip of Lys105. In the post-reaction structure, a map of an ammonium ion appeared near the mainchain of Asn344.

In two metastable conformations, labeled “half-open” and “pre-complex”, respectively, the cofactor maps displayed disorder in the nicotinamide region. We assigned the cofactor molecule NADP based on the differences in the conformational dynamics of NADP and NADPH in solution. As the two conformations had potential maps assignable to glutamate in the reaction pocket, they were categorized as enzyme-cofactor-substrate complexes. The metastable conformation named “pre-open” had a cofactor map that could be fully modeled as NADPH and was assigned as the GDH-NADPH complex after the reaction products were released.

The four metastable conformations were mapped to the ordered bi reaction scheme as illustrated in Fig. 2. The present study suggests that the Michaelis complex, i.e., the GDH-NADP-glutamate complex, in the enzymatic kinetic theory is an ensemble of several metastable conformations.

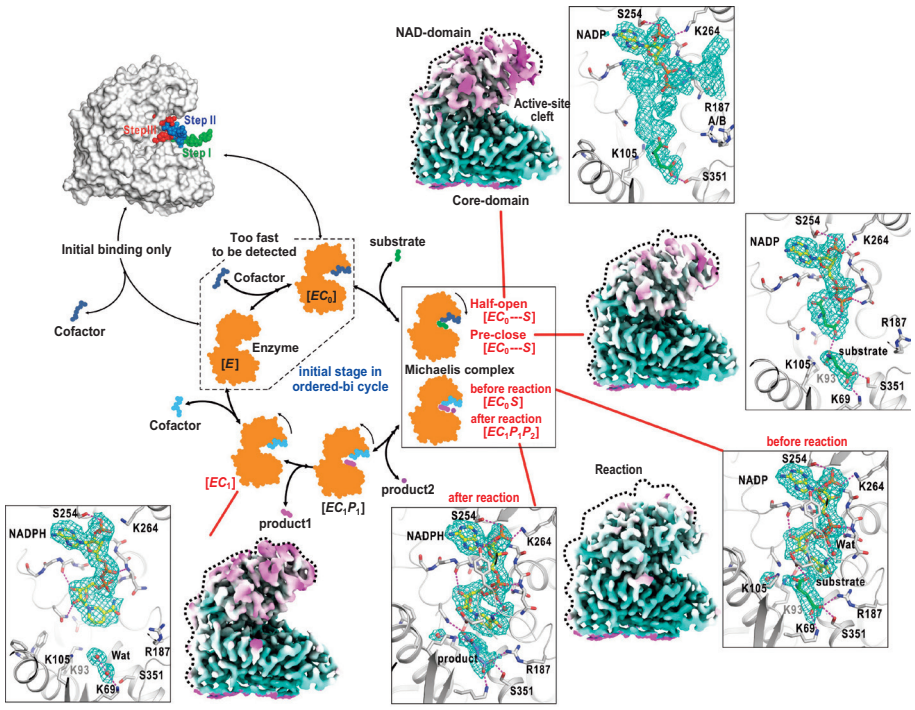

Fig. 2. Structurally identified four metastable conformations of GDH in the initial stage are mapped to kinetic states in the ordered bi reaction cycle. Three of the four metastable conformations are classified into the Michaelis complex from the viewpoint of enzyme kinetic theory. Of these three, the conformations with completely closed active-site clefts are assigned as the pre- and post-reaction states. The other two still had an open cleft and were likely associated with the substrate molecule. The fourth conformation was assigned as the complex of GDH and NADPH. The previous cryoEM study on the GDH-NADP complex suggested that the first NADP binding would occur via a ligand-binding pathway different from that of the ordered bi-cycle. [5]

Taiki Wakabayashi[a,b], Mao Oide[a,b,c,d] and Masayoshi Nakasako[a,b,*]

[a] Department of Physics, Keio University
[b] RIKEN SPring-8 Center
[c] PRESTO, Japan Science and Technology Agency
[d] Protein Research Institute, Osaka University

*Email: nakasako@phys.keio.ac.jp

References

[1] *T. Wakabayashi, M. Oide, M. Nakasako: Sci. Rep.* ***14*** *(2024) 11165.*
[2] M. Nakasako *et al.*: Biochemistry **40** (2001) 3069.
[3] T. Oroguchi and M. Nakasako: Sci. Rep. **6** (2016) 26302.
[4] M. Oide *et al.*: FEBS J. **287** (2020) 3472.
[5] T. Wakabayashi *et al.*: FEBS J. **290** (2023) 5514.

Visualizing magnetic control of nanoparticles for airway gene therapy using ultrafast *in vivo* dark-field X-ray imaging

Cystic fibrosis is the most common life-limiting genetic disorder in Australia, with respiratory disease the leading cause of mortality. Cystic fibrosis is caused by a mutation of the *CFTR* gene, so a proposed treatment strategy is gene-addition therapy, whereby fully functioning copies of the *CFTR* gene are delivered to cells using a transfer vector. Gene vectors need to be transported to the specific airway cells that require correction, and retained in place long enough to interact with those cells. This is made challenging by mucociliary clearance, a process that traps inhaled particles in mucus and clears them from the airways via ciliary motion. A novel approach to overcome these challenges is coupling the gene vector to magnetic nanoparticles, allowing the vector to be retained and controlled within the airways using external magnetic fields [1].

Controlling and visualizing magnetic nanoparticle behavior within airways is challenging. Previously, propagation-based phase-contrast X-ray imaging showed magnetic nanoparticles form strings in the airway under exposure to a magnetic field, but these are very hard to visualize. Here we have explored the use of dark-field X-ray imaging to further enhance nanoparticle contrast and gain new insights into magnetic particle control *in vivo*. X-ray dark-field imaging detects ultra-small angle scattering caused by microstructures within the sample [2]. If these structures are asymmetric and the longest axes are aligned, they can scatter anisotropically (i.e., X-rays are scattered preferentially in one direction, usually orthogonal to the orientation of the scattering object). Detecting this scatter gives the directional dark-field signal [2], allowing the orientation of microstructures to be measured.

The aim of this study was to explore how magnetic nanoparticles behave within a live airway under the influence of dynamic magnetic fields. We hypothesized that the directional X-ray dark-field signal could help visualize the presence of the nanoparticles, showing how they move in response to the magnetic field.

The experiment was undertaken at SPring-8 **BL20XU** beamline. A rat was anaesthetized and a cannula inserted into the trachea to enable delivery of magnetic nanoparticles to the airways using a syringe pump. A 3D-printed motorized magnet holder, shown

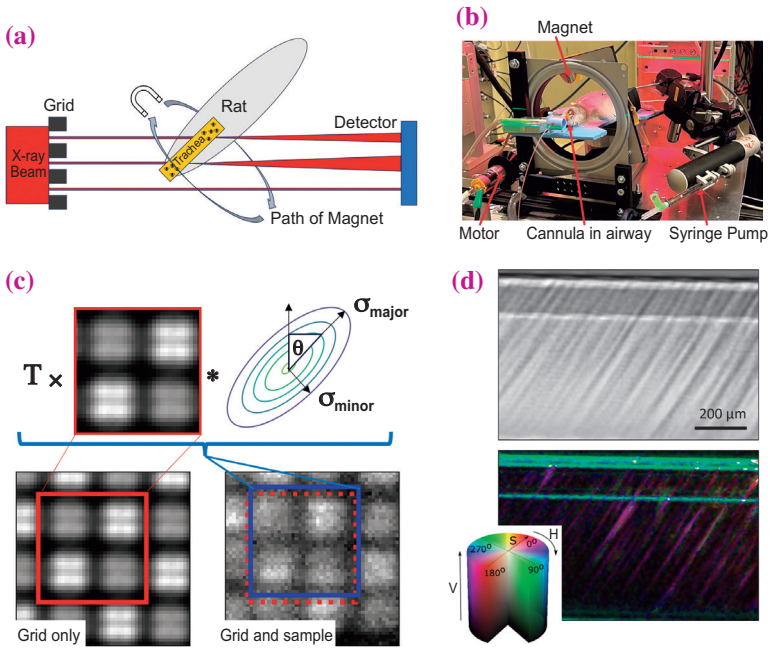

Fig. 1. **(a)** Shows a simplified top-down view of the experiment. The beam is patterned by a phase grid, creating beamlets. These beamlets are diffused as they scatter through the sample, with the dark-field extracted from the strength of the blurring seen downstream at the detector. **(b)** A photo of the motorized magnetic array and rat. **(c)** Shows how the blurring of the beamlets is modelled by the UMPA algorithm, using an intensity scaling for transmission T, and convolution with a directional dark-field kernel. **(d)** Shows that magnetic nanoparticles in a capillary tube (shown in transmission in the upper image) produce a directional dark-field signal (lower image). [3]

in Fig. 1(b) was designed to externally rotate a magnet around the rat.

To extract the X-ray dark-field signal, a checkerboard phase grid was placed into the beam upstream of the sample. Figure 1(a) shows a simplified diagram of the grid producing a pattern of beamlets, with the sample scattering each beamlet. The dark-field images were extracted using the directional dark-field extension to the unified modulation pattern analysis (UMPA) algorithm [2]. UMPA compares windows in the grid pattern with and without the sample in the beam. Attenuation is measured by looking at the reduction of intensity, and phase can be found by looking at how the beamlets are refracted. The directional dark-field signal is modelled as the blurring of the pattern by a two-dimensional Gaussian kernel (Fig. 1(c)).

Images were taken of 'strings' of magnetic nanoparticles in a capillary tube to confirm that they produced a directional dark-field signal (Fig. 1(d)). The directional dark-field image uses a HSV color scheme. The hue (H) relates to the scattering orientation θ and the saturation (S) to the eccentricity of the Gaussian kernel. The value (V) is the scattering magnitude.

Images of the particles during delivery were used to quantify the contrast enhancement of dark-field imaging compared to the attenuation signal. The transmission value decreased by 5.2 standard deviations from the mean background value, while the dark-field signal peaked at 18.6 standard deviations from the background signal, showing that dark-field increased the signal-to-noise ratio of this event 3.5-fold.

Having seen that adding an external magnetic field causes the magnetic nanoparticles to create packed string-like structures, we then rotated a magnet around the outside of the rat's neck to cause these strings to form and rotate within the trachea. Figure 2 shows images of a highly concentrated region of magnetic nanoparticles as the field changes, with a directional dark-field clearly visible. However, in regions with a lower concentration of magnetic nanoparticles, the directional dark-field signal was not as clear. Although we have shown proof-of-concept for *in vivo* directional dark-field airway imaging, we expect that further optimization of the imaging setup will enhance contrast further. This will allow us to continue our goal of developing magnetically guided airway gene therapy treatments.

All animal studies were performed in accordance with protocols approved by the University of Adelaide and SPring-8 animal ethics committees.

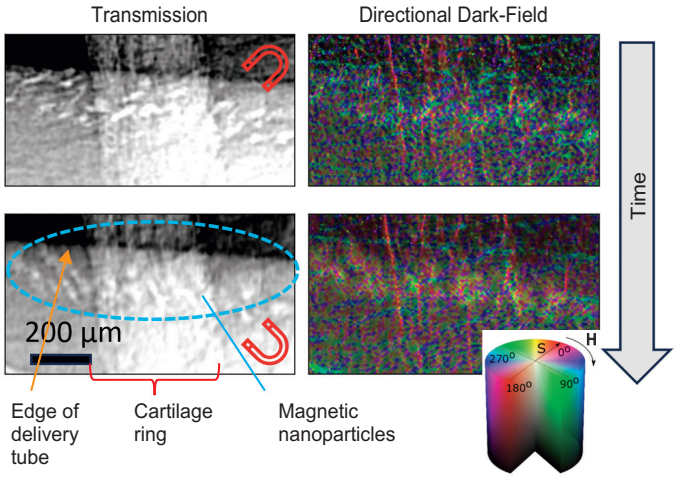

Fig. 2. X-ray transmission and directional dark-field images taken from a time series as the magnet passes around the rat (magnet symbol shows the approximate direction of magnetic field). [3]

Ronan Smith[a,*], Kaye Morgan[b] and Martin Donnelley[a]

[a] Adelaide Medical School, University of Adelaide, Australia
[b] School of Physics and Astronomy, Monash University, Australia

*Email: ronan.smith@adelaide.edu.au

References

[1] M. Donnelley *et al.*: Sci. Rep. **12** (2022) 9000.
[2] A. C. J. Smith *et al.*: PLoS One **17** (2022) e0273203.
[3] *R. Smith, K. Morgan, A. McCarron, P. Cmielewski, N. Reyne, D. Parsons and M. Donnelley: Phys. Med. Biol.* ***69*** *(2024) 105025.*

Increased cardiac muscle calcium sensitivity is associated with impaired coronary vascular flow – Implication for hypertrophic cardiomyopathy

Hypertrophic cardiomyopathy (HCM) is primarily a genetic heart disease that is associated with thickening of the myocardium (heart muscle), which is termed hypertrophy [1]. It is generally accepted that hypertrophy of the myocardium impacts upon the function of the heart by compressing and restricting the flow through the microvessels within the muscle (see Fig. 1, illustrating the main coronary arteries and microvessels within the muscle wall) [2]. The coronary microvessels supply vital oxygen and nutrients to the cardiomyocytes to drive ATP production and meet the energetic demands of the beating heart. Ultimately, this microvascular compression and impaired blood flow accelerates the development of heart failure in HCM patients [1]. On the other hand, however, some patients who are carriers of the genetic mutations in myofilament proteins that are yet to develop pathological hypertrophy demonstrate reduced coronary blood flow, suggesting additional factors underly coronary flow impairment beyond hypertrophy *per se* [1].

Under physiological conditions, blood flows freely though the coronary arteries into the microvessels as the heart is filling with blood during the relaxation (diastolic) phase of the cardiac cycle (Fig. 1(a)), whereas during the contraction (systolic) phase, flow is reduced as the coronary vessels are naturally compressed in a “squeezing” motion [3]. In HCM one of the first pathological features that develops is hypercontractility, where the cardiac muscle becomes hypersensitive to the Ca^{2+}-ion (i.e., calcium sensitivity) and the heart contracts more strongly at much lower concentrations of Ca^{2+} than is normally required [1]. Given that both hypercontractility and impaired coronary blood flow are frequently observed prior to the development of pathological hypertrophy in HCM, we hypothesized that the hypercontractility associated with enhanced Ca^{2+} sensitivity will also impair coronary blood flow (Fig. 1(b)) [1].

This brief study was conducted at SPring-8 **BL20B2**. Absorption imaging with monochromatic X-rays at 34 keV, just above the *K*-edge of iodinated contrast agent provides high spatial and temporal resolution to achieve visualization of coronary vessels < 50 μm in diameter in rodents [4]. We used adult wild-type (WT) C57BL/6J mice (n=4) to avoid potential confounding effects associated with transgenic mouse models of HCM (e.g., myocardial wall thickening, fibrosis) that may mask the effects of hypercontractility [1]. Hypercontractility was pharmacologically induced in mice with an acute bolus of EMD-57033 (10 μM, 150 μL intravenous bolus), which elevates myocardial Ca^{2+} sensitivity and induces a hypercontractile state similar to what is observed in HCM. After inducing deep anesthesia mice were first imaged under baseline conditions (vehicle solution, 150 μL i.v.), then subsequently imaging was repeated 10 minutes post EMD-57033 treatment (Fig. 2). Image frames representing diastolic and systolic phases were manually selected for analysis. Visualized vessel area was determined for three to four microvessels that could be visualized across the entire cardiac cycle for each mouse (Fig. 2).

Under baseline conditions, the coronary microvessel area was reduced by 30 ± 13% during the systolic phase relative to the diastolic phase, which is an expected physiological response (Fig. 3(a)) [1]. By contrast, the

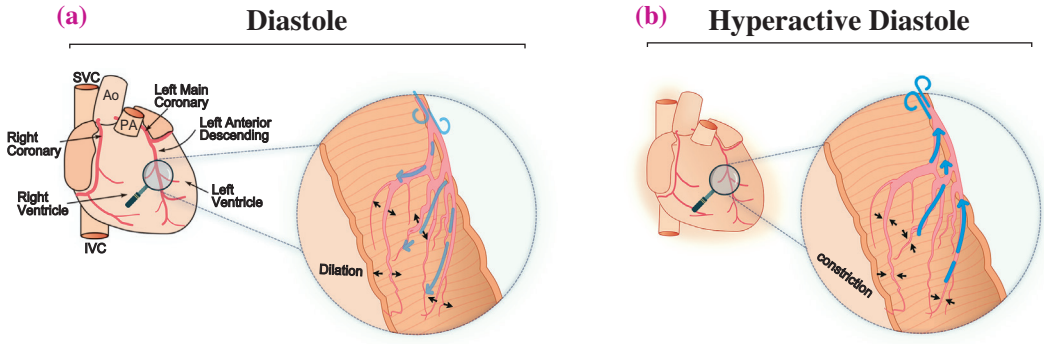

Fig. 1. Hypothesized coronary artery constriction due to hypercontractility. **(a)** In normal diastole, microvessels remain open to support blood flow. **(b)** In hyperactive diastole, excessive contraction compresses microvessels, reducing oxygen supply to deeper muscle within the wall. Ao, aorta; PA, pulmonary artery; IVC, inferior vena cava; SVC, superior vena cava.

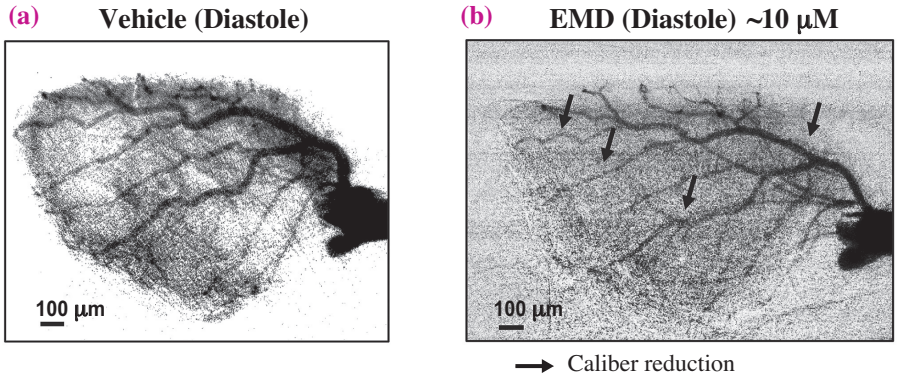

Fig. 2. Synchrotron microangiography showing change in microvascular function. **(a)** Baseline angiogram in diastole after vehicle infusion and **(b)** angiogram 10 minutes post-EMD-57033 infusion shows reduced vessel caliber (arrows). Four wild-type mice were imaged, with 13 microvessels analyzed in total. [1]

coronary vessel area actually increased by 8 ± 7% from the diastolic to systolic phase post-EMD-57033, suggesting that myocardial hypercontractility impaired diastolic coronary flow. Indeed, compared to vehicle baseline, EMD-57033 reduced both the diastolic and systolic vessel areas by 82 ± 16% and 32 ± 11% respectively (Fig. 3(b)). The pronounced constriction of the coronary microvessels observed in this study indicates that myocardial hypercontractility as a result of increased Ca^{2+} sensitivity may be sufficient to impair coronary blood flow.

Our findings in this study have important implications for the management of HCM. Many of the current HCM treatments focus on alleviating the structural manifestations of the myocardium, however, targeting the myocardial hypercontractility from an early stage of HCM may be just as an effective approach. One promising treatment is mavacamten, a novel myosin inhibitor, which is shown to reduce myocardial hypercontractility. Our future studies will further investigate if mavacamten can improve coronary blood flow in animal models of HCM.

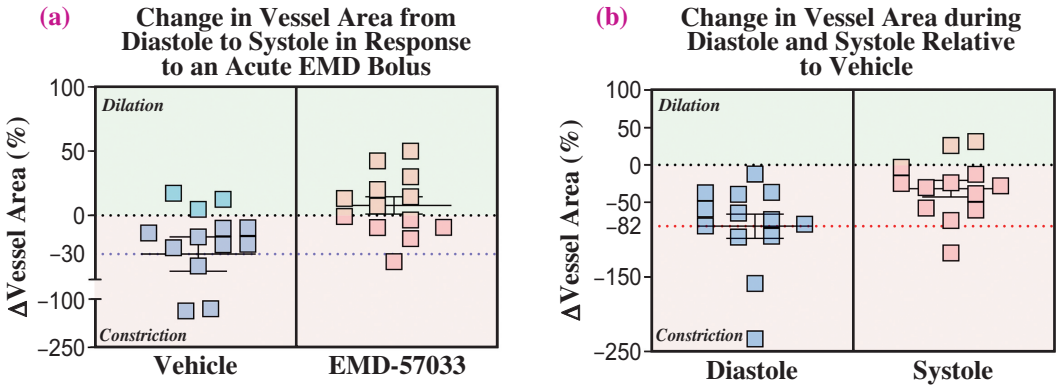

Fig. 3. Percentage changes in vessel area during diastole and systole, with and without EMD-57033. **(a)** Changes from diastole (relaxation) to systole (contraction) following vehicle and EMD-57033 administration. **(b)** Reduction in vessel area in response to the hypercontractile state induced by EMD-57033. Blue and red-dotted lines indicate the mean in the vehicle period and diastole for clarity. [1]

James T. Pearson[a,b,*], Vasco Sequeira[c] and Mark T. Waddingham[a]

[a] Dept. Cardiac Physiology, National Cerebral and Cardiovascular Center Research Institute
[b] Dept. Physiology and Monash Biomedicine Discovery Institute, Monash University, Australia
[c] University Clinic Würzburg, Germany

*Email: jpearson@ncvc.go.jp

References

[1] *V. Sequeira, M. T. Waddingham, H. Tsuchimochi, C. Maack, J. T. Pearson: J. Mol. Cell. Cardiol. Plus* ***4*** *(2023) 100036.*
[2] J. M. Federspiel *et al.*: Circ. Heart Fail. **17** (2024) e011435.
[3] J. E. Davies *et al.*: Circulation **113** (2006) 1768.
[4] J. T. Pearson *et al.*: Sci. Rep. **7** (2017) 18108.

Observation of mammalian living cells by a femtosecond single-shot exposure of a soft X-ray free electron laser

Soft X-ray microscopy in the water window (280–530 eV), situated between the carbon *K*-edge (~280 eV) and the oxygen *K*-edge (~530 eV), enables high-spatial-resolution, high-contrast imaging of biological samples in water without the need for labeling, based on contrast mainly originating from carbons in biomolecules. However, because soft X-ray irradiation causes significant radiation damage on living cells, most soft X-ray imaging studies rely on chemically fixed samples. Chemical fixation, while simplifying sample handling, can result in the loss of fine structures and intracellular elements, thus motivating development of a method to observe living cells while minimizing radiation damage.

Recent advances in soft X-ray free electron laser (SXFEL) sources can address this challenge. SXFELs can produce extremely bright femtosecond pulses, so short that the imaging process is finished before severe structural damage can occur on cells. This principle, sometimes called “imaging before destruction,” has already enabled groundbreaking images of living viruses and bacteria [1], but observing larger mammalian cells has been difficult due to their large size. Because mammalian cells are fundamental models in medical and pharmacological research, developing a damage-free, label-free soft X-ray imaging method has remained a critical goal. We developed a soft X-ray transmission microscope with a single-shot femtosecond illumination using an SXFEL for observation of mammalian living cells [2].

To achieve label-free imaging of living mammalian cells with minimal radiation damage, our group constructed a soft X-ray transmission microscope at the soft X-ray beamline of SACLA **BL1** (Fig. 1) [3]. We developed a pair of Wolter mirrors for condenser and objective optics [4]. Wolter mirrors are grazing-incidence reflective optics for soft X-rays. They inherently minimize spherical aberration and commatic aberration, also providing a long working distance and large acceptance area. The long working distance allows the use of thick sample holders filled with culture medium, while the achromaticity of Wolter optics readily accommodates spectrally-resolved imaging across the water window.

In our setup, the third harmonic of the SXFEL beam, typically with a pulse width of around 30 femtoseconds [5], was directed to the sample through Kirkpatrick–Baez (KB) mirrors and a condenser Wolter mirror (CWM). The transmitted beam was then magnified by an objective Wolter mirror (OWM) onto a CCD detector. The spatial resolution is 230 nm at a photon energy of 390 eV and the field of view is $52 \times 52\ \mu m^2$. The microscope is also equipped with visible-light imaging capabilities, allowing sample positioning based on conventional bright-field images. Because of the strong absorption of carbon at these photon energies and the comparatively lower abundances of nitrogen and oxygen, the resulting soft X-ray images primarily reflect the distribution of carbon within the cell.

We observed Chinese hamster ovary (CHO-K1) cells enclosed in a liquid cell holder containing culture medium. The entire holder was sealed and maintained at 37°C to keep the cells alive. The images on the left side of Fig. 2 shows cells captured at a photon energy of 390 eV by a single 30-femtosecond shot by the SXFEL. A variety of cellular structures were visualized in these images. In particular, accumulations of carbon (biomolecules) were observed in regions thought to correspond to nucleoli and the nuclear membrane

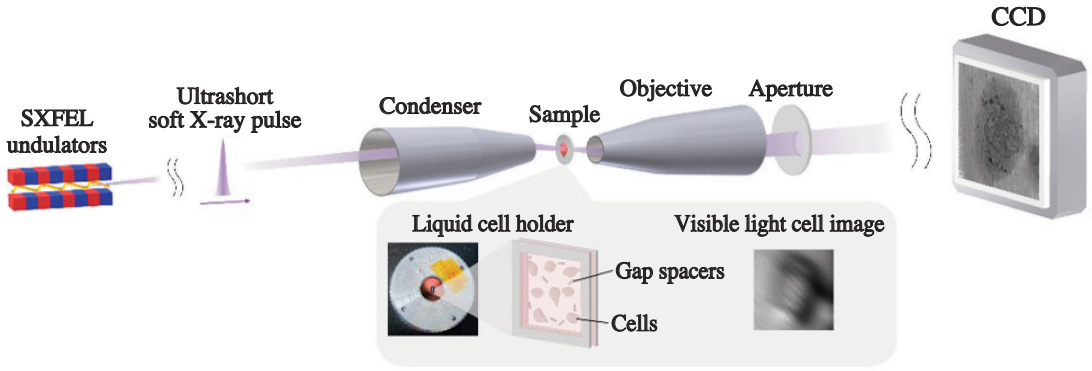

Fig. 1. Schematic illustration of a soft X-ray transmission microscope with SXFEL illumination. [2]

(arrows in Fig. 2). We also detected filamentous structures radiating from the nucleolus to the nuclear membrane. These filamentous structures may constitute an important pathway linking the nucleolus, nuclear membrane, and cytoplasm.

The images on the right side of Fig. 2 are images captured with a 0.5-second multi-shot exposure immediately after the single 30-femtosecond shot. In comparison with the initial single-shot image, we observed some blurriness likely caused by cellular motion or structural changes. Observations were carried out also on paraformaldehyde-fixed cells, but the various structures seen in the living cells were not discernible [2].

In summary, we achieved single-shot label-free imaging of living mammalian cells in culture medium using an SXFEL by overcoming the long-standing issue of X-ray-induced radiation damage on living cells. Numerous cellular structures including previously unknown ones were suggested. As improvements in light source performance allow brighter single-shot images, it will become possible to capture even finer structures with greater clarity. Moreover, soft X-rays can be used not only for carbon imaging but also for analyzing other light elements essential to cellular metabolism such as iron, zinc, phosphorus, and calcium. In the future, this microscope is expected to offer new perspectives in biology by enabling, for example, the visualization of instantaneous changes in chemical states within living cells.

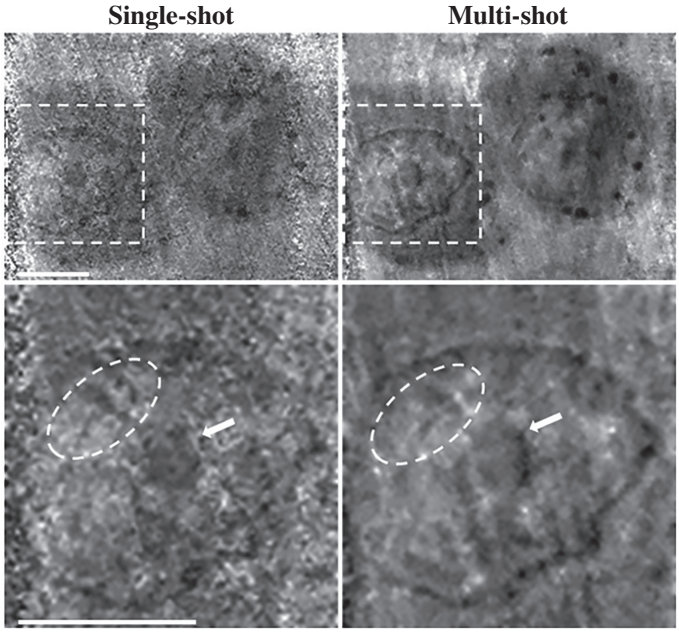

Fig. 2. Soft X-ray images of cells. (Upper left) A soft X-ray image of a living cell captured by a single-shot exposure of an SXFEL pulse. (Upper right) A soft X-ray image of the same cell obtained immediately afterward under 30 shots exposure in 0.5 s. (Lower left and lower right) Magnified views of the cell in the dashed square region. The ovals and arrows (nuclei) indicate the regions at which significant structural changes are observed between the single-shot image and multi-shot image. Scale bars: 5 μm. [2]

Satoru Egawa[a,b,*], Mari Shimura[c,d] and Takashi Kimura[e]

[a] RIKEN Center for Advanced Photonics / Wako
[b] Research Center for Advanced Science and Technology, The University of Tokyo
[c] RIKEN SPring-8 Center
[d] Research Institute, National Center for Global Health and Medicine
[e] The Institute for Solid State Physics, The University of Tokyo

*Email: egawa@upm.rcast.u-tokyo.ac.jp

References

[1] T. Kimura *et al.*: Nat. Commun. **5** (2014) 3052.
[2] *S. Egawa, K. Sakurai, Y. Takeo, K. Yoshinaga, M. Takei, S. Owada, G. Yamaguchi, S. Yokomae, H. Mimura, Y. Yamagata, M. Yabashi, M. Shimura, and T. Kimura: Optica **11** (2024) 736.*
[3] S. Egawa *et al.*: Opt. Express **27** (2019) 33889.
[4] S. Egawa *et al.*: Rev. Sci. Instrum. **94** (2023) 053707.
[5] S. Owada *et al.*: J. Synchrotron Rad. **27** (2020) 1362.

Tracking ultrafast and irreversible creation of light-induced structural orders

Ultrafast light-matter interactions have emerged as a powerful approach for creating and manipulating new states of matter, offering unprecedented control over novel material properties that are challenging or impossible to achieve through conventional equilibrium approaches. For example, in an oxide thin film heterostructure of $PbTiO_3/SrTiO_3$, our team shows that three-dimensionally ordered superstructures, which we dubbed "supercrystals", can emerge after exposing the sample to femtosecond laser pulses [1]. Although the ultrafast light-matter interaction only occurs within 100 femtoseconds of the laser pulse width, this supercrystal can remain stable in ambient conditions for years until thermal cycling to 450 K and back to room temperature restores the initial phases. Despite the knowledge of the initial and final state of the transformation, a fundamental question regarding to the transition pathway remains to be answered, namely, how these new states emerge and evolve into a nonvolatile form. Answering this question can provide precise mechanistic insights into the creation of these exotic functional states of matter.

However, due to the irreversible and ultrafast nature of the process, tracking the creation of supercrystals is challenging because the typical stroboscopic pump-probe technique cannot be applied. In this work [2], we utilize the unique properties of X-ray pulses from free electron lasers, namely the single-bunch brightness and its ultrafast pulse duration, to allow us to access the transient state of irreversible processes. At one pristine site, only one pump-probe event at a specific time delay can be performed. To capture the sequence of the transformation, the sample needs to be replenished by moving to a fresh spot for each pump-probe event at various time delays. By repeating this "move-and-measure" procedure, we were able to record and assemble a time-lapse movie to reveal the structural details on how the supercrystal forms. The initial measurements were performed at SACLA **BL3** beamline and additional data were collected at the X-ray pump-probe beamline at the LCLS.

By tracking the diffraction pattern changes, we found that the creation of supercrystal started with the collapse of the as-grown vortex (V) and ferroelectric (FE) order within 300 fs femtoseconds as the diffraction peaks intensities are significantly reduced (Fig. 1(a)). The FE phase is erased and turns into a weakly disordered metastable nanopolar phase (D-FE) stabilized by the photoinduced charge injection. At the same time, the V phase transforms into a metastable FE-like (c^+/c^-) phase, up-and-down polarized nanoregions; in this phase, the vorticity is suppressed as the vortices unwind. Within a few picoseconds, the collapse of preexisting orders enters the 'soup' state, providing an empty canvas before the vortex supercrystal (VSC) emerges. After a significant incubation time, over a timespan of 10 ps to a few nanoseconds, a labyrinthine stripe phase (L) starts to appear and the c^+/c^- phase strengthens, and its periodic satellite pattern persists throughout the transformation (Fig. 1(b)). This mixing of phases evolves under a long-lasting interplay between the charge carrier screening of depolarizing fields and reduced mesoscopic ferroelastic strains at the phase boundaries. As the sample cools down on tens of nanoseconds due to thermal transport from the film to the substrate, the

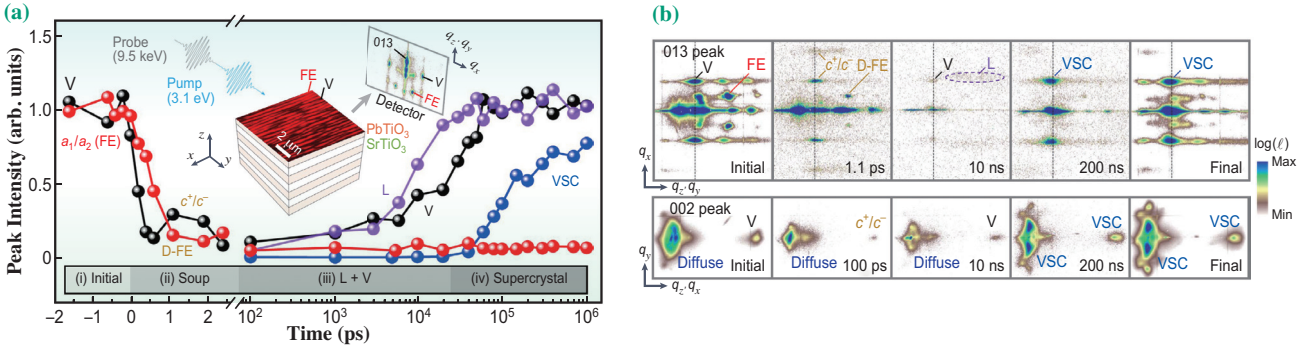

Fig. 1. Capturing the pathway of phase transformation. **(a)**Twin a_1/a_2 FE- and V-phase coexistence in the initial state as superdomains with ~400 nm periodicity along the y axis (inset: dark-field X-ray microscopy). After the initial collapse of the V and FE orders on the ~1 ps timescale, a 'soup' of D-FE and metastable V forms in the intermediate stages, followed by the correlated emergence of an L phase with the recovery of the V phase on a timescale of a few nanoseconds. The L and V phases undergo simultaneous conversion to the VSC supercrystal phase after 20 ns. **(b)** Representative detector images show diffuse diffraction patterns recorded near the 002 and 013 Bragg geometries tracking the evolution of the phases in (a). In the 013 geometry, the black vertical dashed line tracks the q_z value (proportional to ε_{33} normal strain) of the initial V phase, whereas the VSC satellites (marked in the inset at 200 ns and the final state) are shifted to larger q_z, corresponding to its ε_{33} normal strain value. The larger q_z corresponds to the left side of detector images. [2]

original V and FE phases do not recover. Instead, the VSC phase starts to nucleate and grow, as evidenced by the satellite peaks of VSC phases in the diffraction pattern. On microsecond time scales, the phase conversion process completes.

With the direct structural characterization that spans from femtosecond to microseconds, an unprecedented seven orders of magnitude time scale, insights into the formation of new order parameters can be gained by comparing the experimental results with the theoretical simulation. A dynamical phase-field model has been developed to simulate this entire process including important parameters such as time-dependent carrier concentration, inhomogeneous strain, and gradient energy. The microscopic insights obtained by the spatial dependence of the shear strain as well as carrier concentration are shown by Fig. 2(a). The shear strain (ε_{23}) correlated well with the evolution of the carrier concentration: the shear strain arises at the boundary between the nanodomains with varying polar textures due to the mismatch of lattice deformations associated with polarization reorientations across these boundaries. This correlation illustrates the critical role of the optically excited carriers in the formation of VSC. The dynamical trajectory of successive phase transformations is summarized in Fig. 2(b) as a function of charge and ε_{23}, illustrating the reorganization of the starting phases along the pathway of phase conversions. A larger shear strain promotes the FE polarization to continuously 'curl' in an intermediate direction. The VSC structure starts to appear when the combination of carrier concentration, strain, and temperature reaches the optimal condition on nanosecond time scales.

Our work highlights that controlling phase competition is an essential ingredient for creating new ordered states. Most of the nanoscopic information in this work was derived from the characterization of the reciprocal space. Looking forward, direct real-space visualization of these phases would be critical to disentangle the nanoscale interactions among them. Our recent work has demonstrated the capability of imaging mesoscopic domain network creation using *in situ* X-ray diffraction microscopy at synchrotron [3]. We show that a richer phase diagram containing more complex nanostructures can be accessed by controlling the optical dosage. The interplay of emergent phases in real space can be visualized by scanning X-ray diffraction imaging. We envision that the development of spatiotemporal imaging at the FELs can offer unprecedented insights into real-space phase competitions, thus achieving a microscopic understanding of light-induced phase transformation at the level of phonons.

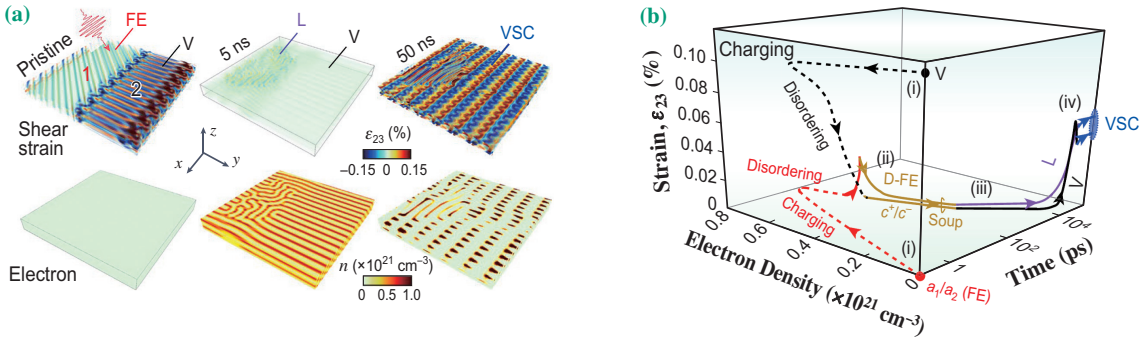

Fig. 2. Understanding the pathway of phase transformation. **(a)** Dynamical phase-field simulation (DPFM) of the spatiotemporal evolution of shear strain ε_{23} and electron concentration within two PTO plus two STO layers after excitation with single optical pulses. L fluctuations form inside the original FE region (region 1) and coexist with V (region 2) at 5 ns after single-shot optical excitation. At 50 ns, the VSC is formed. **(b)** DPFM evolution prediction of ε_{23} and electron density in the spatial regions (marked in (a)) where the initial phases (V and FE) reside. Sub-picosecond non-equilibrium disordering of the V and FE phases observed in experiments is indicated by the dashed lines. After the subsequent thermalization of the system, on the timescale of a few picoseconds, the V phase converts to c^+/c^-, whereas the FE converts to D-FE, forming the 'soup' stage. Until the VSC nucleates after 10 ns, L fluctuations gradually replace D-FE, whereas the V phase re-emerges. At the longest time delays (>20 ns), L and V merge into the VSC phase when a sudden increase in ε_{23} occurs in both 1 and 2 regions. [2]

Haidan Wen[a,*], Venkatraman Gopalan[b] and John W. Freeland[a]

[a] Advanced Photon Source, Argonne National Lab., USA
[b] Department of Materials Science and Engineering, Pennsylvania State University, USA

*Email: wen@anl.gov

References

[1] V. A. Stoica *et al.*: Nat. Mater. **18** (2019) 377.
[2] *V. A. Stoica, T. Yang, S. Das, Y. Cao, H. Wang, Y. Kubota, C. Dai, H. Padma, Y. Sato, A. Mangu, Q. L. Nguyen, Z. Zhang, D. Talreja, M. E. Zajac, D. A. Walko, A. D. DiChiara, S. Owada, K. Miyanishi, K. Tamasaku, T. Sato, J. M. Glownia, V. Esposito, S. Nelson, M. C. Hoffmann, R. D. Schaller, A. M. Lindenberg, L. W. Martin, R. Ramesh, I. Matsuda, D. Zhu, L.-Q. Chen, H. Wen, V. Gopalan, J. W. Freeland: Nat. Mater.* ***23*** *(2024) 1394.*
[3] M. Zajac *et al.*: Adv. Mater. **36** (2024) 2405294.

Femtosecond X-ray imaging of isochorically heated solid-density plasmas with XFELs

The advent of chirped pulse amplification (CPA) technology [1], which earned the Nobel Prize in Physics in 2018, has revolutionized laser science by enabling the production of ultra-intense laser beams. These powerful laser beams can accelerate free electrons to high energies, generating forward-directed electron beams. Such beams have numerous applications, including compact electron accelerators and secondary sources of radiation such as X-rays and γ-rays, and particle beams (ions and neutrons). Additionally, the extreme material conditions induced by energetic electron impacts are of great interest across diverse fields such as astrophysics, aerospace engineering, and fusion energy research.

For more than two decades, high-intensity, short-pulse lasers have been used to study matter under extreme conditions. Energetic (fast) electrons, which carry extremely high currents (mega-amperes) less than tens of picoseconds, rapidly heat targets before significant expansion occurs. This process, known as isochoric (constant volume) heating, is critical to applications such as fast ignition laser fusion [2], where laser-driven charged particle beams assist in initiating fusion reactions. However, diagnosing these highly transient target conditions is challenging due to the lack of diagnostics with sufficient spatial and temporal resolution. In addition, probing the interior of dense materials requires external hard X-ray beams.

Here, we report the first femtosecond and micron-scale resolved measurements of isochorically heated solid-density copper foils using an X-ray free electron laser (XFEL). The experiment was conducted at SACLA **BL2** EH6, combining a high-power, femtosecond laser with an XFEL beam. The experimental setup is illustrated in Fig. 1(a). A 2-μm thick copper foil was irradiated by the optical laser at a peak intensity of ~2×10^{18} W/cm^2, while a 10-fs collimated X-ray pulse provided 2D imaging of the heated region at various delay times.

An initial X-ray image of the foil, captured prior to laser irradiation, showed the unperturbed foil condition. Following laser irradiation, X-ray images revealed slight changes in transmission intensity, as depicted in Fig. 1(c). Division of pre- and post-irradiation images pronounced the transmission-affected region (Fig. 1(d)). By varying X-ray probe energies (9.05, 8.92, 9.12, and 8.05 keV) and delay timings, we measured the temporal evolution of the electron-heated region's size. This approach represents a novel use of spatiotemporally resolved transmission images to characterize heat front propagation [3] and diagnose plasma conditions within the heated material [4].

Figures 2(a–d) show X-ray transmission ratios measured at photon energies of 9.05 keV and 8.92 keV at different delays. At 9.05 keV (above the Cu *K*-edge of 8.99 keV), the heated foil exhibited

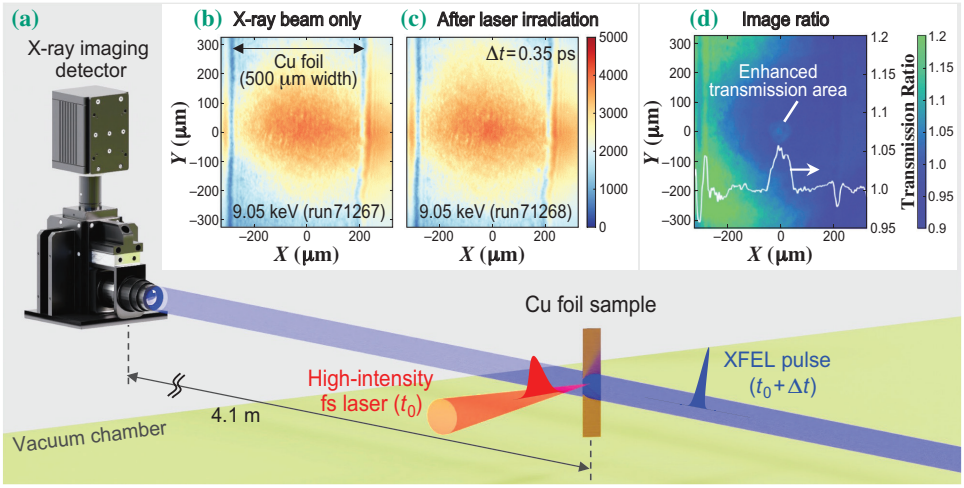

Fig. 1. **(a)** Schematic of the experiment at SACLA BL2 EH6. Measured X-ray transmission images **(b)** before and **(c)** after laser irradiation. **(d)** A transmission ratio image obtained by dividing the two images.

increased transmission and expansion up to ~1.5 ps. Conversely, at 8.92 keV (below the Cu *K*-edge), a decrease in transmission was observed. The energy-dependent transmission changes are attributed to smearing of the *K*-edge spectrum under metal-like conditions (i.e., Fermi degenerate matter) [5], which enabled us to infer an electron temperature of 7~18 eV behind the heat front. The observed expansion of the heated region was compared with 2D particle-in-cell simulations, which constrained the ionization state of the copper foil (mean charge state $\bar{Z}$) to be between 2 and 4, as shown in Fig. 2(e).

Figure 3 summarizes the experimental and simulated results in an electron temperature and density contour map [4]. The inferred plasma conditions (electron temperature T_e of 7~18 eV and $\bar{Z}$ of 2~4) fall within the warm dense matter (WDM) regime, which lies between ideal plasmas and strongly coupled and Fermi degenerate matter. This study reveals that the heated copper foil exhibits two distinct plasma regions: a highly ionized, hot plasma near the laser interaction spot, surrounded by a Fermi degenerate WDM region. Notably, our measurements validate the simulations only for the latter region, highlighting the need for further improvement to accurately characterize the simulated hot plasma condition. These results provide new insights into fast electron heating dynamics in solid-density materials, advancing our understanding of dense plasma heating in high-energy density science and fast ignition research.

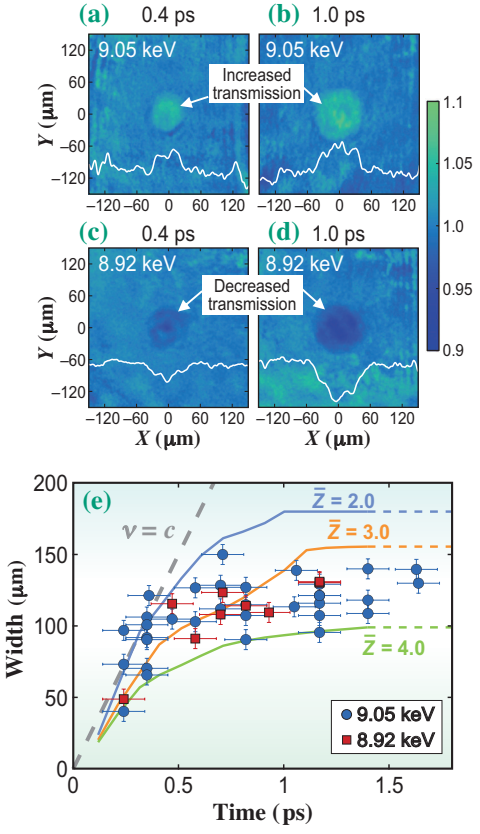

Fig. 2. Measured X-ray transmission ratio images for 9.05 keV at **(a)** 0.4 ps and **(b)** 1.0 ps delay times, and for 8.92 keV at **(c)** 0.4 ps and **(d)** 1.0 ps. **(e)** Comparison of the measured heated width with simulated ionization states between 2 and 4.

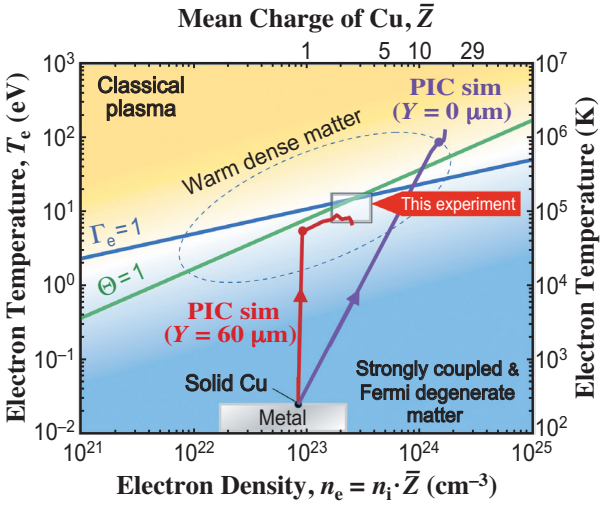

Fig. 3. An electron temperature-density contour. The inferred conditions are illustrated with a white box. Solid lines with arrows represent simulation results near the laser interaction point in purple and a periphery region in red.

Hiroshi Sawada

Department of Physics, University of Nevada Reno, USA

Email: hsawada@unr.edu

References

[1] D. Strickland and G. Mourou: Opt. Commun. **56** (1985) 219.
[2] M. Tabak *et al.*: Phys. Plasmas **1** (1994) 1626.
[3] H. Sawada *et al.*: Rev. Sci. Instrum. **94** (2023) 033511.
[4] *H. Sawada, T. Yabuuchi, N. Higashi, T. Iwasaki, K. Kawasaki, Y. Maeda, T. Izumi, Y. Nakagawa, K. Shigemori, Y. Sakawa, C. Curry, M. Frost, N. Iwata, T. Ogitsu, K. Sueda, T. Togashi, S. Hu, S. Glenzer, A. Kemp, Y. Ping, Y. Sentoku: Nat. Commun.* ***15*** *(2024) 7528.*
[5] F. Dorchies *et al.*: Phys. Rev. B **92** (2015) 085117.

Study on decay of actively pumped isomeric state of ^{229}Th nuclei

Time is a common physical parameter used in various aspects of daily life. Precise measurements of the time and frequency can be achieved using atomic transitions. High-precision frequency standards are important because they have been used in many fields such as satellite navigation, telecommunications, metrology, and fundamental science. By monitoring the transition frequencies of precise clocks, researchers can explore physics beyond the Standard Model (BSM) of particle physics, including potential temporal variations in fundamental constants. Improvements in the precision of frequency standards enable the detection of subtle deviations from established physical models, thereby providing a powerful tool for exploring BSM.

A ^{229}Th nuclear clock is a promising candidate for a new generation of high-precision frequency standards. The ^{229}Th nucleus has the uniquely low first excited state (^{229m}Th) at approximately 8.36 eV. This energy corresponds to vacuum ultraviolet (VUV) light at 148 nm, a region where narrow-linewidth lasers and established atomic-physics techniques are available. In nuclear clocks, even if the frequency precision is comparable to that of atomic clocks, the sensitivity to temporal variation of the fine structure constant is expected to be a few orders of magnitude higher. Furthermore, nuclear clocks can be operated if ^{229}Th is doped into VUV-transparent solid-state hosts, unlike atomic clocks, because the transition frequency is significantly less sensitive to external fields than the atomic transitions.

In recent years, studies on ^{229}Th have progressed rapidly. In 2023, deexcitation light from ^{229m}Th was first successfully observed at the ISOLDE facility at CERN [1]. Our group also successfully observed deexcitation light from ^{229m}Th during beamtime in May and July of the same year [2], as described below.

Our work was conducted at SPring-8 **BL19LXU**. We used 29.19 keV X-rays to actively pump ^{229}Th nuclei to the second excited state, where the branching fraction of this state to ^{229m}Th exceeded 50% [3]. The irradiated target was ^{229}Th-doped calcium fluoride crystals developed by researchers at TU Wien. Recently, a high ^{229}Th concentration of more than 10^{15}/mm^3 with a high transmittance in the VUV region was produced. To mitigate reduced crystal transmittance and the quenching of ^{229m}Th induced by X-ray beam irradiation, three silicon monochromators (Si(111), Si(660), and Si(880)) were installed upstream of the beamline for X-ray energy monochromatization.

The experimental apparatus for detecting the radiative decay signals from ^{229m}Th is described in Ref. [4]. The experimental setup was placed in a vacuum chamber to detect VUV photons. Background events primarily consisted of scintillation photons generated inside the crystals by the decay of ^{229}Th or daughter nuclei (radioluminescence) and those induced by X-ray beam irradiation (XEOL). The total rates of radioluminescence and XEOL were significantly higher than those of radiative decay of ^{229m}Th. To suppress these background events, we employed four dichroic mirrors and a solar-blind photomultiplier tube (PMT). An additional PMT was installed to detect radioluminescence photons and distinguish them from the signal events. Production of ^{229m}Th can be controlled by changing the X-ray beam wavelength

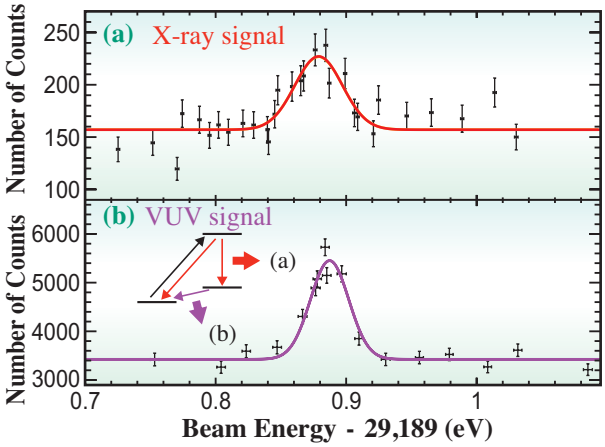

Fig. 1. Measured resonance spectra with changing X-ray beam energy. **(a)** Characteristic X-ray signals from the second excited state. **(b)** VUV photons from ^{229m}Th.

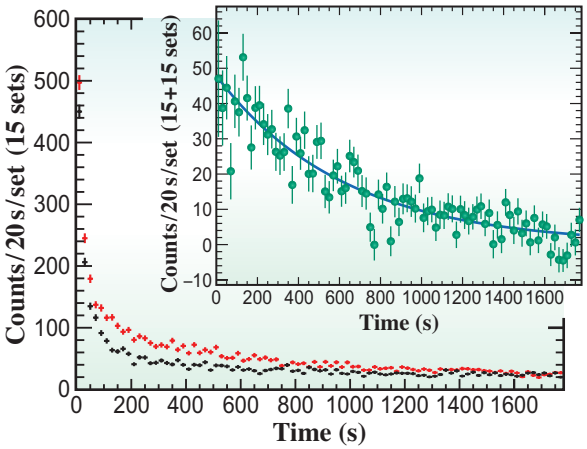

Fig. 2. Time spectra at the on-resonance condition (red) and off-resonance condition (black) averaged over 15 sets. Inset: the difference between these conditions.

near the resonant energy corresponding to the second excited state of the ^{229}Th nuclei. The remaining luminescence events after background reduction were subtracted by comparing the data collected during the on- and off-resonance X-ray beam irradiations.

Figure 1 shows the measured resonance spectra of the nuclear resonance scattering signal (for details, see [3]) and VUV signal at the same beamtime. A peak was observed at almost the same X-ray beam energy, thereby confirming the successful observation of radiative decay photons from ^{229m}Th.

The wavelength of the VUV signal was determined using by six VUV bandpass filters. A motorized wheel was placed in front of the PMT, and filters were inserted during this measurement. The transmittance spectra of each filter were measured in the laboratory. During this measurement, each band-pass filter was alternately inserted. By combining all the filter data, the VUV signal wavelength is determined to be 148.18 ± 0.38(stat.) ± 0.19(syst.) nm.

Figure 2 shows the temporal profile of the VUV events after stopping the X-ray beam irradiation under the on- and off-resonance conditions. By taking the difference in the spectra (Fig. 2, inset), we determined the lifetime of ^{229m}Th by fitting this to an exponential function, τ = 646 ± 23 (stat.) ± 29 (syst.) s.

We also investigated the influence of varying the irradiation time on signal yield. The lifetime during beam irradiation (approximately 60 s) was significantly shorter than that measured after beam irradiation (τ). This phenomenon is referred to as quenching of ^{229m}Th. Subsequently, we measured the X-ray beam flux dependence of lifetime during beam irradiation. The X-ray beam flux was monitored using ionization chambers, and was changed by installing aluminum plates into the beamline or by uninstalling a Si(880) monochromator. The estimated lifetimes under different flux conditions are shown in Fig. 3. Lifetime during irradiation decreases as the beam flux increases.

In summary, we determined the lifetime of ^{229m}Th and the wavelength of deexcitation photons. Furthermore, quenching was observed in the isomeric state. Based on a study by S. Kraemer *et al.* [1] and this study, the wavelength of a laser required to excite ^{229}Th nuclei to the first excited state was determined with a precision of better than 0.5 nm. Finally, in 2024, the first laser excitation was achieved [5], which marked an important milestone in the realization of nuclear clocks.

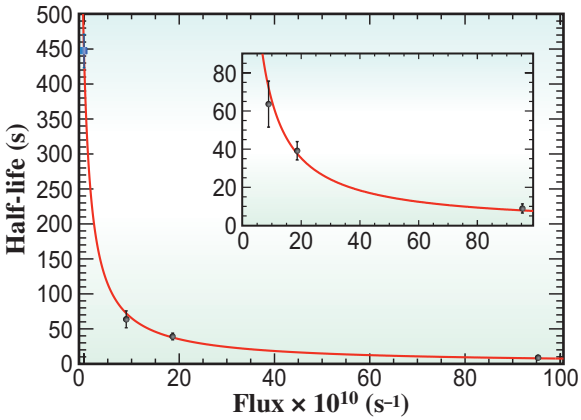

Fig. 3. X-ray beam flux dependence of lifetime during X-ray beam irradiation. The blue point represents lifetime measured after beam irradiation (τ). The red curve represents the result of fitting by a function of $1/\tau' = 1/\tau + (\text{const.}) \times \text{flux}$, where τ' indicates lifetime during irradiation. Inset: enlarged view.

Takahiro Hiraki*, Koichi Okai and Akihiro Yoshimi

Research Institute for Interdisciplinary Science, Okayama University

*Email: thiraki@okayama-u.ac.jp

References

[1] S. Kraemer *et al.*: Nature **617** (2023) 706.
[2] *T. Hiraki, K. Okai, M. Bartokos, K. Beeks, H. Fujimoto, Y. Fukunaga, H. Haba, Y. Kasamatsu, S. Kitao, A. Leitner, T. Masuda, M. Guan, N. Nagasawa, R. Ogake, M. Pimon, M. Pressler, N. Sasao, F. Schaden, T. Schumm, M. Seto, Y. Shigekawa, K. Shimizu, T. Sikorsky, K. Tamasaku, S. Takatori, T. Watanabe, A. Yamaguchi, Y. Yoda, A. Yoshimi and K. Yoshimura: Nat. Commun.* ***15*** *(2024) 5536.*
[3] T. Masuda *et al.*: Nature **573** (2019) 238.
[4] T. Hiraki *et al.*: Interactions **245** (2024) 15.
[5] J. Tiedau *et al.*: Phys. Rev. Lett. **132** (2024) 182501.

Development of a quasi-elastic gamma-ray scattering technique to reveal nanosecond atomic dynamics

Atomic and molecular structures and dynamics are the fundamental origins of various macroscopic properties, such as viscoelasticity. Inelastic and quasi-elastic scattering techniques enable the study of microscopic dynamics in wavenumber vector $\boldsymbol{q}$ space. Inelastic X-ray scattering (IXS) and neutron-based techniques have been widely used to measure the dynamic structure factor $S(\boldsymbol{q},E)$ as a function of energy E, which reflects the two-body space-time density correlation in a system.

Directive Mössbauer gamma rays generated by synchrotron radiation (SR) can be used in quasi-elastic gamma-ray scattering (QEGS) experiments. The energy resolution of Mössbauer gamma rays Γ_0 from ^{57}Fe nuclei is on the order of neV, allowing the measurement of microscopic dynamics on time scales of approximately $\hbar/\Gamma_0$ ~100 ns. Time-domain interferometry (TDI) [1] is a technique used to measure QEGS. Using TDI, the intermediate scattering function (ISF; $F(\boldsymbol{q},t)$), $\boldsymbol{q}$ and time t representations of the two-body space-time correlation function were observed [1]. The time and length scales of the dynamics covered by inelastic and quasi-elastic scattering techniques, including TDI-QEGS, are shown in Fig. 1. However, TDI cannot access timescales in the nanosecond range due to the time resolution limit of the avalanche photodiode detector of ~1 ns. In contrast, the nanosecond time scale is important for many applications, particularly in soft matter studies. Although energy-domain measurement techniques of QEGS have been demonstrated to access nanosecond dynamics [2], their widespread use has been limited due to low measurement efficiency.

Recently, we developed a novel energy-domain quasi-elastic *multiline gamma-ray* scattering technique [3] at SPring-8 **BL35XU**. Figure 2 shows the schematic of the experimental setup. Gamma rays emitted from a $^{57}Fe_2O_3$ nuclear Bragg monochromator (NBM) were introduced into the sample. The multiline energy profile of the gamma rays contained several peaks with a line width of 10 neV. The energy spectrum of the scattered gamma-rays was measured by Mössbauer spectroscopy using a $^{57}Fe_2O_3$ analyzer, which also had a multiline absorption profile, as shown in Fig. 2. These multiline energy profiles of gamma rays emitted by the NBM and absorbed by the analyzer significantly enhanced the incident gamma-ray flux and spectroscopy efficiency. A high-speed two-dimensional X-ray detector, CITIUS, with 840 kpixels, capable of performing quasi-elastic scattering measurements in a two-dimensional $\boldsymbol{q}$ space [4], was introduced. In the following, we present the new system, multiline spectroscopy (MLS) of QEGS, which effectively spans the time scales of dynamics from 100 ps to several tens of nanoseconds, as shown in Fig. 1.

Figure 3(a) shows the obtained energy spectra (absorption profile of the transition-type spectrum) of the forward-scattering gamma-rays (green line). The energy profile remained unaffected by sample dynamics and was used as the resolution function to analyze the quasi-elastic scattering data. The resolution function exhibited multiple energy widths on the order of 10 neV (Γ_1) and 1 μeV (Γ_2), which are sensitive to dynamics in the time scales of $\hbar/\Gamma_1$ ~ several tens of nanoseconds and $\hbar/\Gamma_2$ ~ sub nanoseconds, respectively. The quasi-elastic scattering spectrum obtained for polybutadiene at 235 K at q = 14 nm^{-1}, reflecting interchain correlations, is shown as red dots. The data were well fitted using standard quasi-elastic scattering analysis procedures. Here, we assume a stretched exponential form for the relaxation form of the ISF. Figure 3(b) shows the ISF obtained from the quasi-elastic scattering spectrum via Fourier transformation-based analysis. The ISF follows a stretched exponential function, whose parameters were determined by fitting to the energy spectrum, indicating that the ISF, which has direct information on microscopic dynamics, can be accurately visualized.

Figure 3(c) displays the temperature T dependence of relaxation times obtained by MLS-QEGS (blue circles), as well as those obtained by TDI-QEGS (red squares). All data followed the Vogel-Fulcher-Tammann law (solid curve) with previously reported parameters, indicating the accuracy of the obtained

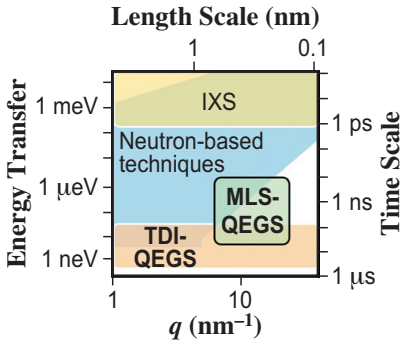

Fig. 1. Time and length scales of dynamics covered by various inelastic/quasi-elastic scattering techniques. The MLS-QEGS technique uniquely covers a specific time and length scale.

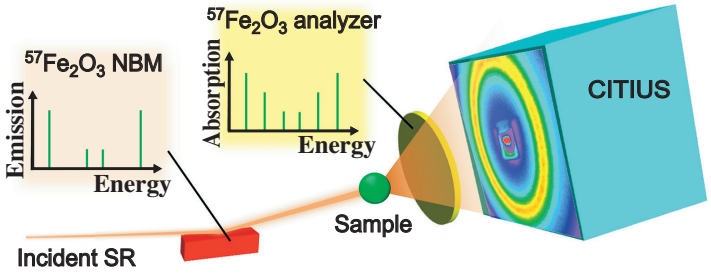

Fig. 2. Schematic of the experimental setup of MLS-QEGS measurement system using the $^{57}Fe_2O_3$ multiline monochromator/analyzer and CITIUS 840k. The energy spectra of the emitted gamma rays from NBM and the absorption profile of analyzer are also shown.

relaxation time over a wide time scale from 100 ps to several tens of nanoseconds. Further analysis revealed that multiple energy resolutions contributed to the broadband nature of the MLS system. Notably, the measurement efficiency was more than 100 times higher than that of previous systems due to the high flux of multiline gamma rays, the high efficiency of multiline spectroscopy, and the efficient two-dimensional q space observation of the quasi-elastic scattering by introducing CITIUS. Recently, we further improved efficiency by developing a high-efficiency multiline energy analyzer system [5].

In conclusion, we successfully developed a novel SR-based energy-domain quasi-elastic scattering technique using multiline Mössbauer gamma-rays. The developed system effectively covers a relatively wide timescale, ranging from 100 ps to several tens of nanoseconds, a part of which has not been fully covered by any other technique. The MLS-QEGS system accelerates the microscopic understanding of various materials such as liquids, glasses, and soft matter systems.

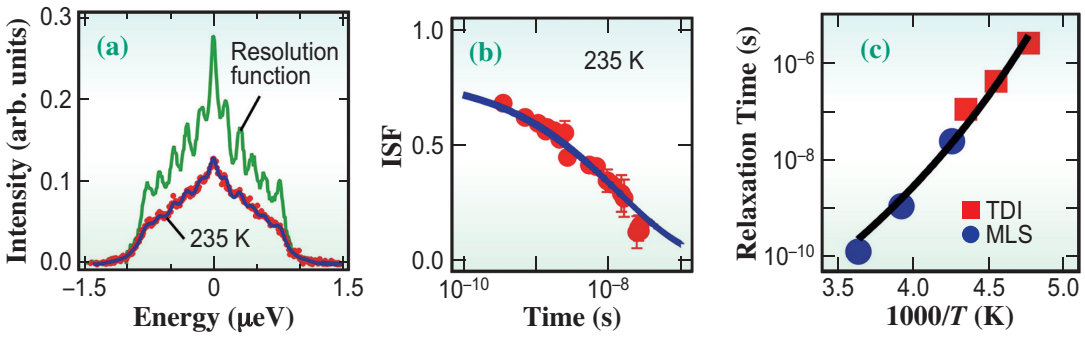

Fig. 3. **(a)** Energy spectra of the resolution function and quasi-elastic scattering spectrum obtained for polybutadiene at q = 14 nm^{-1} at 235 K. **(b)** Intermediate scattering function obtained from the quasi-elastic scattering spectrum via Fourier-transformation-based analysis. **(c)** Temperature dependence of relaxation time obtained by MLS-QEGS (blue circles) and TDI-QEGS (red squares). The solid line represents the fitting curve using the Vogel-Fulcher-Tammann law.

Makina Saito

Department of Physics, Tohoku University

Email: makina.saito.d6@tohoku.ac.jp

References

[1] A. Q. R. Baron *et al.*: Phys. Rev. Lett. **79** (1997) 2823.
[2] T. Mitsui *et al.*: J. Phys. Soc. Jpn. **91** (2022) 064001.
[3] *M. Saito, M. Kobayashi, H. Nishino, T. Nishiyama Hiraki, Y. Honjo, K. Kobayashi, Y. Joti, K. Ozaki, Y. Imai, M. Yamaga, T. Abe, N. Nagasawa, Y. Yoda, R. Mashita, T. Hatsui, Y. Wakabayashi: Phys. Rev. Lett.* ***132*** *(2024) 256901.*
[4] H. Nishino *et al.*: Nucl. Instrum. Meth. Phys. Res. A. **1057** (2023) 168710.
[5] R. Moroboshi *et al.*: Interactions **245** (2024) 349.

3D surface analysis using a synchrotron Mössbauer source

Understanding the chemical states of iron compounds and their three-dimensional (3D) distributions near the surface is crucial for advancing steel science. One of the most effective tools for chemical analysis of iron is ^{57}Fe Mössbauer spectroscopy, which extracts hyperfine parameters from spectra to provide valuable insights into the electronic environment surrounding the nucleus. The isomer shift (*IS*), which reflects the spectral center shift, is proportional to the *s*-electron density at the ^{57}Fe nucleus site. *IS* is particularly useful for determining the valence state of iron and for identifying oxide species in solids. The quadrupole shift (*QS*), caused by the interaction between the nuclear electric quadrupole moment and the electric field gradient, leads to doublet spectra in nonmagnetic materials. *QS* is valuable for examining the site symmetry and ligand configurations. Additionally, the hyperfine field (H_{int}) generated by the spin-polarized *s*-electrons at the ^{57}Fe nucleus site provides important information about the local magnetism.

Mössbauer spectroscopy is commonly performed in a transmission geometry. However, for opaque steel samples, conversion electron Mössbauer spectroscopy (CEMS) is conducted in a backscattering geometry. In CEMS, γ-rays are directed onto the sample, which is placed in a gas flow proportional counter, and the resulting conversion electrons are detected. A CEMS typically provides a surface sensitivity of approximately 100 nm, which corresponds to the escape depth of conversion electrons. This sensitivity can be enhanced by analyzing the electron energy using a method known as depth-selective CEMS (DCEMS). The DCEMS exploits the fact that electrons emitted near the surface lose less energy during their escape. It is a powerful tool for analyzing steel surfaces, with applications in surface modification, corrosion, and welding. In principle, DCEMS enables 3D analysis by scanning the sample surface with a focused probe beam, making it sensitive to both depth and lateral position. However, the non-directional nature of γ-rays emitted from traditional radioactive isotopic sources poses challenges for achieving a small probe γ-ray with sufficient photon flux for practical 3D surface analysis. Recently, we developed an “iron microscope” using a highly brilliant synchrotron Mössbauer source (SMS), beam-focusing mirrors, a precision stage, a gas-flow proportional counter, and multiple multichannel scalers (MCS). This system was successfully applied to the 3D chemical state analysis near the surface of a laser-ablated ^{57}Fe foil [1].

A ^{57}Fe [90%] foil, irradiated with a pulsed YAG laser with a focal spot size of φ19 μm in air, was prepared as the sample (Fig. 1). The SMS study was conducted at the SPring-8 **BL11XU**. The SMS γ-rays were focused to approximately 10 μm (vertical) × 30 μm (horizontal) using a K–B focusing mirror (Fig. 2). The vertical and horizontal beam sizes were evaluated as the FWHM values of the differential peaks of the knife-edge scan profile. The sample, placed inside the CEMS detector, was positioned at the focal point, with the γ-rays incident normal to the foil plane. The γ-ray irradiation positions in this study are indicated by yellow ellipses in Fig. 1. The DCEMS and transmission spectra were measured using a four-pulse-height analyzer-equipped MCSs. The DCEMS spectra were recorded in three distinct energy regions: low energy (2–6.5 keV), medium energy (6.5–11 keV), and high energy (>11 keV) corresponding to approximate depths of 90, 60, and 30 nm, respectively.

Figure 3 shows typical DCEMS and transmission spectra observed near the center of the laser-irradiated region. In the DCEMS spectra, a magnetic sextet (green line) and a nonmagnetic doublet (red line) were observed. The magnetic phase displayed typical hyperfine parameters of α-Fe: H_{int} = 33 T, *QS* = 0 mm/s, and *IS* = 0 mm/s. By contrast, the nonmagnetic phase exhibited *QS* = 0.68 mm/s and *IS* = 0.85 mm/s, corresponding to iron monoxide (wüstite) with a non-stoichiometric crystal structure formed during the rapid cooling of the iron foil surface in air after pulsed laser heating. The abundances of the nonmagnetic phase, estimated from the data analysis, were 28.0%, 17.6%, and 10.3% at different depths. A

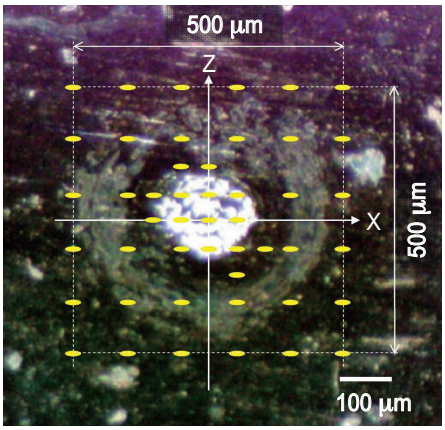

Fig. 1. Photograph of the laser-ablated ^{57}Fe foil for the DCEMS measurements.

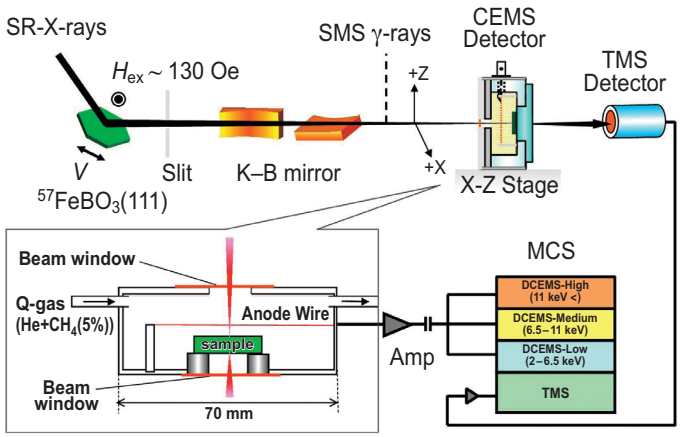

Fig. 2. Measurement system for 3D Mössbauer surface analysis. Multiple MCS were used for DCEMS and transmission measurements.

nonmagnetic oxide formed at a depth of approximately 100 nm from the surface. As expected, the transmission spectrum, which reflects bulk information, was dominated by the ferromagnetic α-Fe component, whereas the nonmagnetic component was negligible.

To visualize the oxidation state transition from the surface to the interior of the iron foil, the spatial distribution of the nonmagnetic phase was mapped using a 3D quadratic spline interpolation method (Fig. 3). The resulting visualization reveals three prominent columnar compositional variations, indicating heterogeneous oxide formation within the iron foil. This heterogeneous distribution is attributed to the complex detachment and scattering of molten fragments from the iron surface during the pulsed laser ablation process.

The developed system successfully visualized the heterogeneous formation of iron oxide near the surface of a laser-ablated iron foil. Currently, 3D surface analysis is primarily applied in fundamental research on ^{57}Fe-rich steel. However, it has considerable potential for practical applications, such as the pinpoint surface analysis of corrosion and welded areas in steel with a natural abundance of ^{57}Fe (2.2%) [2]. In future studies, this method is expected to make substantial contributions to advanced steel science research, including investigations of corrosion, welding, and surface modifications induced by processes such as laser ablation and peening.

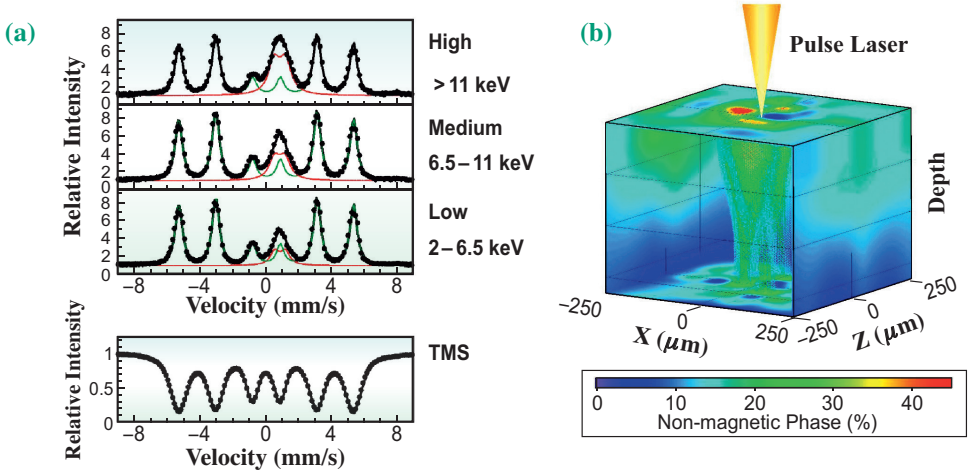

Fig. 3. **(a)** DCEMS and transmission spectra measured near the laser irradiation center [X = –100 μm, Z = 100 μm] on the laser-ablated ^{57}Fe iron foil. **(b)** 3D distribution of the nonmagnetic phase was calculated using spline interpolation.

Takaya Mitsui* and Kosuke Fujiwara

National Institutes for Quantum Science and Technology (QST)

*Email: mitsui.takaya@qst.go.jp

References

[1] *K. Fujiwara, T. Mitsui, N. Hasegawa, M. Nishikino, Y. Kobayashi, K. Mibu, K. Shinoda, R. Masuda and M. Seto: Appl. Phys. Express* ***17*** *(2024) 082002.*
[2] T. Mitsui *et al.*: Interactions **245** (2024) 347.

Work function lowering of photo- and thermionic-cathode by two-dimensional nanomaterial coating beyond anti-corrosion protection

Two-dimensional (2D) nanomaterials such as graphene possesses attractive material properties as anti-corrosion coatings [1]. Graphene is a carbon sheet that is only one atom thick, yet is mechanically and chemically stable, and possesses packed atomic structure in the in-plane direction with geometric pore size of 0.64 Å, which is smaller than the smallest gas molecule, namely the hydrogen molecule. Utilizing the unique capability of supersonic molecular beam (SSBM) at SPring-8 **BL23SU**, we have studied the effectiveness of graphene anti-corrosion coating on copper substrates by X-ray photoelectron spectroscopy (XPS). SSBM is based on free jet expansion and generates gas molecules such as oxygen with imparted kinetic energy of up to ~2 eV with narrow energy distributions with widths that are as low as 1/10 of those generated thermally. We have successfully demonstrated high anti-corrosion performance of monolayer graphene and published the results in 2020 [2]. Our article was featured as one of the cover graphics for the Journal of Physical Chemistry Letters and was publicized in news releases.

Our next goal was to demonstrate an additional functionality for the 2D material coating. Discussion with our theoretical collaborators indicated that we may be able to lower the work function of material surfaces by 2D material coating. This could benefit electron sources of particle accelerators including SPring-8 because lowering the work function would increase the number of emitted electrons and hence the brightness of the beams. Furthermore, long lifetime is another critical performance factor for the electron sources for which anti-corrosion coating by 2D materials would be beneficial [3]. We chose lanthanum hexaboride (LaB_6) for our study because using LaB_6, both photo- and thermionic-cathode performance can be tested with a single material. LaB_6 is an established thermionic cathode that is widely used in electron sources for electron microscopes and particle accelerators. Moreover, its low work function of ~2.4 eV makes it attractive as a photo-cathode. We used photoemission electron microscopy (PEEM) and thermionic emission electron microscopy (TEEM) to investigate the work function of LaB_6. Both techniques probe work function of material surfaces with spatial resolution of few tens nm and show low work-function regions through high intensity of emitted electrons. PEEM and TEEM utilize photoemission and thermionic emission, respectively. We used Xe lamp as the light source for PEEM. The sample preparation was as follows. We purchased a LaB_6 (100) single crystal with a diameter of 3 mm and coated half of the crystal with chemical vapor deposited (CVD) monolayer graphene via the established wet-transfer method. We then coated CVD monolayer hexagonal boron nitride (hBN) via the wet-transfer method such that a quarter of the circle is covered by just hBN and half of graphene was covered with hBN (Fig. 1). When we performed

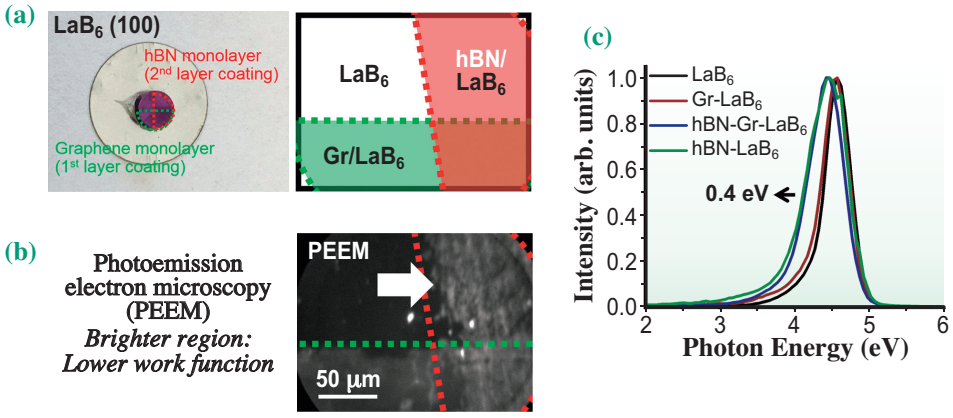

Fig. 1. **(a)** Top view photograph of graphene- and hBN-coated LaB_6 (100). LaB_6 is fixed onto a nickel (Ni) substrate using silver paint. Regions of 2D material coatings are indicated by green (graphene) and red (hBN) dotted lines. Top view schematic illustration of the LaB_6 geometry. White, green, and red regions are bare LaB_6, graphene-coated LaB_6, and hBN-coated LaB_6, respectively. **(b)** PEEM image taken at room temperature after heating up to 905°C. **(c)** PES spectra of LaB_6 coated with graphene and hBN taken at room temperature after heating up to 905°C. The black arrow indicates a shift of low-energy cutoff of the spectra for hBN-coated LaB_6 compared to bare and graphene-coated LaB_6.

PEEM at the center of LaB_6 where four different types of bare, graphene-coated, hBN-coated and graphene/hBN-coated surfaces intersect, the hBN-only coated region exhibited the highest intensity of photoelectrons (i.e., brightest color) [4]. Graphene-only-coated region had similar intensity as the bare region, and graphene/hBN-coated region exhibited intensity between those of hBN-only and graphene-only. TEEM results were consistent with the PEEM results. hBN-only and graphene/hBN-coated regions exhibited measurable intensity at 905°C while no intensity was detected from other regions. A broad and uniform brighter image of the hBN-coated region in PEEM was quantitatively supported by a 0.4 eV decrease of the work function in the photoelectron spectra compared to the bare region. The work function of 4.2 eV that we observed for non-coated LaB_6 (100) (extrapolated low energy cut-off of the spectra) was higher than the value of ~2.4 eV reported for its clean surfaces. This is due to native oxidized layer on top that persists even after annealing at 905°C, which we confirmed by XPS. The work function is also consistent with a reported value of ~4.0 eV for the LaB_6 (100) surface with an oxide layer. A larger decrease of the work function for hBN-coated LaB_6 (100) compared to graphene-coated LaB_6 (100) was qualitatively supported by our density functional theory (DFT) calculations. For both the hBN- and graphene-coating, the degree of work function modification on the oxidized surfaces was smaller compared to the clean surfaces, indicating that the oxide layer reduces the change transfer between LaB_6 and 2D materials.

Band diagrams illustrating the work function changes of oxidized LaB_6 (100) by graphene- and hBN-coating are shown in Fig. 2. For the semi-metallic graphene, the charge transfer from LaB_6 to the conduction bands of the coating materials induces inward-pointing dipoles, which increase the work function (Figs. 2(a) and 2(b)). Figure 2(c) shows the electron transfer at the interface of oxidized LaB_6 (100) surface and graphene. Blue and yellow regions indicate electron depletion and accumulation, respectively. In contrast to graphene, for monolayer hBN, because of its large bandgap, an outward dipole is formed at the interface originating from exchange repulsion, which decreases the work function (Figs. 2(d) and 2(e)). Comparison of Figs. 2(f) and 2(c) clearly shows that the surface dipole has different directions for the graphene- and hBN-coated surfaces.

In summary, we demonstrated that functionalities beyond anti-corrosion protection such as work function lowering of material surface can be provided by 2D material coating.

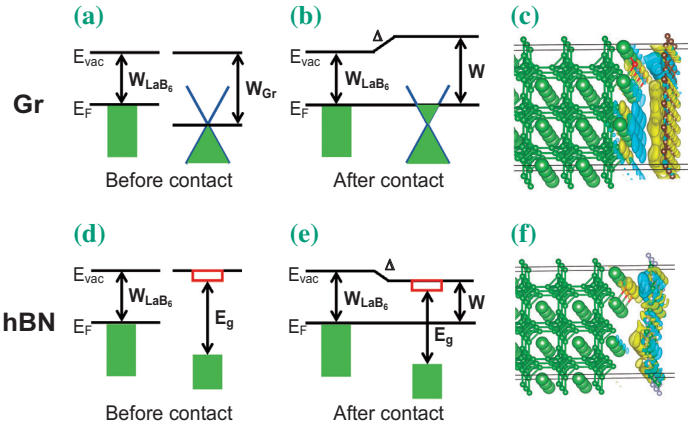

Fig. 2. Schematic band alignment of graphene with the oxidized LaB_6 (100) surface: **(a)** before contact and **(b)** after contact. **(c)** Charge redistribution. Schematic band alignment of hBN with the oxidized LaB_6 (100) surface: **(d)** before contact and **(e)** after contact. **(f)** Charge redistribution. Large green, small green, brown, red, and white spheres in insets of (c) and (f) represent lanthanum (La), boron (B), carbon (C), oxygen (O), and hydrogen (H) atoms, respectively.

Hisato Yamaguchi

Los Alamos National Laboratory, USA

Email: hyamaguchi@lanl.gov

References

[1] H. Yamaguchi *et al.*: Adv. Energy Mater. **4** (2014) 1300986.
[2] S. Ogawa *et al.*: J. Phys. Chem. Lett. **11** (2020) 9159.
[3] L. Guo *et al.*: Sci. Rep. **13** (2023) 2412.
[4] *H. Yamaguchi, R. Yusa, G. Wang, M. T. Pettes, F. Liu, Y. Tsuda, A. Yoshigoe, T. Abukawa, N. A. Moody, S. Ogawa: Appl. Phys. Lett.* ***122*** *(2023) 141901.*

Formation of a zirconium oxide crystal nucleus in the initial nucleation stage in aluminosilicate glass investigated by X-ray multiscale analysis

Glass ceramics are composed of precipitated crystals and a glass matrix, which exhibit unique characteristics that are not observed in conventional glasses, such as high mechanical strength and excellent thermal shock resistance owing to the presence of encrusted crystals [1]. Glass ceramics are synthesized by annealing the quenched pristine glass above the glass transition temperature to obtain homogeneous crystallization. Zirconium oxide is a commonly used nucleation agent in various glass ceramics, in which it aids in controlling the crystallization process [1]. The environments around Zr^{4+} ions in pristine glass and sufficiently crystallized glass ceramics have been studied using various experimental techniques, but the Zr^{4+} environment in the early stages of nucleation in glass is still not well understood.

In this study, we examined ZrO_2-doped lithium aluminosilicate glass and its glass-ceramic, which is an important commercial material. The lithium aluminosilicate glass-ceramics in the initial nucleation stage were prepared by thermal treatment of pristine glass with small amounts of ZrO_2 (2.9 mol%) at 770°C for various durations. To investigate the structural changes associated with a small amount of Zr (1 mol%) in the glass and glass-ceramics at both the short- and intermediate-range scales, we conducted anomalous X-ray scattering (AXS) [2] measurements at SPring-8 **BL13XU** [3]. Furthermore, the nanoscale structures of the pristine glass and glass-ceramics were analyzed using a combination of small-angle X-ray scattering (SAXS) and in-house X-ray diffraction (XRD) measurements. Thus, we performed a state-of-the-art multiscale structural analysis that demonstrated the behavior of a small number of Zr cations from the atomic scale to the nanoscale during the initial nucleation stage in commercially available glass-ceramic materials [4].

The in-house XRD patterns of the samples annealed for longer than 4 h showed subtle diffraction peaks assigned to cubic (c-) or tetragonal (t-) ZrO_2, indicating that glass-ceramics suitable for investigating the structural changes during the initial nucleation stage were obtained. The SAXS profiles of the samples prepared with various annealing durations are shown in Figs. 1(a,b). A relatively low scattering intensity was observed for the 0-h-annealed sample, indicating that the pristine glass had an internal inhomogeneous structure. The SAXS peak height gradually increased with the annealing duration, indicating that the electron density contrast between the scatterers increased. These results indicate that the structural change in the ZrO_2-doped lithium aluminosilicate glass-ceramics during the initial nucleation stage originated from the separation of the Zr-rich and Zr-poor regions. Notably, these structural changes occurred without any change in the spatial nanoscale geometry because the distance between scatterers, which was calculated using $d = 2\pi/Q$ (Q is the peak position in the SAXS profile), did not show any notable change with increasing annealing duration.

The differential structure factors $\Delta_{Zr}S(Q)$ for 0-, 2-, and 4-h-annealed samples obtained from the AXS measurements are shown in Fig. 2(a). $\Delta_{Zr}S(Q)$ markedly changed in the high-Q region ($Q > 0.5$ Å^{-1}), indicating that the Zr-related structure at short- and intermediate-range scales changed upon thermal treatment. Differential total correlation functions, $\Delta_{Zr}T(r)$, for the 0-, 2-, and 4-h-annealed samples obtained from the Fourier transforms of $\Delta_{Zr}S(Q)$ are shown in Fig. 2(b). In addition to the Zr–O correlation peak located at 2.1 Å, the second Zr–Zr correlation peak with a shoulder on the low-r side was observed at 3.6 Å for all $\Delta_{Zr}T(r)$. The shoulder peak on the low-r side of the second peak was likely composed of the tail of the asymmetric Zr–O peak and other Zr-related correlation peaks observed at approximately 2.8–2.9 Å for all $\Delta_{Zr}T(r)$. Because only six partials (Zr–Zr, Zr–Si, Zr–Al, Zr–Na, Zr–P, and Zr–O) contributed to $\Delta_{Zr}S(Q)$ and the weighting factors for

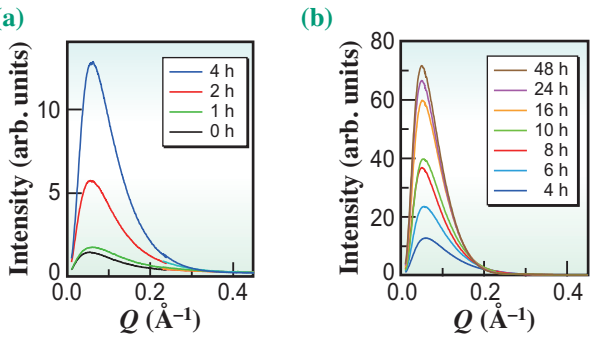

Fig. 1. **(a)** SAXS profiles of the Zr-doped lithium aluminosilicate glass and glass-ceramic samples annealed for less than 4 h. **(b)** SAXS profiles of the Zr-doped lithium aluminosilicate glass-ceramic samples annealed for more than 4 h. [4]

Zr–Si and Zr–Al correlations were relatively large except for the Zr–O correlation in $\Delta_{Zr}S(Q)$, the shoulder peak was assigned to the Zr–Si and/or Zr–Al correlation. The Zr–(Si/Al) distance of 2.8–2.9 Å was considerably short for a Si or Al at the center of a $(Si/Al)O_4$ tetrahedron sharing an oxygen at the corner with a ZrO_x polyhedron. Therefore, the short Zr–(Si/Al) distance indicated the formation of edge-sharing polyhedral connections between ZrO_x and $(Si/Al)O_4$.

To obtain clear insights into the initial nucleation stage from the atomic level to the nanoscale, a schematic representation of the structural change from pristine glass to glass-ceramic (4-h-annealed sample) was constructed, as shown in Figs. 3(a–d). As shown by the SAXS results, the pristine glass exhibited an inherent separation of the Zr-rich and Zr-poor regions (Fig. 3(a)). Thermal treatment of the pristine glass for 4 h caused the aggregation of ZrO_x and an increase in contrast in the electron density between the Zr-rich and Zr-poor regions (Fig. 3(b)). Figures 3(c,d) show schematic representations of the intermediate-range structure in the Zr-rich region for the pristine glass and the 4-h-annealed sample, respectively. SiO_4, AlO_4, and only a few PO_4 tetrahedra formed a tetrahedral network, whereas Zr^{4+}, Li^+, and Na^+ cations were distributed around the network in the pristine glass (Fig. 3(c)). Several ZrO_x polyhedra formed an edge-sharing with the $(Si/Al)O_4$ polyhedra in the structure of the pristine glass. After annealing for 4 h, the Zr^{4+} ions congregated and formed an ordered arrangement, whereby additional edge-sharing connections were formed between the ZrO_x polyhedra and the surrounding $(Si/Al)O_4$ tetrahedra, as shown in Fig. 3(d). The Zr-related specific configuration could be the initial crystal nucleus of the Zr-doped lithium aluminosilicate glass-ceramic. The ZrO_2 nanocrystal surrounded by the $(Si/Al)O_4$ tetrahedral network shown in Fig. 3(d) corresponds to the core–shell structure, which acted as a nucleation barrier that inhibited the increase in the size of ZrO_2 crystals [5]. Although Zr–(Si/Al) correlations beyond the nearest-neighbor distance have rarely been observed using conventional approaches, we succeeded in their observation using Zr-specific pair distribution function analysis with AXS data. These findings may provide new insights into the intermediate-range structures of nucleation agents in glasses and promote a better understanding of the nucleation mechanism in the initial stages of glass-ceramic materials.

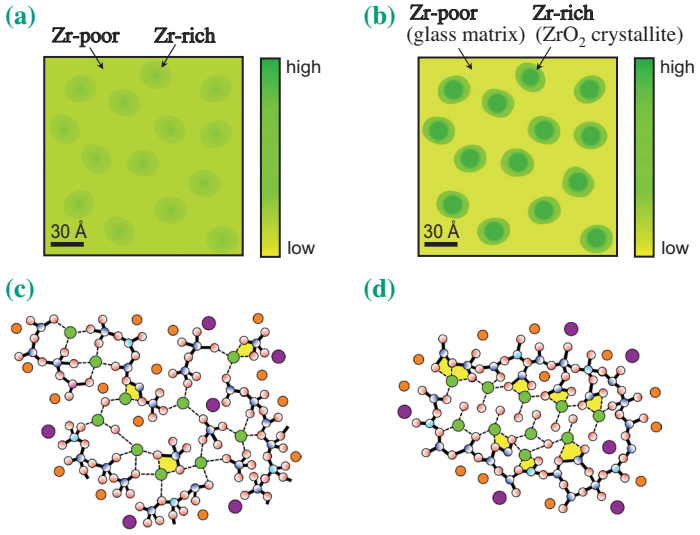

Fig. 3. Schematic representation of the initial nucleation stage in the Zr-doped lithium aluminosilicate glass-ceramic. **(a)** Nanoscale structures of the pristine glass and **(b)** 4-h-annealed sample. **(c)** Representations of the intermediate-range structure in the Zr-rich region of the pristine glass and **(d)** the 4-h-annealed sample. Green: zirconium, blue: silicon, cyan: aluminum, magenta: phosphorus, orange: lithium, purple: sodium, and red: oxygen. The yellow polyhedra indicates edge-sharing polyhedral connections. [4]

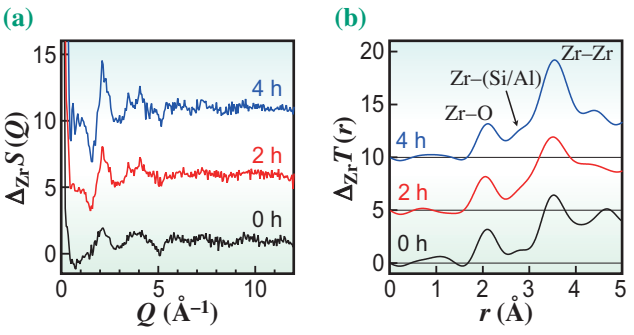

Fig. 2. **(a)** Differential structure factors $\Delta_{Zr}S(Q)$ and **(b)** differential total correlation functions $\Delta_{Zr}T(r)$ of the Zr-doped lithium aluminosilicate samples annealed for 0 h (black), 2 h (red), and 4 h (blue). [4]

Yohei Onodera[a,*], Yasuyuki Takimoto[b] and Shinji Kohara[a]

[a] Center for Basic Research on Materials, National Institute for Materials Science
[b] Innovative Technology Laboratories, AGC Inc.

*Email: ONODERA.Yohei@nims.go.jp

References

[1] E. D. Zanotto: Am. Ceram. Soc. Bull. **89** (2010) 19.
[2] Y. Waseda: Lect. Notes Phys. 204, Springer (1984).
[3] S. Kohara *et al.*: J. Phys. Conf. Ser. **502** (2014) 012014.
[4] *Y. Onodera, Y. Takimoto, H. Hijiya, Q. Li, H. Tajiri, T. Ina and S. Kohara: NPG Asia Mater. **16** (2024) 22.*
[5] T. Höche *et al.*: Cryst. Growth Des. **12** (2012) 1556.

Pressure-induced reversal of Peierls-like distortions elicits the amorphous-amorphous transition in GeTe and GeSe

While polymorphism is a well-known concept in crystalline states, disordered systems such as liquid and amorphous materials may also show two or more states with distinct structure and physical properties within the same chemical composition [1]. The transition between the two liquid states is called liquid-liquid transition (LLT), and the solid-state counterpart is instead called a polyamorphic transition or amorphous-amorphous transition (AAT). A wide range of materials shows the phenomena of LLT and AAT. They were first identified in water and subsequently found in the other systems such as silicon, silica, germanium, tellurium, metallic glasses, and even some molecular liquids [2].

Phase-change materials (PCMs) are one of the best candidates for applications in future non-volatile memory and neuromorphic computing devices. Since the structural and kinetic properties of the amorphous and liquid states are of crucial importance for optimizing the switching speed and data retention abilities, their atomic-scale structure has attracted attention both in fundamental and applicational contexts. Recent studies identified a LLT in some PCMs, using femtosecond diffractions based on X-ray free electron laser (XFEL) in combination with *ab initio* simulations [3]. They revealed that the LLT is characterized by a distortion of the local structural environment, called Peierls-like distortion (PLD), which appears in the supercooled liquid state during quenching, eventually being stabilized in the amorphous state. Figure 1(a) schematically shows the PLD. While liquid PCMs typically show undistorted octahedral-like coordination (OLC), the PLD modifies it by introducing alternating long and short bonds. The LLT is associated with the opening of a pseudo-bandgap around the Fermi level, indicating that the LLT is also associated with a metal-to-semiconductor transition. However, it was unclear whether there is any polyamorphism in the amorphous phase of PCMs, and if it exists, how it is related to the LLTs.

To elucidate this important question, we performed *in situ* high-pressure X-ray scattering experiment at SPring-8 **BL05XU** [4] on a prototypical PCM, amorphous GeTe, and on amorphous GeSe. Both compounds are isoelectronic *p*-bonded systems, but GeSe exhibits stronger covalent bonding than GeTe. We loaded the sample pellets on the Paris-Edinburgh (PE) press for high-pressure experiment up to 10 GPa (Fig. 1(b)). The unique capabilities of BL05XU are available to study the pressure-induced AAT, while the short-lived LLT (in the order of nanoseconds) necessitates the use of an XFEL [3]. The combination of the high-energy (100.1239 keV) pink beam and the PE press with the horizontal aperture about 120° allowed us to access a maximum momentum transfer $Q_{max} = 28$ Å^{-1}, providing high-resolution pair distribution functions (Fig. 2(a)). The experimental throughput was kept high throughout the beamtime, which enabled us to successfully collect 17 datasets in 6 shifts with no significant interruption, taking advantage of the high-flux pink beam and the stable operation of SPring-8.

Since the weak alteration of the long-and-short bonds of the PLD has nearly a double period to the OLC, it manifests itself as a small “pre-peak” in the low-Q range. The inset of Fig. 2(a) shows the pre-peak of GeSe. With increasing pressure, the pre-peak becomes smaller. GeTe shows similar behavior. Pressure suppresses the PLD and transforms it into the OLC, suggesting a pressure-induced AAT. This is the reverse behavior to the LLT in the previous study [3], where the PLD emerged during cooling.

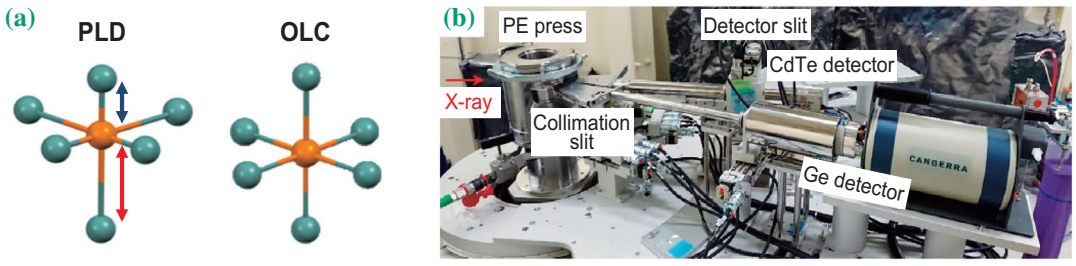

Fig. 1. **(a)** The schematic representation of the Peierls-like distortion and the octahedral-like coordination. **(b)** The setup of high-pressure X-ray scattering experiment at BL05XU [4].

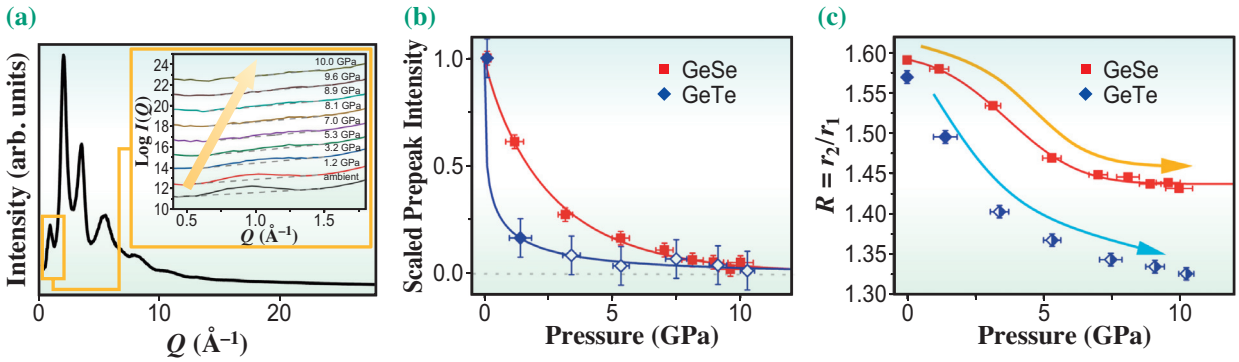

Fig. 2. **(a)** The diffraction profile $I(Q)$ of GeSe. The inset shows the pre-peak. **(b)** The pressure dependence of the pre-peak intensity. **(c)** The pressure dependence of the peak position ratio r_2/r_1 of the pair distribution functions.

Figure 2(b) shows the pressure dependence of the pre-peak intensity. It becomes negligible around 9.0 GPa in GeSe, while it vanishes at lower pressure of 3.4 GPa in GeTe.

Figure 2(c) shows the pressure dependence of the ratio of the 1st and the 2nd peak positions r_2/r_1, obtained from the pair distribution functions. The ratio decreases with increasing pressure in contrast to the rise of r_2/r_1 in the LLT. We estimate the transition pressure P_{aa} of the AAT as P_{aa} = 3.7 ± 0.4 GPa for GeSe, and P_{aa} = 1.8 ± 0.4 GPa for GeTe. The correlation between P_{aa} and the vanishing pressure of the pre-peaks indicates that the suppression of the PLD is the underlying mechanism of the AAT.

To obtain atomic-level insight on the transition mechanism, we performed molecular dynamics simulations of amorphous GeTe using a machine-learned neural-network potential, as well as *ab initio* molecular dynamics simulations of amorphous GeSe. The simulations reproduce the pressure-induced suppression of the PLD, and the suppression occurs at lower pressure in GeTe than in GeSe, in agreement with the experiment. Furthermore, the electronic density of states shows a notable rise around the Fermi level, as opposed to the opening of the pseudo-bandgap reported in the LLT.

Our results demonstrate that the pressure-induced AAT can be understood as suppressing the PLD, which is essentially the reverse mechanism to the temperature-dependent LLT in the supercooled liquid state induced by quenching [5]. Figure 3 shows the directions of the AAT and the LLT on the P–T phase diagram. The two results indicate a transition line with a negative slope. The phase diagram also suggests that we can vary the degree of the PLD by adjusting temperature and pressure, which is potentially useful to tune the properties of PCM-based functional devices.

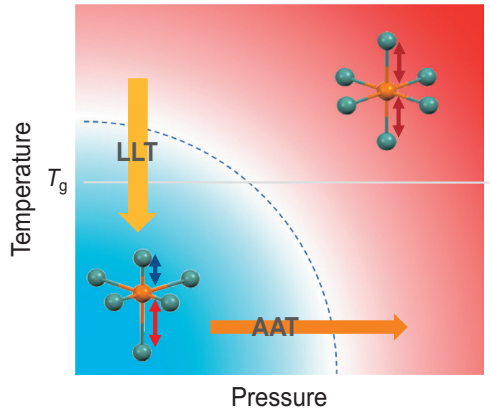

Fig. 3. The schematic of the P–T phase diagram of the PCMs. The directions of the LLT and the AAT indicate the existence of a transition line with a negative slope.

Tomoki Fujita[a,*], Yoshio Kono[b] and Riccardo Mazzarello[c]

[a] Department of Chemistry, Aarhus University, Denmark
[b] Department of Physics and Astronomy, Kwansei Gakuin University
[c] Department of Physics, Sapienza University of Rome, Italy

*Email: tofu@chem.au.dk

References

[1] C. A. Angell: Science **267** (1995) 1924.
[2] H. Tanaka: J. Chem. Phys. **153** (2020) 130901.
[3] P. Zalden *et al.*: Science **364** (2019) 1062.
[4] Y. Kono: SPring-8/SACLA Research Frontier 2022 (2023) 52.
[5] *T. Fujita, Y. Chen, Y. Kono, S. Takahashi, H. Kasai, D. Campi, M. Bernasconi, K. Ohara, H. Yumoto, T. Koyama, H. Yamazaki, Y. Senba, H. Ohashi, I. Inoue, Y. Hayashi, M. Yabashi, E. Nishibori, R. Mazzarello and S. Wei: Nat. Commun.* ***14*** *(2023) 7851.*

Nanophase separation in $K_{1-x}Ca_xC_8$ revealed by X-ray fluorescence holography

Graphite intercalated compounds (GICs) have garnered significant attention due to their novel physical properties, such as superconductivity. In 1965, the first GIC superconductor was discovered in K-doped graphite, KC_8 [1], whose superconducting transition temperature, T_c, was 0.55 K. Among various GICs, the highest value of T_c is 11.5 K, observed in CaC_6 [2]. In addition to single-element intercalations, binary-element intercalations have been explored to achieve higher T_c superconductors. Recently, $K_{1-x}Ca_xC_y$ (T_c = 6.5–11.5 K for $0.33 \leq x \leq 1$) has been synthesized by one of the authors, Kubozono [3]. By X-ray diffraction (XRD), the interlayer distance between graphene layers was estimated to be 5.35 Å, which is the same as that of KC_8. This result implies that intercalated elements with larger radii increase the interlayer distance and determine the *c*-axis length. The structures of KC_8 and CaC_6 are shown in Figs. 1(a,b), respectively. For this reason, the crystal structure of $K_{1-x}Ca_xC_8$ has been assumed to be KC_8-type. Matsui *et al.* characterized a $K_{1-x}Ca_xC_y$ sample using surface-sensitive photoelectron holography to investigate the structure in detail. However, only K holograms could be measured due to the condensation of K atoms on cleaved surfaces [4]. Therefore, we applied bulk-sensitive X-ray fluorescence holography (XFH) to this system to determine the entire structure by measuring both Ca and K holograms [5].

XFH provides three-dimensional (3D) atomic images around specific elements emitting fluorescent X-rays, enabling the determination of local atomic arrangements within a short to intermediate range of up to a few nanometers around these emitting atoms. This technique is particularly effective for identifying the location of impurity sites and local lattice distortions around impurity atoms. Therefore, XFH discovered unexpected local structures around the additive atoms [6].

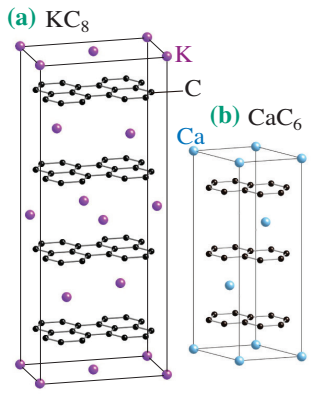

Fig. 1. Crystal structures of **(a)** KC_8 and **(b)** CaC_6.

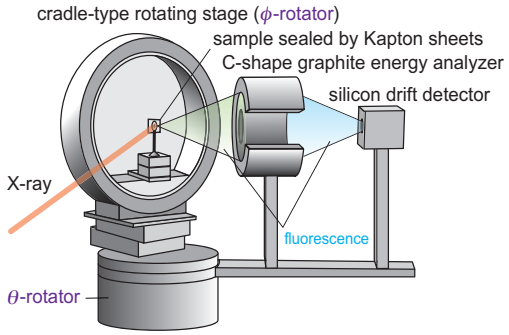

Fig. 2. XFH experimental setup with cradle-type stage.

The $K_{1-x}Ca_xC_8$ samples were prepared using the liquid alloy method. A superconducting quantum interference device (SQUID) measurement found a T_c of ~9.0 K. XRD obtained the lattice parameters and the distance between the graphene layers was 5.35 Å, which is close to the pure KC_8 structure. The X-ray fluorescence spectrum identified the sample composition as $K_{0.7}Ca_{0.3}C_8$. Intriguingly, it shows a high T_c even at such low calcium concentrations.

XFH measurements in inverse mode were conducted at SPring-8 **BL39XU**. The sample size was approximately $2.0 \times 2.0 \times 0.50$ mm^3. To prevent the oxidation of the sample in the atmosphere, the sample was sealed using Kapton sheets in a glove box. The K-*K*α (3.3 keV) and Ca-*K*β (4.0 keV) lines were used for the hologram measurements, as the Ca-*K*α (3.7 keV) line overlapped with the K-*K*β (3.6 keV) lines. Here, we used a C-shaped graphite energy analyzer specifically designed for 3–5 keV X-ray fluorescence [7]. A cradle-type rotating stage was used to collect XFH signals (Fig. 2). Due to the present sample's thinness and composition of light elements, incident X-rays could easily pass through. This stage prevents the incident X-rays passing through the sample from being backscattered by the sample holder. The K-*K*α and Ca-*K*β fluorescent X-rays were collected using an energy-dispersive silicon drift detector via the C-shaped graphite energy analyzer.

Figures 3(a,b) show the K-*K*α and Ca-*K*β holograms of $K_{0.7}Ca_{0.3}C_8$ recorded at 10.0 keV, presented in orthographic projection. Figure 3(c) displays the atomic images around K on the layer parallel to the (001) plane, reconstructed from the K-*K*α hologram. The K atoms occupy the origin of the image. Atomic images

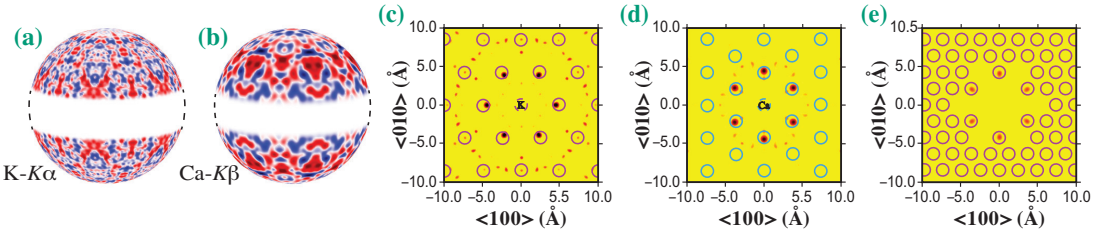

Fig. 3. **(a)** K-*K*α and **(b)** Ca-*K*β holograms of $K_{0.7}Ca_{0.3}C_8$ measured at 10.0 keV. Atomic images parallel to the (001) planes around (a) K and (b) Ca of $K_{0.7}Ca_{0.3}C_8$. **(c)** and **(d)** are reconstructions at the basal plane (z = 0.0 Å). **(e)** is a reconstruction of the plane 1.0 Å above the basal plane.

were shown within the solid red circles, indicating the expected K positions in the KC_8 structure (2×2). However, some weak artifacts were also observed. Figure 3(d) presents atomic images around Ca, reconstructed from the Ca-*K*β hologram, where Ca atoms also occupy the origin of the layer. The expected Ca positions in the CaC_6 structure ($\sqrt{3} \times \sqrt{3} - R30°$) are indicated by solid blue circles. Atomic images were shown within the blue solid circles, indicating that the local structure around Ca retains the CaC_6 structure. These distinct local structures around Ca and K reveal that Ca and K atoms do not form a solid-solution structure, indicating phase separation between the graphene layers.

Among the various reconstructions of the Ca *K*β hologram, meaningful atomic images were identified at z = 1.0 Å (see Fig. 3(e)). While these images could correspond to C, K, or Ca atoms, the possibility of C was excluded due to its low X-ray scattering cross-section. This finding suggests the presence of an additional cation layer 1 Å away from the Ca layer. This layer is composed of K, as Ca and K atoms should be located at different distances from the graphene layer due to their different ionic radii.

Based on these results, we developed the structural model illustrated in Fig. 4. XRD measurements confirmed that the graphene interlayer distance is 5.35 Å, consistent with the KC_8 structure. Therefore, it is believed that the K layer remained in the middle of the C layer. The XFH results indicate that the Ca layer is displaced off-center by 1 Å, suggesting that Ca atoms are closer to one graphene layer. To confirm these considerations, we performed extended X-ray absorption fine structure (EXAFS) measurements for K and Ca in the sample [5]. The results revealed that the distances of Ca-C_{1st} and K-C_{1st} were 2.40 Å and 3.06 Å, respectively, confirming the predictions from XFH. Furthermore, a detailed analysis of the atomic images in Fig. 3(e) revealed an average size of 1 nm for the Ca cluster.

The local structures of Ca and K in $K_{0.7}Ca_{0.3}C_8$ were elucidated using XFH and EXAFS. It was found that Ca and K were phase-separated in the graphite. The CaC_6 and KC_8 phases were separated at the nanometer scale, with Ca clusters displaced off-center by 1 Å. The approach of Ca clusters to graphene layers induces a strong interaction between the Ca 3*d* electrons and phonons in the graphene layer, producing the high superconductivity of $K_{1-x}Ca_xC_y$. The results of this study are essential for exploring high T_c superconducting materials.

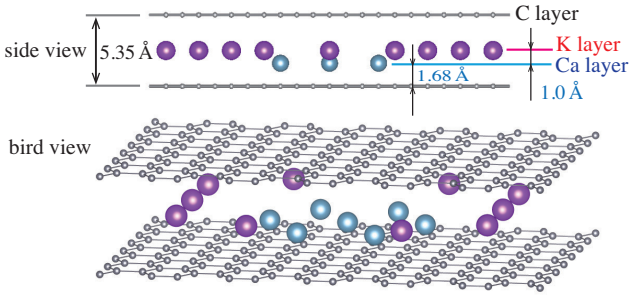

Fig. 4. A 3D structural model obtained from the XFH data.

Naohisa Happo[a,*], Koichi Hayashi[b,c] and Yoshihiro Kubozono[d]

[a] Graduate School of Information Sciences, Hiroshima City University
[b] Research Institute for Interdisciplinary Science, Okayama University
[c] Japan Synchrotron Radiation Research Institute (JASRI)
[d] Department of Physical Science and Technology, Nagoya Institute of Technology

*Email: happo@hiroshima-cu.ac.jp

References

[1] N. B. Hannay *et al.*: Phys. Rev. Lett. **14** (1965) 225.
[2] T. E. Weller *et al.*: Nat. Phys. **1** (2005) 39.
[3] H. T. L. Nguyen *et al.*: Carbon **100** (2016) 641.
[4] F. Matsui *et al.*: Sci. Rep. **6** (2016) 36258.
[5] *N. Happo, A. Kubota, X. Yang, R. Eguchi, H. Goto, M. Ikeda, K. Kimura, Y. Takabayashi, J. R. Stellhorn, S. Hayakawa, K. Hayashi, Y. Kubozono: Chem. Mater. **36** (2024) 4135.*
[6] K. Hayashi *et al.*: J. Phys.: Condens. Matter **24** (2012) 093201.
[7] N. Happo *et al.*: Jpn. J. Appl. Phys. **57** (2018) 058006.

Uniform magnetic structure revealed by X-ray magnetic circular dichroism and spin-torque diode effect in Mn_3Sn/W epitaxial bilayers

To advance beyond the modern electronics, there has been growing interest in spintronics, which leverages both the charge and spin degrees of freedom of electrons. Spintronics primarily focuses on ferromagnets, as they exhibit strong electrical responses to changes in magnetization direction. Recently, antiferromagnets systems have attracted significant attention due to their potential to operate at much faster frequencies than ferromagnets, although their weak electrical response poses substantial challenges for practical application.

Mn_3Sn is an antiferromagnet with an inverse triangular spin structure on the Mn Kagome lattice (Figs. 1(a) and 1(b)). This spin structure breaks macroscopic time-reversal symmetry and can be characterized by octupole polarization. Consequently, Mn_3Sn exhibits strong ferromagnet-like responses, such as the anomalous Hall effect [1] despite its negligible magnetization. Recent advancements in the epitaxial growth of W/Mn_3Sn bilayers have enabled electrical control of its spin structure [2] through spin-torque arising from the spin Hall effect of W. This development makes the material system a compelling building block for spintronics based on antiferromagnets. However, it remained unclear whether the observed spin-torque-induced phenomena are intrinsic to the W/Mn_3Sn interface or are influenced by the inclusion of ferromagnetic second phases.

To address this issue, we performed X-ray magnetic circular dichroism (XMCD) measurements. XMCD is a powerful method for studying ferromagnetic materials; however we recently demonstrated that XMCD can also probe the inverse triangular spin structure via the magnetic dipole term [3]. In this study [4], we utilized both surface-sensitive total electron yield (TEY) mode and bulk-sensitive partial fluorescence yield (PFY) mode to investigate the uniformity of the antiferromagnetic spin structure or octupole polarization in a W/Mn_3Sn/MgO multilayer, from the bottom to top interfaces.

We grew an epitaxial Mn_3Sn thin film using molecular beam epitaxy. The multilayer structure consists of an MgO(110) substrate/W (7 nm)/Mn_3Sn (30 nm)/MgO (3 nm). Figure 1(c) illustrates the experimental setup. The XMCD measurements were conducted at SPring-8 **BL25SU**. The measurement temperature was room temperature. We employed both TEY and PFY modes, which have probing depths of about a few nm and 100 nm, respectively. Thus, the TEY mode probes surface regions, while the PFY mode probes the entire 30-nm-thick Mn_3Sn layer.

Figure 2(a) shows the Mn L_3-edge XMCD spectra recorded using TEY and PFY modes at a magnetic field of 50 mT. Prior to applying 50 mT, a magnetic field of 1.9 T was applied to saturate the octupole polarization. Both spectra exhibit a distinct positive peak at 638.7 eV, characteristic of the inverse triangular spin structure [3]. Notably, the TEY and PFY spectra appear almost identical, indicating uniformity in both the electronic and magnetic structures from the bottom W/Mn_3Sn interface and top Mn_3Sn/MgO interface. Furthermore, the results confirm the absence of unwanted ferromagnetic secondary phases, such as ferromagnetic W-Mn-Sn intermetallic compounds, at the W/Mn_3Sn interface.

Figure 2(b) shows the TEY and PFY XMCD hysteresis loops measured at a photon energy of 638.7 eV, corresponding to the positive XMCD peak, as indicated by vertical line in Fig. 2(a). The coercive fields, approximately 150 mT, are consistent between the TEY and PFY hysteresis loops and align with values reported in a previous study [2]. The PFY XMCD signals exhibit a slight increase as the magnetic field approaches zero from higher values. This suggests that the octupole polarization changes its direction from the magnetic field direction to the surface normal direction, which is parallel to the X-ray incidence direction, due to the perpendicular magnetic anisotropy induced by tensile epitaxial strain [2].

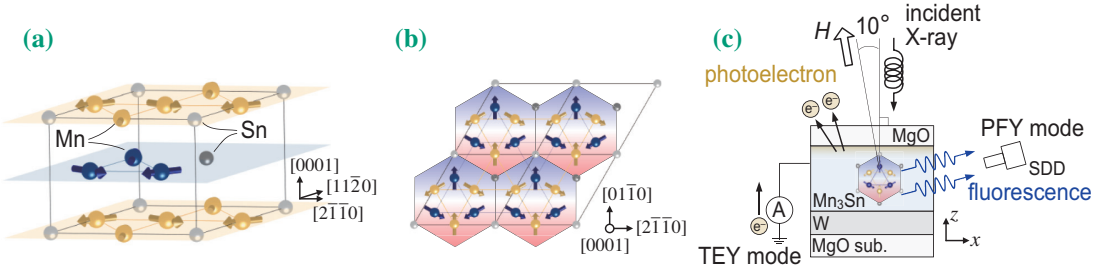

Fig. 1. **(a)** and **(b)** Crystal structure of $D0_{19}$-Mn_3Sn. **(c)** Experimental setup.

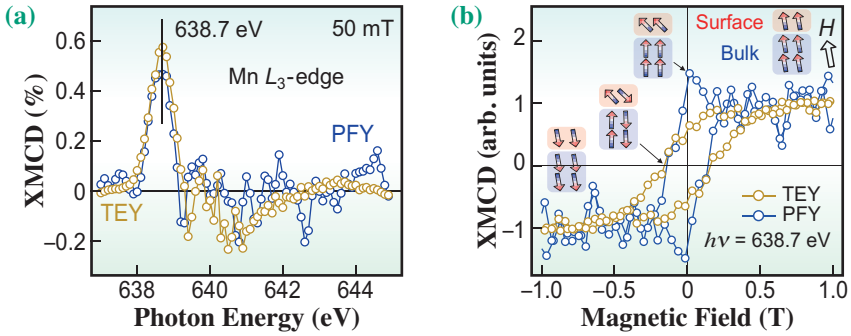

Fig. 2. **(a)** Mn L_3-edge TEY and PFY XMCD spectra. **(b)** TEY and PFY XMCD hysteresis loops. Schematic images along the hysteresis represent the inferred octupole polarization in the surface and bulk regions.

In contrast, the TEY hysteresis curve exhibits the opposite behavior, decreasing as the magnetic field approaches zero from higher values. Therefore, we infer that the perpendicular uniaxial magnetic anisotropy diminishes only near the MgO interface, possibly due to relaxed strain or the influence from the MgO interface, thereby tilting the octupole polarization away from the surface normal. The identical coercive fields observed in both the TEY and PFY hysteresis loops eliminate the possibility of other magnetic inclusions and suggest a finite magnetic coupling between the surface and bulk regions. The magnetization process described above is illustrated in the insets of Fig. 2(b).

The present findings suggest that the recently observed spin-torque-related phenomena [2], which occur at the W/Mn_3Sn interfaces, are intrinsic and arise from the interplay between the spin current and the octupole polarization. Having established this intrinsic nature, we investigated microwave spin-torque-induced phenomena in this W/Mn_3Sn bilayer system [5]. Figure 3(a) depicts the experimental setup, where both DC and microwave current were applied. DC and microwave currents inject DC and microwave spin currents into the Mn_3Sn layer via the spin Hall effect of W. Resultant DC Hall voltages were detected using a lock-in amplifier. Figure 3(b) shows observed DC Hall voltages measured with various DC bias currents and a microwave current of 5 GHz and 13 mW. Distinct peaks were observed when the DC current exceeded 30 mA, which is the threshold current to drive octupole dynamics.

Such conversion of a microwave current to a DC voltage via spin current is known as spin-torque diode effect in ferromagnets, which is considered promising for the development of sensitive microwave detectors. Our observation of the spin-torque diode effect in an antiferromagnet exploits antiferromagnetic exchange interaction and potentially expands the horizon of this effect to much higher frequencies and greater sensitivity [5].

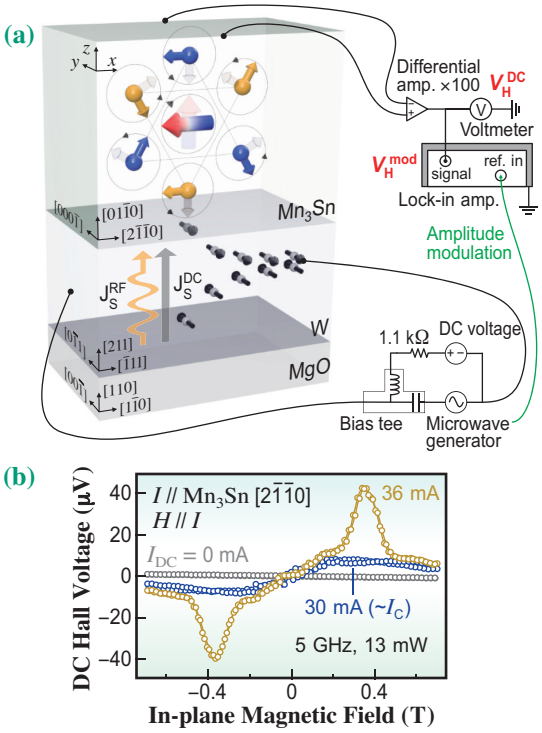

Fig. 3. **(a)** Experimental setup for spin-torque diode effect. **(b)** Observed diode signals.

Shoya Sakamoto*,† and Shinji Miwa

The Institute for Solid State Physics, The University of Tokyo

*Email: shoya.sakamoto.e1@tohoku.ac.jp

† Present address: Institute for Materials Research, Tohoku University

References

[1] S. Nakatsuji *et al.*: Nature **527** (2015) 212.
[2] T. Higo *et al.*: Nature **607** (2022) 474.
[3] S. Sakamoto *et al.*: Phys. Rev. B **104** (2021) 134431.
[4] *S. Sakamoto, T. Higo, Y. Kotani, H. Kosaki, T. Nakamura, S. Nakatsuji and S. Miwa: Phys. Rev. B* ***110*** *(2024) L060412. (Editors' suggestion)*
[5] S. Sakamoto *et al.*: Nat. Nanotechnol. **20** (2025) 216.

Investigation of helicity-dependent optical switching of ferrimagnetic Gd–Fe–Co films

Magnetization control by femtosecond light pulses has been extensively investigated for next-generation magnetic recording technologies. This approach enables the ultrafast manipulation of magnetic ordering on pico- to femtosecond timescales, potentially overcoming the speed limitations of conventional magnetic field-driven magnetization switching [1]. Since the magneto-optical effect is theoretically a non-thermal process, it offers a pathway for designing energy-efficient recording devices. Particularly, selective magnetization switching using right- and left-handed circularly polarized laser pulses, known as helicity-dependent magnetization switching (HDMS), is noteworthy both as a novel physical phenomenon and for its potential device applications (Fig. 1(a)) [2].

The origin of HDMS is explained by the inverse magneto-optical effect, where polarizations of the incident light influence the material's magnetization. Initially discovered in ferrimagnetic thin films composed of 4*f* rare-earth and 3*d* transition metals, HDMS was later observed also in ferromagnetic thin films such as CoPt. However, clear single-shot magnetization switching (monotonic HDMS), as shown in Fig. 1(a), has so far been limited to a few specific ferrimagnetic alloys such as Gd–Fe–Co. In contrast, other magnetic thin films typically exhibit only cumulative HDMS under multi-pulse irradiation, as shown in Fig. 1(b). Achieving monotonic HDMS in a broader range of material systems including rare-earth-free ferromagnetic alloys, remains a significant challenge for resource strategy and the practical development and commercialization of HDMS-based devices.

In ferrimagnetic materials, monotonic HDMS is more easily achieved owing to the difference in magnetization reversal speeds between the 4*f* and 3*d* atomic sites under femtosecond laser pulse excitation, as well as the divergence of magnetization damping near the angular momentum compensation point. These factors are believed to explain why only cumulative HDMS has been observed in ferromagnetic systems so far.

This study systematically examined both monotonic and cumulative HDMS in a series of ferrimagnetic Gd–Fe–Co thin films with varying material parameters. Furthermore, we discovered that the transition between these two types of HDMS modes was strongly influenced not only by the angular momentum compensation characteristics, but also by the thermal conductivity properties of the thin films. This study aims to provide insights into strategies for achieving clear HDMS across a broader range of material systems, including ferromagnets [3].

Figures 2(a–f) show magnetic domain images of Gd–Fe–Co thin films with different compositions after laser pulse irradiation. The magnetic domain images were acquired using a magneto-optical Kerr microscope. The $Gd_{26}Fe_{66}Co_8$ sample has an angular momentum compensation temperature (T_A) above room temperature, whereas $Gd_{22}Fe_{70}Co_8$ has a T_A below room temperature. The former exhibits stronger magnetization damping, promoting faster and clearer magnetization reversal, whereas the latter shows weaker damping, leading to diffuse magnetic relaxation [4]. For the $Gd_{26}Fe_{66}Co_8$ thin film, irradiation at the reversal threshold fluence (20.4 mJ/cm², Fig. 2(a)) induces a clear polarization dependence. Even at a slightly higher fluence (20.9 mJ/cm², Fig. 2(b)), the area of magnetization reversal remains dependent on the laser polarization. Figure 2(c) shows the magnetic domain structure when the laser irradiation spot was slowly moved (50 μm/s, 5 kHz pulse), resulting in multiple irradiations at the same location. This measurement aimed to investigate whether cumulative HDMS occurs when monotonic HDMS is not observed. For this sample, complete HDMS is clearly confirmed. Figures 2(d–f) show the results of similar experiments on $Gd_{22}Fe_{70}Co_8$. The results are nearly identical to those observed in the $Gd_{26}Fe_{66}Co_8$ case.

However, when a similar pulse irradiation was performed in vacuum, clear composition dependence was observed. Figures 2(g–i) illustrate the magnetic

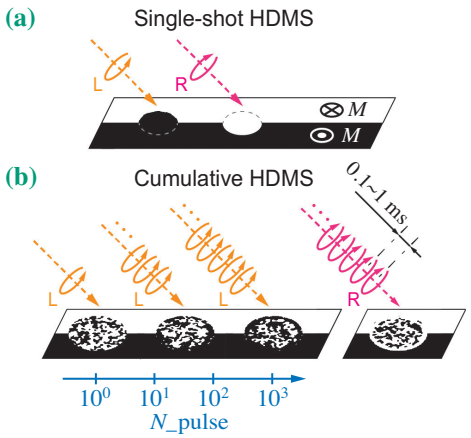

Fig. 1. Schematic illustrations of **(a)** single-shot and **(b)** cumulative HDMS. Magnetization directions of the specimens are indicated by "*M*." "L" and "R" denote the left- and right-handed circular polarizations of the laser pulse, respectively.

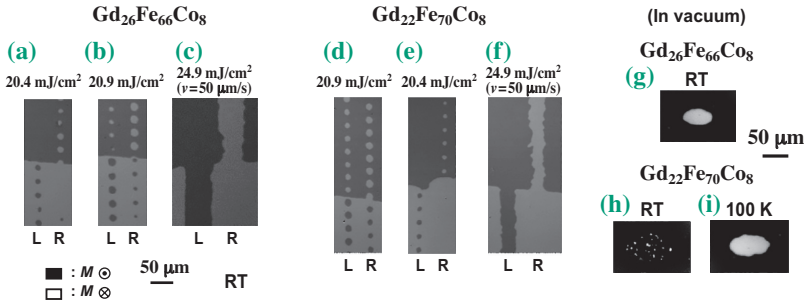

Fig. 2. **(a–f)** Magneto-optical Kerr microscopy images of Gd–Fe–Co films with different alloy compositions and pulse irradiation conditions. **(g–i)** X-ray magnetic circular dichroism (XMCD)-PEEM images of Gd–Fe–Co films with varying alloy compositions and temperatures.

domain images of the Gd–Fe–Co thin films after single laser pulse irradiation in a vacuum chamber, observed by the photoemission electron microscopy (PEEM) apparatus at SPring-8 **BL25SU**. In $Gd_{26}Fe_{66}Co_8$, a clear magnetization reversal was observed (Fig. 2(g)), whereas in $Gd_{22}Fe_{70}Co_8$, where magnetization damping was considered slower (Fig. 2(h)), random magnetic domain structure was observed, suggesting disturbances during the magnetization reversal process. All the experiments were conducted at room temperature. However, when the $Gd_{22}Fe_{70}Co_8$ sample was cooled below its T_A to 100 K (Fig. 2(i)), a clear magnetization reversal similar to that in $Gd_{26}Fe_{66}Co_8$ was observed. These results demonstrate the importance of utilizing the magnetization damping properties owing to angular momentum compensation for monotonic HDMS in ferrimagnetic thin films. Simultaneously, it also suggested that the degree of this property can be controlled by the thermal diffusion properties of the sample (note that the thermal diffusion at the sample surface is slowed down in vacuum).

For further investigation, HDMS properties were examined at room temperature and atmospheric pressure using Gd–Fe–Co thin films where a 5 nm Si_3N_4 thermal blocking layer was inserted between the film and the Ru buffer layer to slow down thermal diffusion. The film compositions were $Gd_{26}Fe_{66}Co_8$, $Gd_{24}Fe_{68}Co_8$, and $Gd_{22}Fe_{70}Co_8$, with their T_A above, near, and below room temperature, respectively. As shown in Fig. 3, the HDMS characteristics clearly changed depending on the differences in T_A of the samples. In particular, for $Gd_{22}Fe_{70}Co_8$, similar to the results in vacuum, a disordered magnetic domain structure was formed, and only a faint cumulative HDMS, as reported for ferromagnetic thin films [5], was observed (Fig. 3(i)).

Other experiments have also suggested that the magnetization reversal characteristics of Gd–Fe–Co thin films are influenced not only by ultrafast magnetization dynamics due to angular momentum compensation on a microscopic timescale but also by macroscopic magnetization dynamics, such as domain wall motion following the reversal process. This indicates that angular momentum compensation, a unique feature of ferrimagnetic materials, is not the sole factor required for achieving monotonic HDMS. Therefore, it suggests the possibility of developing promising HDMS devices even in ferromagnetic thin films, by utilizing other magnetic dynamic properties. Further studies in this direction could lead to the development of practical HDMS devices using more versatile material systems.

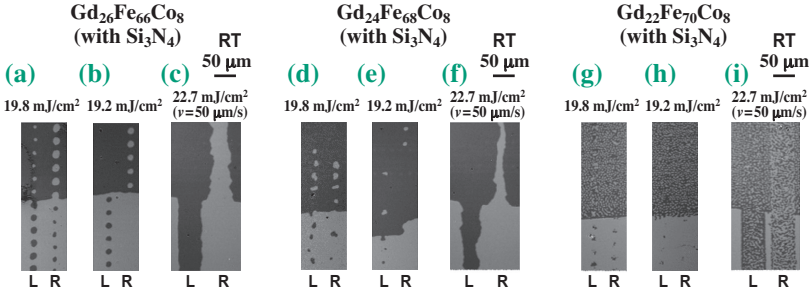

Fig. 3. Similar images to Figs. 2(a–f), but on Gd–Fe–Co films with Si_3N_4 thermal blocking layers underneath.

Takuo Ohkochi

Laboratory of Advanced Science and Technology for Industry, University of Hyogo

Email: o932t023@guh.u-hyogo.ac.jp

References

[1] A. Kirilyuk *et al.*: Rev. Mod. Phys. **82** (2010) 2731.
[2] C. D. Stanciu *et al.*: Phys. Rev. Lett. **99** (2007) 047601.
[3] *T. Ohkochi, R. Takahashi, H. Fujiwara, H. Takahashi, R. Adam, U. Parlak, K. Yamamoto, H. Osawa, M. Kotsugi, A. Tsukamoto, H. Wadati, A. Sekiyama, C. M. Schneider, M. Tsunoda, S. Suga and T. Kinoshita: J. Magn. Magn. Mater.* ***593*** *(2024) 171854.*
[4] K. Vahaplar *et al.*: Phys. Rev. Lett. **103** (2009) 117201.
[5] C.-H. Lambert *et al.*: Science **345** (2014) 1337.

Commensurate locking of magnetic skyrmion and crystal lattice in $Gd_3Ru_4Al_{12}$

Magnetic skyrmions are vortex-like, localized objects formed by the spin degree of freedom in solids. Their winding spin texture, when projected onto a sphere, forms a perfect hedgehog (Fig. 1(a)). Some high-symmetry models of frustrated magnetism show a tendency to form a skyrmions lattice (SkL): for example, Heisenberg models of localized spins with beyond-nearest neighbor interactions [1] or models of itinerant electrons coupled to localized spin moments [2]. In these types of models, the size of a magnetic vortex can be exceedingly small, measuring only a few lattice constants across; due to their localized nature, such nano-skyrmions may be suitable to carry and store information in future electronic circuitry. Previously, all skyrmion textures experimentally observed in nature were found to be incommensurate to the underlying lattice, that is, their period is not a multiple of the lattice constant of the atomic structure that supports them. However, relativistic spin-orbit coupling – which causes magneto-crystalline anisotropy (MCA) and anisotropic exchange energies – can lock the skyrmion to the lattice [3]. In this case, the period of the magnetic texture is a multiple of the lattice constant and the core of the spin vortex has a well-defined relationship with respect to the atomic lattice ('on-site' or 'off-site', for example).

Our target material is hexagonal $Gd_3Ru_4Al_{12}$, which crystallizes in space group $P6_3/mmc$ (#194). In this structure, the magnetic gadolinium ion forms a distorted ('breathing') Kagome network of triangles and hexagons, where certain gaps or holes in the lattice may favor the commensurate locking. The crystals were grown by the floating zone technique and thoroughly characterized by chemical and X-ray methods. Magnetization and electric resistivity are measured to verify the bulk magnetic phase transitions and phase diagram of the material. High quality pieces are polished into a regular shape (rectangular) and aligned by in-house Laue X-ray diffraction. Thus, flat and oriented surfaces are prepared for the synchrotron experiment.

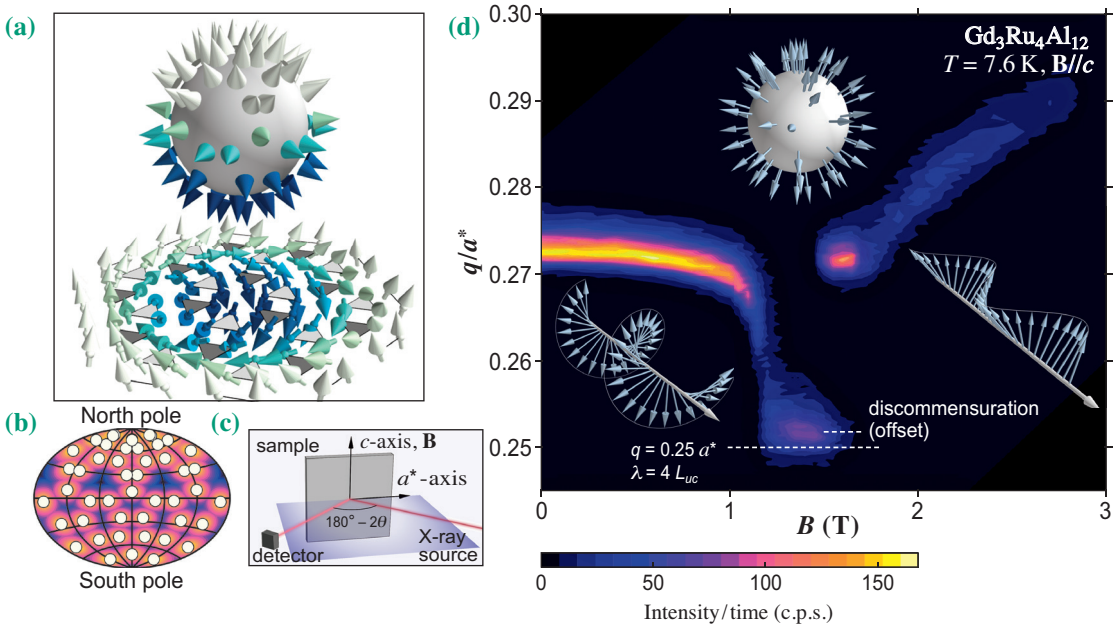

Fig. 1. Commensurate locking of the skyrmion lattice phase in $Gd_3Ru_4Al_{12}$. **(a)** Magnetic moments of a skyrmion winding a sphere (top), and corresponding two-dimensional magnetic moment texture in real space (bottom). Each arrow corresponds to a site of the magnetic sublattice. **(b)** Map projection showing a hemisphere of (a) unfolded, with white dots indicating directions of magnetic moments. The color code indicates the distance of each point on the sphere from the nearest moment on the sphere, in radians. **(c)** Experimental geometry of resonant elastic X-ray scattering (REXS), where the pink line is the trajectory of the X-ray beam. **(d)** Scattering intensity in REXS as a function of magnetic field (B) and momentum transfer q from $\boldsymbol{q} = (q, 0, 0)$; $q = 0.25$ corresponds to four times the projection of the lattice constant parallel to $\boldsymbol{q}$. Incommensurate proper screw (IC-PS), commensurate skyrmion lattice (C-SkL), and IC fan phases are illustrated by insets. In C-SkL, the periodicity of the magnetic texture is locked to the crystal lattice up to a weak discommensuration (offset) of $\Delta q = 0.0018$ r.l.u. B denotes magnetic induction after demagnetization correction.

We studied the magnetic structure of the intermetallic $Gd_3Ru_4Al_{12}$ by resonant elastic X-ray scattering (REXS) at SPring-8 **BL19LXU**. The energy of SPring-8's powerful synchrotron X-ray beam was set to 7.9 keV, around the L_2 absorption edge of Gadolinium. Focusing on the (electric) dipole component of the resonant scattering process to detect magnetic textures, we find that the SkL in this material is nearly perfectly locked to the underlying crystal lattice, barring some defects every 100 unit cells or so [4]. More specifically, we discovered that the magnetic phases that surround the SkL in the *B*–*T* phase diagram – proper screw spiral, transverse cone cycloidal, and fan-type – are incommensurate, while the SkL is commensurate. In particular, Fig. 1(d) shows the wavevector $q = 2\pi/\lambda$ measured in units of the reciprocal lattice constant a^*. It shows a sharp dip when entering the skyrmion lattice phase, to a commensurate value, and remains flat as long as the SkL is stable. This type of study is enabled by the flexible sample environment of BL19LXU, where various magnets, a four-circle diffractometer, etc. can be installed at-will to support specific and promising scattering experiments.

The spin at the core of a skyrmion points parallel to the magnetic field, and the corresponding magnetic moment – which is antiparallel to the spin – is opposed to the magnetic field. Therefore, the core spin of a skyrmion is generally not favored by the Zeeman energy, but still stable when an SkL is incommensurate to the crystal lattice, due to the exchange energy. We studied the commensurate SkL of $Gd_3Ru_4Al_{12}$ by measurements of the single-ion anisotropy via electron spin resonance, combined with model calculations. The analysis shows that the commensurate SkL in $Gd_3Ru_4Al_{12}$ likely arranges itself on the lattice in such a way that the core spin is located on a "hole" of the lattice, due to the magneto-crystalline anisotropy.

Among materials with twisted spin textures, so-called 'noncoplanar magnets', the commensurate SkL in $Gd_3Ru_4Al_{12}$ represents a link between short-period, commensurate antiferromagnets – on the left side in Fig. 2 – and longer-period, incommensurate skyrmion crystal lattices (right side). On the ordinate, this plot illustrates the largest solid angle that remains uncovered by arrows when the magnetic structure is projected onto a sphere, as in Fig. 1(a). Thus, the observation of a commensurate SkL represents an essential link between various classes of magnetic materials, with many opportunities for future discoveries: For example, studies of the magnetic excitation spectrum, which likely consists of coupled phonon and spin wave modes under the influence of Berry's quantum phase [5].

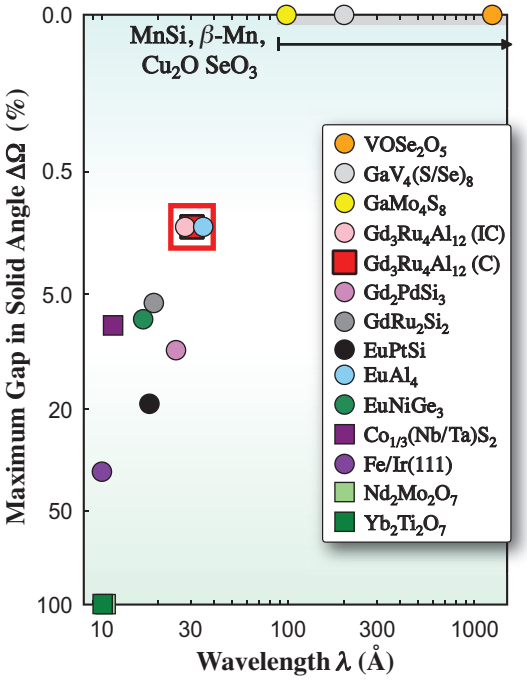

Fig. 2. Relationship of magnetic texture dimensions (λ) and coverage of directions on the sphere for various materials with noncoplanar textures and spin chirality. At the center of the plot, the commensurate C-SkL state in $Gd_3Ru_4Al_{12}$ is highlighted by a red box. On the *y*-axis, a continuous magnetic texture has zero uncovered solid angle, i.e., we assign a value of 0%. Note the stretched scale of the *y*-axis.

Max Hirschberger[a,b,*], Yoshikazu Tanaka[c] and Hiroyuki Ohsumi[c]

[a] Department of Applied Physics and Quantum-Phase Electronics Center, The University of Tokyo
[b] RIKEN Center for Emergent Matter Science (CEMS)/Wako
[c] RIKEN SPring-8 Center

*Email: hirschberger@ap.t.u-tokyo.ac.jp

References

[1] T. Okubo *et al.*: Phys. Rev. Lett. **108** (2012) 017206.
[2] S. Hayami *et al.*: Phys. Rev. B **95** (2017) 224424.
[3] S. Hayami and R. Yambe: Phys. Rev. Res. **3** (2021) 043158.
[4] *M. Hirschberger, B. G. Szigeti, M. Hemmida, M. M. Hirschmann, S. Esser, H. Ohsumi, Y. Tanaka, L. Spitz, S. Gao, K. K. Kolincio, H. Sagayama, H. Nakao, Y. Yamasaki, L. Forró, H.-A. K. von Nidda, I. Kezsmarki, T. Arima and Y. Tokura: npj Quantum Mater.* ***9*** *(2024) 45.*
[5] T. Weber *et al.*: Science **375** (2022) 1025.

Giant modulation of antiferromagnetic spin reversal field by magnetoelectric effect

Antiferromagnetic (AFM) materials exhibit no net magnetization because magnetic moments are fully compensated within the chemical unit cell. This inherent feature provides robustness of the AFM spin states against magnetic field perturbations. This feature is used in spintronic devices to define the reference magnetic layer. In other words, the functionality of AFM materials is static, and the dynamic control of AFM spins remains a considerable challenge. Spintronics is a research field that aims to control the magnetic moment based on the interplay between spin and charge. An object to be controlled in spintronics is not limited to spontaneous magnetization; the AFM materials also become the target of spintronics. The magnetoelectric (ME) effect is referred to as electric polarization ($\boldsymbol{P}$) by a magnetic field ($\boldsymbol{H}$) and magnetization ($\boldsymbol{M}$) induced by an electric field ($\boldsymbol{E}$) through ME susceptibility α: $\Delta\boldsymbol{P} = \alpha\cdot\boldsymbol{H}$ and $\Delta\boldsymbol{M} = {}^{t}\alpha\cdot\boldsymbol{E}$. As illustrated in Fig. 1(a), E increases or decreases the expectation value of $\langle m_z \rangle$ of two spin sublattices, yielding a finite $\Delta\boldsymbol{M}$. α is nonzero in materials in which the spatial- and time-inversion symmetries are simultaneously broken. Because spatial inversion symmetry is inherently broken at the surface/interface, the surface of ME materials exhibits a spin-polarized FM-like state called boundary magnetization (BM) [1]. Cr_2O_3 is a prototypical ME-AFM material, and the presence of the BM on Cr_2O_3 (0001) was predicted based on symmetry arguments. The BM couples to the bulk AFM order parameter, and the magnitude can be a few orders of magnitude larger than the attainable magnetization owing to the bulk ME effect. Because BM localizes at the surface or the interface with another layer, reducing the ME layer thickness is a valid and feasible way to effectively use BM. To experimentally access the BM, we developed a detection technique based on interfacial spin-dependent transport, for example, the anomalous Hall effect (AHE) at heavy-metal/ME-AFM interfaces such as Pt/Cr_2O_3 [2]. In this study, we investigated voltage control of the BM in a Pt/Cr_2O_3/Pt epitaxial trilayer. We demonstrated the giant modulation efficiency of the switching field of the order of a few T·nm/V [3].

Figure 1(b) shows the magnetic-field dependence of the AHE resistance R_{xy} for the Pt (2 nm)/Cr_2O_3 (8 nm)/Pt (20 nm) epitaxial trilayer. The device structure was designed such that the sense current flowed into the top Pt (2 nm) layer. Rectangular hysteresis was observed, indicating isothermal and reversible switching of the BM. The switching field $\mu_0 H_{SW}$, 600 mT at zero V_G, decreased with increasing V_G. Under the V_G application, the rectangular shape was maintained. To ensure voltage-induced modulation of the switching field, we measured the V_G-dependence of R_{xy} while maintaining the magnetic field strength. After introducing the spin state into that with negative R_{xy}, we measured R_{xy} while sweeping V_G at −0.58 T. As shown in Fig. 1(c), R_{xy} switched from negative to positive at V_G = 55 mV, supporting the V_G-induced modulation of the switching field. The detailed V_G dependence of the switching field (Fig. 1(d)) showed the monotonic decrease of the switching field in the V_G range from −0.3 V to +0.3 V. Roughly assuming the linear relationship between $\mu_0 H_{SW}$ and V_G, the modulation efficiency $\Delta\mu_0 H_{SW}/\Delta V_G$ was −180 mT/V, corresponding to −1400 mT·nm/V. Notably, the temperature dependence of the modulation efficiency yielded the highest value of −500 mT/V (−4800 mT·nm/V). These values are 50 times larger than those of the FM counterpart based on the voltage-controlled magnetic anisotropy (VCMA) effect.

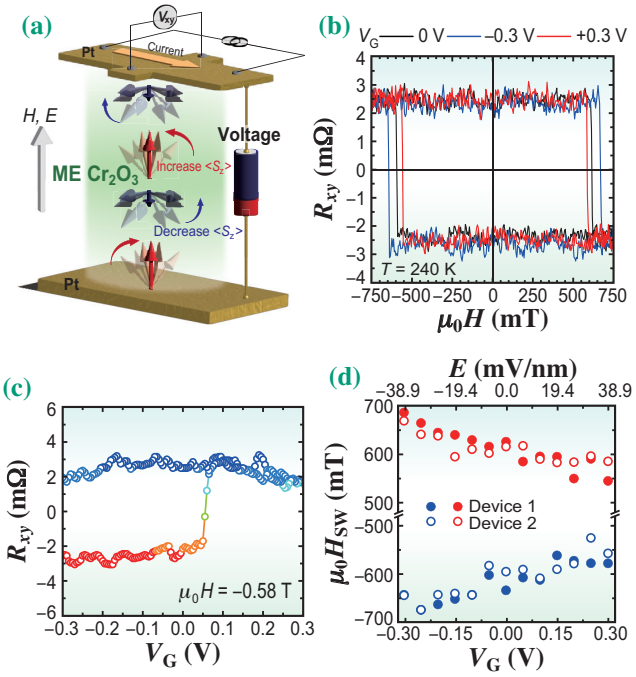

Fig. 1. **(a)** Schematic of a device structure of magnetoelectric (ME) Cr_2O_3 equipped with Pt gate electrodes. Voltage application impacts the bulk spin state via the ME effect. **(b)** R_{xy} as a function of $\mu_0 H$ under the application of V_G. **(c)** R_{xy} as a function of V_G at a constant $\mu_0 H$. **(d)** $\mu_0 H_{SW}$ as a function of V_G and electric field E (referred to as the top axis).

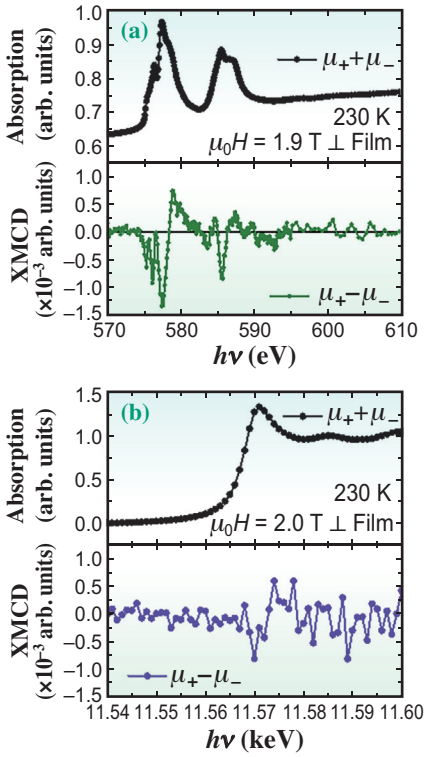

Fig.2. XAS and XMCD spectra at **(a)** Cr $L_{2,3}$ and **(b)** Pt L_3 edges, respectively.

To address the microscopic origin of the huge modulation efficiency, we measured X-ray magnetic circular dichroism (XMCD) using soft and hard X-rays at SPring-8 **BL25SU** and **BL39XU**, respectively. The film used for these measurements was a Pt/Cr_2O_3 bilayer because the thick bottom Pt layer masked the tiny signal from the top Pt. Figure 2 shows the X-ray absorption spectrum (XAS) and XMCD spectrum at the Cr $L_{2,3}$ edges and Pt L_3 edge. A magnetic field was applied perpendicular to the film plane to define the AFM spin orientation. XAS at the Cr $L_{2,3}$ edges indicates that the valence state of Cr was trivalent, Cr^{3+}. The clear XMCD signal indicates the presence of spin-polarized Cr^{3+} which agrees with the BM prediction. Sum-rule analysis with the spin-correction factor gives the effective spin magnetic moment and orbital magnetic moment per Cr^{3+} as m_{s_eff} = 0.016 ± 0.007 μ_B and m_{orb} = 0.006 ± 0.004 μ_B, respectively. The m_{orb}/m_{s_eff} value was 0.3 ± 0.3, which is comparable to that of an FM-based system with a low $\Delta\mu_0 H_{SW}/\Delta V_G$. No appreciable XMCD signal was observed at the Pt L_3 edge, suggesting that the alternative mechanism of the VCMA effect was inappropriate for the observed giant modulation efficiency. First-principles calculations revealed that the VCMA effect at the Pt/Cr_2O_3 interface was comparable to that in the FM cases, which supports the idea that the ME effect is the main mechanism of the giant modulation of the switching field.

Finally, we demonstrate a novel functionality based on the ME effect. According to the ME effect, the Zeeman energy gain of *E*-induced *M* is expressed as αEH. Because of the sign α coupled with the AFM order parameter, the stable AFM spin state is determined by the sign of the *EH* product. Figure 3 plots $\mu_0 H_{SW}$ as a function of *E*. In the figure, the stable spin states are denoted by painted areas. Two hyperbolas corresponding to αEH = constant with positive and negative α values were observed. The four painted areas outside the hyperbola show monostable regions. The presence of these areas indicates that deterministic access to any of the four quadrants is possible, which is the principle of the logic-operation. The yellow area indicates a bistable region inside the hysteresis shown in Fig. 1(b), which works as the memory function of the device. These functionalities shed light on the ME-AFM materials, and our demonstration will advance the field of voltage-based AFM spintronics.

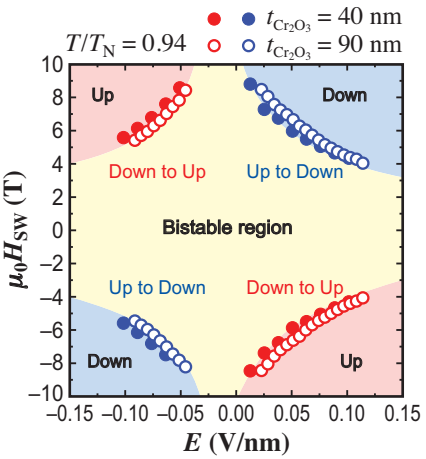

Fig. 3. *E*-dependence of switching field exhibiting the four quadrants access of the AFM spin state. Up and down shown in the red and blue painted areas are denoted by the sign of R_{xy} shown in Fig. 1(b).

Yu Shiratsuchi

Graduate School of Engineering, Osaka University

Email: shiratsuchi@mat.eng.osaka-u.ac.jp

References

[1] K. D. Belashchenko: Phys. Rev. Lett. **105** (2010) 147204.
[2] T. Moriyama *et al.*: Phys. Rev. Appl. **13** (2020) 034052.
[3] *K. Ujimoto, H. Sameshima, K. Toyoki, T. Moriyama, K. Nakamura, Y. Kotani, M. Suzuki, I. Iino, N. Kawamura, R. Nakatani and Y. Shiratsuchi: NPG Asia Mater.* ***16*** *(2024) 20.*

Exploration of chemical bonds in real-space

Chemical bonds not only function as glues that connect atoms but also play a crucial role in providing functionality to molecules. With the recent advancements in organic synthesis techniques, a wide variety of functional molecules have been developed, and unique chemical bonds that cannot be explained by the conventional simplified concept of hybrid orbitals have been proposed. In this context, the experimental elucidation of the electronic states of chemical bonds has become increasingly important.

X-ray structural analysis and nuclear magnetic resonance (NMR) are commonly used to investigate the structure and arrangement of molecules. Spectroscopic methods are used to obtain experimental insights into the electronic states of molecules and molecular orbitals in momentum space. On the other hand, information about the spatial distribution of bonding electrons and molecular orbitals is mostly derived from quantum chemical calculations, such as density functional theory (DFT). As an experimental approach, methods for deriving the real-space distribution of molecular orbitals from spectroscopic data are also being actively developed; however, it is also necessary to discuss the validity of the theoretical model assumed in the analysis.

Here, we focused on the core differential Fourier synthesis (CDFS) method, which enables direct observation of valence electron density (VED) distributions from single-crystal X-ray diffraction data using synchrotron radiation without assuming theoretical models of electronic states [1,2]. In this study, we aimed to elucidate the detailed real-space distribution of bonding electrons by observing high-precision, high-resolution VED distributions using two typical molecular crystals (Glycine and Cytidine) [3]. Single-crystal X-ray diffraction experiments were conducted at SPring-8 **BL02B1** using a four-circle diffractometer (Rigaku Co., Japan). Long scans for VED observation were performed at 45 K for Glycine and 35 K for Cytidine. When applying the CDFS method, [He] type electronic configurations were assumed as the core electrons for C, N, and O atoms.

Figure 1 shows the VED distribution of the Glycine molecule. Unlike the typical recognition of smoothly distributed electron density across the entire molecule, the VED obtained by the CDFS method reveals fine structures. To interpret these fine structures, we consider 2*s* and 2*p* orbitals on a carbon atom. The carbon-carbon bond within the Glycine molecule is conventionally understood as a bonding orbital formed between sp^2 hybrid orbitals on each carbon atom. Here, since the 2*s* orbital contains nodes, the electron density distribution around the carbon atoms exhibits nodal structures. Thus, the experimentally observed nodal structures reflect the nodal plane of 2*s* orbital. By experimentally discerning such structural features in the VED distribution, it becomes possible to know how wavefunctions contribute to bond formation.

In recent years, these types of molecular orbitals are commonly obtained through quantum chemical calculations. However, due to the lack of clear guidelines on the reliability of these calculations, it has been difficult to determine whether various corrections are appropriate. Therefore, we compared the experimentally observed VED distribution with one of the most reliable calculation methods, long-range-corrected density functional theory (LC-DFT) (Fig. 1(d)). As a result, our experimentally observed and theoretically calculated VED are in good agreement, including nodal structures. This fact enables the complementary use of experimental VED and theoretical VED.

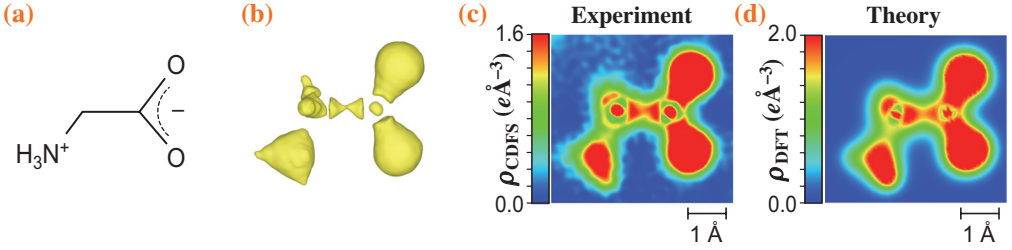

Fig. 1. **(a)** Molecular structure and **(b)** three-dimensional (3D) experimental VED of Glycine. Isosurface level is 1.4 e/Å^3. 2D contour plots of **(c)** experimental and **(d)** theoretical VED.

Subsequently, we explored the possibility of visualizing π-bonds. Figure 2 presents the structure of the Cytidine molecule, consisting of a six-membered ring and a five-membered ring, and its experimental VED. The C2–C1 bond in six-membered ring, where π-bond contributions are expected, exhibits a higher electron density compared to the C3–C4 bond in the five-membered ring. As shown in Fig. 3(a), the cross-section of the C4–C5 bond in the experimental VED exhibits isotropic characteristics, consistent with the features of a σ-bond. However, when examining the cross-section of the C2–C1 bond, an isotropic distribution was also observed (Fig. 3(a)). This can be attributed to the spatial coexistence of σ- and π-bonds, which makes it challenging to observe the anisotropy of the π-bond. To address this, the σ-bond component calculated using DFT was subtracted from the total experimental VED distribution (Fig. 3(b)). As a result, the anisotropic characteristics of π-bonds—nodes in the molecular plane and extensions perpendicular to it—was successfully observed (Fig. 3(a)). Focusing on the energy decomposition

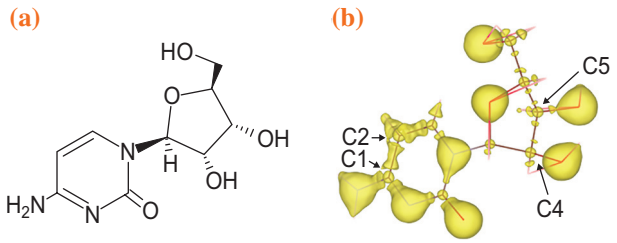

Fig. 2. **(a)** Molecular structure and **(b)** 3D surface plot of experimental VED of Cytidine molecule at an isosurface level of 1.7 e/Å^3.

of molecular orbitals and complementarily utilizing high-precision DFT calculations is crucial for a comprehensive understanding of specific molecular orbitals. Experimentally visualizing the electronic distribution in molecules is expected to contribute to various research fields where π–π interactions influence functions and structural stability, such as organic semiconductors and DNA double helix.

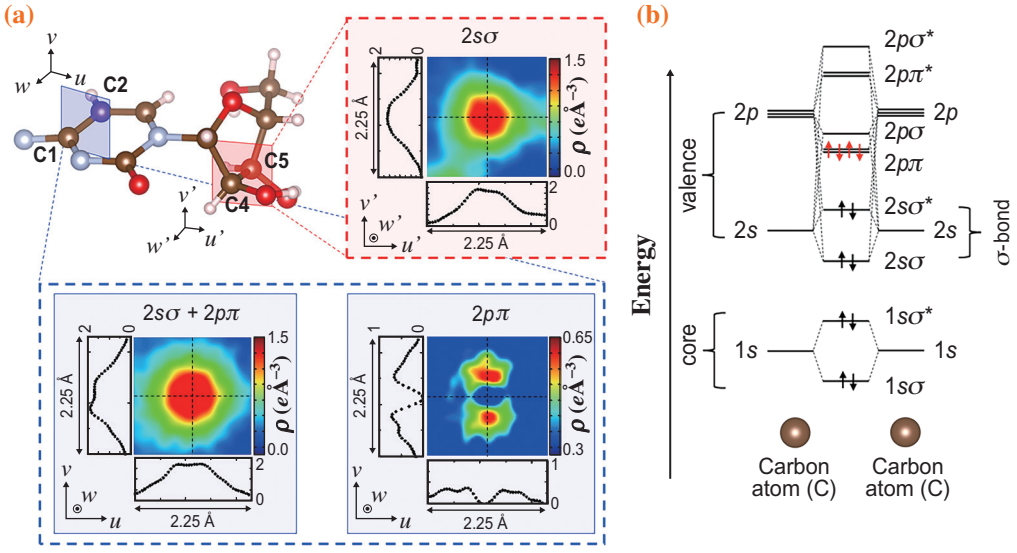

Fig. 3. **(a)** Cross section of the C4–C5 bond in experimental VED $\rho_{CDFS}(r)$ is shown within the red dashed frame, and the cross sections of the C2–C1 bond in $\rho_{CDFS}(r)$ (left side) and $\rho_{CDFS}(r) - \rho_{DFT,2\sigma}(r)$ (right side) are shown in the blue dashed frame. Here, $\rho_{DFT,2\sigma}(r)$ is the theoretically calculated VED corresponding to the 2σ bond between C4–C5. **(b)** Energy level representation for a C=C double bond.

Takeshi Hara*,† and Hiroshi Sawa‡

Department of Applied Physics, Nagoya University

*Email: takeshi.hara.d2@tohoku.ac.jp

Present address: † Department of Physics, Tohoku University
‡ Nagoya Industrial Science Research Institute

References

[1] S. Kitou *et al.*: Phys. Rev. Lett. **119** (2017) 065701.
[2] S. Kitou *et al.*: Phys. Rev. Res. **2** (2020) 033503.
[3] *T. Hara, M. Hasebe, T. Tsuneda, T. Naito, Y. Nakamura, N. Katayama, T. Taketsugu, and H. Sawa: J. Am. Chem. Soc.* ***146*** *(2024) 23825.*

Investigation of the electronic state of poly-tetrafluoroethylene under bending stress using near-ambient pressure hard X-ray photoelectron spectroscopy

Polymer materials exhibit excellent chemical and physical properties, including formability, chemical stability, and electrical insulation, which are determined by differences in their molecular structure and crystallinity. Among these materials, polytetrafluoroethylene (PTFE, Fig. 1(a)) stands out owing to its remarkable chemical stability, heat resistance, and abrasion resistance. Consequently, it finds widespread applications in diverse fields such as medical engineering (including artificial joints), electrical engineering, and biology. Although PTFE is often subjected to external forces and stresses from multiple directions during use, the effects of these stresses on its surface interactions with the external environment have not been thoroughly investigated. Thus, it is essential to examine the surface states of PTFE under stress, including its electronic and chemical conditions.

X-ray photoelectron spectroscopy (XPS) is a powerful tool for elucidating surface states. However, investigating the electronic states of PTFE under multiple stresses has been challenging owing to its insulating nature, which causes charge-up and hinders accurate measurements.

In this study, the surface state of PTFE under multiple stresses, particularly changes in its electronic state and chemical composition induced by bending stress (multidirectional stress), was examined using near-ambient pressure hard X-ray photoelectron spectroscopy (NAP-HAXPES). The issue of charge-up during HAXPES measurements was resolved by introducing nitrogen gas and employing an efficient differential pumping system. This approach enabled the first successful HAXPES measurements of PTFE under applied stress. Notably, previously unreported changes in the chemical composition of PTFE were observed as tensile strain increased because of bending stress [1].

HAXPES measurements were performed using SPring-8 **BL24XU** (Fig. 1(b)) [2]. The X-ray energy was set at 8 keV, with an incidence angle θ of 4°. Initial measurements in a vacuum failed to produce usable spectra due to charge-up effects from the insulating properties of PTFE. To address this issue, environmental change compensation was implemented by introducing inert nitrogen gas. In conventional setups, the distance d from the cone tip to the sample surface is 0.3 mm. However, at this distance, inert gas introduction does not effectively prevent

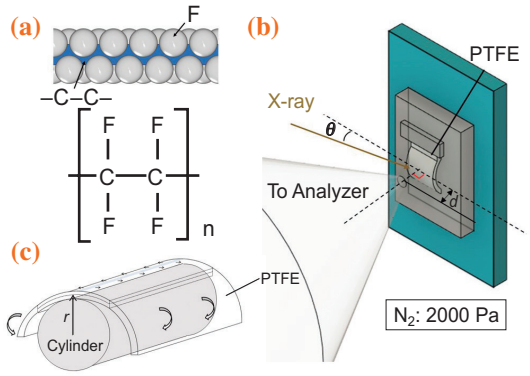

Fig.1. **(a)** Structural formula of PTFE. **(b)** Experimental setup for HAXPES measurement of PTFE under bending stress. **(c)** Schematic diagram of PTFE under bending stress.

charge-up or cone contamination from desorbed PTFE material [2]. Recent findings indicate that increasing d can achieve environmental charge compensation even at low pressures [2-5]. In this study, a distance of 1.8 mm was used, with nitrogen gas introduced at 2000 Pa, successfully eliminating charge-up effects. To investigate the dependence of PTFE surface states on bending strain, the strain was adjusted by varying the radius of curvature r applied to the material under stress (Fig. 1(c)).

Figure 2(a) shows the HAXPES spectra of C1*s* at different bending strains, obtained by adjusting the radius of curvature. Measurements were conducted on the outer surface (tensile stress surface) of the bent PTFE under bending stress. Curve fitting for each spectrum was performed using the Voigt function. In the spectrum of the unstressed PTFE in Fig. 2(a), peaks at binding energies around 295.1 and 293.2 eV correspond to CF_3 and CF_2, respectively. Additionally, peaks associated with C–C bonds in the main PTFE chain were scarcely observed. By contrast, the peak at 285.6 eV, corresponding to C–C bonds, became pronounced with an increase in the bending tensile strain. The F/C intensity ratio also decreases with increasing strain [1]. These results indicate that bending tensile stress induces the cleavage of C–F bonds in the side chains and fluorine desorption. Notably, this is the first report of a phenomenon where the C–C peak becomes pronounced under bending tensile stress.

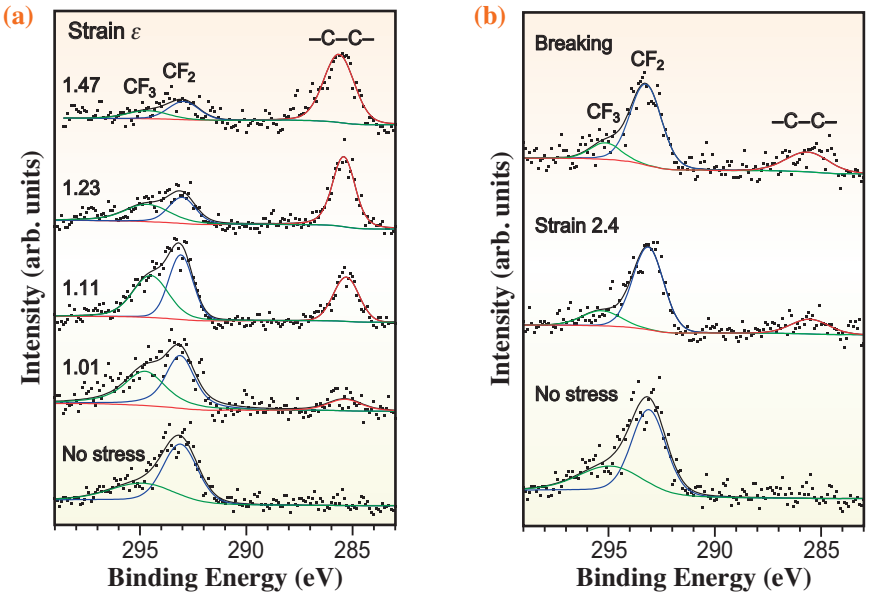

Fig. 2. Narrow scan analysis of C1*s* of PTFE with changing strain by applying **(a)** flexural tensile stress and **(b)** uniaxial tensile stress.

Based on these results, it was hypothesized that the C–F bond scission and desorption of F might also occur under uniaxial tensile stress. Figure 2(b) shows the C1*s* HAXPES spectrum of PTFE subjected to uniaxial tensile stress (tensile strain: 2.4). CF_3, CF_2, and C–C peaks were observed in the spectrum of the non-stressed PTFE, but the C–C intensity was significantly lower than that under flexural tensile stress, as shown in Fig. 2(b). Measurements of PTFE fractured by uniaxial tensile stress showed even low C–C peak intensities. These findings demonstrate that C–F bond scission occurs minimally under uniaxial tensile stress but progresses significantly with flexural tensile stress. However, measurements of the inner surface (compression stress surface) of bent PTFE revealed almost no C–C peak [1]. These results indicate that tensile stress due to bending, rather than compressive or uniaxial tensile stress, leads to significant side-chain scission on the PTFE surface (Fig. 3).

These findings reveal that using NAP-HAXPES will lead to a better understanding of the microscopic surface of PTFE when bending stress is applied, which is expected to contribute to further applications in microelectric mechanical systems (MEMS) and medical engineering.

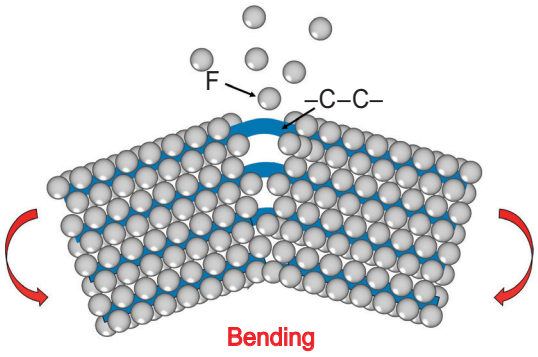

Fig. 3. Schematic of the surface of PTFE under bending stress.

Kaito Fujitani[a,*] and Satoru Suzuki[b]

[a] Graduate School of Engineering, University of Hyogo
[b] Lab. Advanced Science and Technology for Industry, University of Hyogo

*Email: fujitani@eng.u-hyogo.ac.jp

References

[1] *K. Fujitani, Y. Utsumi, A. Yamaguchi, H. Sumida and S. Suzuki: Appl. Surf. Sci.* ***637*** *(2023) 157891.*
[2] K. Fujitani *et al.*: Heliyon **9** (2023) e15794.
[3] K. Takenaka *et al.*: J. Vac. Sci. Technol. B **41** (2023) 044204.
[4] S. Suzuki: Vacuum and Surface Sci. **67** (2024) 106.
[5] S. Suzuki *et al.*: J. Electron Spectrosc. Relat. Phenom. **257** (2022) 147192.

Revisit to the old-but-totally-unknown fluorine polymer – *atactic* poly(vinylene fluoride) is amorphous ? –

So-called man-made polymers, such as polyethylene and nylon, were first produced approximately a century ago and are utilized as alternative materials for metals, ceramics, papers, wood, and so on. These synthetic polymers are expected to be developed further as soft materials that are indispensable in everyday life. Among the numerous synthetic polymers, fluorine polymers have been playing an important role in the development of polymer science and industry. Polytetrafluoroethylene [-$(CF_2CF_2)_n$-, PTFE], the most representative fluorine polymer, has a simple chemical structure: polyethylene [-$(CH_2CH_2)_n$-] with all the H atoms replaced with F atoms. However, PTFE has attracted significant research attention because of its unique properties, such as high water resistance, high heat resistance, low friction, and high chemical resistance. Various types of fluorine polymers have been developed, including fluoro-olefine polymers such as poly(vinyl fluoride) [-$(CH_2CHF)_n$-, PVF] with H/F = 3/1, poly(trifluoroethylene) [-$(CF_2CHF)_n$-, PTrFE] with H/F = 1/3, and poly(vinylidene fluoride) [-$(CH_2CF_2)_n$-, PVDF] with H/F = 2/2. Among them, PVDF was the first ferroelectric polymer to be applied to piezoelectric sensors, high-dielectric materials, etc. In this way, various types of fluorine polymers have been developed, and their structures and physical properties have been investigated in detail.

It is, however, quite curious to notice that another fluorine polymer having the same H/F ratio as PVDF, or poly(vinylene fluoride) [-$(CHFCHF)_n$-, PVLF] had been totally forgotten in the long history of fluorine polymers. Why is this polymer not interesting at all? Is this polymer totally useless nor worthless for stimulating any research?

This situation is well understood in the literature. In this half-century, only a few reports on PVLF have been published. PVDF has been characterized as chemically irregular or an *atactic* polymer with random arrays of H and F atoms along the main chain. Unfortunately, without sufficient study, PVLF was previously considered *amorphous* because of its *atactic* configuration [1]. Consequently, interest in this polymer was lost and only recently reinvigorated by us. The questions remain whether *atactic* polymers are always amorphous. There are many examples against this hypothesis. For example, the above-mentioned PVF was completely *atactic*, but it shows a highly crystalline wide-angle X-ray diffraction (XRD) pattern. This may be a good opportunity to address the problem of PVLF.

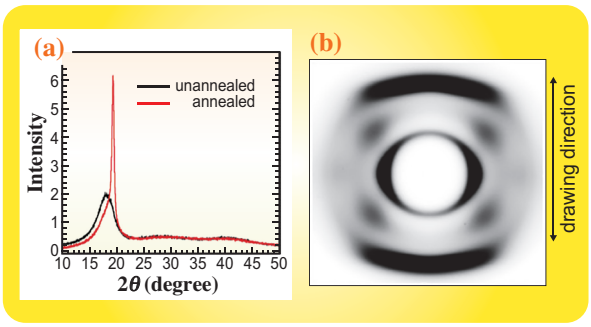

Fig. 1. **(a)** X-ray diffraction profiles of PVLF film measured before (black curve) and after the heat treatment (red curve) [3]. The wavelength of incident X-rays was 1.54 Å. **(b)** The 2D WAXD pattern measured for an oriented and annealed PVLF sample.

Recently, we synthesized a PVLF and characterized its behavior from various perspectives [2]. ^{19}F-nuclear magnetic resonance (NMR) spectral data analysis confirmed that the newly produced PVLF is still *atactic*, similar to that reported in the literature [1]. The wide-angle XRD patterns, which were collected mostly using a synchrotron X-ray beam at SPring-8 **BL38B1**, revealed that (i) the melt-quenched or solution-cast PVLF film gave only amorphous halo peaks; however, (ii) the sample annealed above 100°C or the glass transition temperature (T_g) exhibited significantly sharp and strong crystalline peaks, as shown in Fig. 1. The uniaxially oriented sample clearly exhibited a two-dimensional crystalline XRD pattern. At this moment, PVLF has come back from a long sleep as one

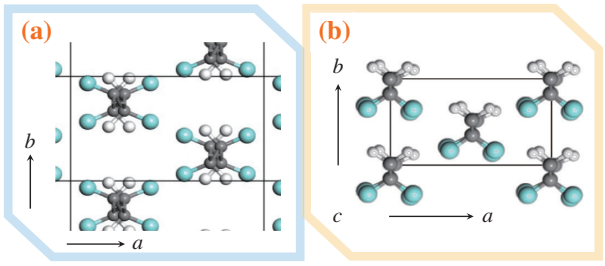

Fig. 2. Crystal structures viewed along the chain axis: **(a)** PVLF low-temperature phase [5] and **(b)** PVDF β form. In (a), the two chains are overlapped at the same lattice point at 50% probability because of statistically-disordered *atactic* configuration. In (b), the zigzag chains are packed in parallel along the *b* axis to give the polar crystal.

important member of *crystalline* fluorine polymers approximately 60 years after its initial studies.

Our research revealed extensive basic structural information such as the crystal structure (Fig. 2(a)) and higher-order structure composed of complicated aggregations of crystalline and amorphous regions (or the stacked lamellar structure) in addition to the physical properties, including the mechanical, thermal, and chemical properties. The temperature-dependent data of wide-angle (WAXD) and small-angle X-ray scatterings (SAXS), which were simultaneously measured, revealed that PVLF exhibits a thermodynamically second-order phase transition at around 100°C. The T_g is also located at about 100°C, above which the higher-order structure changed significantly.

Figure 3 shows the temperature dependence of the SAXS pattern of the as-drawn PVLF sample during heating. The pattern and its scattering intensity changed remarkably above T_g, resulting in a significant improvement in the mechanical properties. The higher-order structural changes that occurred during this process are shown in Figs. 3(a–c). The pink blocks indicate the oriented amorphous regions in the as-drawn and unannealed samples, which possess an electron density similar to that of the crystalline region (yellow), although the chains are irregular in conformation. When this sample was heated above T_g, the thermally activated chains in the oriented amorphous regions relaxed, resulting in a clear SAXS pattern corresponding to the high electron density contrast between the crystalline and amorphous regions.

Thus, PVLF is a semi-crystalline fluorine polymer with appreciably different behavior from that of other fluorine polymers. This important knowledge may allow us to develop PVLF as a novel but still primarily unknown fluorine polymer with excellent functional properties.

In addition, it is challenging to develop a novel type of VLF polymer, that is, a copolymer of VDF and VLF monomeric units. As previously discussed, PVDF is a ferroelectric polymer with a polar crystal structure composed of a parallel packing of zigzag chains (β form, Fig. 2(b)). However, VDF-trifluoroethylene (TrFE) copolymers, as members of the PVDF family, have attracted more attention than PVDF itself because the polar β form can be obtained more easily through slow cooling after melting. A ferroelectric phase transition between the polar and nonpolar phases, which is intrinsic to ferroelectric substances, was also observed for the VDF-TrFE copolymer. However, the ferroelectric transition temperature is limited to a relatively low temperature range of 60–120°C [4], above which ferroelectric properties, such as piezoelectricity and pyroelectricity, disappear. Compared with VDF-TrFE copolymers, the newly-developed VDF-VLF copolymers maintained the polar structure up to the higher temperature of approximately 140°C [5], thereby enabling the formation of a ferroelectric polymer with improved properties.

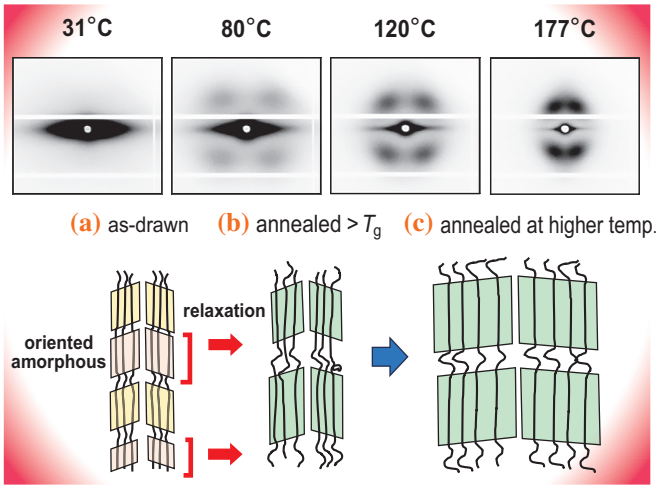

Fig. 3. Temperature dependence of 2D SAXS patterns measured for the as-drawn PVLF sample in the heating process. **(a–c)** Illustration of higher-order structure change of as-drawn PVLF by the heat treatment [5].

Ryouichi Yano[a,b], Kohji Tashiro[c,d,e,*] and Sono Sasaki[a,f,g]

[a] Dept. Biobased Materials Science, Kyoto Institute of Technology
[b] The Chemicals Division, Daikin Industries Ltd.
[c] Aichi Synchrotron Radiation Center
[d] Dept. Future Industry-oriented Basic Science and Materials, Toyota Technological Institute
[e] Comprehensive Research Organization for Science and Society (CROSS)
[f] RIKEN SPring-8 Center
[g] Faculty of Fiber Science and Engineering, Kyoto Institute of Technology

*Email: ktashiro_001@yahoo.co.jp

References

[1] R. E. Cais: Macromolecules **13** (1980) 806.
[2] *R. Yano, K. Tashiro, H. Masunaga, D. Ota, S. Watanabe, Y. Seto and S. Sasaki: Macromolecules* ***57*** *(2024) 3271.*
[3] *R. Yano, K. Tashiro, H. Masunaga and S. Sasaki: Macromolecules* ***57*** *(2024) 8498.*
[4] K. Tashiro *et al.*: Ferroelectrics **57** (1984) 297.
[5] R. Yano *et al.*: Polymer Preprints, Japan **73** (2024) 3K08.

Oxidative surface roughening of Pt electrode depending on electrolyte cations

The formation of surface oxides on solid metal electrodes, which affects the activity and selectivity of electrocatalytic reactions, is a primary concern in the development of high-performance electrocatalysts. Platinum (Pt) is a fundamental cathode element for low-temperature fuel cells owing to its exceptionally high activity in the oxygen reduction reaction (ORR). The roughening and dissolution of the surface atomic layer induced by oxide formation and reduction results in a restructuring of the surface morphology, which governs the ORR activity and durability. At positive potentials, where the irreversible surface oxidation of Pt occurs, the place exchange of surface Pt atoms with oxygen atoms is induced, forming a complex Pt oxide. The ions in the electrical double layer (EDL) affect the surface oxidation of the Pt electrode. In a LiOH solution, the stable adsorbed hydroxide (OH_{ad}) interacting with hydrophilic Li^+ inhibits further oxidation of Pt(111), whereas in a CsOH solution without hydrophilic cations, the absence of stable OH_{ad} results in surface roughening [1]. Hydrophobic cations are effective for ORR activation [2]. Surface oxidation in the presence of hydrophobic cations is interesting owing to the compatibility between activity and stability of electrocatalysts in alkaline media. Determination of the detailed interfacial structure provides insights into the EDL structure for highly active and durable electrocatalysis under oxide formation/reduction conditions. In this study, three-dimensional structural determination using *in situ* X-ray diffraction revealed that the hydrophilicity/hydrophobicity of cations at the interface plays an essential role in oxide formation.

X-ray diffraction (XRD) was performed using SPring-8 **BL13XU** with an X-ray energy of 20 keV. Structural analysis along the surface-normal direction was conducted using X-ray specular crystal truncation rod (CTR) scattering, which reflected the atomic structure along the out-of-plane direction. The specular CTR profiles were obtained between 0.5 and 1.2 V (RHE) in 0.1 M KOH and tetramethylammonium hydroxide (TMAOH), as shown in Fig. 1(a). The atomic-scale structures of Pt(111) in KOH and TMAOH

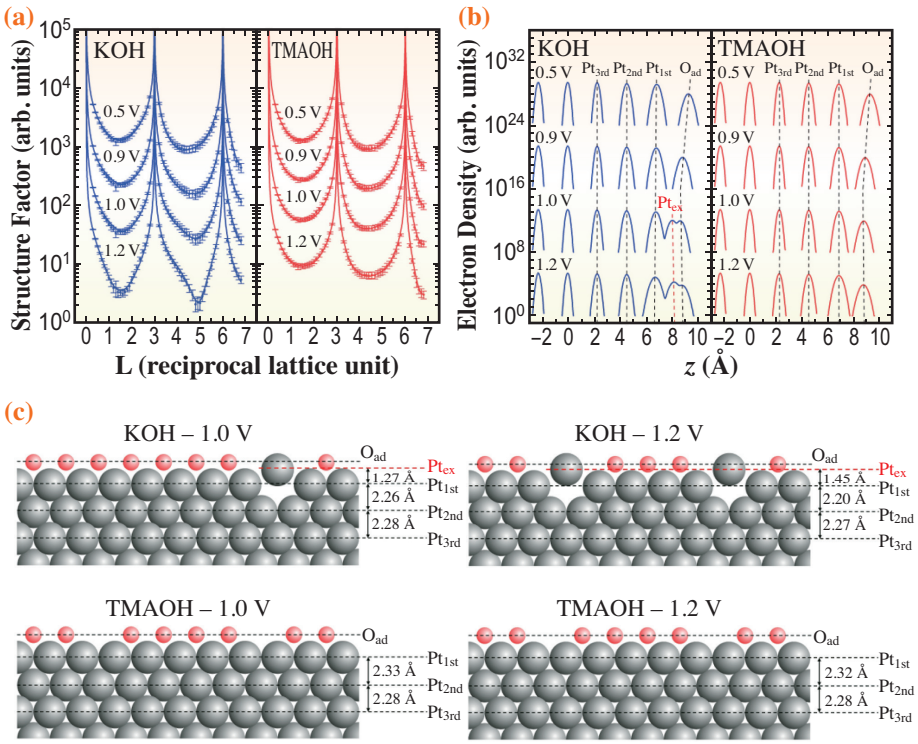

Fig. 1. **(a)** Specular CTR scattering profiles of Pt(111) in 0.1 M KOH and TMAOH. The dots and the solid lines represent the experimental data and the structure factors calculated from the optimized model, respectively. **(b)** Electron density profiles of Pt(111) along the direction normal to the surface calculated from the optimized model. **(c)** Side view of the optimized structure of Pt(111) in 0.1 M KOH and TMAOH.

solutions were determined by optimizing a model consisting of three layers of Pt and a monolayer of adsorbed oxygen to fit the CTR profiles. The vertical atomic position, occupancy factor, and Debye–Waller factors of the Pt and oxygen layers were optimized using the least-squares method. The electron-density profiles and schematic models of the interfacial structure are shown in Figs. 1(b) and 1(c), respectively.

At 0.5 V, the distance between the first Pt (Pt_{1st}) and adsorbed oxygen (O_{ad}) layers was approximately 2.4 Å in both solutions, corresponding to the oxygen atoms of the adsorbed water. The layer distance between Pt_{1st} and the second Pt (Pt_{2nd}) was approximately 2.32 Å in both solutions, which represents a 2% expansion compared to the value in the bulk. The interaction between the Pt surface and adsorbed water weakened the bonding between Pt_{1st} and Pt_{2nd}, resulting in surface relaxation of the Pt_{1st} layer. At 0.9 V, the Pt_{1st}–O_{ad} distance contracted to ~2.0 Å in both solutions due to the formation of an adsorbed OH_{ad} layer, assumed to be the major adsorbed species on Pt(111). Additional electron density resulting from the extracted Pt atoms (Pt_{ex}) appeared at 1.27 Å from the surface in KOH at 1.0 V, representing the precursor of place exchange. At the more positive potential of 1.2 V, the Pt_{1st}–Pt_{ex} distance expanded to 1.45 Å, and the coverage of the Pt_{ex} layer reached 0.18 in KOH. By contrast, no significant changes were observed in the interfacial structure of TMAOH up to 1.2 V.

Figure 2 shows the X-ray diffraction intensity during the anodic and cathodic scans at the reciprocal lattice position of (0 0 1.5), which is sensitive to surface roughness. In KOH, the intensity between Bragg peaks decreased above 0.9 V during the anodic scan. The diffraction intensity gradually decreased with potential cycling, suggesting that the reduction of surface Pt oxides irreversibly roughened the surface. Conversely, in TMAOH, the diffraction intensity slightly decreased above 1.0 V but recovered during the cathodic scan to 0.05 V, and remained independent of potential cycles. Hydrophilic Li^+ strongly stabilizes OH_{ad}, hindering the extraction of surface Pt atoms (Fig. 3). Interestingly, bulky hydrophobic cations, such as TMA^+, also reduce irreversible oxidation despite the absence of strong interactions with OH_{ad}. Hydrophobic TMA^+ inhibits the formation of complex Pt oxides associated with Pt extraction. By contrast, the moderate hydrophilicity of K^+ has no protective effect against irreversible oxidation. Moderate hydrophilicity enabled the formation of a complex Pt oxide layer (Fig. 3). The electrostatic repulsion in this complex oxide layer promotes Pt extraction.

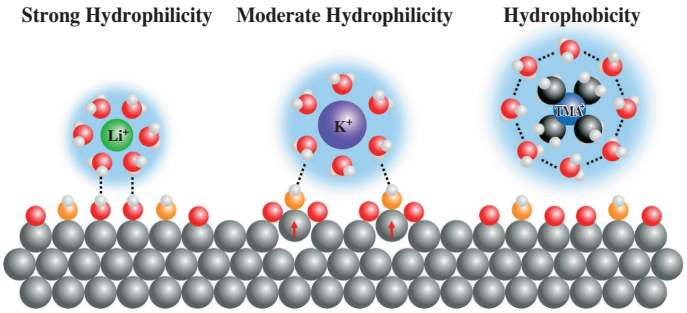

Fig. 3. Schematic model of the interfacial structure of Pt(111) in LiOH, KOH, and TMAOH solutions. The black dots and red arrows denote the noncovalent interactions and surface extraction, respectively. The gray, red (orange), and white balls represent platinum, oxygen, and hydrogen atoms.

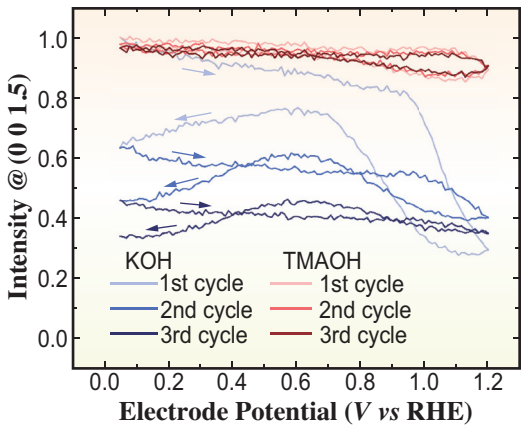

Fig. 2. Potential-dependent X-ray diffraction intensity at the reciprocal lattice position of (0 0 1.5) in 0.1 M KOH and TMAOH. The scan started from 0.05 V to the positive direction with a scanning rate of 0.002 Vs^{-1}.

Tomoaki Kumeda and Masashi Nakamura*

Graduate School of Engineering, Chiba University

*Email: mnakamura@faculty.chiba-u.jp

References

[1] M. Nakamura *et al.*: ChemPhysChem. **14** (2013) 2426.
[2] D. Strmcnik *et al.*: Nat. Chem. **1** (2009) 466.
[3] *T. Kumeda, K. Kondo, S. Tanaka, O. Sakata, N. Hoshi, M. Nakamura: J. Am. Chem. Soc.* ***146*** *(2024) 10312.*

Unveiling adsorption distribution in a metal–organic framework crystal with 3D XAFS-CT mapping

Metal-organic frameworks (MOFs) are crystalline solids with nanosized pores, formed by infinite linkages between metal ions and organic ligands. Their design flexibility, ease of synthesis, and periodic structures make them ideal adsorbents. Understanding MOF adsorption behavior is crucial for developing new functionalities. While X-ray diffraction (XRD) has clarified molecular-level behaviors within unit cells, meso- and macro-scale properties in MOF crystals remain unresolved. Meanwhile, studying transient states during adsorption, including surface adsorption, diffusion, and pore filling, is particularly challenging as XRD averages spatial and temporal information, making it unsuitable for capturing local heterogeneities.

Recent advances in hard X-ray imaging, such as XAFS-CT, enable 3D visualization of mesoscale behaviors and local chemical states, revealing defect structures in MOFs [1]. However, studies so far have focused on static heterogeneities, failing to capture dynamic adsorption processes. Here, we use 3D XAFS-CT imaging to visualize adsorption distribution across entire single MOF-74-Co crystals [2].

For XAFS-CT measurements, MOF-74-Co, featuring hexagonal one-dimensional pores and exposed metal sites, was selected (Fig. 1(a)) [3]. Pillar-shaped single crystals were prepared, treated with methanol, and desolvated under vacuum. Bulk crystallinity and porosity were confirmed by powder XRD and nitrogen adsorption isotherms at 77 K. The water adsorption isotherm at 298 K showed a stepwise profile, with a saturated capacity of 4.85 H_2O molecules per Co ion, consistent with reported structures (Fig. 1(b)). Isosteric heat of adsorption indicated strong host–guest interactions for up to one H_2O molecule per Co ion. Co *K*-edge XAFS spectra, sensitive to hydration, revealed a significant increase in white-line height at 7717 eV during hydration (Fig. 1(c)).

In situ XAFS-CT measurements were conducted under controlled water vapor pressures at SPring-8 **BL36XU** (Fig. 2). Crystals in a glass capillary connected to a vacuum/vapor control line were scanned around the Co *K*-edge. 2D transmission images were captured at 181 angles in 1° increments. Original 2048 × 2048 pixel images were binned to 512 × 512 to enhance the signal-to-noise ratio. XAFS spectra were analyzed via linear combination fitting (LCF) using dehydrated and hydrated Co spectra as references. Reconstructed 3D images provided voxel-level Co density and hydration ratio (hydrated Co/all Co) information with a voxel resolution of 0.995 μm³ (Fig. 3).

Co density, proportional to the number of Co ions per voxel, remained constant regardless of vapor pressure, but inhomogeneity was observed at the tapered edges, linked to micro-displacements during adsorption/desorption. This inhomogeneity corresponded to local crystallinity disorders.

Figure 3(c) shows 3D maps of Co hydration ratio across the particle. At low vapor pressure, the crystal

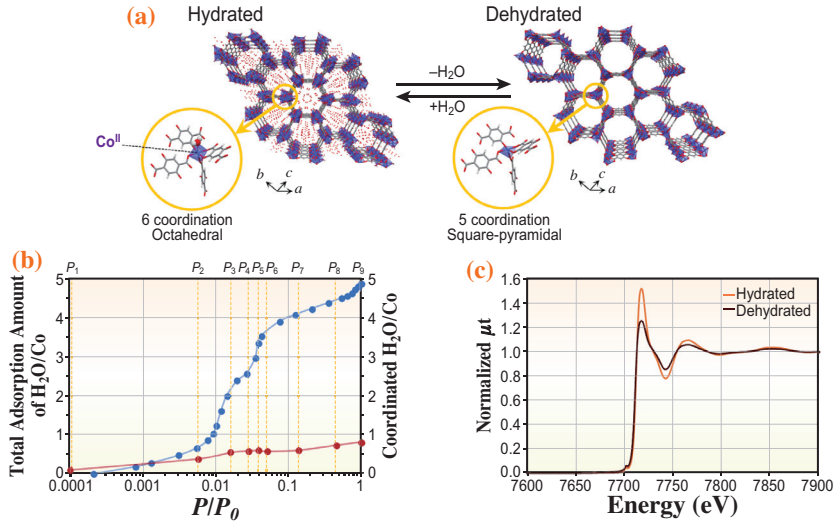

Fig. 1. **(a)** Crystal structures of MOF-74-Co in the hydrated and dehydrated states. **(b)** H_2O adsorption isotherms of bulk MOF-74-Co at 298 K (blue plot). P_1–P_9 on the upper axis indicate the relative pressures at which the XAFS-CT measurements were carried out. The red plot is the coordination adsorption isotherm of the Co ion, derived from XAFS-CT analyses. **(c)** Co *K*-edge XAFS spectra of MOF-74-Co in the hydrated and dehydrated states. [2]

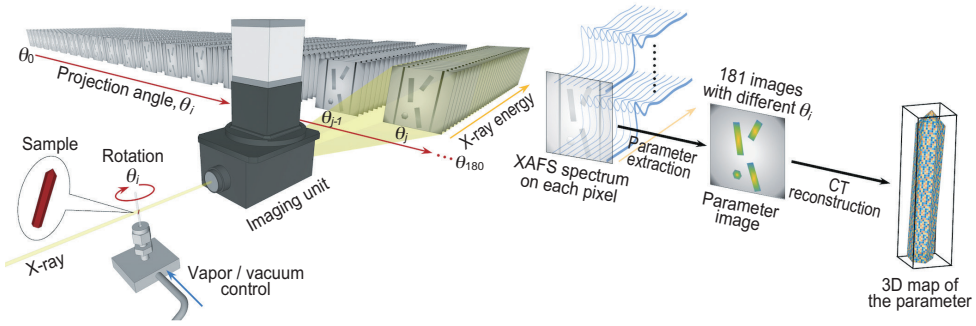

Fig. 2. Schematic illustration of the XAFS-CT method to obtain three-dimensional spatial distributions of adsorption states in a single crystalline particle. [2]

appeared entirely blue, indicating minimal hydration. At P_2, water molecules began coordinating with Co, significantly changing the hydration distribution. By P_3, red regions emerged at the center. From P_4 to P_7, hydration distribution stabilized, and near saturation pressure, the particle turned red or pale pink, indicating saturation at exposed Co sites. The histograms quantitatively illustrate H_2O coordination within the particle. The mean hydration ratio across voxels represents the average H_2O coordinatively adsorbed per Co ion. Plotted with the bulk isotherm (Fig. 1(b)), it revealed competition between coordination and non-coordination adsorption. Between P_1 and P_4, coordinated H_2O increased gradually but remained at 0.5 H_2O/Co by P_3, even as total adsorption reached 2.0 H_2O/Co. From P_4 to P_7, bulk adsorption rose rapidly to 4.0 H_2O/Co, driven by H_2O–H_2O interactions, while coordination adsorption stayed constant. Eventually, both coordination and physisorption saturated, completing hydration.

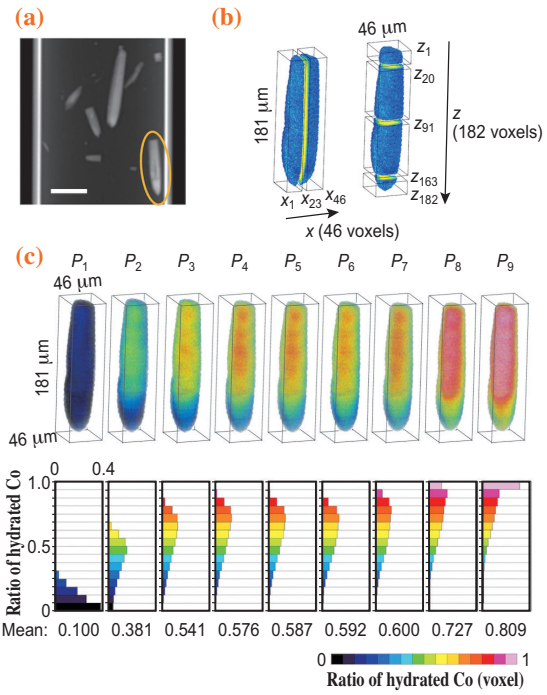

Fig. 3. **(a)** X-ray absorbance image of MOF-74-Co crystals in a capillary with a 100 μm scale bar. **(b)** 3D reconstructed image of Co density of the particle, showing the voxel coordinates and the cross sections of interest. **(c)** 3D distribution map of the Co hydration ratio with voxel transparency of 75%. Below are the histograms of relative frequencies of the voxels classified with the Co hydration ratio in each voxel. The values in the histograms are the mean values of the Co hydration ratio. [2]

Microbeam X-ray diffraction at SPring-8 **BL40XU** confirmed single crystallinity throughout the particle, with consistent lattice parameters matching reported MOF-74-Co structures. However, diffraction spots at the edges were broader than those at the center, indicating reduced crystallinity and increased orientational disorder. The mosaicity parameter at the edge was larger than at the edge, highlighting significant local differences while preserving the overall structure.

In conclusion, 3D visualization of Co hydration revealed heterogeneous H_2O affinity within MOF-74-Co crystals, particularly at the edges where reduced crystallinity affected adsorption. These findings emphasize the importance of local crystallinity in determining adsorption properties. While ideal particles exhibit uniform adsorption, XAFS-CT imaging and microbeam diffraction captured true heterogeneities, offering critical insights for optimizing MOFs as functional materials.

Hirotoshi Sakamoto

Institute for Integrated Cell-Material Sciences (iCeMS), Kyoto University

Email: sakamoto.hirotoshi.2k@kyoto-u.ac.jp

References

[1] D. Ferreira Sanchez *et al.*: Angew. Chem. Int. Ed. **60** (2021) 10032.
[2] *E. Yamada, H. Sakamoto, H. Matsui, T. Uruga, K. Sugimoto, M.-Q. Ha, H.-C. Dam, R. Matsuda, M. Tada: J. Am. Chem. Soc.* ***146*** *(2024) 9181.*
[3] P. D. C. Dietzel *et al.*: Angew. Chem. Int. Ed. **44** (2005) 6354.

In situ HERFD-XANES study on CO_2 activation on niobium oxide clusters

Metal oxide clusters consisting of several MO_6 metal oxide units (M: metal ions), called polyoxometalates, exhibit unique reactivities and physical properties owing to their electronic and geometric structures, unlike their bulk materials counterparts. We found that group 5 transition metal Nb/Ta oxide clusters, such as $[M_6O_{19}]^{8-}$ (MV = Nb, Ta) and $[Nb_{10}O_{28}]^{6-}$, possess large negative charges and have demonstrated effectiveness as base catalysts [1,2]. Notably, the $[Ta_6O_{19}]^{8-}$ (**Ta6**) cluster shows high activity for CO_2 fixation reactions with styrene oxide and amine compounds. DFT calculations predict that the terminal oxygen (Ta=O) on the surface of **Ta6** acts as a Lewis base, facilitating monodentate CO_2 coordination [2]. Understanding the structural dynamics of CO_2 adsorbed on **Ta6** is crucial to elucidating its high catalytic activity.

The recent development of a high-energy-resolved fluorescence detection (HERFD) method has garnered attention for its ability to measure XANES spectra with high-energy resolution. This method detects fluorescent X-rays with specific wavelengths, achieving an energy resolution beyond the core electron lifetime width, thereby enhancing the clarity of peaks in XANES spectra [3]. This technique has revealed small peaks that conventional methods often miss and has been applied to evaluate the symmetry of Ce_n oxide clusters (n = 2, 6, 24, 38, 40) [4]. However, HERFD-XANES studies remain relatively limited.

In this study, we measured *in situ* Ta L_3-shell HERFD-XAFS of **Ta6** in DMF during CO_2 adsorption at SPring-8 **BL36XU** beamline (Fig. 1) [5]. The HERFD-XANES measurements revealed previously undetected peaks within the white line region, that could not be observed by the conventional transmission method. In addition, we traced the CO_2 adsorption process on **Ta6** and experimentally clarified that the ligand field splitting is changed by the local structural change of Ta due to CO_2 adsorption.

The Ta L_3-edge HERFD-XANES spectrum of Ta_6 prior to CO_2 adsorption in DMF solution is shown in Fig. 2(a). Peaks (A_1 and B_1) along with a shoulder peak (C_1), which were not visible using the conventional transmission method at SPring-8 **BL01B1** with a Si(111) double crystal, were detected using the HERFD method. These peaks correspond to the electronic transition from 2*p* to 5*d* orbitals, which are expected to split due to the ligand field in the distorted octahedral **Ta6** units. These distortions approximate C_{4V} symmetry, enabling a detailed discussion of local distortions using Ta L_3-edge HERFD-XANES.

From the *in situ* HERFD-XANES spectra, we observed gradual changes in the electronic state of **Ta6** in DMF under CO_2 gas flow (Fig. 2(b)). The secondary differential spectra of Ta L_3-edge HERFD XANES showed slight shifts in peaks A_1 and B_1 to A_2 (−0.2 eV) and B_2 (+0.2 eV), respectively, while peak C_2 emerged at 9885.6 eV, replacing the vanished C_1 peak (Fig. 2(c)). Experimental data revealed that five CO_2 molecules were adsorbed onto **Ta6**, with spectral changes attributed to structural modifications around the Ta centers.

To further elucidate the structural changes, DFT calculations were employed to CO_2 adsorbed **Ta6** (**Ta6-CO_2**) model. The surface Ta=O bonds within the {TaO_6} unit elongated, while the bridged Ta–O bonds

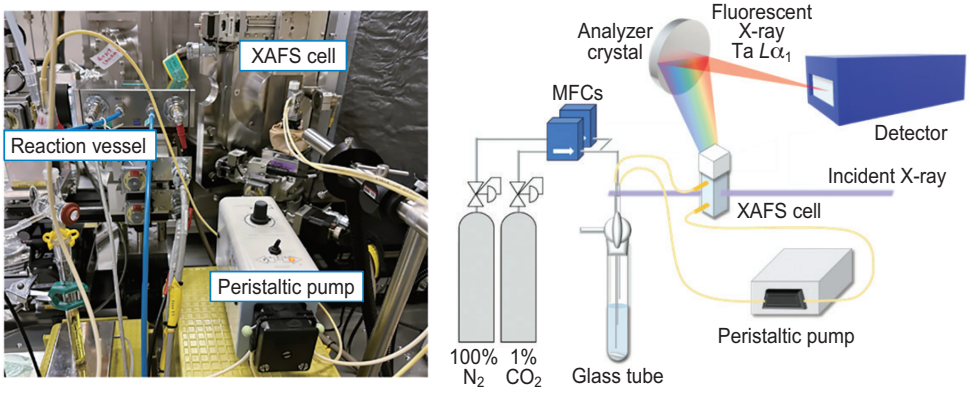

Fig. 1. Experimental setup for *in situ* HERFD-XANES measurement.

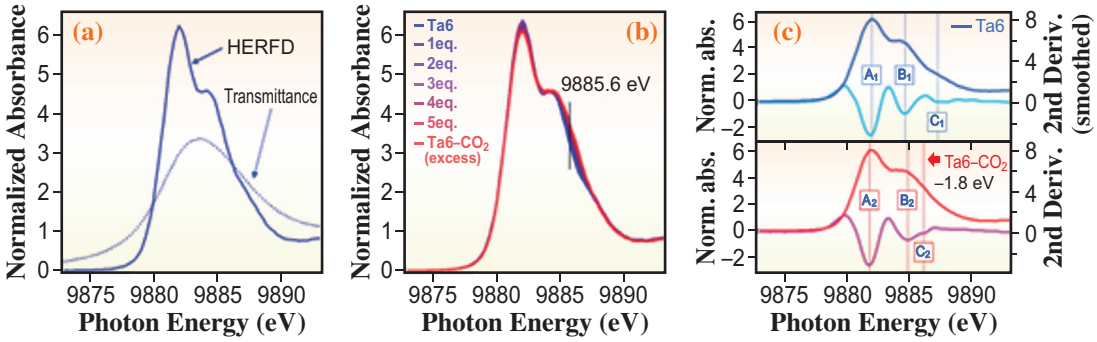

Fig. 2. **(a)** Comparison of XANES spectra of **Ta6** measured by HERFD and transmittance mode. **(b)** *In situ* HERFD-XANES spectra of **Ta6** during CO_2 adsorption. **(c)** HERFD-XANES spectra of **Ta6** and **Ta6-CO_2** along with their corresponding second derivative spectra.

shortened upon CO_2 adsorption (Fig. 3). This structural adjustment indicated a shift of the Ta atom toward the octahedral center, pushing the {TaO_6} unit closer to O_h symmetry. Energy calculations and electronic structure analyses were performed for the {TaO_6} and CO_2 adsorbed one ({TaO_6-CO_2}), as shown in Fig. 3. In the {TaO_6} unit, regions A_1 (d_{xy}, d_{yx}, d_{zx}), B_1 (d_{z2}, d_{x2-y2}, $d_{z2}+\sigma_O$), and C_1 ($d_{x2-y2}+\sigma_O$) unit correlated with peaks A_1, B_1, and C_1 of **Ta6**. Upon CO_2 adsorption, these evolved into regions A_2 (d_{xy}, d_{yx}, d_{zx}), B_2 (d_{z2}, $d_{z2}+\sigma_O$), and C_2 (d_{x2-y2}), corresponding to peaks A_2, B_2, and C_2 of **Ta6-CO_2**. The disappearance of C_1 and the appearance of C_2 were linked to the destabilization of the d_{x2-y2} orbitals, including the hybrid orbital of Ta d_{x2-y2} + 2*p* orbitals and stabilization of d_{z2} orbitals caused by the structural centering effect. This is mainly due to the compression of the bridged Ta–O bonds and the elongation of the Ta=O bonds.

In summary, we observed a change in the ligand-field splitting of the Ta 5*d* orbitals in a **Ta6** catalyst upon CO_2 interaction, using *in situ* Ta L_3-edge HERFD-XANES. Theoretical calculations indicated that the three peaks observed before CO_2 adsorption correspond to transitions to molecular orbitals with significant contributions from the Ta 5*d* orbitals, which are split by the ligand field of the distorted O_h symmetrical {TaO_6} units. The observed peak replacement reflects the destabilization of the d_{x2-y2} orbitals and the stabilization of the d_{z2} orbital, induced by the centering effect from the off-center arrangement of the {TaO_6} units upon CO_2 attachment to the terminal oxygen. We demonstrate that HERFD-XANES is an effective tool for tracking subtle changes in the electronic and geometric structures of materials in their working state.

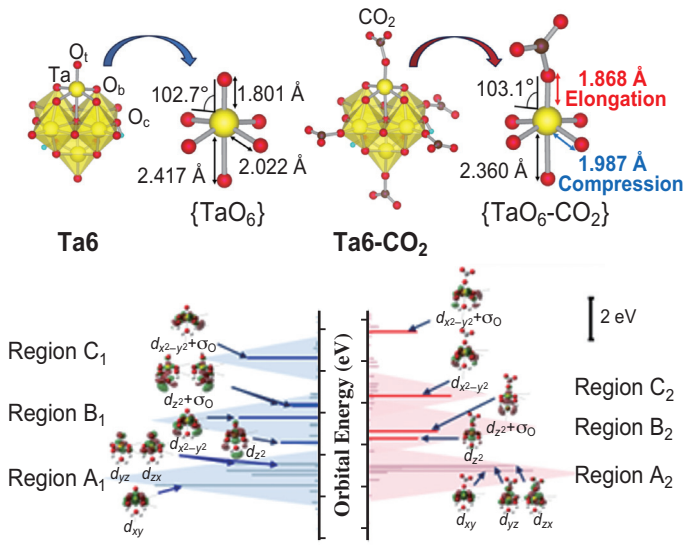

Fig. 3. Schematic illustration showing the contribution of Ta-based *d*-orbitals in TaO_6 and TaO_6-CO_2.

Seiji Yamazoe

Department of Chemistry, Tokyo Metropolitan University

Email: yamazoe@tmu.ac.jp

References

[1] S. Hayashi *et al.*: Chem. Asian J. **12** (2017) 1635.
[2] S. Hayashi *et al.*: J. Phys. Chem. C **122** (2018) 29398.
[3] K. Hämäläinen *et al.*: Phys. Rev. Lett. **67** (1991) 2850.
[4] P. Estevenon *et al.*: Chem. Mater. **35** (2023) 1723.
[5] *T. Matsuyama, S. Kikkawa, N. Kawamura, K. Higashi, N. Nakatani, K. Kato, and S. Yamazoe: J. Phys. Chem. C* ***128*** *(2024) 2953.*

Double-layered perovskite positive electrode with high capacity involving O–O bond formation for all-solid-state fluoride-ion batteries

Lithium-ion batteries (LIBs) are widely used in various electronic devices owing to their high energy density, high power density, and long-term durability. However, with the growing demand for longer-range electric vehicles, there is a need to develop high-energy-density batteries that do not rely on lithium. One strategy to surpass the energy density of current LIBs is to utilize electrode materials that enable multielectron reactions. However, using polyvalent ions such as magnesium ions (Mg^{2+}) as carriers presents kinetic disadvantages, such as slow diffusion within solid electrodes. In contrast, fluoride ions (F^-), which are monovalent and have a small ionic radius (1.33 Å), can enable multielectron reactions with fast ionic conduction. Owing to these characteristics, all-solid-state fluoride-ion batteries (FIBs) that use F^- as a carrier have attracted attention for their potential to achieve high energy and power densities [1,2]. While metal/metal fluorides have been developed as typical positive electrodes, they suffer from poor cyclability and power density due to large volume changes during charging and discharging. To address these issues, electrode materials based on topotactic F^- intercalation reactions have been developed. Compared to metal/metal fluorides, these materials significantly improve cyclability and power density. However, their usable capacity is limited because of their relatively large chemical formula weight. In this study, to increase the capacity of intercalation-type positive electrode materials, anion redox, as reported in LIB cathodes [3], was applied to a double-layered perovskite $La_{1.2}Sr_{1.8}Mn_2O_{7-\delta}F_2$ [4].

The $La_{1.2}Sr_{1.8}Mn_2O_{7-\delta}F_2$ delivered a charge capacity of approximately 250 mA·h/g (Fig. 1(a)) after the initial discharge. The subsequent discharge yielded a large capacity of 190 mA·h/g, nearly double the initial discharge. Excess electrochemical fluorination was confirmed to be topotactic through X-ray diffraction (XRD), scanning transmission electron microscopy (STEM) and atomic resolution electron energy loss spectroscopy (EELS). The XRD pattern of the 3.0 V charged $La_{1.2}Sr_{1.8}Mn_2O_{7-\delta}F_2$ remained similar to that of the pristine state (Fig. 1(b)), while STEM imaging indicated regular cation arrangements (Fig. 1(c)). EELS mapping of the 3.0 V charged $La_{1.2}Sr_{1.8}Mn_2O_{7-\delta}F_2$ (Fig. 1(c)) revealed the presence of excess F^- in the perovskite block alongside the interstitial site within the rock-salt slabs. Upon discharge, the defluorinated

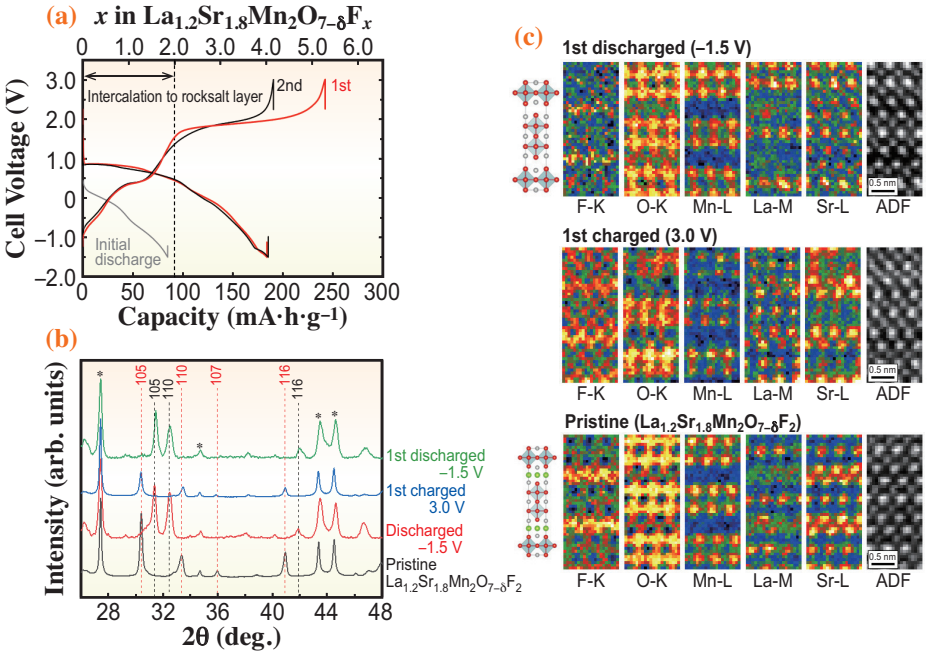

Fig. 1. **(a)** Charge/discharge curves of $La_{1.2}Sr_{1.8}Mn_2O_{7-\delta}F_2$. **(b)** XRD patterns of cathode composites containing $La_{1.2}Sr_{1.8}Mn_2O_{7-\delta}F_2$ during charge/discharge. Red and black broken lines correspond to $La_{1.2}Sr_{1.8}Mn_2O_{7-\delta}F_2$ and $La_{1.2}Sr_{1.8}Mn_2O_{7-\delta}$, respectively. Asterisks denote the $La_{0.9}Ba_{0.1}F_{2.9}$ electrolyte. **(c)** Atomic resolution STEM-EELS mapping images of $La_{1.2}Sr_{1.8}Mn_2O_{7-\delta}F_2$ during charge/discharge along the [010] crystallographic axis.

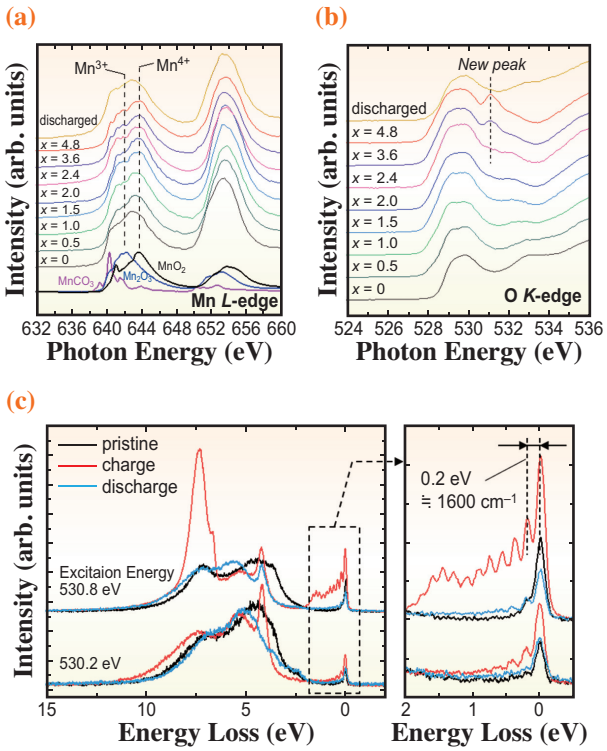

Fig. 2. **(a)** Mn *L*-edge and **(b)** O *K*-edge XAS spectra collected at SPring-8 **BL27SU** of $La_{1.2}Sr_{1.8}Mn_2O_{7-\delta}F_2$ during charge/discharge. The parameter x in the figure represents the fluoride content (x in $La_{1.2}Sr_{1.8}Mn_2O_{7-\delta}F_x$). **(c)** O *K*-edge RIXS spectra recorded at excitation energies of 530.2 and 530.8 eV at SPring-8 **BL07LSU** for the pristine, charged (3.0 V), and discharged (–1.5 V) states, respectively.

$La_{1.2}Sr_{1.8}Mn_2O_{7-\delta}$, phase was identified by both XRD and EELS (Figs. 1(b,c)). The charge compensation mechanism during (de)fluorination was analyzed using soft X-ray absorption spectroscopy (XAS) and resonant inelastic X-ray scattering (RIXS) (Fig. 2). The Mn *L*-edge spectrum of $La_{1.2}Sr_{1.8}Mn_2O_{7-\delta}F_2$ (Fig. 2(a)) showed a shift to higher energy from $x = 0$ to $x = 2.0$ but no further shift was observed from $x = 2.0$ to $x = 4.8$. This behavior indicates that Mn ions are oxidized from Mn^{3+} to Mn^{4+} during the initial charging phase and remain as Mn^{4+} in the later stage of charge. In the O *K*-edge spectrum, the intensity at 529 eV increased during the early stage of charging ($x < 2$) (Fig. 2(b)) owing to the oxidation of Mn^{3+} to Mn^{4+}. However, as charging progressed beyond $x \sim 2$, a new O *K*-edge peak emerged at ~530.8 eV. The intensity of this peak increased with further charging and reversibly disappeared upon discharge. To investigate the origin of this new peak, RIXS measurements were performed at excitation energies between 528.5 and 533.0 eV. The RIXS spectra at 530.8 eV (Fig. 2(c)) revealed discrete energy loss peaks near the elastic line from 5 to 0 eV. The vibrational frequency of the first level was measured at 1591 cm^{-1}, closely matching the molecular O_2 (~1600 cm^{-1}), observed in charged $Na_{0.75}[Li_{0.25}Mn_{0.75}]O_2$ by RIXS [5]. This result indicates the formation of an O–O bond in charged $La_{1.2}Sr_{1.8}Mn_2O_{7-\delta}F_2$. Upon discharge, this vibration signature disappeared, confirming the reversible nature of O–O bond formation/breaking.

These results demonstrate that $La_{1.2}Sr_{1.8}Mn_2O_{7-\delta}F_2$ undergoes two distinct fluoride (F^-) intercalation processes: initial (de)intercalation into rock-salt slabs with conventional Mn redox and subsequent (de)intercalation of excess F^- into the perovskite layer involving the formation of an oxygen–oxygen bond (anion redox) (Fig. 3). This study is the first to demonstrate the introduction of electronic holes and the associated formation of O–O bonds following the electrochemical intercalation of an anionic species. Given the abundance of perovskite compounds, these findings are expected to advance the development of cathode materials for FIBs, where mixed-anion compounds with anion redox reactions may serve as effective active materials.

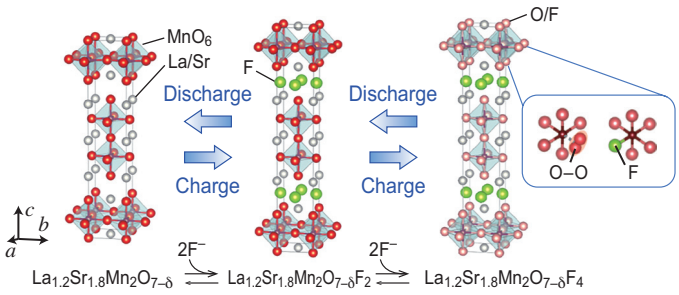

Fig. 3. Discharge/charge scheme of $La_{1.2}Sr_{1.8}Mn_2O_{7-\delta}F_2$. The specific locations of the O–O bond and excess F^- in the charged $La_{1.2}Sr_{1.8}Mn_2O_{7-\delta}F_2$ are not clear.

Kentaro Yamamoto

Faculty of Engineering, Nara Women's University

Email: k.yamamoto@cc.nara-wu.ac.jp

References

[1] M. Anji Reddy and M. Fichtner: J. Mater. Chem. **21** (2011) 17059.
[2] D. Zhang *et al.*: ACS Appl. Mater. Interfaces **13** (2021) 30198.
[3] M. Sathiya *et al.*: Nat. Mater. **12** (2013) 827.
[4] *H. Miki, K. Yamamoto, H. Nakaki, T. Yoshinari, K. Nakanishi, S. Nakanishi, H. Iba, J. Miyawaki, Y. Harada, A. Kuwabara, Y. Wang, T. Watanabe, T. Matsunaga, K. Maeda, H. Kageyama, Y. Uchimoto: J. Am. Chem. Soc.* ***146*** *(2024) 3844.*
[5] R. A. House *et al.*: Nature **577** (2020) 502.

Reconstruction of chitosan network order using the meniscus splitting method for design of pH-responsive materials

As natural polymers, polysaccharides are expected to serve as alternative materials toward the development of sustainable society in a broad range of fields such as food packaging, functional foods, drug delivery, cosmetics, and agriculture. The natural polysaccharide chitosan is a product of deacetylated chitin, which is extracted from the exoskeletons of crustaceans and insects and fungal cell walls. Moreover, chitosan is a cationic polymer that has attracted the attention of numerous researchers in various biomedical fields, such as wound healing, hemodialysis membranes, drug and gene delivery systems, and tissue engineering/regeneration [1]. In the chitosan side chain, amino and hydroxyl groups can be employed as cross-linkable groups. Amino groups can be protonated to ammonium groups below pH 6.4, making chitosan a pH-responsive soft material [2].

Recently, several methods, such as pre-stretching and drying, directional freezing, and electrospinning, have been reported for the preparation of polysaccharide-based materials with anisotropic microstructures. Distinct from these methods, we have developed a meniscus splitting method [3,4] for preparing a three-dimensionally ordered polymer membrane by exploiting viscous fingering phenomena. Affected by temperature and humidity, the evaporative interface of the polymer solution/dispersion from a cell induces the orientation of polymeric microfibers along the contact line of the interface by capillary force. During water evaporation, the concentrated polymer at the interface bridges the millimeter-scale gap between the two substrates and forms vertical membranes. The limitation for the bridging distance is essentially ~2 mm, depending on the capillary length.

In particular, chitosan was initially dispersed in an aqueous mixture containing acetic acid and deposited by bridging the gaps and forming a membrane during drying [5]. Polarized light microscopy observation of the membrane revealed that the polarizers and first-order retardation plate (λ = 530 nm) were directionally set, as shown in Fig. 1(a). The membrane formed from two air-liquid phases is shown in blue. This result strongly implies that the membrane has a structure that is oriented parallel to the *Y*-gap axis. However, a part of the membrane appeared somewhat yellow because the sample was slightly curved toward the *X*-axis or tilted to the *Z*-axis rather than parallel to the *Y*-axis. After rewetting the membrane with pure water, and without any additional crosslinker from air, the membrane behaved as a hydrogel with anisotropic swelling (Fig. 1(a)). The swelling ratios, L_{WET}/L_{DRY} in the *X*-, *Y*- and *Z*-directions were 3.1, 1.3, and 1.8, respectively. During drying of the chitosan solution, chemical crosslinkers or crosslinking points were not introduced. Notably, the membrane rapidly and anisotropically swelled in pure water while maintaining its hydrogel shape.

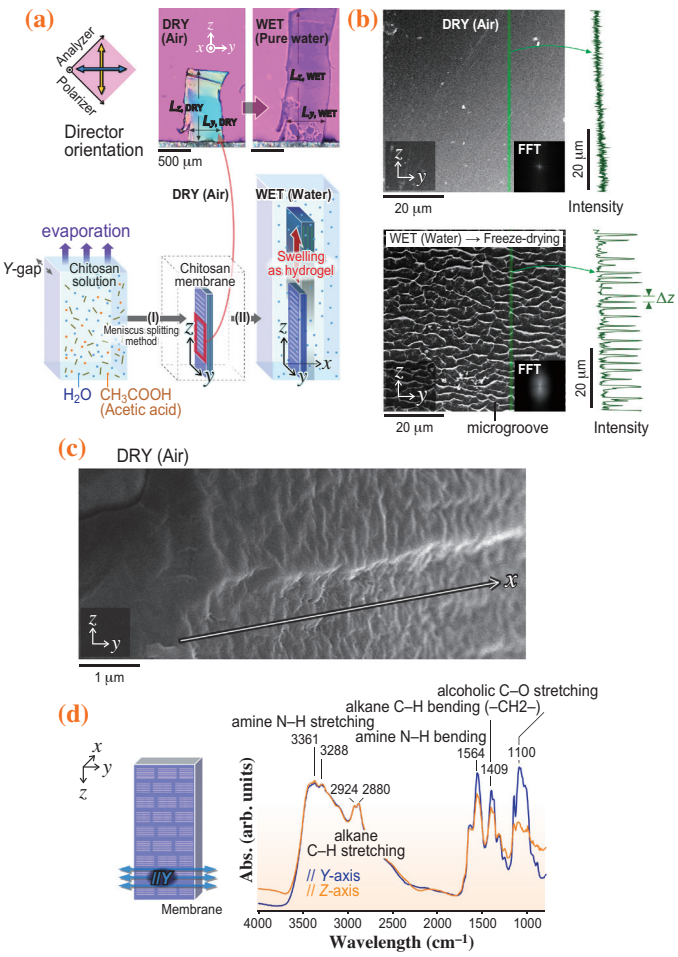

Fig. 1. Chitosan hydrogel swelling anisotropically in pure water and its microstructures. **(a)** Polarized optical microscopy images in air and in pure water. The process of the chitosan solution for the preparation of the DRY membrane and WET hydrogel. **(b)** SEM images of the heat-dried sample prepared using the meniscus splitting method as DRY (air) and freeze-dried sample as WET (water). Inset: Fast Fourier Transform (FFT) analysis of SEM images. The charts indicate surface asperity along the *YZ*-plane of samples by analyzing the intensity of the gray value along the green line in the SEM images. **(c)** SEM images of the heat-dried sample, focusing on the cross-section in the *X*-direction. **(d)** IR spectra of the membrane through polarized light. The blue and orange spectra correspond to measurements with the polarized aligned parallel to the cell gap (*Y*-direction) and cell depth (*Z*-direction), respectively. Room temperature ~25°C; relative humidity ~50%. [5]

To study the microstructures in the DRY/WET states, the samples were observed by scanning electron microscopy (SEM) (Fig. 1(b)). A WET (water) sample was prepared by freeze drying. In contrast to the DRY sample, the WET sample showed striped patterns with microgrooves parallel to the *Y*-axis. This tendency was also confirmed by the results of FFT analysis (Fig. 1(b), inset). Microgrooves were generated during the sample preparation under reduced pressure, enabling mechanical stress. By analyzing the gray values of the green line on the images, the intervals between the microgrooves (Δz) were measured. The average value of Δz was 2.1 μm, and the groove width was <0.3 μm. Such submicron-scale periodicity was also confirmed in the cross-section of the DRY membrane as layers of the *YZ* plane stacked in the *X*-direction (Fig. 1(c)). Considering that the layer-to-layer distance varied in the 0.3–0.5 μm range, the chitosan fibers were easily self-assembled at this submicron-scale, together with the chitin. Furthermore, to elucidate the anisotropy of molecular structures, the dried sample was evaluated by infrared (IR) spectroscopy carried out with polarized light at SPring-8 **BL43IR**. To determine the anisotropy of molecular structures, the dried sample was evaluated by IR spectroscopy carried out with polarized light at 50% relative humidity (Fig. 1(d)). The two significant peaks at approximately 3361 and 3288 cm^{-1} were attributed to the O–H and N–H stretching vibrations of the functional groups, respectively, which are involved in the hydrogen bonding between the chitosan molecules. The peaks at 2880 and 2924 cm^{-1} indicated alkane C–H stretching. The characteristic peaks at 1564, 1409, and 1100 cm^{-1} are attributed to the N–H bending vibration of amine II, alcoholic C–O stretching, and alkane C–H bending, respectively. All bands, except for those at 3288, 3361, and 2880–2924 cm^{-1}, in the direction parallel to the *Y*-axis were stronger than those in the direction parallel to the *Z*-axis. These results can be attributed to the fact that the chitosan nanofibers in the bundled state exposed more side chains parallel to the *Y*-axis.

To understand the three-dimensional anisotropic swelling, the dried membrane was directly immersed into each buffered solution with a wide pH range (2.2–8.0) at ~25°C. Figure 2 shows typical images at a given pH and the pH dependence of the equilibrium swelling ratio. The ratio, *r*, is defined as the ratio of the length in the wet state to that in the dry state, L_{WET}/L_{DRY}. Swelling ratios in each direction are defined as $r_x = L_{WET,\,x}/L_{DRY,\,x}$, for example. In this pH range, r_x was significantly higher than r_y and r_z, and all of the swelling ratios (r_x, r_y, and r_z) in acidic conditions with pH 2.2–4.0 showed higher values. Under acidic conditions, protonation enables water molecules to penetrate the interspaces among the fibers and chains in the fibers. Consequently, certain crosslinking points based on hydrogen bonds can be eliminated. Based on the pH-responsive swelling ratio, this material can be applied in an aqueous environment with a pH signal, with irreversible changes in the pH range of 2–5 and reversible changes in the pH range of 5–8. The decrease in pH from normal cells to cancer cells can be a switching signal not only for mass transporters, such as nanogels and micelles, but also for tissue engineering using stimuli-responsive soft materials.

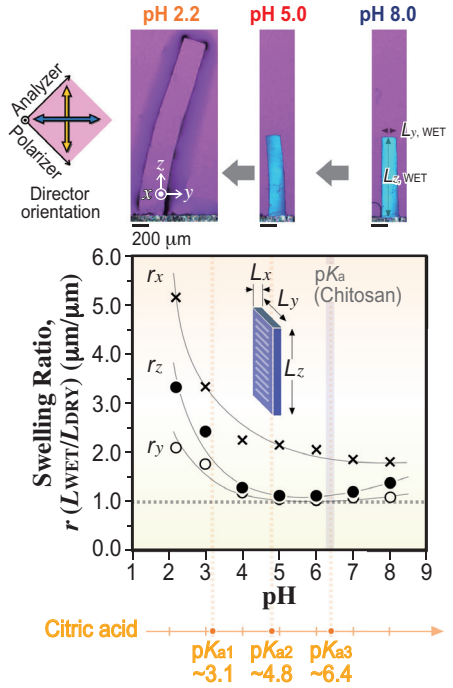

Fig. 2. Chitosan hydrogel with an anisotropic pH response in three dimensions. L_x, L_y, and L_z are the sample lengths in *X*-, *Y*- and *Z*-directions. DRY signifies a condition under air atmosphere at approximately 25°C. The DRY samples were equilibrated in initial pH buffer solutions as the WET state. Buffer solutions consisted of citric acid and disodium. [5]

Thi Kim Loc Nguyen[a], Yuka Ikemoto[b] and Kosuke Okeyoshi[a,*]

[a] Graduate School of Advanced Science and Technology, Japan Advanced Institute of Science and Technology
[b] Japan Synchrotron Radiation Research Institute (JASRI)

*Email: okeyoshi@jaist.ac.jp

References

[1] R. de S. Victor *et al.*: Materials **13** (2020) 4995.
[2] R. Heras-Mozos *et al.*: Carbohyd. Polym. **283** (2022) 119137.
[3] K. Okeyoshi *et al.*: Sci. Rep. **7** (2017) 5615.
[4] K. Okeyoshi: Polym J. **52** (2020) 1185.
[5] *T. K. L. Nguyen, Y. Tonomura, N. Ito, A. Yamaji, G. Matsuba, M. Hara, Y. Ikemoto and K. Okeyoshi: Langmuir* ***40*** *(2024) 11927.*

Advanced characterization of passivation layers in perovskite solar cells via GIWAXS

Organic–inorganic perovskite solar cells (PSCs) are highly anticipated as next-generation photovoltaic devices owing to their high efficiency and ease of fabrication. These devices can be conveniently fabricated using a solution-based process, which is generally followed by thermal treatment [1]. However, the A-site cations in halide perovskite crystals (ABX_3) include organic cations, making them susceptible to the formation of cation vacancies due to external factors such as heat and light. Additionally, halide perovskite crystals contain halide anions such as iodide (I^-), which is particularly prone to oxidation. Upon photoirradiation, iodide vacancies tend to form, leading to the generation of defects on the perovskite crystal surface during thermal treatment. The formation of these ion vacancies facilitates ion migration, which has been reported to be a critical factor affecting device durability. Theoretical calculations indicate that halide ions are the predominant migrating species, and the presence of methylammonium (MA) vacancies (V'_{MA}) enhances iodide ion (I^-) migration. An increase in the V'_{MA} concentration has been correlated with a higher ionic conductivity for I^-. Furthermore, detached iodide ions migrate within the perovskite crystal and device, leading to electrode corrosion and perovskite degradation, and thereby significantly reducing device longevity.

The introduction of passivation layers has been investigated to mitigate ion vacancies and suppress ion migration. A promising approach involves the formation of low-dimensional perovskite structures to compensate for the defects in halide perovskite crystals. Two-dimensional perovskites incorporating organic halide compounds such as PEAX (X = I, Br, and Cl) have been found to be effective. Additionally, nonreactive organic polymers such as polyetherimide, which do not interact with perovskite crystals, have also demonstrated beneficial effects. Thus, compensating for surface defects in halide perovskite crystals using these methods may effectively enhance the device stability. However, commonly reported passivation materials generally exhibit low conductivity, necessitating the formation of ultrathin films on the order of a few nanometers. Achieving precise control over such thin-film deposition via solution processes remains a significant challenge.

We used gallium hydroxide phthalocyanine (OHGaPc, Fig. 1(a)) as a passivation layer [2]. Unlike conventional insulating passivation materials, OHGaPc is a crystalline p-type organic semiconductor that facilitates charge transport. Additionally, its hydroxyl functional groups allow it to compensate for defects on the outermost surface of the perovskite crystals. Because of these properties, OHGaPc is expected to function as both a charge-transport material and passivation layer. Grazing incidence wide-angle X-ray scattering (GIWAXS) was used to examine the structural characteristics of the OHGaPc films on the perovskite layers. Two-dimensional GIWAXS patterns represented in reciprocal space were obtained at SPring-8 **BL19B2**. The samples were irradiated with X-rays of 12.39 keV (λ = 1 Å) at a fixed incident angle of 0.12°. GIWAXS measurements of the OHGaPc films deposited on the perovskite thin layers are shown in Figs. 2(a,b). The observed diffraction pattern resembles that of OHGaPc on a Si substrate, suggesting a similar molecular packing arrangement. The crystal structure of OHGaPc has been identified as triclinic (P-1), with the following lattice constants: a = 11.52 Å, b = 12.75 Å, c = 8.89 Å, α = 95.87°, β = 96.00°, and γ = 69.45° [3]. The diffraction signal corresponding to the (010) crystal plane derived from these structural parameters aligned with the peak observed in the q_z axis direction. Additionally, the azimuthal angle (90°–γ) and position of the (100) diffraction peak (located at an azimuthal angle of 20°) supported the conclusion that the OHGaPc polycrystalline film primarily adopted a (010) preferred orientation. As depicted in Fig. 2(c), two distinct π–π stacking arrangements were observed. The first configuration exhibited an intermolecular centroid separation of 3.690 Å and offset distance of 1.173 Å, while the second structure had a centroid separation of 3.895 Å and an offset distance of 1.253 Å. Because these π–π stacking distances were less than 4 Å, they indicated the possibility of effective charge transport pathways. However, because of the predominant in-plane alignment of the π–π stacking direction, charge mobility along the stacking axis may have been constrained. Thus, tuning the molecular orientation

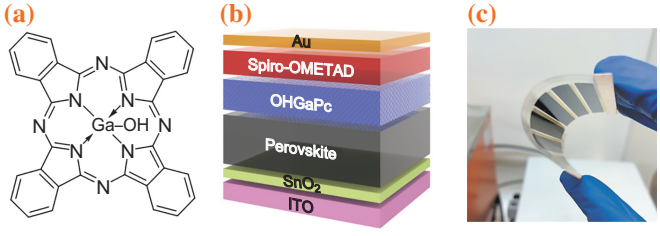

Fig. 1. **(a)** Chemical structure of OHGaPc. **(b)** Structure of perovskite solar cell. **(c)** Flexible perovskite solar cell.

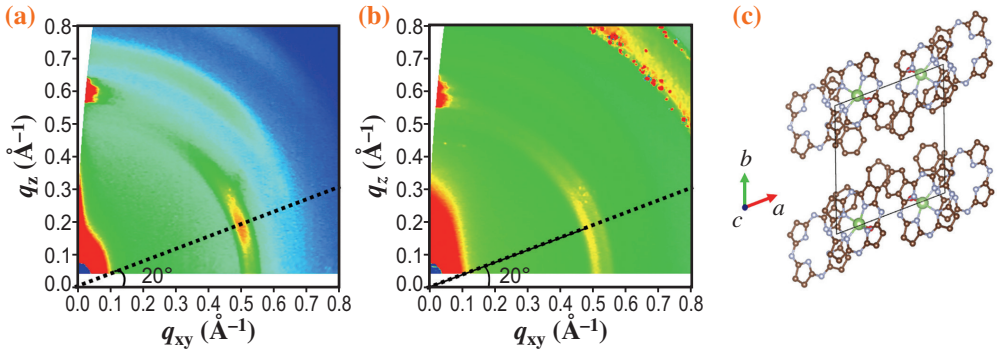

Fig. 2. GIWAXS patterns of OHGaPc thin films on **(a)** PVK and **(b)** Si, along with **(c)** detailed crystal structure of OHGaPc.

could be a key factor in optimizing the charge-transport properties.

To evaluate the impact of OHGaPc on the device durability, PSCs incorporating an OHGaPc interlayer were fabricated. The device structure was [ITO/SnO_2/perovskite/OHGaPc/spiro-OMeTAD/Au] (Fig. 1(b)). The highest power conversion efficiency (PCE) achieved for PSCs with OHGaPc was 21.0%. In contrast, the best PCE obtained for the PSCs without the OHGaPc interlayer was 21.8%. Although the introduction of OHGaPc resulted in a slight reduction in PCE, this decrease was attributed to an increase in the series resistance. Generally, the thickness of the passivation layer is on the order of a few atomic layers. However, in this study, despite the OHGaPc film reaching a thickness of several tens of nanometers, only a minor increase in the resistance was observed, demonstrating its high charge-transport capability. In addition, durability tests of the PSCs incorporating OHGaPc were conducted to evaluate their photostability. Their improved stability was attributed to the suppression of ion migration, which was analyzed using time-of-flight secondary-ion mass spectrometry (TOF-SIMS). The extent of ion migration was assessed by examining the ion distribution along the film stacking direction (Fig. 3). A significant increase in I^- and Br^- ion intensity was observed within the hole transport layer (HTL) in samples without OHGaPc, indicating substantial ion migration during the photostability test. In contrast, no increase in I^- and Br^- intensity was detected within the HTL in samples containing OHGaPc, demonstrating that the OHGaPc interlayer effectively blocked ion migration. These findings suggested that the incorporation of OHGaPc suppressed ion migration and significantly enhanced the photostability of the device.

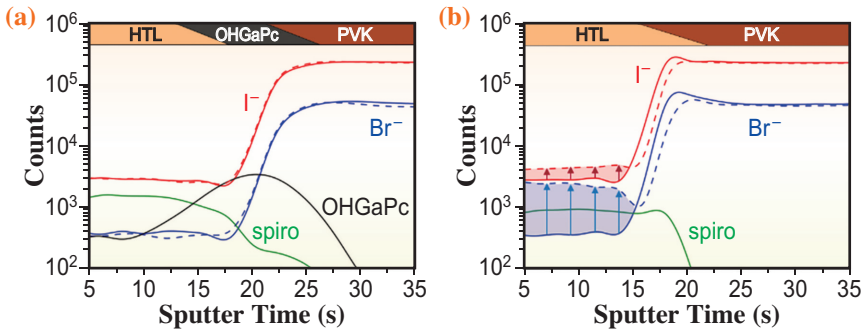

Fig. 3. Depth profiles of ions in perovskite solar cells measured using TOF-SIMS: **(a)** with and **(b)** without OHGaPc.

Naoyuki Shibayama

Toin University of Yokohama

Email: shibayama@toin.ac.jp

References

[1] T. Miyasaka *et al.*: J. Am. Chem. Soc. **131** (2009) 6050.
[2] *T. Ohsawa, N. Shibayama, N. Nakamura, S. Tamura, A. Hayakawa, Y. Murayama, K. Makisumi, M. Kitahara, M. Takayama, T. Matsui, A. Okuda, Y. Nakamura, M. Ikegami, T. Miyasaka: J. Mater. Chem. A* ***12*** *(2024) 22510.*
[3] K. Daimon *et al.*: J. Imaging Sci. Technol. **40** (1996) 249.

Valence fluctuation in ultrasmall CeO_2 nanoparticles

The size-dependent properties of nanoparticles have been intensively studied to better understand and utilize the unique behaviors of materials. Recently, ultra-small particles (i.e., approximately < 5 nm) have attracted attention because of their distinct characteristics compared to larger particles. Nanoparticles usually have distorted lattice structures depending on their particle size, which significantly affect their material properties [1,2]. These distortions vary depending on the material systems [3]. For example, the distortion of metals and metal oxides usually shows different tendencies for nanosizing; that is, lattice shrinkage occurs for metals and lattice expansion occurs for metal oxides [3]. The chemical state of oxygen plays a key role in the formation of nanoparticles.

While ultrasmall particles have been studied primarily for metals, investigations into ultrasmall metal oxides have been limited due to challenges in synthesis. Recently, ultrasmall metal oxides ranging from 1.5 nm have been successfully synthesized using a continuous-flow hydrothermal method with *in situ* surface organic modification [4], which opened a new research field of ultrasmall metal oxides [4,5]. This study presents the valence fluctuation phenomena observed in ultrasmall CeO_2 nanoparticles. Previously, for CeO_2 nanoparticles, research focused on the formation of oxygen vacancies, as redox properties are key for their application as solid catalysts. However, the intrinsic size effects without oxygen vacancy-related phenomena are not sufficiently understood.

The distortion and corresponding chemical states of ultrasmall CeO_2 were studied using high-energy-resolution fluorescence-detected X-ray absorption near-edge structure (HERFD-XANES) at SPring-8 **BL39XU**, X-ray absorption spectroscopy (XAS) and resonant inelastic X-ray scattering (RIXS) at SPring-8 **BL27SU**. Figure 1(a) shows the Ce L_3-edge HERFD-XANES spectra of CeO_2 nanoparticles. Peak A, which reflects the transition of Ce electrons from the 2*p* orbital to the 4*f* orbital, appears at 5721.9 eV for all the synthesized CeO_2 nanoparticles, suggesting that the valence of Ce in all the nanoparticles is predominantly +4. The splitting of peaks B_1, B_2, C_1, and C_2 based on the dipole transition from Ce $2p_{3/2}$ to $5d_{5/2}$ was affected by the crystal field in the CeO_2 fluorite structure, where the Ce atoms were surrounded by eight O atoms (O_h point group). Peaks based on crystal-field splitting were observed even at a grain size of 2.0 nm, indicating that the fluorite-type structure was maintained, although the peak splitting became less distinct with decreasing grain size.

Figure 1(b) shows the O *K*-edge XAS spectra of the ultrasmall CeO_2 (BL27SU). The three peaks between 530 and 545 eV were assigned to the interactions of O 2*p* with Ce 4*f*, Ce 5*d*-e_g, and Ce 5*d*-t_{2g}. With decreasing particle size, the peaks of O 2*p*–Ce 5*d*-e_g and O 2*p*–Ce 5*d*-t_{2g} were broadened, indicating disordering of the O atom positions. The CeO_2 nanoparticles contain few O vacancies; in turn, O displacement occurs within the framework of the fluorite structure. Furthermore,

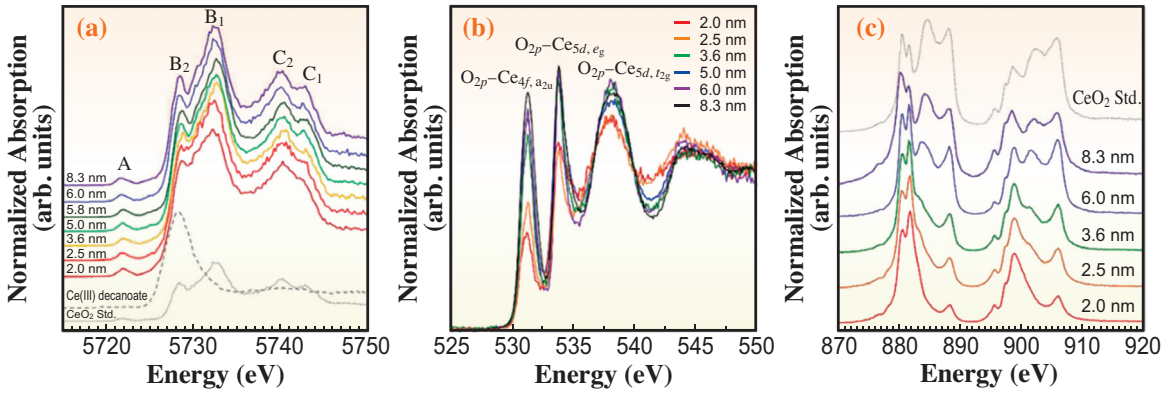

Fig. 1. X-ray absorption spectra of ultrasmall CeO_2 with different particle sizes. **(a)** Ce L_3-edge HERFD-XANES spectra. Ce(III) decanoate and purchased CeO_2 (Aldrich) were used as references. **(b)** O *K*-edge, and **(c)** Ce $M_{5,4}$-XAS profiles. [4]

the intensity of the O 2*p*–Ce 4*f* peak diminishes with decreasing particle size, particularly for particles smaller than 3 nm. This change likely results from reduced O 2*p*–Ce 4*f* hybridization. As shown in Fig. 1(c), the $M_{5,4}$-edge XAS spectra differs significantly from the Ce L_3-edge spectra (Fig. 1(a)) with respect to the appearance of Ce^{3+}, and the changes in the $M_{5,4}$-edge XAS spectra correspond to changes in the O states observed at approximately <3 nm.

Figures 2(a) and 2(b) show the RIXS map data for the Ce $M_{5,4}$-edges of CeO_2 with different particle sizes. The emission line starting at 874 eV is attributed to charge–transfer transitions with the hybridization of the valence electronic states of the 4*f* electrons and O ions. In Fig. 2(c), the Ce M_5 pre-edge (878.4 eV) was set as the excitation energy to investigate the grain-size dependence of the Ce $M_{5,4}$-edge RIXS spectrum. The peak intensity at loss energies of –7 to –4 eV decreases as the particle size decreases. This energy loss corresponds to a charge–transfer transition, which weakens the interaction between Ce 4*f* and O 2*p* as the particle size decreases. According to the L_3- and $M_{5,4}$-edge XAS spectra, the 4*f* electrons were localized in the <3 nm particles, irrespective of O vacancies, leading to the strong appearance of Ce^{3+} in the $M_{5,4}$-edge XAS spectra, but not in the L_3-edge and XAS spectra. Note that the existence of Ce^{3+} in the ultrasmall particles was caused by distortion rather than oxygen release. The local structure of the CeO_8 hexahedra became more disordered with the weakening of the O–Ce interaction and the localization of the 4*f* electrons. The ultrasmall CeO_2 nanoparticles here exhibit a distinctive electronic state with valence fluctuations due to their large lattice expansion/distortion, maintaining high crystallinity and oxidation state.

Ultrasmall metal oxides with unusual electronic states have great potential for exploiting new properties in the future, where the synthesis method is applicable to various metal oxides, including mixed oxides [4,5].

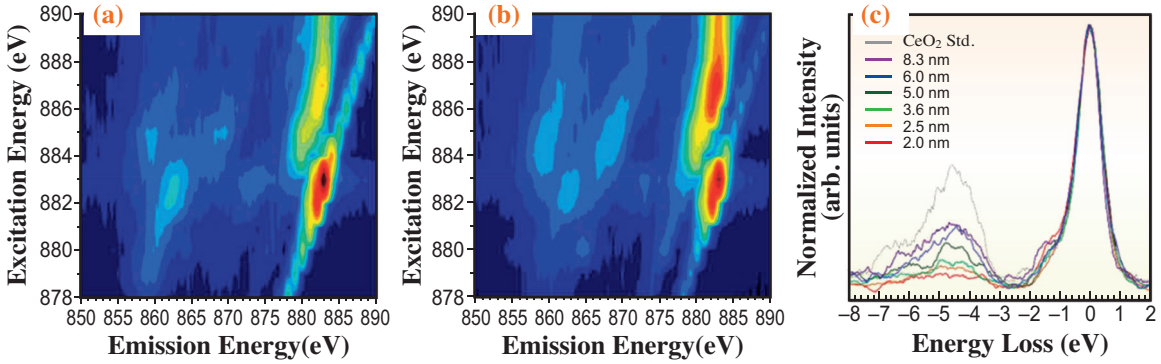

Fig. 2. Ce M_5-edge RIXS maps of CeO_2 nanoparticles with sizes of **(a)** 2.0 and **(b)** 6.0 nm. The fluorescence at 855–875 eV was attributed to $5p \rightarrow 3d$ emission and the Coster–Kronig transition ($3d_{5/2} \rightarrow 3d_{3/2}$ emission). **(c)** Ce M_5-edge RIXS spectra of CeO_2 nanoparticles of different sizes. The incident X-ray energy was set to 878.4 eV. [4]

Akira Yoko[a,b,*], Kakeru Ninomiya[a] and Maiko Nishibori[a,c]

[a] International Center for Synchrotron Radiation Innovation Smart, Tohoku University
[b] WPI-Advanced Institute for Materials Research, Tohoku University
[c] Institute of Multidisciplinary Research for Advanced Materials, Tohoku University

*Email: akira.yoko.c7@tohoku.ac.jp

References

[1] X. Hao *et al.*: Small **14** (2018) 1802915.
[2] X. Hao *et al.*: Acta Mater. **203** (2021) 116473.
[3] P. M. Diehm *et al.*: ChemPhysChem **13** (2012) 2443.
[4] *A. Yoko, Y. Omura, K. Ninomiya, M. Nishibori, T. Fujita, H. Kasai, E. Nishibori, N. Chiba, G. Seong, T. Tomai, T. Adschiri: J. Am. Chem. Soc.* ***146*** *(2024) 16324.*
[5] C. Han *et al.*: Chem. Eng. J. **496** (2024) 154022.

A systematic understanding of adsorption reaction on clay minerals focusing on radium as a key element

Clay minerals, primarily phyllosilicate minerals with layered structures, adsorb numerous cations and are widely distributed on the Earth's surface, thereby influencing the environmental behavior of various elements. For example, radioactive cesium (Cs) released during the Fukushima Daiichi Nuclear Power Plant accident is fixed on the soil surface owing to its strong adsorption onto clay minerals [1,2]. Similarly, rare earth elements (REEs) form ion adsorption-type deposits in weathered granite and adsorb onto clay minerals [3]. However, their mobilities differ significantly: Cs^+ is difficult to extract, while REE^{3+} has a high extraction rate. This difference is attributed to their adsorption structures at the atomic scale. Cs^+ and REE^{3+} are adsorbed onto clay minerals with and without dehydration, forming inner-sphere and outer-sphere complexes, respectively (Fig. 1). Thus, clarifying the factors controlling inner- and outer-sphere complexes is essential for understanding and predicting the environmental behavior of various cations.

To elucidate these factors, we systematically investigated the adsorption structures of various cations, including radium (Ra^{2+}), at the atomic scale using extended X-ray absorption fine structure (EXAFS) [4]. Ra is a decay product of uranium and thorium and can cause environmental pollution in uranium mines. Additionally, ^{226}Ra has recently gained attention as a source for producing actinium (Ac)–225, which is used for α-particle cancer treatment. Therefore, understanding the environmental behavior of Ra is critical in geochemistry. However, Ra lacks stable isotopes, making atomic-scale experiments challenging. To address this, our group developed a novel technique, including a radiation-safe sample holder, enabling the acquisition of Ra-EXAFS data for the first time at SPring-8 **BL22XU** [5]. This method was used to elucidate the adsorption structure of Ra^{2+} on clay minerals. Additionally, EXAFS measurements at SPring-8 **BL01B1** were conducted to examine the adsorption structures of other elements, such as barium (Ba), strontium (Sr), Cs, and rubidium (Rb). For each element, both clay mineral sample with adsorbing ions and hydration solution sample were analyzed.

Figure 2 presents a portion of the EXAFS results. The EXAFS spectrum of a cation adsorbed onto a clay mineral was compared with that of a hydrated cation. When the adsorbed cation forms an outer-sphere complex, its EXAFS spectrum closely resembles that of the hydrated cation, displaying only the first shell corresponding to oxygen atoms in the hydration water molecules. Conversely, if the cation forms an inner-sphere complex, its EXAFS spectrum exhibits a second shell derived from the Si and/or Al atoms in the layered structure of the clay mineral. Accordingly, Fig. 2 reveals that Ra^{2+} adsorbed onto clay minerals formed inner-sphere complexes, while Ba^{2+} and Sr^{2+} primarily formed outer-spheres complexes.

The EXAFS results indicated that Ra^{2+}, Cs^+, and Rb^+ formed inner-sphere complexes, while Ba^{2+} and Sr^{2+} formed outer-sphere complexes. This observation can be attributed to differences in ionic radii, highlighting the significance of size compatibility between the cation and the cavity of the six-membered ring within the layered structure of clay minerals—a phenomenon known as the size-matching effect. In this study, the size-matching effect was determined by the ionic radius and valence of the adsorbed cation, which were evaluated through *ab initio* calculations.

However, the results of systematic EXAFS measurements and *ab initio* calculations revealed that the size-matching effect alone could not fully explain the formation of inner-and outer-sphere complexes.

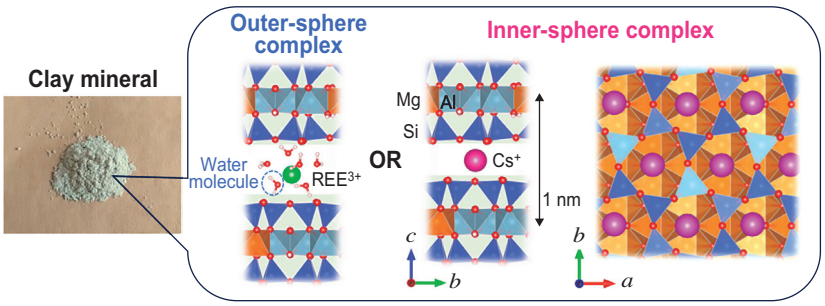

Fig. 1. Adsorption structures on clay minerals at the atomic scale. A cation forming an inner-sphere complex resides within a six-membered ring in the layered structure of the clay mineral.

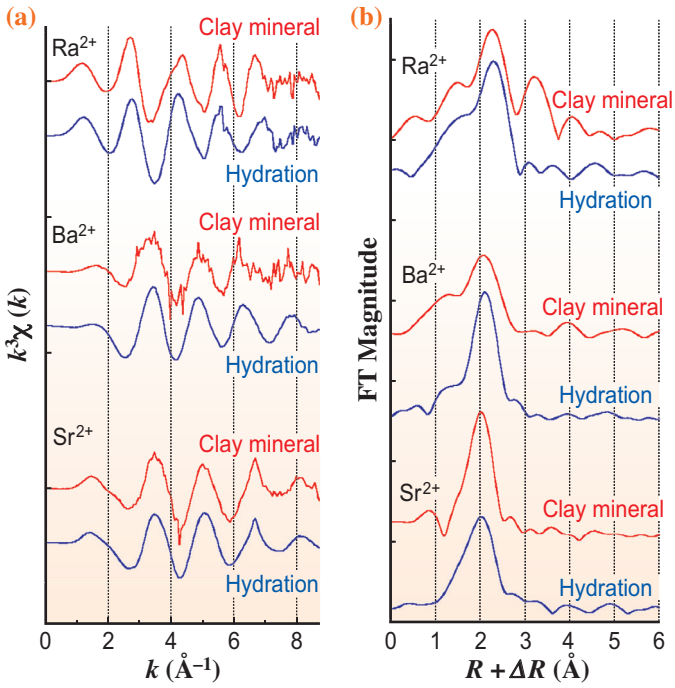

Fig. 2. EXAFS spectra of Ra, Ba, and Sr (**a**) in *k*-space and (**b**) in *R*-space. The intensities of Sr-EXAFS are plotted after division by 3.

These findings suggest that the hydration energy of the adsorbed cation also plays a crucial role, as the formation of inner-sphere complexes requires a dehydration reaction when hydrated cations in solution are adsorbed onto clay minerals. The hydration energy can be evaluated using hydration enthalpy. Consequently, this study concluded that the combined influence of the ionic radius and hydration enthalpy of cation governs the formation of inner- and outer-sphere complexes (Fig. 3).

This systematic understanding of adsorption reaction on clay minerals provides valuable insights for predicting the environmental behavior of various elements. To validate this framework, soil samples collected from the Ningyo-toge uranium mine were analyzed to investigate the mobility of several elements, including Ra. Chemical analyses, such as quantification of chemical composition and sequential extraction, indicated that Ra^{2+} is adsorbed onto clay minerals and immobilized within a weathered granite layer. These findings are consistent with the EXAFS results and the systematic model presented in Fig. 3. This study confirms that this approach effectively explains and predicts the environmental behaviors of various cations.

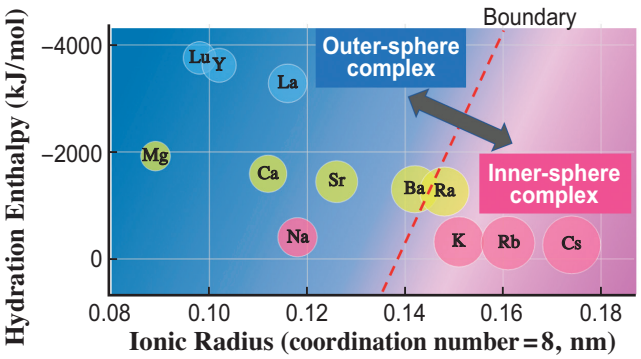

Fig. 3. Factors controlling the formation of outer- and inner-sphere complexes.

Akiko Yamaguchi[a,b,*], Masahiko Okumura[a] and Yoshio Takahashi[b]

[a] Center for Computational Science and e-Systems, Japan Atomic Energy Agency
[b] Department of Earth and Planetary Science, The University of Tokyo

*Email: yamaguchi.akiko@jaea.go.jp

References

[1] Y. Takahashi *et al.*: Treatise on Geochemistry (Third edition) **6** (2025) 105.
[2] A. Yamaguchi *et al.*: J. Radioanal. Nucl. Chem. **317** (2018) 545.
[3] A. Yamaguchi *et al.*: Geochem. J. **52** (2018) 415.
[4] *A. Yamaguchi, Y. Kurihara, K. Nagata, K. Tanaka, S. Higaki, T. Kobayashi, H. Tanida, Y. Ohara, K. Yokoyama, T. Yaita, T. Yoshimura, M. Okumura, Y. Takahashi: J. Colloid Interface Sci.* ***661*** *(2024) 317.*
[5] A. Yamaguchi *et al.*: iScience **25** (2022) 104763.

Visualization of the accurate distribution of trace uranium in environmental sample using superconducting technology

Uranium (U) is widely utilized as a fuel for nuclear power generation across the globe. Many countries are planning geological disposal of spent nuclear fuels. The migration behavior of U in subsurface environment is critical for nuclear waste disposal, and a deeper understanding of the interactions between minerals in these subsurface environments and U is essential for assessing the safety of natural barriers involved in its geological disposal [1]. Micro-X-ray fluorescence-X-ray absorption near edge structure (μ-XRF-XANES) analysis is a powerful tool for determining U distribution and chemical species. However, the energy resolution of commonly used semiconductor detectors is insufficient owing to the presence of various elements in environmental samples. Fluorescence X-rays from trace amounts of U can be interfered with by the fluorescence X-rays of other elements (such as Rubidium (Rb)) in the Earth's crust, which complicates the accurate determination of U distribution and chemical species [2].

In this study [3], we utilized a superconducting transition-edge sensor (TES) [4], which offers both high energy resolution and high detection efficiency. The micro-XRF-XANES experiments were conducted at SPring-8 **BL37XU**. The experimental setup is illustrated in Figs. 1(a,b). The XRF spectra of the NIST610 sample were obtained using both a conventional silicon drift detector (SDD) and TES at an excitation energy of 17.2 keV to compare the energy resolutions of the conventional semiconductor detector and TES in the hard X-ray energy region (Fig. 2). Figure 2(a) shows the XRF spectra measured using SDD and TES. The XRF spectrum measured by TES revealed several finer peaks compared to those measured by SDD, indicating that high-energy resolution was maintained from the low- to high-energy regions. Figure 2(b) shows the XRF spectra in the energy range that includes the Rb $K\alpha$ and U $L\alpha_1$ lines, measured using both SDD and TES. In the XRF spectrum obtained with SDD, the Rb $K\alpha$ line at 13.376 keV and the U $L\alpha_1$ line at 13.615 keV were not completely separated, and the XRF peak of the U $L\alpha_1$ line was observed as a structure near the shoulder of the Rb peak in Fig. 2(b). Thus, when using a conventional semiconductor detector, the X-ray fluorescence peaks of Rb and U overlap. By contrast, the XRF spectrum of NIST 610 measured by TES showed that the Rb $K\alpha$ line at 13.376 keV was split into the Rb $K\alpha_1$ line at 13.395 eV and the Rb $K\alpha_2$ line at 13.336 eV. The XRF peak of the U $L\alpha_1$ line at 13.615 keV was fully separated from the Rb $K\alpha_1$ line at 13.395 keV, demonstrating that TES enabled ultrahigh energy resolution analysis.

For the environmental sample, we used biotite collected from the Ningyo Toge U mine in Japan. Figures 3(a,b) show the biotite thin-section sample and a magnified SEM image of the biotite sample, respectively. Mapping analysis was performed on a 75 μm long and 400 μm wide area from the basal of the thin biotite section, indicated by the red square in Fig. 3(b). Figures 3(c,d) compare the mapping analysis results of the biotite sample obtained using SDD and TES. The conventional SDD could only detect the fluorescence X-ray of the Rb $K\alpha$ line (Fig. 3(e)), which is abundant in biotite, and could not accurately detect the signal of trace amounts of U (Fig. 3(c)). Furthermore, TES mapping results revealed that the distribution of Rb and U were different (Fig. 3(d)), as the Rb $K\alpha$ and U $L\alpha_1$ peaks were clearly separated in the XRF spectra obtained using high-energy resolution TES, as shown in Fig. 3(f). These results demonstrate that TES allows for accurate determination of the distribution of trace amounts of U, which is difficult to analyze using conventional semiconductor detectors.

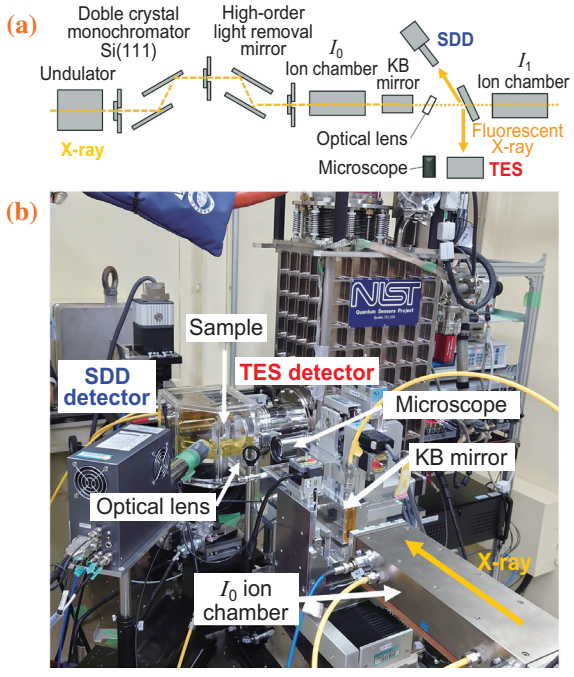

Fig.1. Overview of the experimental setup. **(a)** Schematics illustrate the experimental setup at BL37XU. **(b)** The picture of the setup.

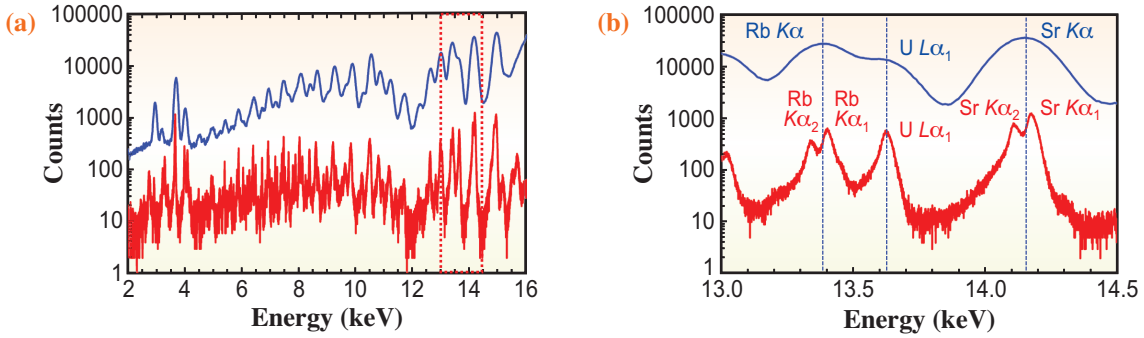

Fig. 2. Comparing energy resolution of SDD and TES in hard X-ray energy region. **(a)** X-ray fluorescence spectra of NIST 610 measured by SDD (blue line) and TES (red line) at an excitation energy of 17.2 keV. **(b)** XRF spectra are indicated by the red dotted line in (a).

Additionally, simultaneous μ-XANES measurements successfully identified the chemical state of U in the biotite, revealing that some of the U was reduced to U(IV). This indicates that U was partially reduced and fixed in biotite, thereby lowering its mobility.

Although this experiment focused on U and Rb in environmental samples, TES has been shown to provide high energy resolution up to the high-energy region of 17 keV. Consequently, TES can be applied to the analysis of other elements with fluorescent X-rays in this energy range up to 17 keV, and its application to various environmental samples is expected in the future.

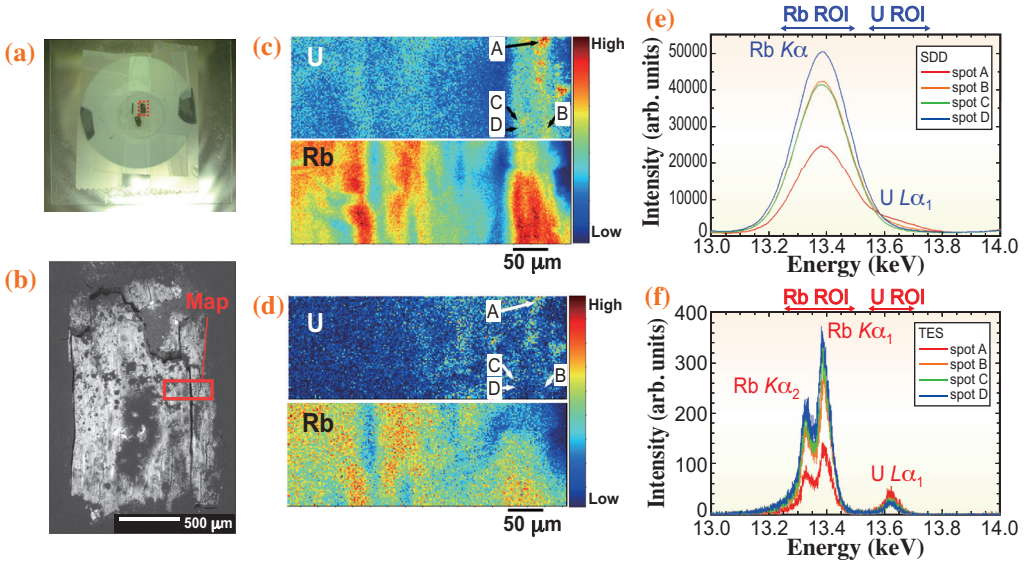

Fig. 3. Micro-X-ray fluorescence imaging of biotite thin sample. **(a)** Optical image of the thin-sectioned sample. **(b)** The magnified SEM image of the red dotted line in (a). The micro-XRF mapping area was shown in a red solid line. Micro-XRF U and Rb map images by **(c)** SDD and **(d)** TES. Micro-XRF spectra of the thin biotite sample measured by **(e)** SDD and **(f)** TES. The region of interest (ROI) of Rb *Kα* and U *Lα*$_1$ is shown in the upper part of the figures.

Takumi Yomogida[a,b,*], Shinya Yamada[c] and Yoshio Takahashi[b]

[a] Nuclear Science and Engineering Center, Japan Atomic Energy Agency
[b] Department of Earth and Planetary Science, The University of Tokyo
[c] Department of Physics, Rikkyo University

*Email: yomogida.takumi@jaea.go.jp

References

[1] Y. Takahashi *et al.*: Treatise on Geochemistry (Third Edition) **6** (2025) 105.
[2] Y. Yamamoto *et al.*: Appl. Geochem. **23** (2008) 2452.
[3] *T. Yomogida, T. Hashimoto, T. Okumura, S. Yamada, H. Tatsuno, H. Noda, R. Hayakawa, S. Okada, S. Takatori, T. Isobe, T. Hiraki, T. Sato, Y. Toyama, Y. Ichinohe, O. Sekizawa, K. Nitta, Y. Kurihara, S. Fukushima, T. Uruga, Y. Kitatsuji, Y. Takahashi: Analyst. **149** (2024) 2932.*
[4] S. Yamada *et al.*: Rev. Sci. Instrum. **92** (2021) 013103.

Measuring the effect of water on the seismic wave and its application to the lithosphere and asthenosphere boundary

The weakened asthenosphere below rigid lithosphere is a critical research target for understanding the mechanisms of plate tectonics on Earth. Traditionally, the asthenosphere was defined as a region softened primarily due to thermal activation. However, with advancements in seismological techniques, a more complex understanding has emerged [1]. New mechanisms are required to explain the sharp seismic anomalies observed at the lithosphere-asthenosphere boundary (LAB), which cannot be entirely accounted for by thermal processes alone.

Several mechanisms have been proposed to explain these seismic observations [2,3]. One prominent hypothesis involves the effect of water on the rheology of upper mantle minerals, suggesting that variations in water content between the lithosphere and asthenosphere might play a significant role. This hypothesis is particularly compelling in regions where seismic anomalies occur at relatively low-temperature boundary areas. To explore this possibility, our research focuses on studying the influence of water on seismic wave properties within the mantle [4].

Olivine, the dominant mineral in the upper mantle, was selected as the starting material for our study due to its significance in controlling mantle rheology and seismic properties. To eliminate potential interference from oxygen fugacity, we used iron-free olivine in our experiments. The olivine samples with varying water contents were synthesized at the Institute for Planetary Materials, ensuring precise control over their composition and hydration levels.

The core of our experimental work involved measuring anelasticity using a developed *in situ* short-period cyclic loading system integrated into a multianvil press [5]. This setup was located at SPring-8 **BL04B1** beamline, enabling measurements under simulated upper mantle conditions. The experiments were conducted at pressures of approximately 3 GPa and temperatures ranging from 1173 to 1373 K, conditions representative of the LAB. These parameters allowed us to closely replicate the physical environment of the upper mantle and investigate how water influences seismic wave behavior.

Our results demonstrated a clear relationship between water content and seismic properties.

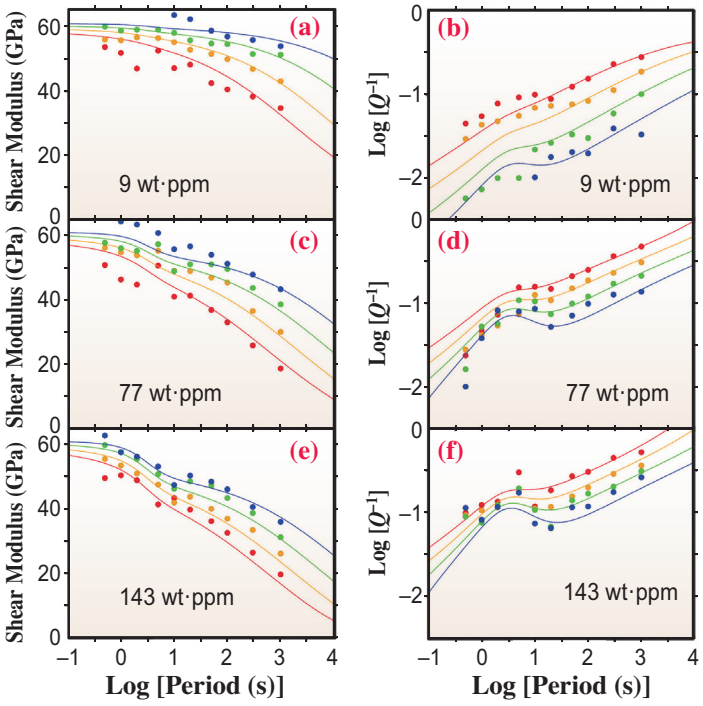

Fig. 1. The anelastic experimental results. The **(a)**, **(c)**, and **(e)** are the shear modulus and **(b)**, **(d)**, and **(f)** are the attenuation of samples at various water contents at different temperature.

As water content increased, the Young's modulus of the olivine samples decreased, while attenuation—a measure of energy dissipation in seismic waves—increased. Notably, we observed attenuation peaks directly associated with water content, a phenomenon identified for the first time in our study (Fig. 1). These peaks indicate that water significantly enhances anelastic behavior, providing a potential explanation for the seismic anomalies observed at the LAB.

To bridge the gap between our laboratory findings and Earth's seismic observations, we utilized the generalized Burger's model [6]. This physical model allowed us to extrapolate our experimental results to geophysical scales and predict the effect of anelasticity on seismic wave propagation in the upper mantle (Fig. 2). Our analysis revealed that as water content increases, the strength of anelasticity also increases. This finding aligns with the hypothesis that water plays a crucial role in modifying the seismic properties of the mantle.

Further, by considering plausible grain sizes in the upper mantle, we extrapolated our results to seismic observations in regions such as the western North Pacific. The comparison revealed that differences in water content between the lithosphere and asthenosphere could account for the observed seismic anomalies in low-temperature boundary areas (Fig. 3). These results support the notion that water content variations at the LAB are a key factor in understanding the transition between the lithosphere and asthenosphere.

This study provides significant insights into the role of water in influencing seismic properties and the mechanical behavior of the upper mantle. By demonstrating the impact of water on anelasticity and seismic wave attenuation, we offer a plausible explanation for the sharp seismic contrasts at the LAB. Our findings also highlight the importance of integrating experimental, theoretical, and observational approaches to advance our understanding of mantle dynamics.

Future research could build on our results by exploring additional factors that may influence seismic properties at the LAB, such as the presence of iron or variations in mineral composition and oxygen fugacity.

In conclusion, this research underscores the critical role of water in shaping the seismic and rheological properties of the upper mantle. By linking experimental observations with geophysical models, we provide a robust framework for interpreting seismic anomalies at the lithosphere-asthenosphere boundary.

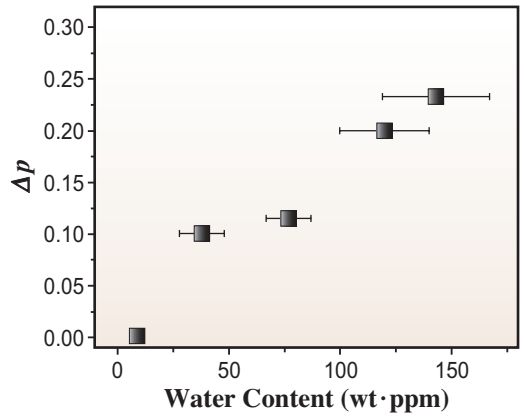

Fig. 2. The effect of water content on the strength of anelasticity.

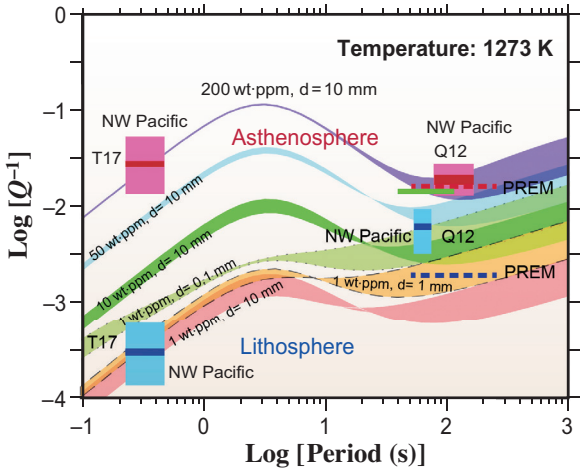

Fig. 3. The effect of water on seismic wave attenuation at different periods at 1273 K.

Chao Liu[a,*] and Takashi Yoshino[b]

[a] State Key Laboratory of Ore Deposit Geochemistry, Chinese Academy of Science, China
[b] Institute for Planetary Materials, Okayama University

*Email: Liuchao@mail.gyig.ac.cn

References

[1] C. A. Rychert *et al.*: Nature **436** (2005) 542.
[2] S. Karato: Earth Planet. Sci. Lett. **321-322** (2012) 95.
[3] C. A. Rychert *et al.*: J. Geophys. Res.: Solid Earth **125** (2020) e2018JB016463.
[4] *C. Liu, T. Yoshino, D. Yamazaki, N. Tsujino, H. Gomi, M. Sakurai, Y. Zhang, R. Wang, L. Guan, K. Lau, Y. Tange and Y. Higo: Proc. Natl. Acad. Sci. USA **120** (2023) e2221770120.*
[5] T. Yoshino *et al.*: Rev. Sci. Instrum. **87** (2016) 105106.
[6] U. Faul and I. Jackson: Annu. Rev. Earth Planet. Sci. **43** (2015) 541.

Transient creep in olivine controls the post-seismic deformation

The flow of the crust (thickness of ~50 km) and uppermost mantle (depth: 50–150 km) is a fundamental process that controls post-seismic deformation (Fig. 1). Geodetic observations have revealed that the deformation of the crust and uppermost mantle after a great earthquake sometimes continues for decades. Viscosities of the uppermost mantle estimated from early post-seismic deformation are often significantly low (10^{17}–10^{18} Pa·s) and continuously increase to a typical value of ~10^{20} Pa·s. Such time-dependent and short-term (on the geological timescale) phenomena needs to be considered from the viewpoint of the transient creep of olivine, which is the most abundant mineral in the lower crust and upper mantle [1].

The deformation of rocks can be divided into three regimes: i) elastic, ii) transient, and iii) steady-state regimes. The elasticity and steady-state creep strength are independent of time. However, the strength changes with time during the transient creep. The time-dependent behavior of the transient creep can be described by the Burgers model, which can be expressed as the follows:

$$\dot{\varepsilon} = \dot{\varepsilon}_{ss}\left[1 - \exp\left(-\frac{t}{\tau}\right) + \frac{\eta_{ss}}{\eta_t}\exp\left(-\frac{t}{\tau}\right)\right] \qquad (1)$$

where $\dot{\varepsilon}$ is strain rate, $\dot{\varepsilon}_{ss}$ is the steady-state strain rate, t is time, τ is the transient relaxation time, and η_{ss}/η_t is the ratio of the steady-state to the transient viscosity [2]. The Burgers model has been adopted in numerical studies to evaluate the three-dimensional response of the lower crust and uppermost mantle following a large earthquake [3]. However, such studies assumed hypothetical values for the constants (τ and η_{ss}/η_t) in Eq. (1). This is because the values of the constants in Eq. (1) have not been determined for olivine at upper mantle pressures and temperatures because of the challenges in obtaining laboratory measurements. The transient creep of olivine was observable within a few minutes of a deformation experiment. Observations of such "short-term" characteristics of the transient creep inevitably require high time-resolution stress/strain measurements for experiments. For the first time, my colleagues and I performed stress-relaxation (i.e., deformation just after stress release) experiments on olivine using advanced high-flux synchrotron X-ray technology under upper mantle pressures and temperatures. We successfully constrained the time dependence of transient creep of olivine [4].

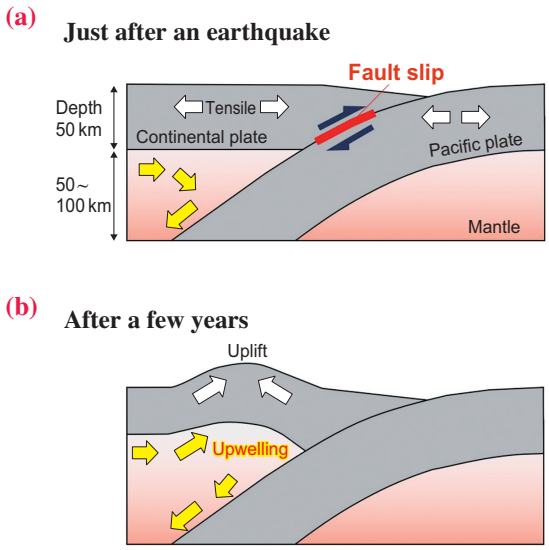

Fig. 1. Post-seismic deformation. **(a)** Cross-sectional view of a subduction zone just after an earthquake on the plate boundary. Tensile stress is coseismically induced in the plates. **(b)** Few years after the earthquake. Post-seismic displacements of land are significant due to the upwelling flow of the uppermost mantle induced by the earthquake [5].

We conducted stress-relaxation experiments on mantle olivine samples combined with synchrotron *in situ* X-ray observations at pressures of 1.7–3.6 GPa and temperatures up to 1020 K using a "mobile" multianvil apparatus at SPring-8 **BL05XU**. This "mobile" multianvil apparatus (~5 ton in total weight), specifically designed for high-pressure experiments at this beamline, was transported into the experimental hutch just before each beamtime (Fig. 2) and was returned to a repository area (SPring-8 BL04B1) after the end of the beamtime. The temperature and pressure ranges were set equivalent to those of the shallow upper mantle. The olivine sample was first semihydrostatically pressurized to the desired pressure at room temperature. Shortening of the sample started when the temperature rapidly increased (up to 1020 K) at high pressures. The combination of a high-flux pink beam (energy 100 keV) from an undulator source and a cadmium telluride (CdTe) imaging detector (WidePix 5×5) with 0.4 s of exposure time enabled us to acquire two-dimensional radial diffraction patterns (for the determination of

pressure and stress) and radiographic images (for strain measurements). The exposure time for the two-dimensional radial diffraction pattern (0.4 s) was two orders of magnitude shorter than that for BL04B1.

A series of stress-relaxation runs showed that the transient creep of olivine followed Eq. (1) with the transient relaxation time (τ) ranging from 50 to 1880 s. To confirm the occurrence of the transient creep of olivine, the temperature was rapidly increased from 570 to 840 K to observe the responses of pressure, stress, and strain to the increase in temperature (~100 K·s^{-1}: Fig. 3). An instantaneous pressure increase (ΔP ~ 0.5 GPa) caused by the thermo-elastic expansion of olivine crystals was synchronized with the temperature increase. Figure 3 shows a 25-second delay of softening –indicated by a decrease in stress and an increase in strain– following the temperature increase. This observation supports the conclusion that a value of τ ~ 50 s is the most accurate for describing the transient creep of olivine, rather than the significantly higher τ observed in other runs. Based on the obtained values of the parameters in Eq. (1), the time-dependent increase in viscosity of the shallow upper mantle reported in late post-seismic deformation (10^{18}–10^{20} Pa·s) is explained by the Burgers rheology for olivine. Time-dependent crustal deformation, which continues for decades after a great earthquake (Fig. 1), is explained by the transient creep of olivine.

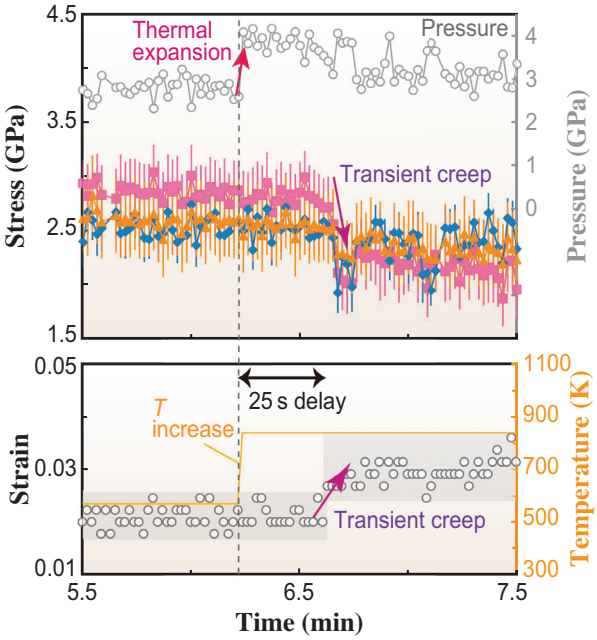

Fig. 3. Differential stress (color symbols), pressure and strain (gray circles), and temperature (orange line) plotted against time in a stress-relaxation run for an olivine sample. A sudden increase in temperature (from 570 to 870 K) was followed by a synchronized pressure jump (due to thermal expansion of olivine). The decrease in stress and the increase in strain (due to transient creep of olivine) delayed for 25 s. Note that stress values were obtained from the diffraction peaks of olivine (blue: 021; pink: 101; orange: 130).

Fig. 2. Installation of the "mobile" multianvil apparatus to the experimental hutch of beamline BL05XU just before a high-pressure experiment.

Tomohiro Ohuchi

Geodynamics Research Center, Ehime University

Email: ohuchi.tomohiro.mc@ehime-u.ac.jp

References

[1] R. Sabadini *et al.*: Geophys. Res. Lett. **12** (1985) 361.
[2] A. M. Freed *et al.*: J. Geophys. Res. Solid Earth **117** (2012) B01409.
[3] F. F. Pollitz: Earth Planet. Sci. Lett. **215** (2003) 89.
[4] *T. Ohuchi, Y. Higo, N. Tsujino, Y. Seto, S. Kakizawa, Y. Tange, Y. Miyagawa, Y. Kono, H. Yumoto, T. Koyama, H. Yamazaki, Y. Senba, H. Ohashi, I. Inoue, Y. Hayashi, M. Yabashi and T. Irifune: Geophys. Res. Lett.* ***51*** *(2024) e2024GL108356.*
[5] T. Sun *et al.*: Nature **514** (2014) 84.

Does water escape from subducted slabs at the core-mantle boundary?

Hydrated SiO_2 phase is the main carrier of water in the subducting slabs of the Earth's lower mantle. Recent experiments performed along cold-to-normal lower-mantle geotherms have demonstrated that SiO_2 can hold up to ~3.5 wt% H_2O [1,2]. Regardless of the high water holding capacity of dense SiO_2, it has been speculated that subducted slabs will dehydrate at high temperatures in the core-mantle boundary (CMB) region, and the released water will give rise to chemical heterogeneities, as indicated by seismological observations. Water can induce melting, melt migration, and hydration of the lowermost mantle materials, creating large low-shear-velocity provinces. Furthermore, the reaction of water with the core metal can form superoxidized $FeOOH_x$ ($x < 1$), which accounts for ultralow velocity zones. Nevertheless, the solubility and partitioning of water into Al-bearing hydrous SiO_2 within subducted former crustal rocks, especially mid-oceanic ridge basalt (MORB), have not been investigated under the high pressure and temperature (P–T) conditions in the CMB region; therefore, the dehydration of subducted slabs and its associated effects remain unverified.

We conducted 19 separate melting experiments on hydrous MORB up to the lowermost mantle pressure range at 4100 K in a laser-heated diamond-anvil cell by collecting X-ray diffraction (XRD) patterns at SPring-8 **BL10XU** [3]. Melting textures and chemical compositions, including the H_2O content in the melt and coexisting solids, were examined in the recovered samples. They exhibited a concentric texture: a round pocket of quenched partial melt at the center surrounded by a SiO_2 phase, $CaSiO_3$ perovskite (davemaoite), SiO_2–AlOOH solid solution (ss.) and bridgmanite at 25–59 GPa (Fig. 1(a)). At 100 GPa and above, SiO_2 was still present next to the melt pool, and the bridgmanite/post-perovskite appeared closer to the melt than it did at lower pressures (Fig. 1(b)). The XRD patterns of these samples indicated that $CaCl_2$-type SiO_2 appeared down to at least 25 GPa at 2900 K. This observation is consistent with earlier findings that $CaCl_2$-type SiO_2 stabilizes over stishovite in the presence of Al_2O_3 and H_2O [2], whereas it forms above 65–75 GPa at 1500–2000 K in Al-free dry SiO_2 and SiO_2–H_2O systems [1]. Furthermore, the crystal structure of SiO_2 transformed from $CaCl_2$-type to α-PbO_2-type (seifertite) above 128 GPa in the lowermost mantle (Fig. 2).

Water concentrations in the SiO_2 phase, SiO_2–AlOOH ss., and partial melts were determined by

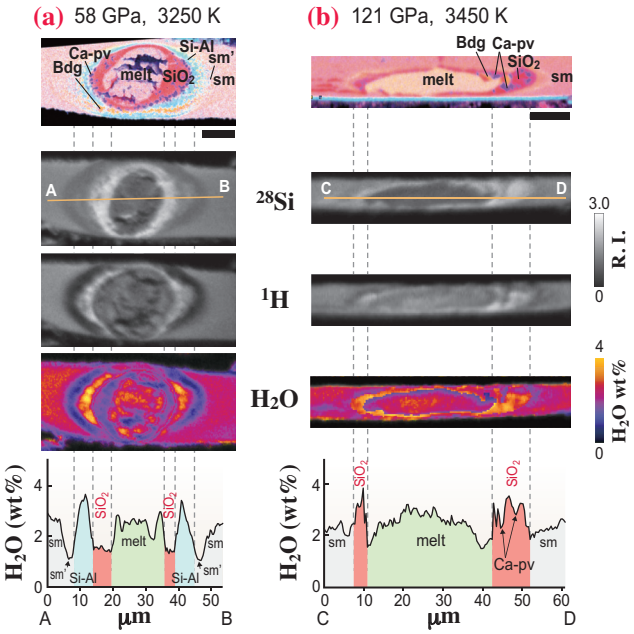

Fig. 1. Cross sections of partially molten samples. Samples were recovered from (**a**) 58 GPa and 3250 K and (**b**) 121 GPa and 3450 K. (Uppermost panels) EDS X-ray elemental maps combined for Si, Al, Ca, and Mg, showing melt, hydrated SiO_2 (red), $CaSiO_3$ perovskite (Ca-pv; blue), SiO_2–AlOOH ss. (Si–Al; light blue), bridgmanite (Bdg; orange), and dehydrated (sm') and original starting material (sm). (Middle panels) Corresponding secondary ion images for $^{28}Si^+$ and $^1H^+$ and the distribution maps of H_2O. Scale bar: 10 μm.

secondary ion mass spectrometry coupled with high-resolution imaging (Fig. 1). The water content in Al-bearing $CaCl_2$-type SiO_2 substantially increased with increasing pressure, reaching 3.6 wt% H_2O at 121 GPa under 3450 K (Figs. 2(a,b)). This value is considerably higher than the recent H_2O solubility estimate of only 0.4 wt% under the same P–T condition based on experiments on the Al-free SiO_2–H_2O system [1]. This discrepancy suggests that the charge-coupled substitution $Si^{4+} = Al^{3+} + H^+$ is the key mechanism for water incorporation into Al-bearing $CaCl_2$- [2] and α-PbO_2-type SiO_2 (Fig. 2(c)). Our XRD study found that the magnitude of the orthorhombic distortion increased with increasing pressure (Fig. 2(d) and Fig. 3), and this crystallographic distortion correlated strongly with the water content (Fig. 2(e) and Fig. 3). The enhanced distortion shortened the distance between specific pairs of oxygen atoms, making the hydrogen bonds stronger and stabilizing hydrogen in SiO_2. Moreover, the overall increase in water concentration in $CaCl_2$-type SiO_2 with increasing pressure resulted in an increase in the partition coefficient of water (D_{H_2O} ($CaCl_2$–SiO_2/melt)) from ~0.2 at 25 GPa to 1.4 under deep lower-mantle conditions at 120 GPa (Fig. 2(f)). The H_2O content in Al-bearing α-PbO_2-type SiO_2, formed at 3650–4100 K and 128–144 GPa—conditions corresponding to the Earth's CMB region—remained nearly constant at 2 wt% (Fig. 2(a)). Moreover, D_{H_2O} (α-PbO_2–SiO_2/melt) ranged from 1.1 to 2.1 (Fig. 2(f)), indicating that water preferentially partitions into hydrated SiO_2 rather than into coexisting partial melts under CMB conditions.

The dehydration of subducted slabs at the base of the mantle has been highlighted, and its consequences have been extensively discussed. However, our discovery of the high H_2O storage capacity—approximately 2 wt% in α-PbO_2-type SiO_2 and ~0.3–0.6 wt% in subducted MORB crust—suggests that, in practice, water does not escape from slabs even under the high temperature conditions of the CMB region.

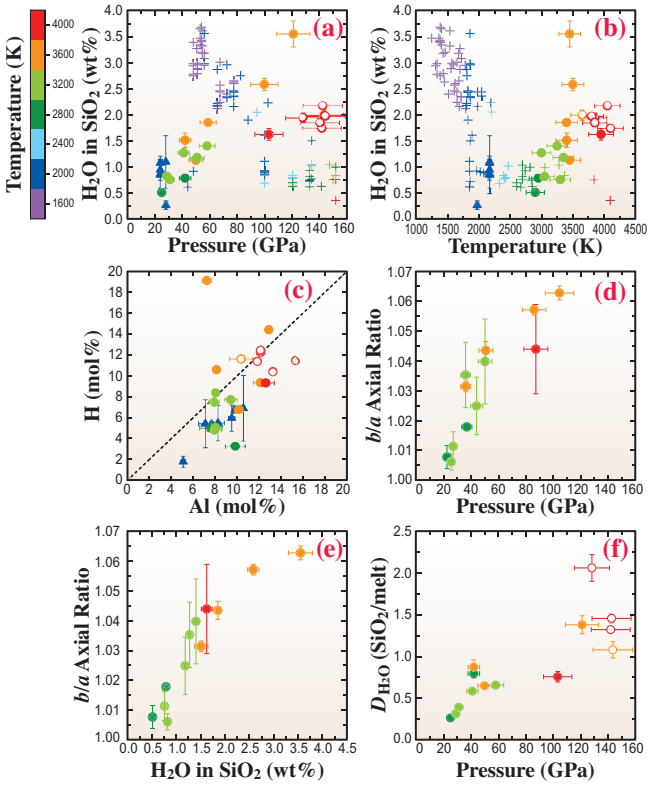

Fig. 2. Variations in hydrated SiO_2. The present experiments on hydrous MORB show data for $CaCl_2$-type (closed circles) and α-PbO_2-type SiO_2 (open circles). Earlier data obtained in water-saturated SiO_2–H_2O (pluses) [1] and SiO_2–Al_2O_3–H_2O systems (triangles) [2] are also given. Color indicates temperature. Water concentrations in SiO_2, plotted as functions of **(a)** pressure and **(b)** temperature. **(c)** Correlation between Al and H concentrations in SiO_2, indicating that the charge-coupled substitution $Si^{4+} = Al^{3+} + H^+$ is a main mechanism for water incorporation. **(d)** b/a axial ratio of the $CaCl_2$-type structure observed at 300 K, representing the magnitude of the orthorhombic distortion from a tetragonal structure with $b/a = 1$. **(e)** Correlation between the H_2O content and b/a ratio. **(f)** SiO_2/melt partition coefficient of H_2O, demonstrating that water is preferentially partitioned into SiO_2 rather than into silicate melt in the lowermost mantle.

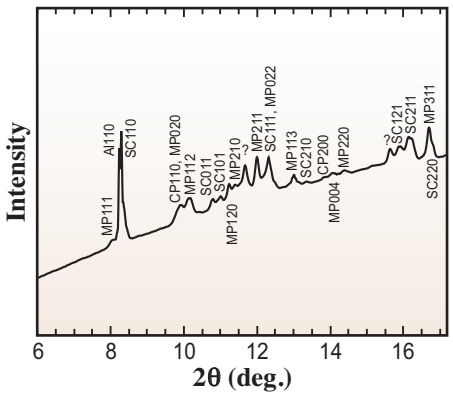

Fig. 3. XRD patterns of the solid part around a melt pocket obtained after quenching. SC, hydrated $CaCl_2$-type SiO_2; MP, bridgmanite; CP, $CaSiO_3$ perovskite; Al, SiO_2–AlOOH ss. Peak separations of SC121/211 and SC011/101 indicate the orthorhombic distortion of the $CaCl_2$-type structure.

Yutaro Tsutsumi* and Kei Hirose

Department of Earth and Planetary Science,
The University of Tokyo

*Email: ytsutsumi0113@gmail.com

References

[1] Y. Lin *et al.*: Earth Planet. Sci. Lett. **594** (2022) 117708.
[2] T. Ishii *et al.*: Proc. Natl. Acad. Sci. USA **119** (2022) e2211243119.
[3] *Y. Tsutsumi, N. Sakamoto, K. Hirose, S. Tagawa, K. Umemoto, Y. Ohishi, H. Yurimoto: Nat. Geosci. **17** (2024) 697.*

Mechanism of frizz phenomenon occurring in bleached hair

Owing to the spread of social networking service (SNS), bleached hair has become popular, especially among young people. Bleaching can lighten hair compared to coloring alone. However, bleaching causes serious problems that differ from those occurring during the coloring process.

The cortex cells, which are hierarchical structures that make up hair, are composed of intermediate filaments (IFs) with α-crystals embedded in amorphous intermediate filament-associated proteins (IFAPs) [1]. In hair and wool, IFAPs suppress the hydration swelling of IFs and play a crucial role in maintaining their elastic modulus and strength in water [2]. Therefore, it is hypothesized that the oxidative decomposition of IFAP caused by bleaching reduces hair strength. However, hair oxidized with bleaching agents becomes frizzy and spreads out when washed and dried, and measures to prevent frizzing have become important (Fig. 1). To elucidate the mechanism underlying the frizz phenomenon caused by bleaching, we reproduced frizzy-bleached hair and analyzed its internal structure.

Bleached hair becomes frizzy through the process of forcible tangling during washing, and subsequently untangled during drying with a hair dryer. It was found that this frizziness could be eliminated by soaking the hair in water and air-drying it. Next, small-angle X-ray scattering measurements were performed at SPring-8 **BL24XU** on untreated hair (UT), thrice-bleached hair (BL3), "frizzy portion of BL3" produced by forcibly tangling and untangling BL3, and "unraveled frizzy portion of BL3," which was the frizzy portion of BL3 soaked in water and air-dried [3,4].

Fig. 1. Effect of shampooing and drying on hair bundle shape. Hair bundle shape: **(1)** dry state before washing, **(2)** wet state after washing, and **(3)** dry state after drying with a hair dryer.

The results of the small-angle X-ray scattering measurements (Fig. 2) suggested that the bleaching treatment tended to increase the thickness of the IFAP and decrease the IF orientation. It is believed that the physical load that occurs during the untangling process compresses the IFAP, resulting in thinner and improved IF orientation. When the frizzy hair is immersed in water, the accumulated strain in the IFAP of the frizz part is relieved, and the IFAP is restored to its original thickness. In addition, the orientation of the IF returns to its original state before the physical load is applied. (See details in [4].)

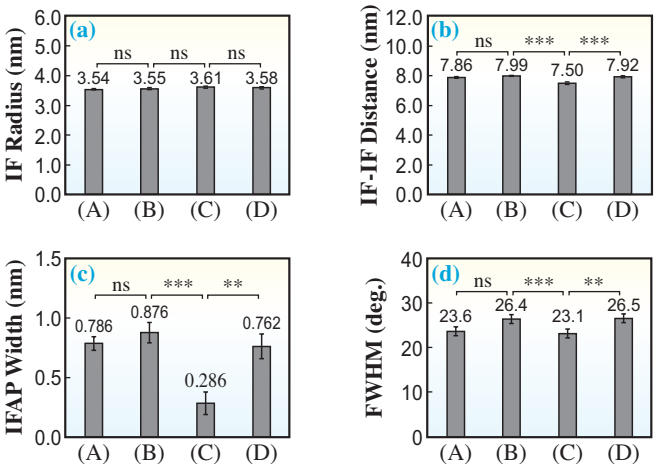

Fig. 2. Structural parameters on the aggregate structure of IF and IFAP characterized by small-angle X-ray scattering profile for (A) UT, (B) BL3, (C) frizzy portion of BL3, and (D) unraveled frizzy portion of BL3. Parameter: **(a)** IF radius, **(b)** IF-IF distance, **(c)** IFAP width and **(d)** Full width at half maximum (FWHM). Data are represented as means ± SE, n = 10, ns: not significant, **: $p < 0.01$, ***: $p < 0.001$ (Tukey–Kramer multiple comparison test)

Based on the above results, Fig. 3 summarizes the mechanism of the frizz phenomenon occurring in bleached hair during the hair-washing process. Untreated hair had a straight shape, as shown in Fig. 3(A). As shown in Fig. 3(a), the IF/IFAP molecular chains were cross-linked by disulfide bonds, and IF was oriented along the fiber axis. Similarly, the bleached hair exhibited a straight shape, as shown in Fig. 3(B). However, as shown in Fig. 3(b), some

disulfide bonds between the IF/IFAP molecular chains were oxidatively cleaved. This tends to reduce the orientation of the IF. In the wet state, water penetrates the space between the IF and IFAP, where disulfide bonds are broken, resulting in swelling of the IF and reduction in its elasticity and strength in water. The surface of bleached hair is highly hydrophilic; therefore, water easily spreads between the hairs. Therefore, during shampoo and water washing, the bleached hairs adhered to each other in a curved state and became tangled. The appearance of hair in this state is shown in Fig. 3(C). Furthermore, when the tangled bleached hair, as shown in Fig. 3(D), dried while being untangled, the tangled intersections moved and stretched, causing the frizz phenomenon, as shown in Fig. 3(E). In this case, when the cross-section of the hair shrinks as it is stretched, the IFAP is compressed, and its thickness decreases without inducing denaturation of the secondary structure of IF or cleavage of disulfide bonds, as shown in Fig. 3(c). When the frizzy-bleached hair was immersed in water, the frizz portion was eliminated. In the air-drying process, the hydrogen bonds broken by water recombined, straightening the hair shape, as shown in Fig. 3(F). When the frizzy-bleached hair was immersed in water, the water penetrated between the IF/IFAP molecular chains and facilitated their movement. The accumulated strain in the IFAP was relieved, its thickness, which had been compressed and thinned, returned to its original thickness, and the orientation of the IF returned to the state before the cross-stretching sliding treatment (Fig. 3(d)).

In this study, we investigated the mechanism of the frizz phenomenon in bleached hair, which is a serious concern for hair-bleaching customers. We found that the bleached hair became frizzy during the drying process and tangled after washing. Furthermore, small-angle X-ray scattering measurements revealed that the tangled intersections moved and stretched, resulting in a thinner, compressed IFAP. This revealed that the frizz phenomenon caused by the washing and drying of bleached hair led to the discovery of a method for dealing with frizzy-bleached hair. This result has been applied to products such as Mizulisse and Elujuda Bleach Care Serum, which are sold not only in Japan, but also in many other countries.

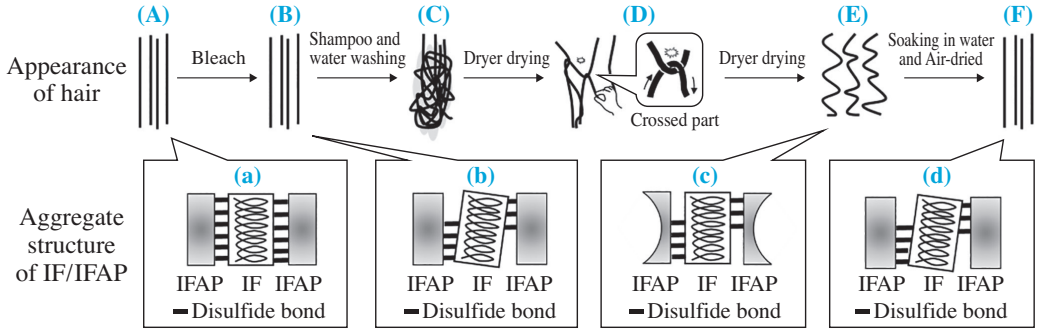

Fig. 3. Mechanism of the frizz phenomenon occurring in bleached hair. Hair appearance: **(A)** untreated hair, **(B)** bleached hair, **(C)** tangled bleached hair after washing, **(D)** bleached hair in the dry step, **(E)** frizzy-bleached hair, **(F)** bleached hair removed frizz by soaking in water.
Structure of IF/IFAP: **(a)** untreated hair; **(b)** bleached hair: decrease in disulfide bonds and reduction in IF orientation; **(c)** frizzy-bleached hair: improvement in IF orientation and compression of the IFAP; **(d)** bleached hair removed frizz: reduction of IF orientation, recovery from compression of IFAP.

Junichiro Kamikado*, Nobuyuki Fujiwara and Hironori Kimura

Central Research Institute, Milbon Co., Ltd.

*Email: jkamikado@milbon.com

References

[1] K. Arai: J. Soc. Cosmet. Chem. Jpn. **49** (2015) 2.
[2] D. S. Fudge and J. M. Gosline: Proc. R. Soc. Lond. B **271** (2004) 291.
[3] Y. Kajiura *et al.*: J. Struct. Biol. **155** (2006) 438.
[4] *J. Kamikado, Y. Toyota, N. Fujiwara, K. Kobayashi, K. Suzuta and K. Joko: J. Soc. Cosmet. Chem. Jpn. **57** (2023) 251.*

Discovery of anisotropy in Johari–Goldstein-β process of stretched crosslinked polybutadiene by time-domain interferometry

Polymers are essential to our daily lives. Improving fracture strength is particularly important for safety and resource conservation, and understanding the mechanism of fracture progression is key to this improvement. Additionally, imparting directionality to fracture strength is important. For example, materials that are rigid in the stretching direction but flexible in the perpendicular direction can meet various market demands.

The fundamental source of many material properties is the atomic/molecular structure and dynamics. In glass-forming systems, such as polymers, the α process and Johari–Goldstein (JG)-β process are common. The microscopic origin of the α process is cooperative diffusive motions within the polymer chains, while its sub-process, whose origin is elusive, is responsible for the JG-β process. Below the glass transition temperature, the α process is effectively frozen, while the JG-β process occurs much more frequently. Therefore, the JG-β process is often the major source of stress relaxation and is the dominant contributor to the failure strength of amorphous systems. As fracturing occurs at the end of stress-induced deformation, the JG-β process under stretching determines the fracture properties. We have found that stretching facilitates the JG-β process, indicating that the system strengthens against fracture [1]. Because the polymer is oriented by stretching, changes in the molecular environment can cause its dynamics to be directionally dependent. However, this directional dependence is poorly understood, despite its importance in various applications.

In this study, we measured the strain dependence of the JG-β relaxation time under stretching in detail and determined its directional dependence for crosslinked polybutadiene (PB). The cross-linked PB was prepared using a literature method [1]. Microscopic dynamics were studied using quasi-elastic gamma ray scattering (QEGS) with time-domain interferometry (TDI) [2,3]. A normalized intermediate scattering function was observed using the temporal beat pattern of the TDI time spectra. The QEGS measurements were performed at SPring-8 **BL35XU**. The sample was stretched to a target strain value of $\lambda = (l - l_0)/l_0$, where l_0 and l are the lengths of the sample before and after stretching, respectively. QEGS measurements on uniaxial stretching in the λ range between 0 and 1 were conducted at $q = 29$ nm^{-1} and 215 K, the conditions at which the JG-β process has been observed [1].

Figure 1 shows the obtained TDI time spectra, which were analyzed using a literature method [1].

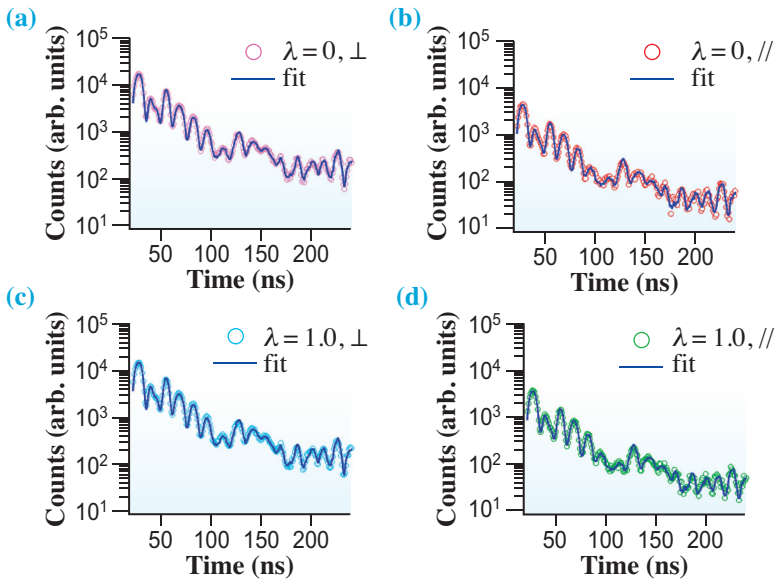

Fig. 1. TDI time spectra of the crosslinked PB on uniaxial stretching at 215 K **(a)** perpendicular to the stretching direction at $\lambda = 0$, **(b)** parallel to the stretching direction at $\lambda = 0$, **(c)** perpendicular to the stretching direction at $\lambda = 1.0$, and **(d)** parallel to the stretching direction at $\lambda = 1.0$ at $q = 29$ nm^{-1}. The solid lines in (a)–(d) represent the fitting curves. [4]

Figure 2 shows the strain dependence of the mean JG-β relaxation time perpendicular ($\langle\tau_{\perp}\rangle_{\text{JG-}\beta}$) and parallel ($\langle\tau_{//}\rangle_{\text{JG-}\beta}$) to the stretching direction. These relaxation times reflect the average timescale of the local few-angstrom-scale motions. Notably, $\langle\tau_{\perp}\rangle_{\text{JG-}\beta}$ tended to decrease with the increase in stretching, as reported previously [1]. By contrast, we found that $\langle\tau_{//}\rangle_{\text{JG-}\beta}$ did not change significantly on stretching. Thus, the strain dependence of the JG-β relaxation time was deemed to be anisotropic.

The observed anisotropy contrasts with the isotropic strain dependence of the α-relaxation time found previously [1]. Therefore, our finding hints at the origin of the mysterious JG-β process in polymeric materials. The activation energy, E_a, of the JG-β process is known to be ≈35 kJ/mol [1,4], approximately 2–3-fold higher than that of carbon–carbon torsional or vibrational motions, which occur mainly in the direction perpendicular to the main chain. The high activation energy indicates that several segments rotate or translate cooperatively, rather than individually. With respect to cooperativity, the observed anisotropy of the JG-β relaxation time can be explained as follows. Before stretching, the segments in the randomly oriented main chains are in collective local motion, as shown in the left panel of Fig. 3. Upon stretching, the main chains became slightly more aligned, facilitating collective motion in a direction perpendicular to the main chains. The right panel in Fig. 3 shows a schematic of the structure and dynamics proposed in our study, depicting the decrease in relaxation time $\langle\tau_{\perp}\rangle_{\text{JG-}\beta}$. It can be seen that the dynamics of the polymer chains remain relatively unaffected by stretching in the parallel direction, which explains the insensitivity of $\langle\tau_{//}\rangle_{\text{JG-}\beta}$ to stretching.

Thus, we directly observed that the anisotropic mobility of the polymer chains is dominated by the JG-β process during stretching. Anisotropy is essential to understanding the origin of the JG-β process and the mechanism of how the JG-β process relates to the material property under stretching.

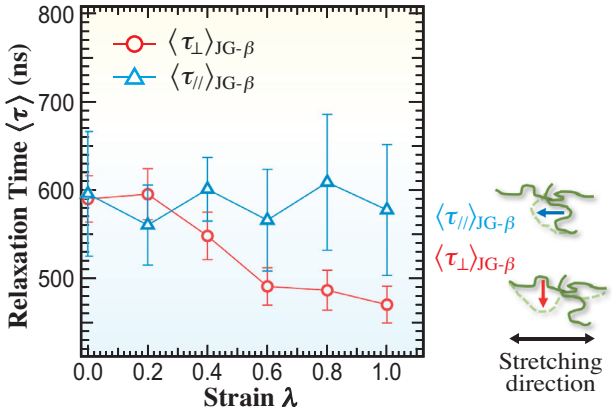

Fig. 2. Strain dependences of the mean relaxation times $\langle\tau\rangle$ of the crosslinked PB at q = 29 nm^{-1} and T = 215 K perpendicular and parallel to the stretching direction. On the right side, the dark green curves represent polymer chains. The red and blue arrows represent the direction of polymer chain motions, which are the origin of the relaxations occurring perpendicular and parallel to the stretching direction, respectively. [4]

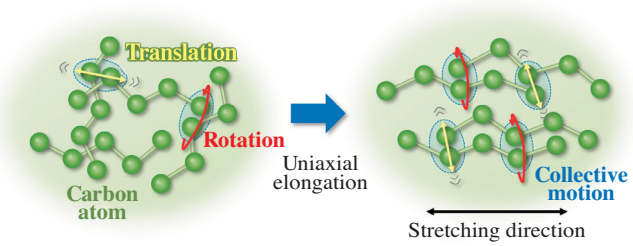

Fig. 3. Schematic of the JG-β process in crosslinked polybutadiene under uniaxial elongation (with the example of cooperative motion of two units). [4]

Ryo Mashita[a,*] and Makina Saito[b]

[a] Research Center for Advanced Technology & Innovation, Research & Development HQ, Sumitomo Rubber Industries Ltd.
[b] Department of Physics, Tohoku University

*Email: r-mashita.az@srigroup.co.jp

References

[1] R. Mashita *et al.*: J. Synchrotron Rad. **29** (2022) 1180.
[2] A. Q. R. Baron *et al.*: Phys. Rev. Lett. **79** (1997) 2823.
[3] M. Saito *et al.*: Sci. Rep. **7** (2017) 12558.
[4] *R. Mashita, M. Saito, Y. Yoda, N. Nagasawa, Y. Bito, T. Kikuchi, H. Kishimoto, M. Seto, T. Kanaya: ACS Macro Lett.* ***13*** *(2024) 847.*

Hexavalent iridium oxide for proton-exchange membrane water electrolysis

The production of hydrogen via electrolysis ($2H_2O \rightarrow 2H_2 + O_2$), powered by renewable energy resources such as solar and wind, is pivotal in the global effort to achieve carbon neutrality by 2050. Among the available technologies, proton-exchange membrane water electrolysis (PEMWE) is advantageous because of its high energy efficiency, rapid on-off response, and low hydrogen crossover, making it an ideal match for the intermittent nature of renewable energy sources. However, a critical barrier to large-scale PEMWE deployment is the reliance on iridium, a rare and expensive metal, as the anode catalyst for the oxygen evolution reaction (OER). The global annual production of iridium is limited to only 7–8 tons, leading to an unsustainable iridium supply for scaling up hydrogen production to meet future demands [1-5]. Addressing this challenge is essential to unlock the full potential of PEMWE in driving the hydrogen economy.

Our research addresses this challenge by developing novel atomically dispersed hexavalent iridium oxide (Ir^{VI}-*ado*) on manganese dioxide (MnO_2) [1]. This catalyst reduces iridium usage by over 95% compared to conventional catalysts while maintaining high catalytic activity and stability. This work not only makes green hydrogen production more cost-effective, but also accelerates the global transition to a sustainable hydrogen economy.

The synthesis of Ir^{VI}-*ado* involves an oxidative ligand-substitution reaction using potassium hexachloroiridate (K_2IrCl_6) and manganese dioxide (MnO_2) as reactants. Comprehensive structural and chemical characterizations were performed using *in situ* and *ex situ* techniques at SPring-8 **BL14B2** (XAFS), **BL39XU** (HERFD-XANES), **BL36XU** (HERFD-XANES), **BL17SU** (XPS and XAFS), and **BL44B2** (SR-PXRD). XAS at the Ir L_3-edge was used to monitor changes in the oxidation state and coordination environment during synthesis, whereas XPS was used to determine the binding energy and oxidation state of Ir in the final catalyst. High-angle annular dark-field scanning transmission electron microscopy (HAADF-STEM) was used to visualize the atomic dispersion of Ir on the MnO_2 support. The electrochemical performance of Ir^{VI}-*ado* was evaluated using a PEM electrolyzer. Additionally, *in situ* XAS was performed to assess the stability of Ir^{VI}-*ado* under operational conditions with current density up to 2 $A \cdot cm^{-2}$.

Successful synthesis of Ir^{VI}-*ado* was achieved by leveraging the oxidative potential of MnO_2, which facilitated the transformation of Ir^{IV} into Ir^{VI}. The XAS spectra showed a shift in the white-line (WL) position of the Ir L_3-edge, reflecting the transition of Ir from the +4 oxidation state in K_2IrCl_6 to a higher oxidation state in the Ir^{VI}-*ado* catalyst during the synthesis process (Fig. 1(a)). The EXAFS results indicated that the Cl ligand in the precursor K_2IrCl_6 was substituted by oxygen in MnO_2, forming Ir–O and Ir–O–Mn coordinations (Fig. 1(b)). The WL intensity, proportional

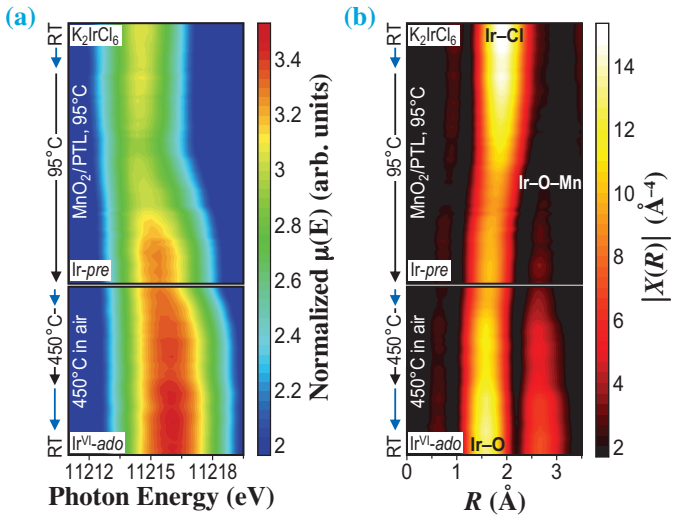

Fig. 1. *In situ* XAS analysis of Ir^{VI} formation. Two-dimensional color maps showing the shift of the absorption edge **(a)** and the coordination shell **(b)** at the iridium L_3-edge peak as a function of time during the synthesis of Ir^{VI}-*ado*. Simplified temperature profiles for heating and cooling (blue arrows) and constant temperature (black arrows) are shown on the left. RT, room temperature.

to the population of 5*d* holes in the iridium atom, indicated an average oxidation state of +5.8 ± 0.1 for Ir^{VI}-*ado* (Fig. 2(a)). Consistently, XPS confirmed that over 80% of the Ir in Ir^{VI}-*ado* existed in the oxidation state of +6, as evidenced by its characteristic binding energy of 62.61 eV for the Ir $4f_{7/2}$ peak. The average Ir–O bond length in Ir^{VI}-*ado* (1.959 Å) was shorter than that in rutile IrO_2 (1.986). *In situ* XAS measurements confirmed that the Ir^{VI} oxidation state was maintained even at high current densities (2.3 A·cm^{-2}) and elevated temperatures (80°C). Scanning electron microscopy (SEM) revealed that the obtained Ir^{VI}-*ado* uniformly covered the porous transport layer (PTL) substrate (Fig. 2(b)). Atomic-resolution HAADF-STEM images showed that Ir was atomically dispersed on the MnO_2 support (Figs. 2(c-e)).

The Ir^{VI}-*ado* catalyst demonstrates remarkable mass-specific activity and stability during the OER under acidic conditions. At an iridium loading of 0.08 mg_{Ir}·cm^{-2}, Ir^{VI}-*ado* achieved a current density of 4.0 A·cm^{-2} at 2 V in a PEM electrolyzer. Long-term stability tests showed minimal degradation over 2700 h operation at 1.8 A·cm^{-2}, highlighting the durability of Ir^{VI}-*ado* under industrial PEMWE operation. Turnover numbers of up to 1.5×10^8 were recorded, which were higher than those of previously reported Ir-based catalysts (Fig. 2(f)). Its ability to maintain high activity and stability under industrial conditions demonstrates the practical viability of Ir^{VI}-*ado* for large-scale hydrogen production. Furthermore, the atomically dispersed nature of Ir enhances its utilization efficiency, enabling >95% reduction in Ir loading compared to that of conventional catalysts. By reducing the Ir requirement to 0.08 mg_{Ir}·cm^{-2}, the annual global production of Ir could support the deployment of over 300 GW of PEMWE capacity per year, representing a significant step toward meeting the 2000 GW target required for carbon neutrality.

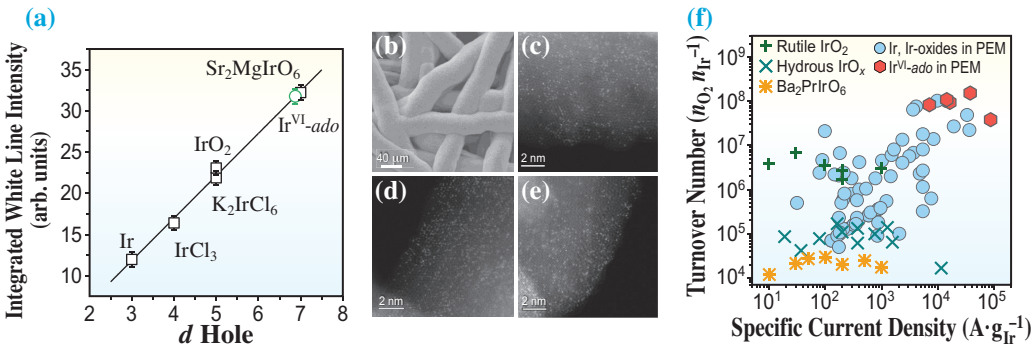

Fig. 2. Characterization of Ir^{VI}-*ado*. **(a)** High-energy resolution fluorescence detected X-ray absorption near edge structure (HERFD-XANES) spectra at the Ir L_3-edge of Ir^{VI}-*ado* and the reference samples. (**b**) SEM image of Ir^{VI}-*ado* fabricated on MnO_2/PTL. Scale bar, 40 μm. (**c** to **e**) HAADF-STEM images of Ir^{VI}-*ado* taken from different sample locations. Iridium atoms (bright dots) are embedded in the surface of MnO_2. Scale bars, 2 nm. (**f**) Turnover numbers plotted *versus* mass-specific current densities for Ir^{VI}-*ado* (I to V; red hexagons) and Ir-based electrocatalysts reported in the literature.

Ailong Li*, Shuang Kong and Ryuhei Nakamura

Biofunctional Catalyst Research Team,
RIKEN Center for Sustainable Resource Science/Wako

*Email: ailong.li@riken.jp

References

[1] *A. Li, S. Kong, K. Adachi, H. Ooka, K. Fushimi, Q. Jiang, H. Ofuchi, S. Hamamoto, M. Oura, K. Higashi, T. Kaneko, T. Uruga, N. Kawamura, D. Hashizume and R. Nakamura: Science* ***384*** *(2024) 666.*
[2] A. Li *et al.*: Angew. Chem. Int. Ed. **58** (2019) 5054.
[3] A. Li *et al.*: Nat. Catal. **5** (2022) 109.
[4] S. Kong *et al.*: Nat. Catal. **7** (2024) 252.
[5] A. Li *et al.*: Innov. Mater. **2** (2024) 100094.

Accelerators & Beamlines Frontiers

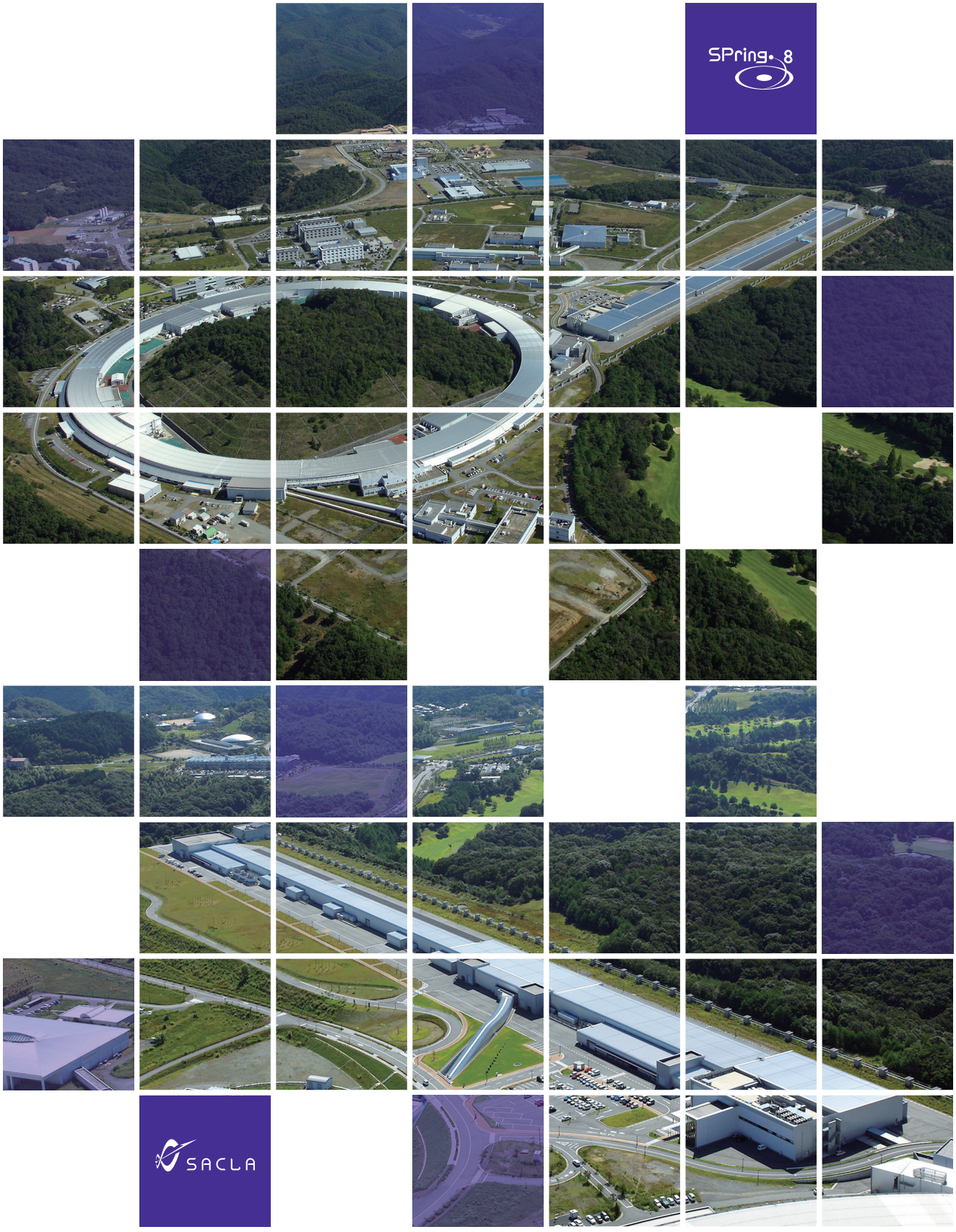
SPring-8
SACLA

Sub-micrometer focusing of intense 100 keV X-rays with multilayer reflective optics

High-energy X-rays serve as powerful tools for the non-destructive analysis of thick heavy metals, devices enclosed in protective casings, and materials subjected to high-pressure conditions. For high-energy X-ray applications, such as transmission X-ray imaging, X-ray fluorescence spectroscopy, and total-scattering measurements with pair-distribution function analysis, an incident X-ray beam with a high-energy resolution below 0.1% is not required. Instead, a "pink" beam with a moderate energy resolution of 1–10% is preferred, as it enhances photon flux. Focusing such a high-flux beam on a small region enables analysis with high spatiotemporal resolution.

Several types of devices have been developed to focus high-energy X-rays above 50 keV, including Fresnel zone plates (FZPs), multilayer Laue lenses (MLLs), compound refractive lenses (CRLs), and total-reflection Kirkpatrick–Baez (K–B) optics. Both FZPs and CRLs are on-axis devices that maintain a simple optical geometry; however, they exhibit chromatic aberration, which reduces throughput. MLLs offer high diffraction efficiency and a small focal spot size but are also subject to chromatic aberration and have a small acceptance aperture. We note that the chromatic aberrations of these devices are proportional to the photon energy E (E^2) for the FZPs and MLLs (CRLs), which limits the ability to generate a small, intense focus with a pink beam due to constraints on the numerical aperture (NA). While total-reflection K–B optics exhibit achromatic properties, their critical angle decreases significantly for high-energy X-rays, leading to reduced spatial acceptance and low throughput. In contrast, multilayer K–B optics can be designed to accommodate a reasonably wide bandwidth of a few percent at a specific photon energy, facilitating the generation of an intense, small focus with large spatial acceptance, large NA, and high reflectivity.

In this study, we developed a 100 keV K–B focusing system comprising laterally graded multilayers deposited on high-precision figured mirrors [1]. The focusing mirror system features a wide bandwidth of 5% and a high peak reflectivity of 74%. The system's performance was evaluated at the undulator beamline SPring-8 **BL05XU** [2], which generated an intense 100 keV X-ray beam with a bandwidth of 1%.

Figure 1 illustrates the layout of the main optical components within the optics hutches (OH1 and OH2). In this study, the 19th harmonic of the 5.3 keV fundamental radiations, with an energy width of 0.93%, was utilized. The entire spectrum of the 19th harmonic was extracted using a double multilayer monochromator (DMM). To suppress the total-reflection low-energy component (< 30 keV) reflecting from the DMM, attenuators were employed. As shown in the bottom left of Fig. 1, a photon flux of 3×10^{13} photons/s with an energy bandwidth of 1% was achieved at 100 keV.

We designed laterally graded multilayer focusing mirrors (Fig. 2) with a $[W/C]_{50}$ coating to generate a sub-micrometer beam in the vertical direction. A comparable size in the horizontal direction was

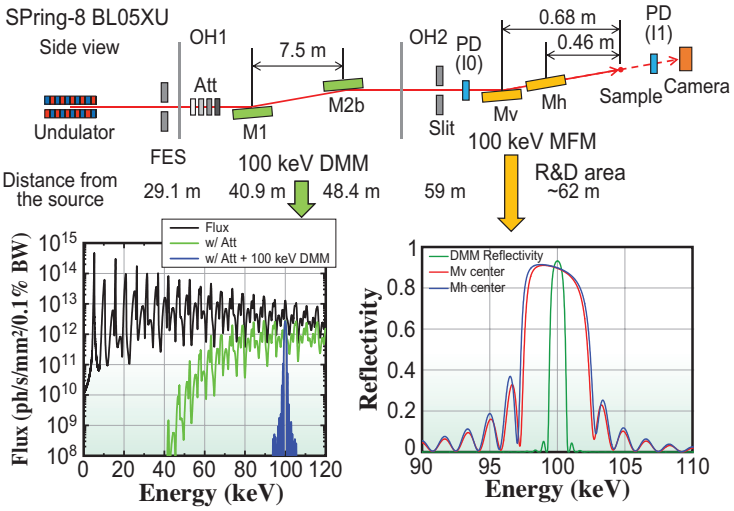

Fig. 1. Layout of the main optical components in the optics hutches (OH1 and OH2) at BL05XU. FES: front-end slit, Att: attenuators, DMM: double multilayer monochromator, MFM: multilayer focusing mirror, and PD: photo diode detector. Bottom left: The calculated undulator spectrum, along with attenuators, and DMM. Bottom right: Reflectivity curves of the DMM, vertical (Mv) and horizontal (Mh) focusing mirrors.

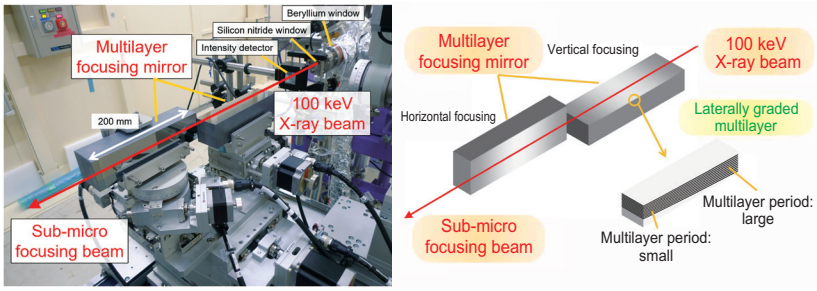

Fig. 2. Photograph and schematic of the developed 100 keV multilayer focusing mirrors.

achieved by restricting the horizontal size of the front-end slit (FES), which acted as a secondary source. The multilayer focusing mirror was designed with a bandwidth of approximately 5% along its entire length to fully encompass the DMM bandwidth (1%), as shown in Fig. 1 (bottom right), while allowing sufficient tolerance for potential alignment and/or multilayer deposition errors.

The mirror substrate surfaces were finished by JTEC Corporation, while the multilayer coatings were deposited at our SPring-8 in-house laboratory. The deposition system, based on DC magnetron sputtering, was designed to coat substrates up to 600 mm in length and 50 mm in width. To achieve uniform long coatings and thickness gradients, the substrates were moved in front of the sputtering sources during deposition. The multilayer deposition process had an error margin of approximately ±1%, which was acceptable given that the reflection energy width of the multilayer was as wide as 5%.

The focusing mirrors were installed in OH2, as shown in Fig. 2. The mirror system operated in an atmospheric environment without a vacuum or gas chamber. We evaluated the system's performance by measuring reflectivity, focusing beam size, and photon flux. The peak reflectivity was 74% for two bounce reflections. The beam profiles of the focusing beams were characterized using the knife-edge scanning method with tantalum blades. In the high spatial resolution mode, with the 20 μm horizontal width of FES, the beam size was measured to be 0.25 μm (V) × 0.26 μm (H), as shown in Figs. 3(a,b), with a corresponding flux of 6×10^{10} photons/s. In high flux mode, with the horizontal FES opened to 1.5 mm, the focusing beam size was measured to be 0.32 μm (V) × 5.3 μm (H), achieving a high flux of 1×10^{12} photons/s. To evaluate imaging performance, we conducted scanning transmission imaging of a tantalum Siemens star chart (XRESO-100, NTT Advanced Technology Corporation) with a tantalum thickness of 1 μm in high-spatial resolution mode, as shown in Fig. 3(c). The structure of the 200 nm line and space was successfully resolved.

For a 4th-generation synchrotron light source, such as the forthcoming SPring-8-II, which features a smaller horizontal source size, a small horizontal focus can be achieved without relying on a secondary source formed by FES, thereby significantly enhancing the available photon flux. Additionally, the undulator spectrum consists of single peaks without satellite profiles. The multilayer K–B focusing system enables the selective extraction of a specific harmonic with an energy bandwidth of a few percent, further increasing the beam intensity.

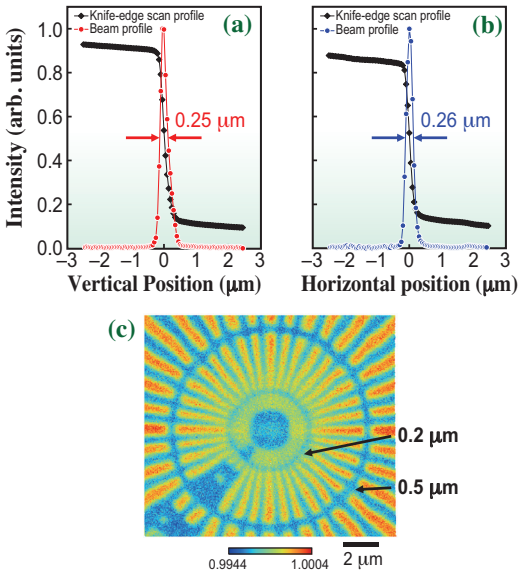

Fig. 3. Measured focusing beam size and observation result of the test chart.

Takahisa Koyama

Japan Synchrotron Radiation Research Institute (JASRI)

Email: koyama@spring8.or.jp

References

[1] *T. Koyama, H. Yumoto, T. Miura, Y. Matsuzaki, M. Yabashi and H. Ohashi: J. Synchrotron Rad.* ***31*** *(2024) 276.*
[2] H. Yumoto *et al.*: Proc. SPIE **11492** (2020) 114920I.

High-throughput and high-resolution powder X-ray diffractometer with innovative automation system

Powder X-ray diffraction plays an essential role in material characterization and is important in the fields of material science and engineering. When combined with synchrotron radiation sources, it enables a high angular and temporal resolution across a wide Q range in a significantly reduced time. Consequently, several synchrotron facilities worldwide have dedicated powder diffraction beamlines. SPring-8 BL02B2 beamline has been in operation since 1999 and has contributed significantly to material research by utilizing a two-dimensional (2D) imaging plate detector for accurate data collection and charge density studies [1]. In the 2010s, six sets of one-dimensional (1D) Si microstrip MYTHEN detectors were introduced into a powder diffractometer [2] to meet the requirements for *in situ* measurements under various sample conditions. This allows for faster and more automated data collection by rapidly collecting the whole powder pattern with a high angular resolution [3].

Recent trends indicate that user needs are becoming even more diverse, and the following issues remain to be addressed to meet a wider range of user needs: (i) the Q range ($Q = 4\pi\sin\theta/\lambda$) needs to be wider than 20 Å^{-1} to investigate partially disordered materials; (ii) rapid *in situ* experiments require measurement times shorter than 1 s, and a highly automated measurement system capable of acquiring large amounts of diffraction data is needed to accelerate high-throughput measurements; and (iii) sample environments larger than 100 mm^3 should be available for *operando* experiments. To overcome these challenges, we installed a new powder diffractometer at the ID beamline SPring-8 **BL13XU** for highly automated and high-speed data collection, *in situ* and *operando* experiments, and data collection for pair distribution function (PDF) analysis.

Figure 1 shows the high-resolution powder diffractometer [4] developed in the third experimental hutch of BL13XU. The diffractometer is equipped with six sets of 2D CdTe detectors (LAMBDA 750k, X-Spectrum GmbH), and it is possible to acquire data with high detection efficiency even for high-energy X-rays. Three scan modes (standard, single-step, and high-resolution) were developed. In the standard scan, data with Q-values exceeding 20 Å^{-1} at 35 keV can be acquired in tens of seconds. In the high-resolution mode, measurements with a full width at half maximum of less than 0.01° can be acquired at low 2θ angles. In single-step mode, in which multiple detectors are asymmetrically arranged in the positive and negative 2θ directions, continuous data acquisition in milliseconds is possible. Capillary samples can be set on a 6-axis spinner, which can rotate at speeds of up to 200 rpm. Small *in situ* cells can also be mounted on the spinner. In addition to these measurement systems, we developed various automation systems. A maximum 100 powder capillary samples can be mounted on the sample changer. This allows capillary alignment by image recognition in addition to automatic sample exchange. A fully automatic system using a combination of temperature control nitrogen gas blowers and a robotic sample changer allows automatic measurements in the temperature range from 90 K to 1100 K in a short time. This sample changer is mounted on an automatic equipment switching system and can be automatically inserted in front of the diffractometer. The switching system is also equipped with a large sample table that can accommodate a maximum weight of 500 kg and

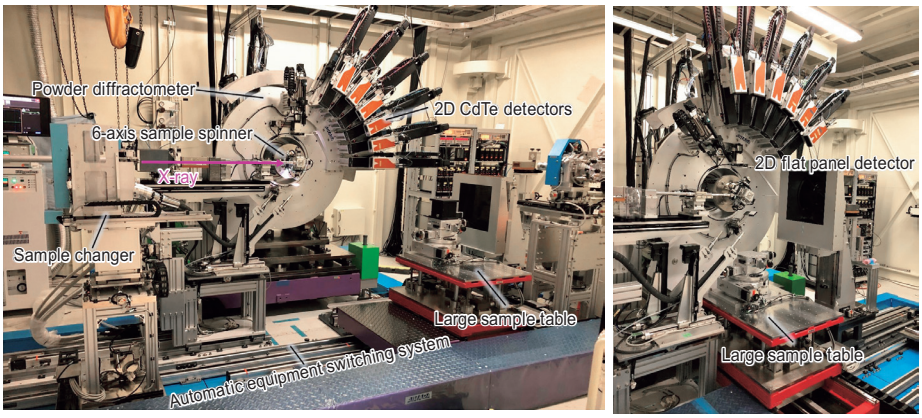

Fig. 1. Photographs of the high-resolution powder diffractometer equipped with six sets of 2D CdTe detectors and various automation systems at the third experimental hutch of BL13XU.

more than 1 m of external equipment. This provides a large sample space and allows for the development of a variety of *in situ* and *operando* experiments. Automatic measurements using a sample changer and *in situ* measurements using a large sample table can be easily switched on a PC. In addition, the alignments of the sample changer and the table are automatically adjusted with reference to the diffractometer position.

The powder diffraction data for the NIST LaB_6 sample, measured using a high-resolution powder diffractometer, are shown in Fig. 2(a). High-energy X-rays of 60 keV were used for measurements in the standard scan mode. To facilitate the observation of the peaks in the high-Q region, the sample was cooled to 100 K using a cryostream nitrogen gas blower. Diffraction data over Q = 30 Å^{-1} were obtained, as shown in Fig. 2(b). The inset shows the data averaged over six repetitions of the same scan to compare intensities at high angles. By repeating the scans, a weak peak 4–5 orders of magnitude below the most intense peak was detected, even in the $Q \sim 30$ Å^{-1} region. The statistical quality of the high-angle data was enhanced owing to the amplified X-ray flux from the ID source and the improved detection efficiency of the 2D CdTe detectors. Thus, this diffractometer enables the rapid measurement of diffraction and scattering data up to the high-Q region, facilitating active research on nanoparticles and crystalline materials using Rietveld refinement and PDF analysis. The results of the crystal structure analysis based on the powder diffraction data measured in milliseconds are shown in Fig. 2(b). The CeO_2 data were measured using a single-step mode with 35 keV X-rays. The acquisition time was 2 ms. Rietveld refinement yielded an R_B value of approximately 3%, and the isotropic atomic displacement parameters could be refined. These results demonstrate the potential for visualizing continuous changes in the crystal structure on a millisecond timescale. The single-step mode provides continuous data acquisition within milliseconds. Although the measurable 2θ range is narrower than that of standard scanning, a sufficient Q range can be obtained even with high-energy X-rays such as 35 keV and 60 keV. Using this method, time-resolved experiments are frequently performed to observe the synthesis process of a large number of samples, structural changes under rapid temperature changes, gas adsorption, and reaction processes.

In summary, a high-throughput and high-resolution powder diffraction system was developed at the third experimental hutch of BL13XU. The system is equipped with six sets of 2D CdTe detectors for high-energy X-rays (16–72 keV), and includes automation systems for switching between large sample environments. This supports the Rietveld refinement and PDF analysis of the data collected under ambient and non-ambient conditions. Three scan modes—standard, single-step, and high-resolution—have been established with the ability to measure whole powder patterns at millisecond resolution and achieve high-Q data (exceeding 30 Å^{-1}) within seconds. This capability is expected to significantly contribute to new research using machine learning and artificial intelligence by leveraging the large amount of data obtained from high-throughput measurements. In addition, millisecond time-resolved powder diffraction measurements are required to elucidate the crystal structures of various chemical reactions and synthetic processes.

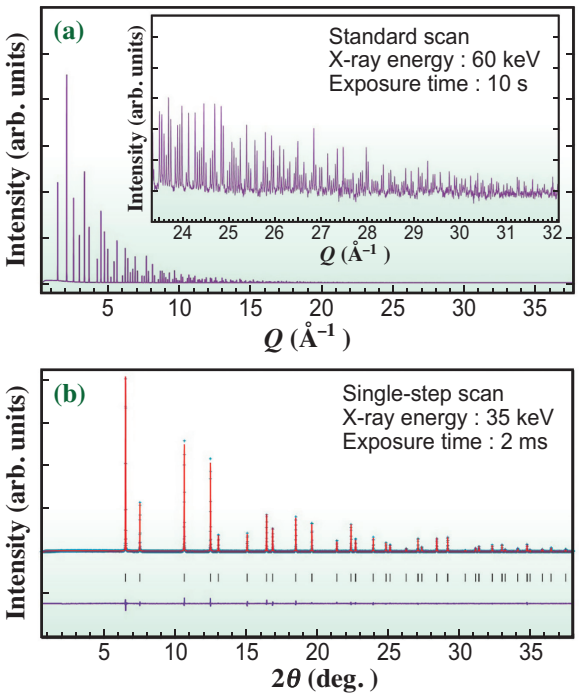

Fig. 2. **(a)** Powder diffraction pattern of NIST LaB_6 using the standard scan mode. **(b)** Rietveld refinements of NIST CeO_2 powder data obtained in the single-step scan mode.

Shogo Kawaguchi

Japan Synchrotron Radiation Research Institute (JASRI)

Email: kawaguchi@spring8.or.jp

References

[1] E. Nishibori *et al.*: Nucl. Instrum. Methods Phys. Res. A **467-468** (2001) 1045.
[2] S. Kawaguchi *et al.*: Rev. Sci. Instrum. **88** (2017) 085111.
[3] S. Kawaguchi *et al.*: J. Synchrotron Rad. **27** (2020) 616.
[4] *S. Kawaguchi, S. Kobayashi, H. Yamada, H. Ashitani, M. Takemoto, Y. Imai, T. Hatsui, K. Sugimoto and O. Sakata: J. Synchrotron Rad.* ***31*** *(2024) 955.*

Ultracompact mirror device for forming 20-nm achromatic soft-X-ray focus toward multimodal and multicolor nanoanalyses

X-ray focusing devices play a crucial role in generating X-ray nanoprobes for scanning microscopy. These devices can be characterized by their nanofocusing capabilities, achromaticity, and focusing throughput. Achromatic focusing ensures a constant probe position irrespective of the incident photon energy, whereas high focusing throughput enables efficient conversion of incident X-rays into a nanoprobe with minimal intensity loss. An ideal X-ray focusing device meets all three of these criteria.

In the soft X-ray region, solely total-reflection-based X-ray focusing mirrors offer both achromaticity and high focusing throughput. However, fabricating soft X-ray nanofocusing mirrors with high precision presents significant challenges, as nanoscale smoothness must be achieved on a highly curved (submeter radius) surface. When such surface perfection is attained, the focus size can reach the diffraction limit, which is proportional to the X-ray wavelength. A soft-X-ray focusing mirror has barely achieved a diffraction-limited focus size of 241 nm × 81 nm at photon energy of 0.3 keV [2]. A study found that the size of the achromatic soft X-ray nanoprobe did not decrease with a shorter X-ray wavelength; rather, it expanded [3]. The nanofocusing capability of soft X-ray focusing mirrors can be severely constrained by fabrication process limitations.

To achieve ideal nanoprobes across the entire soft X-ray range, we employed a novel strategy in addition to the straightforward development of new fabrication techniques [4]. With the large grazing angle allowed in the soft X-ray region, millimeter-scale mirrors can moderately accept incident X-rays and achieve focusing throughput that is superior or comparable to that of common soft-X-ray nanofocusing devices (zone plates). These mirrors can be fabricated with high precision, as mirror fabrication and metrology techniques can be optimized for a specific figure frequency range (1 cm^{-1} to 10 μm^{-1}). Additionally, short mirrors allow their focal points to be positioned much closer to the mirror center. Millimeter-scale focal lengths enhance focusing robustness by ensuring that X-rays reach the focal plane before significant spreading occurs due to mirror figure errors. However, fabricating such ultracompact mirrors presents a challenge, as shorter focal lengths proportionally reduce the tangential radii of curvature. A robust focusing strategy, supported by advancements in fabrication technologies, is essential for achieving ideal achromatic soft X-ray nanoprobes.

Figure 1(a) presents a schematic layout of the ultracompact Kirkpatrick–Baez (ucKB) mirror. The KB geometry simplifies a doubly curved focusing mirror into a pair of elliptic-cylindrical surfaces, namely, a vertically focusing mirror (VFM) and a horizontally focusing mirror (HFM). To achieve an extremely short focal length for the component mirrors of the ucKB mirror, the downstream mirror length and focal length were both reduced to 2 mm, an approach that deviates from conventional mirror design principles. The ucKB mirror was specifically designed to focus 1-keV soft X-rays onto a sub-50-nm diffraction-limited spot. Each mirror, designed with a primary grazing angle of 25 mrad, can theoretically achieve a reflectivity of 50.9% at a photon energy of 1 keV.

To efficiently fabricate their highly curved surfaces, angstrom-scale smooth cylindrical surfaces were figure-corrected into the designed elliptic-cylindrical reflective surfaces through Ni deposition. Figure 1(b) shows that the residual figure errors were controlled within 0.5% of

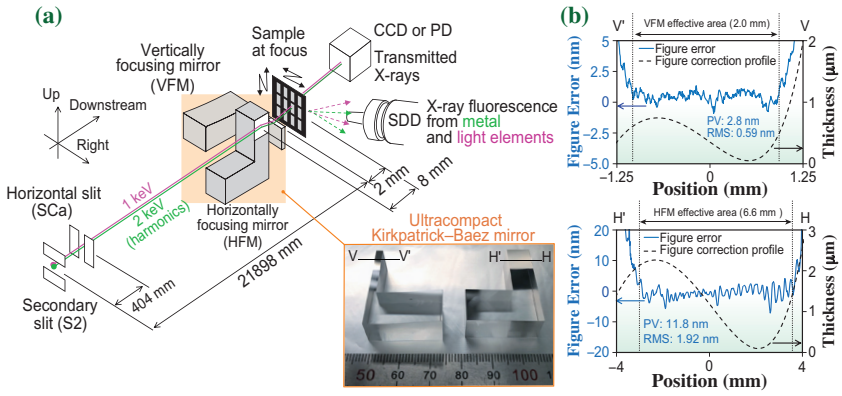

Fig. 1. Experimental configuration using ultracompact Kirkpatrick–Baez (ucKB) mirror. **(a)** Layout of soft-X-ray microscope. Elliptic cylindrical reflective surfaces were fabricated on L-shaped glass cylinder substrates (ruler units: mm). **(b)** Film thickness profile for figure correction of substrates (dashed line) and residual figure errors (solid line). Figure errors within this area are presented in terms of peak-to-valley (PV) and root-mean-square (RMS) values.

the maximum Ni film thickness. Considering the peak-to-valley (PV) residual errors, the VFM is expected to achieve optimal focusing performance for soft X-rays below 2 keV.

The performance of the ucKB mirror was evaluated at SPring-8 **BL25SU** A-branch, which offers photon energy tunability from 0.3 to 2 keV. As shown in Fig. 2(a), the focus spot was evaluated using knife-edge scanning and ptychography. The focus positions remained mostly constant across different photon energies. The difference in focus size between knife-edge scanning and ptychography arises from the bluntness of the knife edge, with the ptychographic measurement providing a more precise focus size. Overall, the ptychographic focus size aligns well with the design specifications. Notably, the focus size decreases with increasing photon energy, reaching a minimum spot size of 20.4 nm × 40.7 nm at 2 keV.

Such achromatic nanoprobes can not only broaden the energy bandwidth but also enable the use of multiple X-ray photon energies for photon-hungry techniques. For instance, the low-energy X-ray fluorescence technique faces challenges due to the inherently low fluorescence yields of light elements, even at micrometer-scale spatial resolution. As shown in Fig. 1(a), with the undulators and monochromator tuned for a 1-keV fundamental and 2-keV second-order harmonics, the ucKB mirror generated a sub-100-nm two-color nanoprobe. This approach allowed simultaneous fluorescence excitation of both light elements and metal elements.

This method was applied to analyze, for instance, hippocampal neurons cultured from rat brains and chemically fixed, as shown in Fig. 2(b). The region where a neuronal structure, known as the spine, seemed to have disappeared was examined using a scanning pitch of 100 nm. Based on the results of soft X-ray fluorescence and transmitted X-ray measurements, distribution maps for the mass of chemical elements and the effective thickness of the samples were produced and applied to concentration analyses, as shown in Fig. 2(c). The analysis revealed that Zn was homogeneously distributed, whereas Cu and Fe exhibited more localized distribution. Such information is not easily obtained through conventional techniques.

The ucKB mirror is an ideal X-ray focusing device in terms of nanofocusing capability, broadband energy, and focusing throughput. These properties make it highly suitable for enhancing multimodal and multicolor techniques in soft X-ray analysis, which can evaluate structural, chemical, elemental, and magnetic characteristics. Additionally, integrating the ucKB mirror with a tabletop X-ray source has the potential to extend the accessibility of scanning X-ray nanoanalyses, which has been limited to synchrotron radiation-based X-rays.

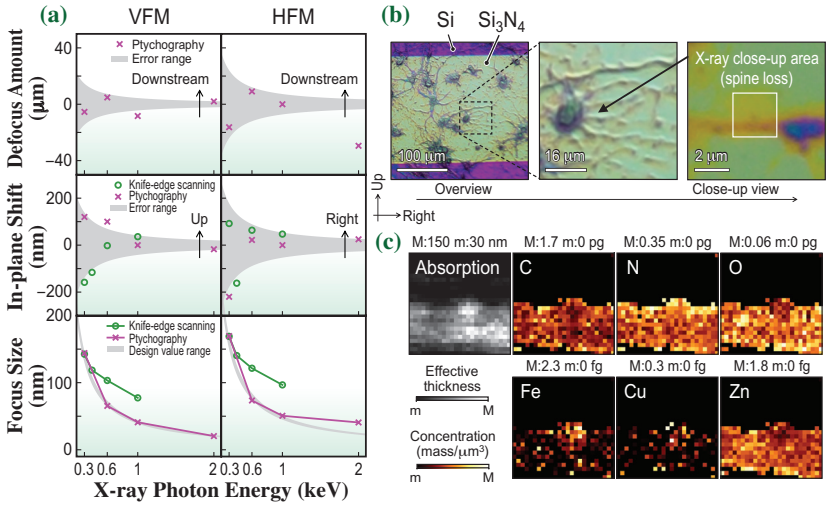

Fig. 2. Achromatic soft-X-ray nanoprobe formed by ucKB mirror. **(a)** Focus position and full width at half maximum (FWHM) focus size *versus* X-ray photon energy. The error ranges for the defocus amount and in-plane shift were calculated based on the ±Rayleigh range and ±FWHM focus size, respectively. **(b)** Visible-light micrographs of primary hippocampal neurons. The close-up area is indicated either by the box or the tip of the arrow. **(c)** X-ray absorption and fluorescence images, with units of nm and mass μm^{-3}, respectively, for primary hippocampal neurons.

Takenori Shimamura[a,*] and Hidekazu Mimura[b]

[a] Institute for Solid State Physics, The University of Tokyo
[b] Research Center for Advanced Science and Technology, The University of Tokyo

*Email: tshimamura@issp.u-tokyo.ac.jp

References

[1] B. Rösner *et al.*: Optica **7** (2020) 1602.
[2] Y. Takeo *et al.*: Appl. Phys. Lett. **117** (2020) 151104.
[3] Y. Takeo *et al.*: Appl. Phys. Lett. **116** (2020) 121102.
[4] *T. Shimamura, Y. Takeo, F. Moriya, T. Kimura, M. Shimura, Y. Senba, H. Kishimoto, H. Ohashi, K. Shimba, Y. Jimbo, H. Mimura: Nat. Commun.* ***15*** *(2024) 665.*

Time-resolved anomalous small angle X-ray scattering at BL28XU

Small angle X-ray scattering has been widely used in the characterization of colloids, gels, metals, polymers and proteins on a length scale from just above atomic size up to several 100 nanometers. Anomalous small angle X-ray scattering (ASAXS) is a contrast variation scattering technique that enables us to estimate the partial structure factors in a multi-component system [1,2]. In the ASAXS experiment, we measured the change in the scattered intensity with incident X-ray energy near the absorption edges of one component in the multi-component system. Near absorption edges, the scattering length or contrast factor of X-ray for scattering drastically changes. The analyses of the scattered intensity variation with the incident X-ray energy yielded each partial structure factor of the multi-component system. However, in the previous ASAXS experiments, it was difficult to conduct the time-resolved ASAXS measurement quickly since it took several ten seconds to adjust the X-ray energy of the incident beam. Thus, we constructed the anomalous ultra-small-angle X-ray scattering (AUSAXS) system at SPring-8 **BL28XU** for a time-resolved AUSAXS experiment [3]. At BL28XU, we can quickly adjust the energy of the incident X-ray without drifting the beam position [4], and conduct the time-resolved AUSAXS measurement. We also extended the path length to 9.1 m and attained the minimum $q = 0.0069$ nm^{-1} at 9 KeV.

Figure 1 shows a schematic illustration of the AUSAXS equipment for BL28XU. This beamline consists of optics hutch, experimental hutch 1, and experimental hutch 2. The optical setup includes the first mirror (M1), second mirror (M2), a monochromator (MONO), two jaw slits (SLIT1 and SLIT2) in the optics hutch, and third mirror (M3), fourth mirror (M4) and the other two jaw slits (SLIT3 and SLIT4) in the experimental hutch 1. The details of each component are described in the previous paper (Tanida *et al.* [4]). The setup enables us to change the energy of the X-ray with the beam position at the focal point being virtually constant. In addition to the existing optical setup, we installed the new components for the AUSAXS setup, consisting of the attenuator box, the scatterless slit, and the guard slit, as shown in Fig. 1.

The sample changer can be replaced with the heater block, which allows a sample to be heated up to 200°C, and the tensile machine for *in situ* observations during heating and stretching processes of samples. The ion chamber is mounted behind the sample to measure the transmittance of the samples. All components, including the glove box and the following polyvinyl chloride (PVC) flight paths, are evacuated to reduce parasitic scattering, as schematically shown at the bottom of Fig. 1. As a result, the AUSAXS system was completed with a sample-to-detector distance of 9.1 m. The beam stopper was a tungsten rod with

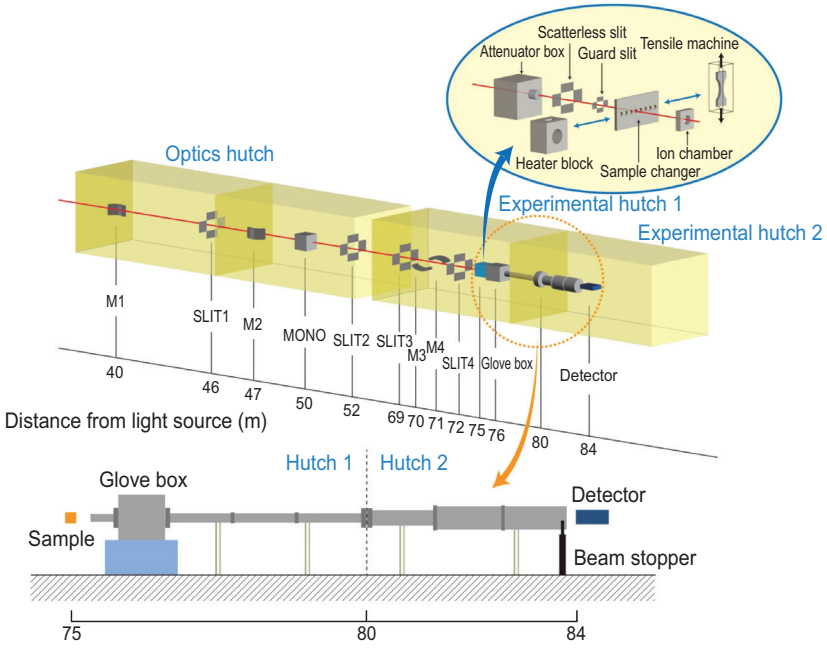

Fig. 1. A schematic illustration of the BL28XU beamline.

a width of 2 mm and an optical axis length of 4 mm. The USAXS/AUSAXS profiles were obtained with a two-dimensional hybrid pixel array detector, PILATUS 300K-W.

To check the availability of time-resolved AUSAXS, we observed the change of zinc oxide (ZnO) structures with time during the vulcanization of rubber. It is well-known that the addition of ZnO in rubber accelerates the vulcanization with sulfur and that the spatial distribution of ZnO affects the physical properties of vulcanized rubbers. By applying time-resolved AUSAXS near zinc *K*-edge to the vulcanization of rubber, we can extract the information on the change in the structures of ZnO during the vulcanization. We used poly(styrene-*ran*-butadiene) (SBR) as rubber.

We measured the scattering profiles at the following 17 different energies in one cycle with 30 s. The scattered intensity varied with the energy of X-ray. $I(q,E)$ is, thus, expressed by

$$I(q,E) = (\mu/A)^2 \left[f_0^2 F_0^2(q) + 2 f_0 f'(E) F_0(q) \nu(q) + (f'^2(E) + f''^2(E)) \nu^2(q) \right] \quad (1)$$

where f_0, A, μ, $f'(E)$, $f''(E)$, $F_0(q)$ and $\nu(q)$ are, respectively, the atomic scattering factor, molar mass, specific gravity, real parts of anomalous dispersion, imaginary parts of anomalous dispersion, the non-resonant and resonant amplitudes. We estimated $\nu^2(q)$ from the scattered intensity below the *K*-edge of Zn. Figure 2 shows the change in $\nu^2(q)$ with t. We found the shoulder at q = 0.01 nm^{-1} in $\nu^2(q)$, indicating that the clusters of ZnO with their size being about 100 nm in the system. We fitted $\nu^2(q)$ with the following the Unified Guinier/power-law equation:

$$\nu^2(q) = \nu^2(0)\, exp(-R_g^2/3) + Bq^{-p} \quad (2)$$

where $\nu^2(0)$, R_g, B and p are, respectively, $\nu^2(q)$ at $q = 0$, the radius of gyration of ZnO clusters, the prefactor of the power-law and the exponent of the power-law. The equation can be well fitted with the experimental results and the fitting results yielded the characteristic parameters. We listed them in Table 1. The size of particles of ZnO and the exponent decrease with time associating with the progress of the vulcanization.

We succeeded in constructing the AUSAXS measurement system by taking advantage of SPring-8 BL28XU beamline. The *q*-range for the AUSAXS measurement system was estimated to be 0.0069–0.3 nm^{-1}. We can obtain the scattering profiles at the 17 different X-ray energies in 30 s and conduct time-resolved measurements to investigate the changes in the structure of zinc compounds in SBR rubber during vulcanization. The change in the energy dependence of $I(q,E)$ with time was found during vulcanization, suggesting the transformation of zinc by the vulcanization reaction.

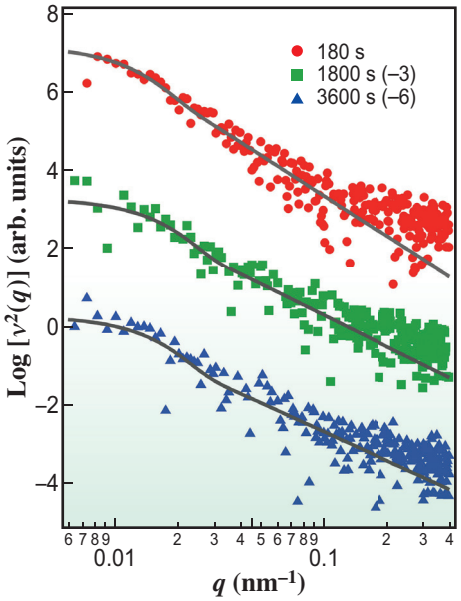

Fig. 2. The change in $\nu^2(q)$ with time plotted as a function of q. The amount of shift of the plots is shown in the legend.

Since we can conduct time-resolved AUSAXS measurement with the system, we can investigate the kinetics of the element-specific structure in the order of submicron scale. Thus we can apply the system to the basic research on the association processes of metal ion in gelation and phase separation dynamics of metal alloys, and the industrial materials including metals.

Table 1. Characteristic parameters obtained by fitting Eq. (2)

Time (s)	ν^2 (0)	R_g (nm)	B	p
180	1.50×10^{7}	1.7×10^{2}	8.1×10^{-1}	3.4
1800	2.0×10^{6}	1.3×10^{2}	4.30	2.7
3600	1.9×10^{6}	1.4×10^{2}	7.1	2.4

Mikihito Takenaka

Institute for Chemical Research, Kyoto University

Email: takenaka@scl.kyoto-u.ac.jp

References

[1] O. Lyon and J. P. Simon: Phys. Rev. B Condens. Matter. **35** (1987) 5164.
[2] Y. Watanabe *et al.*: J. Appl. Crystallogr. **56** (2023) 461.
[3] *Y. Nakanishi, S. Fujinami, M. Shibata, T. Miyazaki, K. Yamamoto and M. Takenaka.: J. Appl. Crystallogr. **57** (2024) 215.*
[4] H. Tanida *et al.*: J. Synchrotron Rad. **21** (2013) 268.

SACLA Beam Performance

Introducing 476 MHz solid-state amplifiers

Beam injection from the SACLA linear accelerator into the SPring-8 storage ring was implemented in 2020. In response to increasing demands for higher availability and greater reliability of the SACLA accelerator, new 476 MHz solid-state pulse amplifiers have been introduced.

The 476 MHz booster cavity, located at the most upstream section of SACLA, is highly sensitive to beam performance, as shown in Fig. 1. The radio frequency (RF) source for this cavity must deliver 100 kW of power with 50 μs pulse width, maintaining high pulse-to-pulse stability of $\delta_A/A < 0.05\%$ for amplitude and $\delta_\phi < 0.025$ degrees for phase. Previously, this requirement was fulfilled by an inductive output tube (IOT). However, the operational range of the IOT had diminished due to aging-related degradation, and procurement of replacement parts has become increasingly difficult. Consequently, a transition to solid-state amplifiers has been undertaken. The modular configuration of solid-state amplifiers, utilizing a combiner, enables continuous operation in the event of individual module failure and simplifies repairs. Furthermore, unlike IOTs, their design eliminates the necessity for high voltage, which is expected to improve fault tolerance.

A new solid-state amplifier (SSA) was initially introduced to the SACLA main linac, which provides both hard X-ray free electron laser (XFEL) and beam injection into the SPring-8 storage ring. The standalone performance of this SSA was independently evaluated in 2020. Following this assessment, it was installed at SACLA (Fig. 2(a)) as an addition to the existing IOT, facilitating a smooth transition of SSA into actual beam operation and improving availability by maintaining the other RF source as an active spare. XFEL lasing and its performance were successfully verified using the SSA outputs at the end of 2021. After undergoing minor modifications in 2022 to enhance operational efficiency, the SSA began continuous operation as the main RF source at the beginning of 2023, and has maintained stable operation to date.

Following the successful introduction of the SSA to the SACLA main linac, an additional SSA was introduced to SCSS+ (BL1 linear accelerator), which provides soft-XFEL. This SSA was manufactured in 2023, tested and evaluated in the first half of 2024,

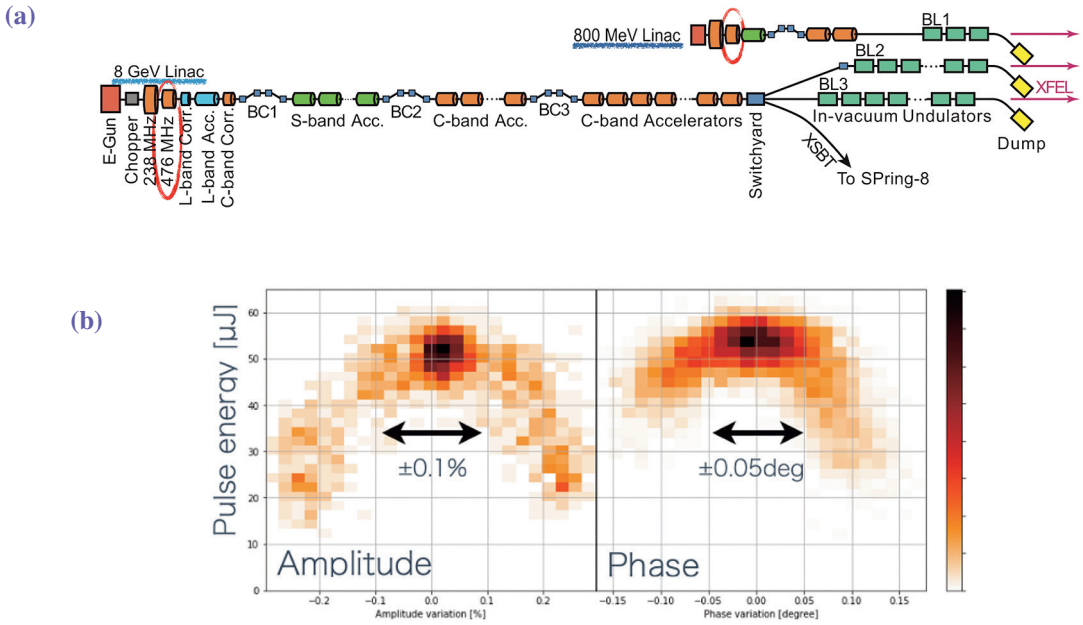

Fig. 1. **(a)** Locations of the 476 MHz booster cavities. **(b)** Dependences of XFEL pulse energy on the 476 MHz amplitude and phase (SCSS+ case as an example).

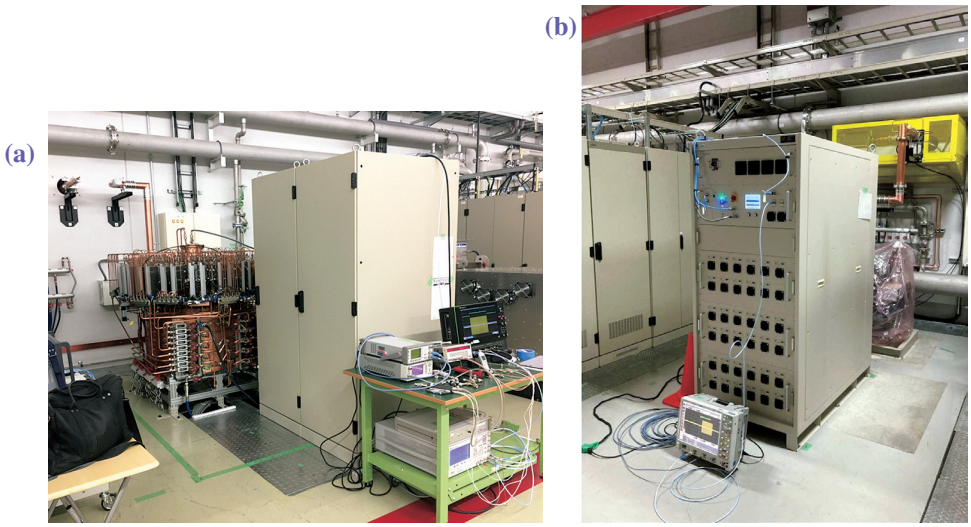

Fig. 2. **(a)** The 476 MHz solid-state amplifiers installed in the SACLA and **(b)** SCSS+.

and then installed in the summer of 2024 to 'replace' the existing IOT (Fig. 2(b)). Continuous operation commenced after the summer shutdown period in 2024, and this SSA has likewise maintained stable operation to date.

As noted, both SSAs have maintained stable operation without any failures since their continuous operation began. The observed pulse-to-pulse stability for the SACLA SSA is $\delta_A/A = 0.007\%$ for amplitude and $\delta_\phi = 0.022$ degrees for phase. For the SCSS+ SSA, the corresponding values are $\delta_A/A = 0.028\%$ for amplitude and $\delta_\phi = 0.022$ degrees for phase as shown in Fig. 3 (these values include intrinsic fluctuations of the RF inputs and the resolution of measuring instruments). The observed stabilities satisfy the requirements of the RF sources used in the 476 MHz booster cavities.

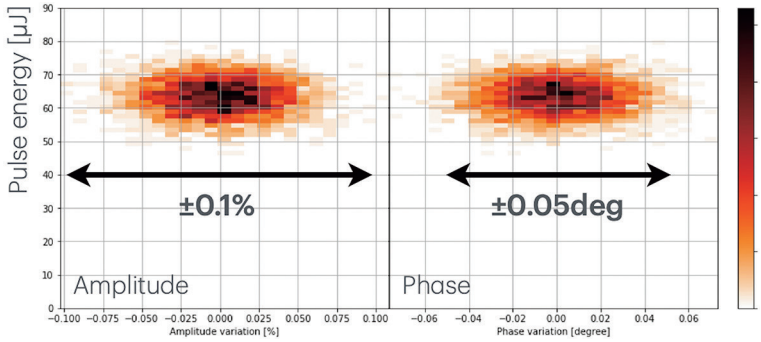

Fig. 3. Measured amplitude and phase stability of the SSA with respect to XFEL pulse energy (SCSS+).

Eito Iwai[a,b]

[a] Japan Synchrotron Radiation Research Institute (JASRI)
[b] RIKEN SPring-8 Center

Email: iwai@spring8.or.jp

FACILITY STATUS

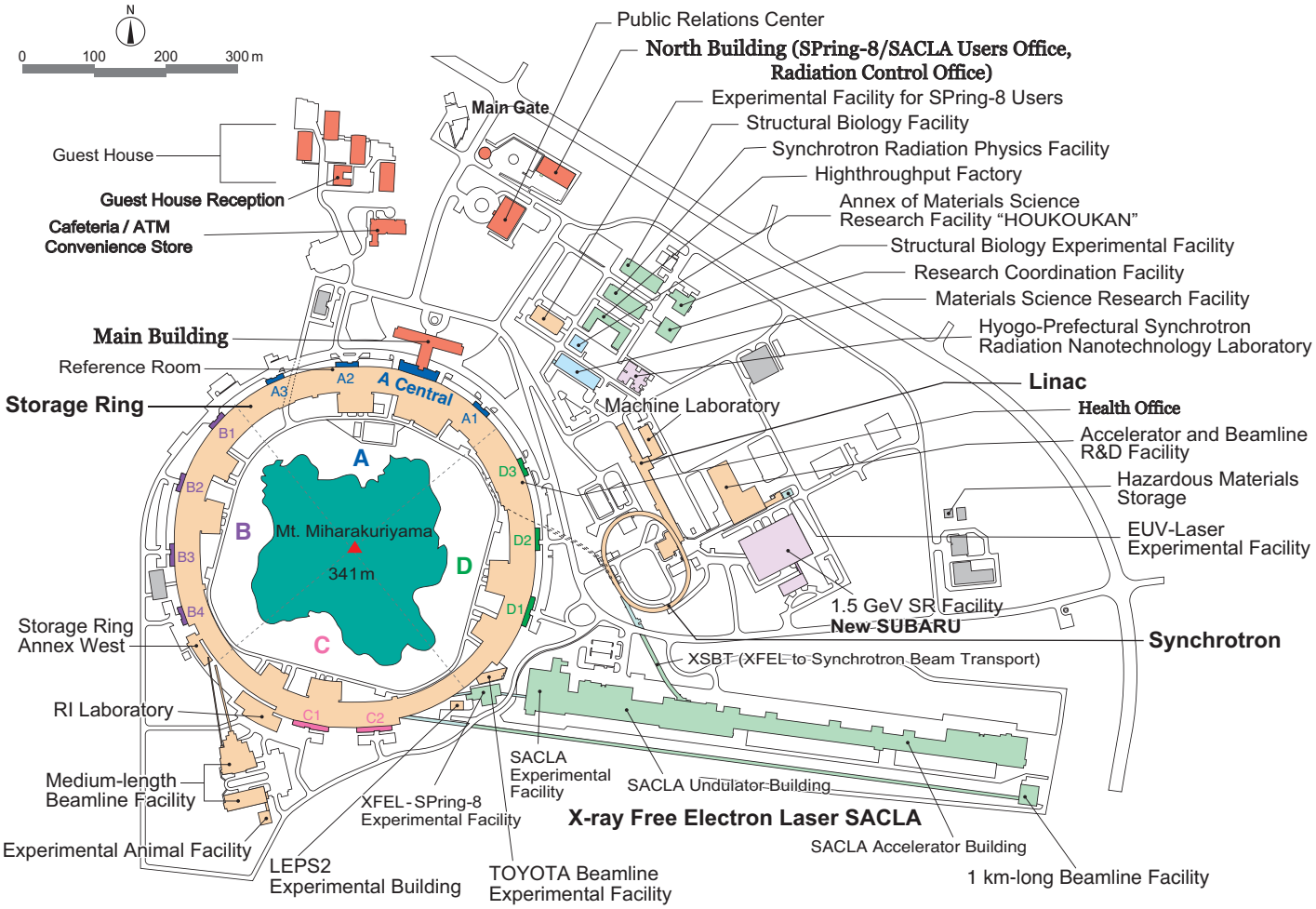

SPring-8

I. Introduction

SPring-8 was stably operated throughout FY2024 achieving a total accelerator complex operation time of 5187.1 h, user beam time of 4416.9 h, and a total downtime of 21.6 h. SPring-8 completed all its operations by mid-February 2025.

Concerning the contract beamlines, there were interim review and extend review conducted for Laser-Electron Photon II (BL31LEP, Research Center for Nuclear Physics, Osaka University), and Macromolecular Assemblies (BL44XU, Institute for Protein Research, Osaka University), respectively. As a result, the projects were authorized to continue. Toyota (BL33XU, Toyota Central R&D Labs., Inc.) also received a review, and their proposal for the next term was approved. Post-evaluations of Hyogo BM (BL08B2, Hyogo Prefecture), Hyogo ID (BL24XU, Hyogo Prefecture), and Advanced Softmaterial (BL03XU, Advanced Softmaterial Beamline Consortium) were also conducted. In addition, concerning Advanced Softmaterial (BL03XU, Advanced Softmaterial Beamline Consortium), its name will change to Analytical Science III (BL03XU, RIKEN BL) due to the expiration of their contract terms on 1st of April.

The Specific Synchrotron Radiation Facility Users Community (SpRUC) was established on March 1, 2025, through the merger of the SPring-8 Users Community (SPRUC) and the NanoTerasu Users Community (NTUC). At present, the number of SPring-8 users is about 13,000, all of whom are members of the SpRUC.

To facilitate dialogue between users and facility staff, it is important for SPring-8 to organize scientific events in collaboration with SPRUC, such as the SPring-8 Symposium. In 2024, the SPring-8 Symposium was held both online and on-site on September 5–6, with 365 participants. SPring-8 also facilitates communication between users and industry. The Joint Conference on Industrial Applications of SPring-8 was held in Hyogo Prefecture on September 10–11, with 216 participants. Moreover, as part of its continuous effort towards fostering human resources in synchrotron sciences, SPring-8 organized the 24th SPring-8 Summer School with 84 graduate students nationwide. Furthermore, SPring-8 and SPRUC organized the 8th SPring-8 Autumn School with 67 participants, which included university students and corporate researchers.

II. Beamlines

The SPring-8 storage ring can accommodate up to 62 beamlines: 34 insertion devices, 4 long undulators, and 24 bending magnets. At present, 56 beamlines are in operation, covering a wide variety of research fields involving synchrotron radiation science and technology. The beamlines are classified into the following three types.

(1) Public Beamlines (26 beamlines operating),
(2) Contract Beamlines (12 beamlines operating), and
(3) RIKEN Beamlines (18 beamlines operating).

There are now 26 public beamlines in full operation. The beamlines that have been proposed and constructed by external organizations, such as universities, research institutes, private companies and consortiums, are called contract beamlines and are used exclusively by the contractors for their own research purposes. At present, 10 contract beamlines are in operation. The beamlines constructed by RIKEN or transferred to RIKEN, except for public beamlines, are called RIKEN beamlines and are mainly used for RIKEN's own research activities, with partial availability for public use. RIKEN is now operating 18 beamlines.

To illustrate the beamline portfolio of SPring-8, a beamline map is shown in Fig. 1 together with the beamline classification. The research fields of each beamline are presented in Table 1.

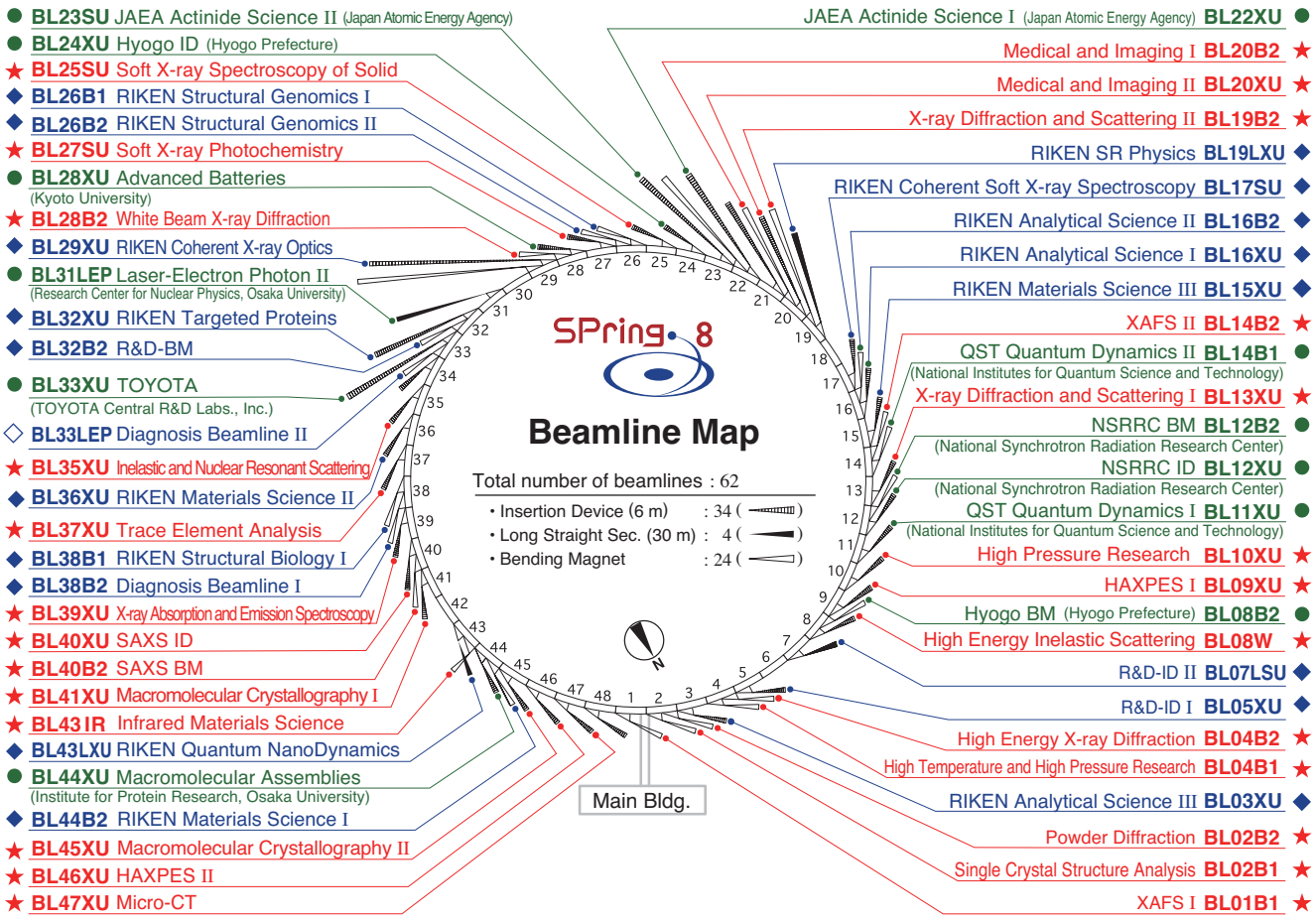

BL: Beamline
B1, B2: Bending Magnets
XU: X-ray Undulator
SU: Soft X-ray Undulator
W: Wiggler
NSRRC: National Synchrotron Radiation Research Center, Taiwan
IR: Infrared Radiation
LEP: Laser-Electron Photon
LXU: Long-length X-ray Undulator
LSU: Long-length Soft X-ray Undulator

★ : Public Beamlines
● : Contract Beamlines
◆ : RIKEN Beamlines
◇ : Planned or Under Construction

Fig. 1. Beamline map as of April 2025.

Table 1. List of beamlines

BL #	Beamline Name	(Public Use) or (First Beam)	Areas of Research and Available Techniques
★ Public Beamlines			as of April 2025
BL01B1	XAFS I	(Oct. 1997)	Wide energy range (3.8–113 keV), XAFS of dilute systems and thin films, time-resolved XAFS by quick scan (time-resolved QXAFS), depth-resolved XAFS, XAFS at low and high temperatures, simultaneous XAFS and XRD measurements, simultaneous XAFS and IR measurements.
BL02B1	Single Crystal Structural Analysis	(Oct. 1997)	Charge density study using high energy X-ray, *in situ* single crystal experiments, microcrystal structure analysis.
BL02B2	Powder Diffraction	(Sep. 1999)	Charge density study from powder diffraction, structural phase transition, *ab initio* structure determination from powder diffraction, crystal structure refinement by Rietveld method, *in situ* powder diffraction experiment under gas and vapor adsorption/desorption.
BL04B1	High Temperature and High Pressure Research	(Oct. 1997)	X-ray diffraction measurements and radiography under extreme conditions using large-volume press.
BL04B2	High Energy X-ray Diffraction	(Sep. 1999)	Structural analysis of glass, liquid, and amorphous materials.
BL08W	High Energy Inelastic Scattering	(Oct. 1997)	Magnetic Compton scattering, high-resolution Compton scattering, Compton scattering imaging, high-energy X-ray scattering, high-energy X-ray fluorescence analysis (XRF), time-resolved pair distribution function analysis (PDF).
BL09XU	HAXPES I	(Oct. 1997)	Resonant hard X-ray photoelectron spectroscopy (HAXPES), polarization-dependent HAXPES using diamond phase retarder, depth analysis of electron state, materials science, and applied materials science.
BL10XU	High Pressure Research	(Oct. 1997)	Crystal structure analysis under high pressure using diamond-anvil cells, *in situ*/*operando* observation of phase transition and compression behavior under extreme conditions, material sciences under extreme conditions, high pressure Earth and planetary science.
BL13XU	X-ray Diffraction and Scattering I	(Sep. 2001)	X-ray diffraction and reflectivity measurements, atomic-scale structural analysis of crystal surfaces and interfaces, ultrathin films, and nanostructures, residual stress measurement, time-resolved X-ray diffraction, *in situ* process observation using X-ray diffraction, *operando* X-ray diffraction, high-resolution powder X-ray diffraction and X-ray total scattering, structural refinement using Rietveld analysis, *in situ*/*operando* powder X-ray diffraction, time-resolved powder X-ray diffraction, analysis of local structures using nanodiffraction.
BL14B2	XAFS II	(Sep. 2007)	X-ray imaging, XAFS in a wide energy range (3.8–72 keV), XAFS of dilute systems and thin films, time-resolved XAFS by quick scan (time-resolved QXAFS), XAFS at low and high temperatures, simultaneous XAFS and XRD measurements.
BL19B2	X-ray Diffraction and Scattering II	(Nov. 2001)	Residual stress measurement, structural analysis of thin film, surface and interface, powder X-ray diffraction, X-ray topography, ultrasmall-angle X-ray scattering.
BL20B2	Medical and Imaging I	(Sep. 1999)	Micro-radiography, micro-angiography, micro-tomography, and refraction-contrast imaging are the mainly used techniques. BL20B2 is also applicable to small-animal experiments for medical research. Research and development of basic techniques for evaluation of optical devices and X-ray imaging.
BL20XU	Medical and Imaging II	(Sep. 2001)	X-ray micro-/nano-imaging: micro-tomography (micro-CT), nano-CT (15–37.7 keV), refraction/phase contrast imaging, X-ray diffraction tomography (XRD-CT), microbeam/scanning X-ray microscope, research and development of X-ray optics and optical elements, coherent X-ray optics, ultrasmall-angle X-ray scattering (USAXS, 23 keV).
BL25SU	Soft X-ray Spectroscopy of Solid	(Apr. 1998)	Research on electronic structures by soft X-ray core-level photoemission spectroscopy (XPS) and angle-resolved photoemission spectroscopy (ARPES), research on magnetic states by soft X-ray magnetic circular dichroism (MCD) of soft X-ray core-level absorption (XAS), analysis of surface atomic arrangement by photoelectron diffraction (PED), analysis of the nano-scale chemical states using low-energy/photoemission electron microscope (SPELEEM).
BL27SU	Soft X-ray Photochemistry	(May 1998)	Soft X-ray absorption spectroscopy of dilute samples in partial fluorescence yield mode, surface and interface analysis using depth-resolved soft X-ray absorption spectroscopy, soft X-ray absorption spectroscopy under ambient atmospheric pressure, spectroscopy using soft X-ray microbeam, observation of electron state in solids by soft X-ray emission spectroscopy.
BL28B2	White Beam X-ray Diffraction	(Sep. 1999)	White X-ray diffraction: X-ray topography, energy-dispersive strain measurement, high energy (~200 keV) X-ray microtomography, high-speed X-ray imaging.
BL35XU	Inelastic and Nuclear Resonant Scattering	(Sep. 2001)	Phonons in solids and atomic dynamics in disordered materials by inelastic X-ray scattering, atomic and molecular dynamics by nuclear resonant inelastic scattering and quasi-elastic scattering, synchrotron-radiation-based Mössbauer spectroscopy, nuclear excitation.
BL37XU	Trace Element Analysis	(Nov. 2002)	X-ray microbeam/nano-beam spectrochemical analysis, X-ray spectroscopic imaging, ultratrace-element analysis, high-energy X-ray fluorescence analysis. Projection/scanning/imaging XAFS microscopy, high brightness XAFS, coherent diffraction imaging XAFS microscopy.
BL39XU	X-ray Absorption and Emission Spectrosocpy	(Oct. 1997)	X-ray magnetic circular dichroism (XMCD) spectroscopy and element-specific magnetometry (ESM), XAFS and XMCD spectroscopy under extreme conditions (high pressure, high magnetic field, and low/high temperature), XAFS and XMCD spectroscopy using micro/nanobeam and variable X-ray polarization (horizontally/perpendicularly linear or circular), scanning XAFS and XMCD microscopy using micro/nanobeam, X-ray emission spectroscopy (XES) and high-energy resolution fluorescence detected (HERFD) XAFS spectroscopy.
BL40XU	SAXS ID	(Apr. 2000)	Fast time-resolved X-ray diffraction and scattering experiments, X-ray photon correlation spectroscopy, microbeam X-ray diffraction and scattering experiments.
BL40B2	SAXS BM	(Sep. 1999)	Small-angle X-ray scattering (SAXS).
BL41XU	Macromolecular Crystallography I	(Oct. 1997)	Macromolecular crystallography, micro-crystallography, ultrahigh resolution structural analysis.
BL43IR	Infrared Materials Science	(Apr. 2000)	Infrared microspectroscopy.
BL45XU	Macromolecular Crystallography II	(Apr. 2019)	Macromolecular crystallography, micro-crystallography, automation and high throughput data collection for protein crystallography.
BL46XU	HAXPES II	(Nov. 2000)	Hard X-ray photoemission spectroscopy, ambient pressure hard X-ray photoemission spectroscopy.
BL47XU	Micro-CT	(Oct. 1997)	X-ray micro-/nano-imaging including CT (7–15 keV), refraction/phase contrast imaging, high speed X-ray imaging, microbeam/scanning X-ray microscope. User on-demand experiments using their own instruments.

BL #	Beamline Name	(Public Use) or (First Beam)	Areas of Research and Available Techniques
● Contract Beamlines as of April 2025			
BL08B2	**Hyogo BM** (Hyogo Prefecture)	(Jun. 2005)	Small angle X-ray scattering, X-ray imaging, X-ray computed tomography, X-ray topography.
BL11XU	**QST Quantum Dynamics I** (National Institutes for Quantum Science and Technology)	(Oct. 1998)	Mössbauer spectroscopy, resonant inelastic X-ray scattering, X-ray emission spectroscopy, surface X-ray diffraction (*in situ* studies on crystal growth of III-V group semiconductor), coherent X-ray diffraction imaging.
BL12B2	**NSRRC BM** (National Synchrotron Rad. Res. Center)	(Oct. 2000)	X-ray absorption spectroscopy, powder X-ray diffraction.
BL12XU	**NSRRC ID** (National Synchrotron Rad. Res. Center)	(Dec. 2001)	Non-resonant or resonant inelastic X-ray scattering, hard X-ray photoemission spectroscopy.
BL14B1	**QST Quantum Dynamics II** (National Institutes for Quantum Science and Technology)	(Dec. 1997)	High-temperature and high-pressure X-ray diffraction measurements mainly on hydrogen materials, XAFS for dilute samples, time-resolved energy-dispersive XAFS, irradiation research on biomaterials.
BL22XU	**JAEA Actinide Science I** (Japan Atomic Energy Agency)	(May 2002)	HAXPES, microbeam XAFS, residual stress/strain distribution analysis, X-ray imaging, time-resolved X-ray diffraction, surface X-ray diffraction, high-energy X-ray diffraction, high-pressure science.
BL23SU	**JAEA Actinide Science II** (Japan Atomic Energy Agency)	(Feb. 1998)	Surface chemistry with supersonic molecular beam, photoelectron spectroscopy, magnetic circular dichroism, STXM.
BL24XU	**Hyogo ID** (Hyogo Prefecture)	(May 1998)	Imaging microscope, micro-tomography, microbeam X-ray diffraction and bright field X-ray topography for electronic device materials, near-ambient pressure hard X-ray photoelectron spectroscopy.
BL28XU	**Advanced Batteries** (Kyoto University)	(Apr. 2012)	Characterization of rechargeable battery reactions and battery related materials by *operando* X-ray diffraction (XRD), X-ray absorption spectroscopy (XAS), and hard X-ray photoelectron spectroscopy (HAXPES).
BL31LEP	**Laser-Electron Photon II** (RCNP, Osaka University)	(Oct. 2013)	Quark nuclear physics (hadron physics) studied in photon-nucleon and photon-nucleus reactions using high-intensity linearly polarized GeV photon beams from laser-induced Compton scattering; testing detectors using electrons or positrons converted from GeV photons.
BL33XU	**TOYOTA** (Toyota Central R&D Labs., Inc.)	(Apr. 2009)	Time-resolved XAFS. 3DXRD, characterization of industrial materials and devices (e.g., catalysts, lightweight bodies, secondary batteries, fuel cells, and power modules).
BL44XU	**Macromolecular Assemblies** (IPR, Osaka University)	(May 1999)	Crystal structure analysis of biological macromolecular assemblies (e.g., membrane protein complexes, protein complexes, protein-nucleic acid complexes, and viruses).
◆ RIKEN Beamlines as of April 2025			
BL03XU	**Analytical Science III**	(Nov. 2009)	Characterization of materials and products using multiple analytical techniques (e.g., SAXS).
BL05XU	**R&D-ID I**	(Mar. 2004)	R&D of high-energy X-ray optics, instruments, and applications; structural and dynamical research using small and wide angle scattering.
BL07LSU	**R&D-ID II**	(Oct. 2009)	R&D of soft X-ray optics, instruments, and applications.
BL15XU	**RIKEN Materials Science III**	(Oct. 2021)	Advanced diffraction and scattering with high-energy X-rays.
BL16XU	**Analytical Science I**	(Oct. 1998)	Characterization of materials and products using multiple analytical techniques (e.g., multi-axis diffractometer).
BL16B2	**Analytical Science II**	(Oct. 1998)	Characterization of materials and products using multiple analytical techniques (e.g., X-ray digital topography).
BL17SU	**RIKEN Coherent Soft X-ray Spectroscopy**	(Sep. 2003)	High resolution photoemission spectroscopy; soft X-ray emission spectroscopy; soft X-ray diffraction spectroscopy; soft X-ray microspectroscopy.
BL19LXU	**RIKEN SR Physics**	(Oct. 2000)	SR science with highly brilliant X-ray beam.
BL26B1	**RIKEN Structural Genomics I**	(Apr. 2002)	Structural biology research based on single crystal X-ray diffraction.
BL26B2	**RIKEN Structural Genomics II**	(Apr. 2002)	Structural biology research based on single crystal X-ray diffraction.
BL29XU	**RIKEN Coherent X-ray Optics**	(Dec. 1998)	X-ray optics, especially coherent X-ray optics.
BL32XU	**RIKEN Targeted Proteins**	(Oct. 2009)	Protein microcrystallography.
BL32B2	**R&D-BM**	(May 2002)	X-ray computed tomography; X-ray diffraction; X-ray absorption fine structure; R&D of SR instruments.
BL36XU	**RIKEN Materials Science II**	(Mar. 2020)	Time resolved XAFS and X-ray diffraction; 2D/3D scanning XAFS imaging; 3D computed tomography/laminography XAFS imaging; X-ray emission spectroscopy; pink beam experiments.
BL38B1	**RIKEN Structural Biology I**	(Oct. 2000)	Structure study of non-crystalline biological materials using small-angle scattering and diffraction techniques.
BL38B2	**Diagnosis Beamline I**	(Sep. 1999)	Accelerator beam diagnostics.
BL43LXU	**RIKEN Quantum NanoDynamics**	(Oct. 2011)	High resolution inelastic X-ray scattering for investigating atomic and electronic dynamics.
BL44B2	**RIKEN Materials Science I**	(Feb. 1998)	Structural materials science research using powder X-ray diffraction.

III. User Program and Statistics

SPring-8 calls for public use proposals twice a year, in principle. Since 2022B term, nine public beamlines started to invite proposals six times annually, including the beamlines previously intended for industrial application. The submitted proposals are reviewed by the SPring-8 Proposal Review Committee (SPring-8 PRC). Since 1997, SPring-8 has accepted a variety of proposals. For the promotion of research on industrial applications at SPring-8, currently, Industrial Application Proposals account for approximately 16%–20% of the total number of proposals conducted at various public beamlines. There always exist those companies and research institutes that find it difficult to retain specialized staff and to accommodate the need for quick access to SPring-8. To appropriately respond to this circumstance, the SPring-8 Measurement Service is provided. In this framework of service, JASRI staff members perform measurements on behalf of users. It is up to the users whether to come to SPring-8 and be present during the measurements or to simply send their samples to SPring-8. BL28XU has been added to the Measurement Service BL from 2022B. Currently, JASRI has expanded the purview of the SPring-8 Measurement Service to five measurement methods (XAFS, Powder X-ray Diffraction, Small Angle X-ray Scattering, High energy X-ray CT, Hard X-ray Photoemission Spectroscopy). In addition, JASRI provides the Protein Crystallography Automatic Data Collection at Macromolecular Crystallography beamlines. Therefore, users can choose whether to come to SPring-8 and be present during the measurements or to simply send their samples to SPring-8. Since 2022A term, JASRI has started calling for Hour-based use at most public beamlines as part of proprietary time-designated proposals. According to this change, the Feasibility Study Proposals for Industrial Application has been integrated into this proposal program. SPring-8 is developing a remote-operation system that allows users to control experimental instruments from outside to promote remote access. The number of experiments conducted, and the number of user visits at the public and contract beamlines are summarized in Fig. 2. Part of the proposals are for proprietary use, for which refereed reports are not required. Figures 3 to 12 show the information on user programs.

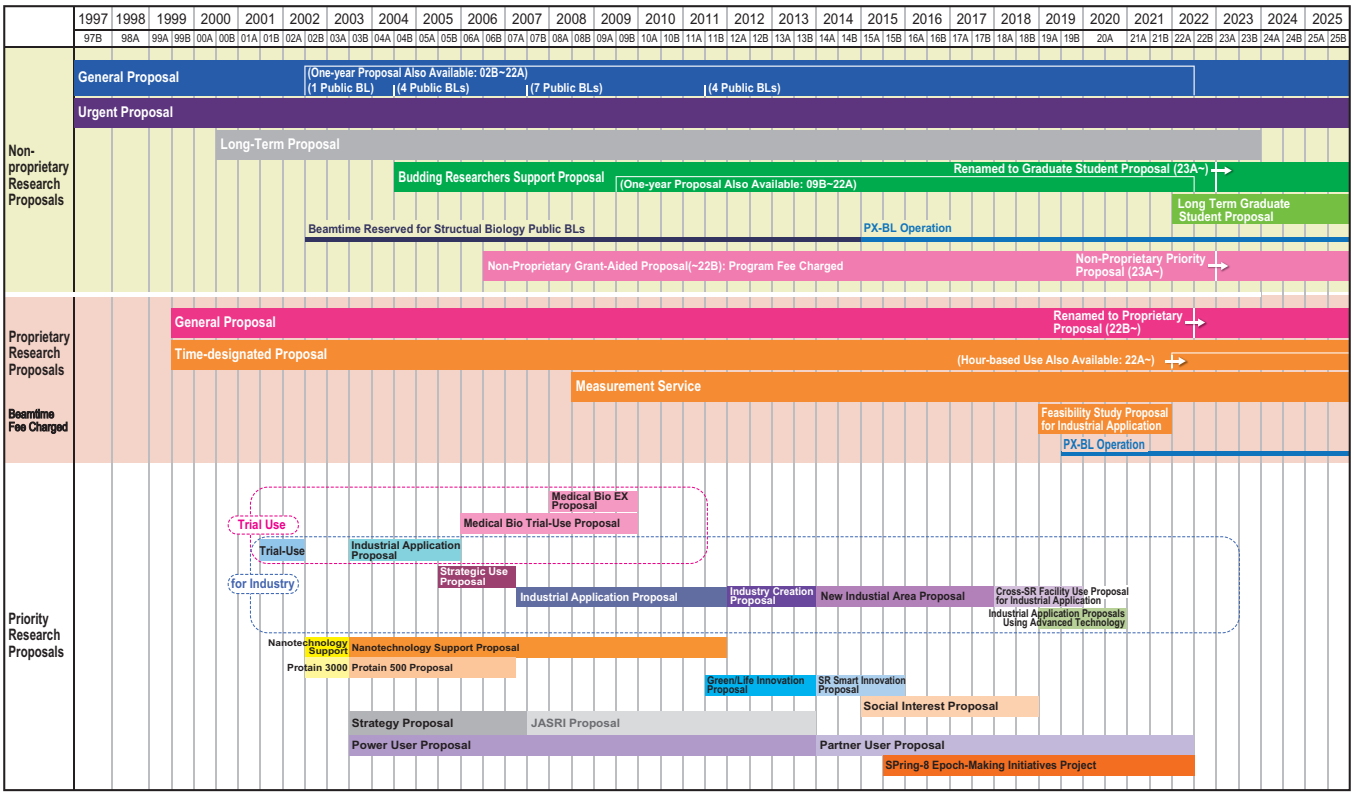

Fig. 2. Categories of proposals for the public beamlines.

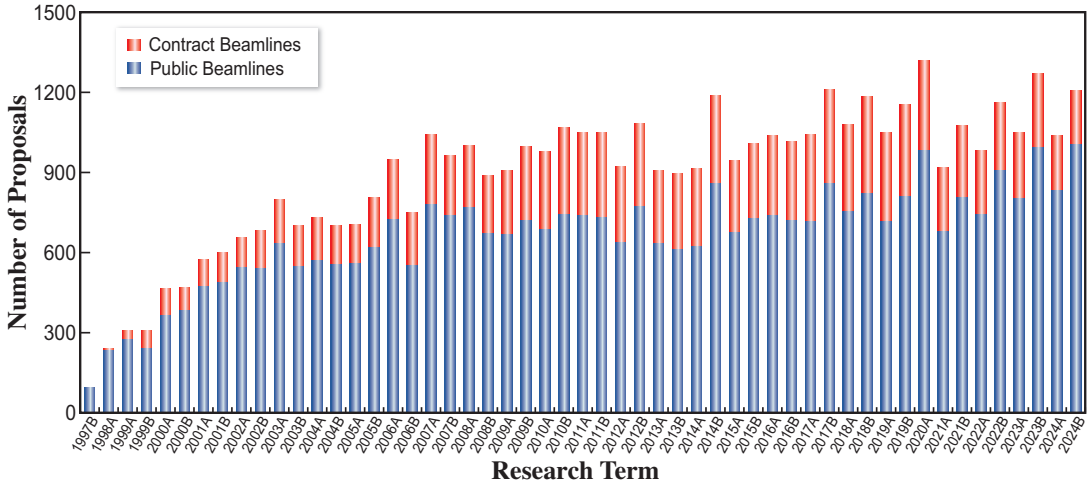

Fig. 3. Numbers of conducted experiments.

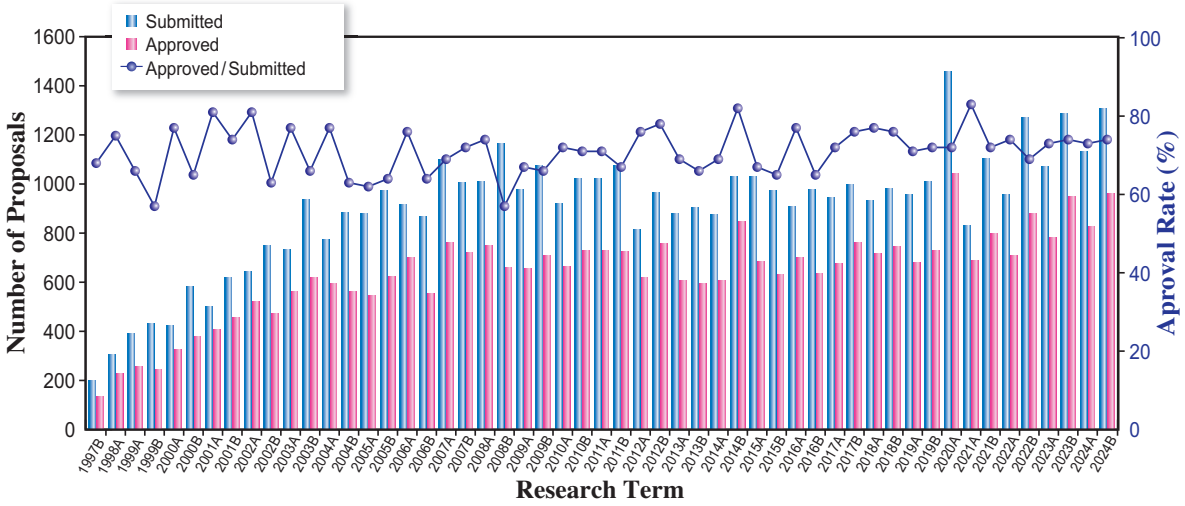

Fig. 4. Numbers of submitted proposals and approved proposals by research term (public beamlines).

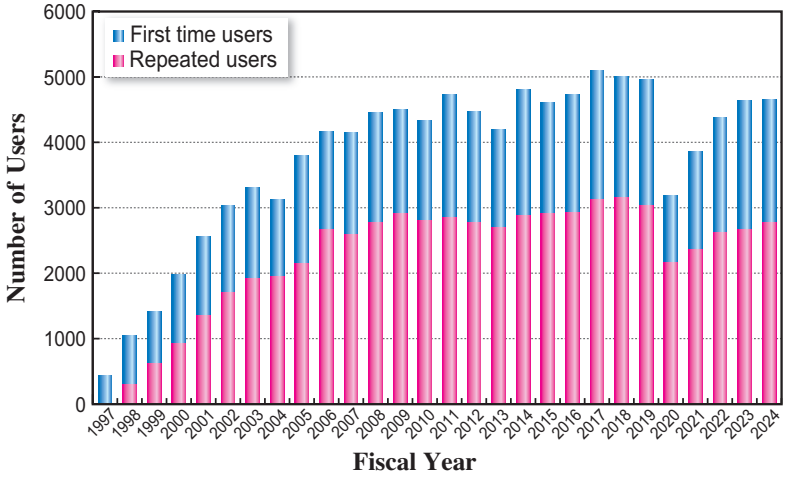

Fig. 5. Numbers of users by fiscal year.

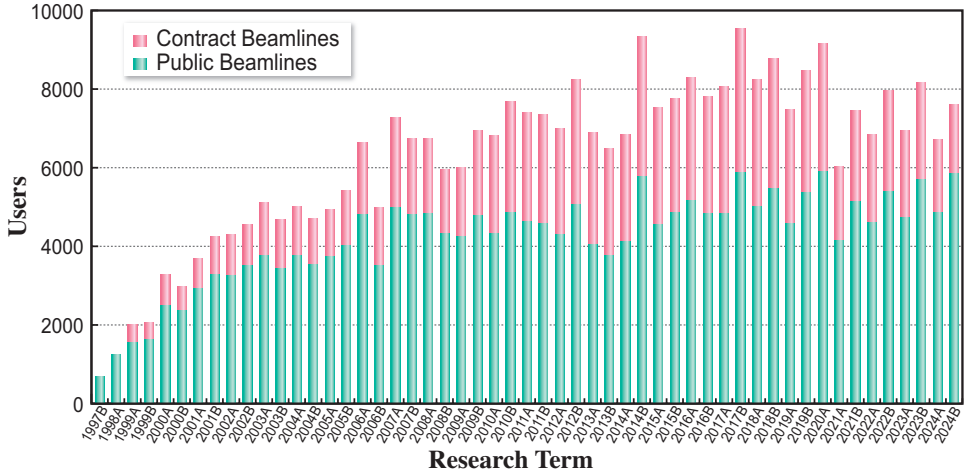

Fig. 6. Numbers of users visits by research term.

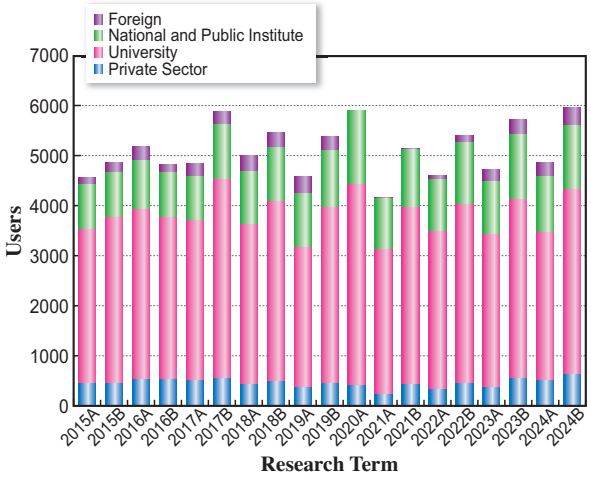

Fig. 7. Numbers of users by affiliation categories (public beamlines).

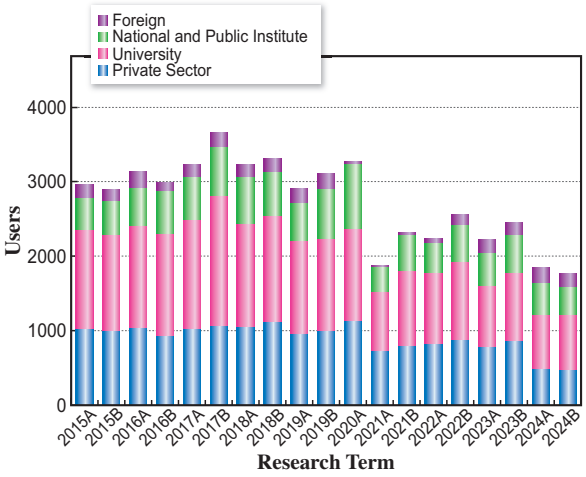

Fig. 8. Numbers of users by affiliation categories (contract beamlines).

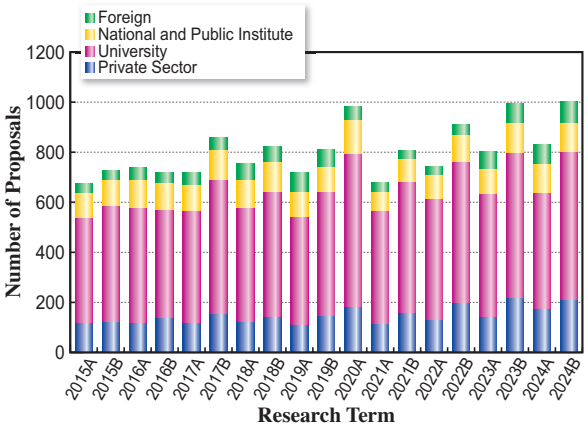

Fig. 9. Numbers of conducted proposals by affiliation categories (public beamlines).

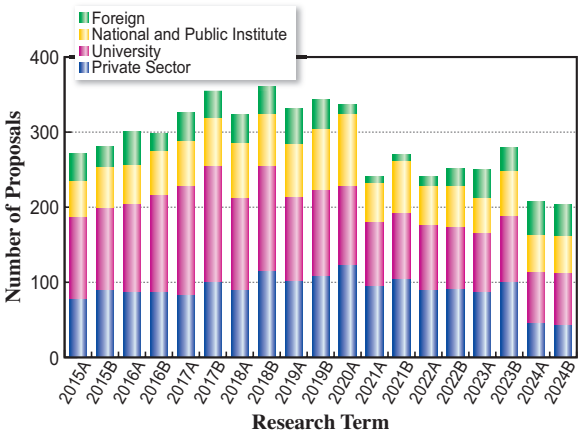

Fig. 10. Numbers of conducted proposals by affiliation categories (contract beamlines).

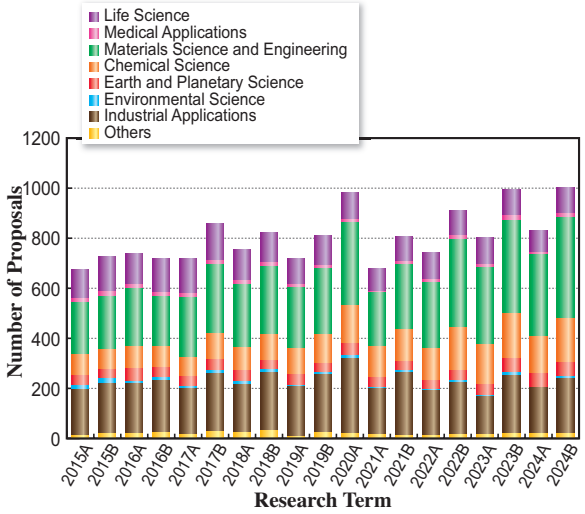

Fig. 11. Numbers of conducted proposals by research area (public beamlines).

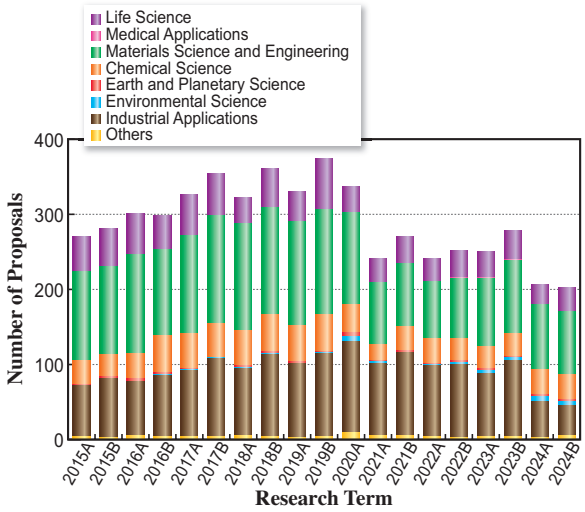

Fig. 12. Numbers of conducted proposals by research area (contract beamlines).

IV. Research Outcome

As of March 2025, the total number of registered refereed papers from SPring-8 and SACLA is 23,376. Figure 13 shows the annual statistics of refereed papers.

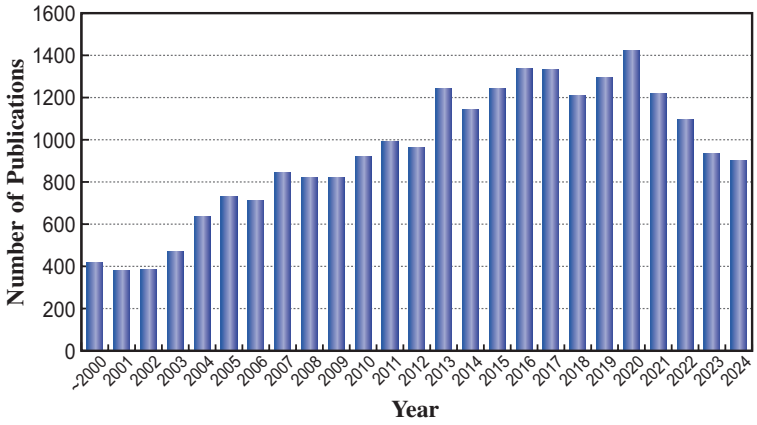

Fig. 13. Number of refereed publications.

V. Research Complex

The facilities of SPring-8, SACLA, and NewSUBARU form the Center of Excellence (COE) on the SPring-8 campus where JASRI, public beamline users, contractors of contract beamlines, RIKEN, and the University of Hyogo work in close cooperation. Thus, a research complex has been formed, where each member has their own role in achieving high-quality results in the field of synchrotron radiation science and technology. The organizational charts of RIKEN and JASRI, which are at the center of this research complex, are shown in Fig. 14 and Fig. 15, respectively.

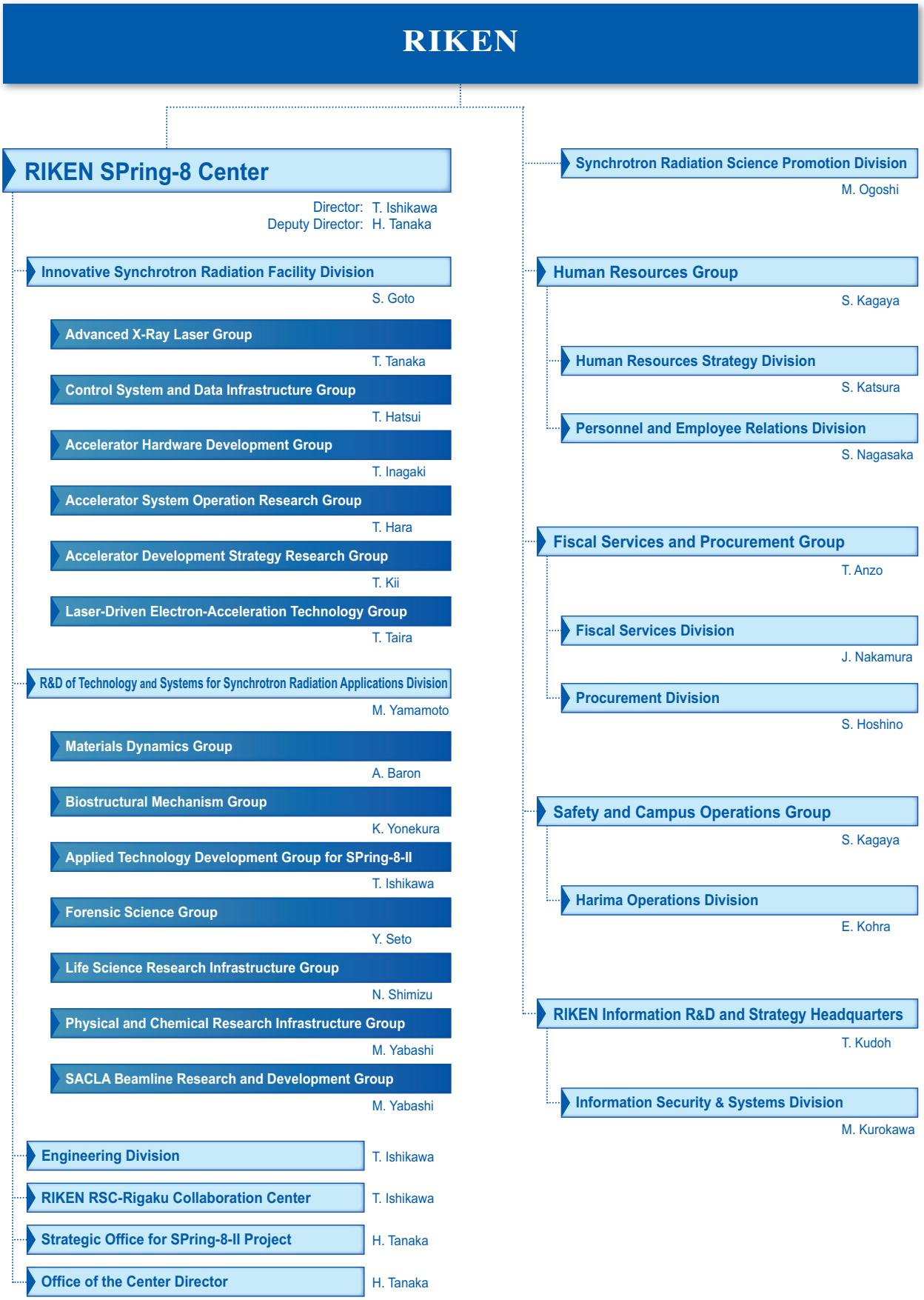

Fig. 14. RIKEN Harima Campus chart as of April 2025.

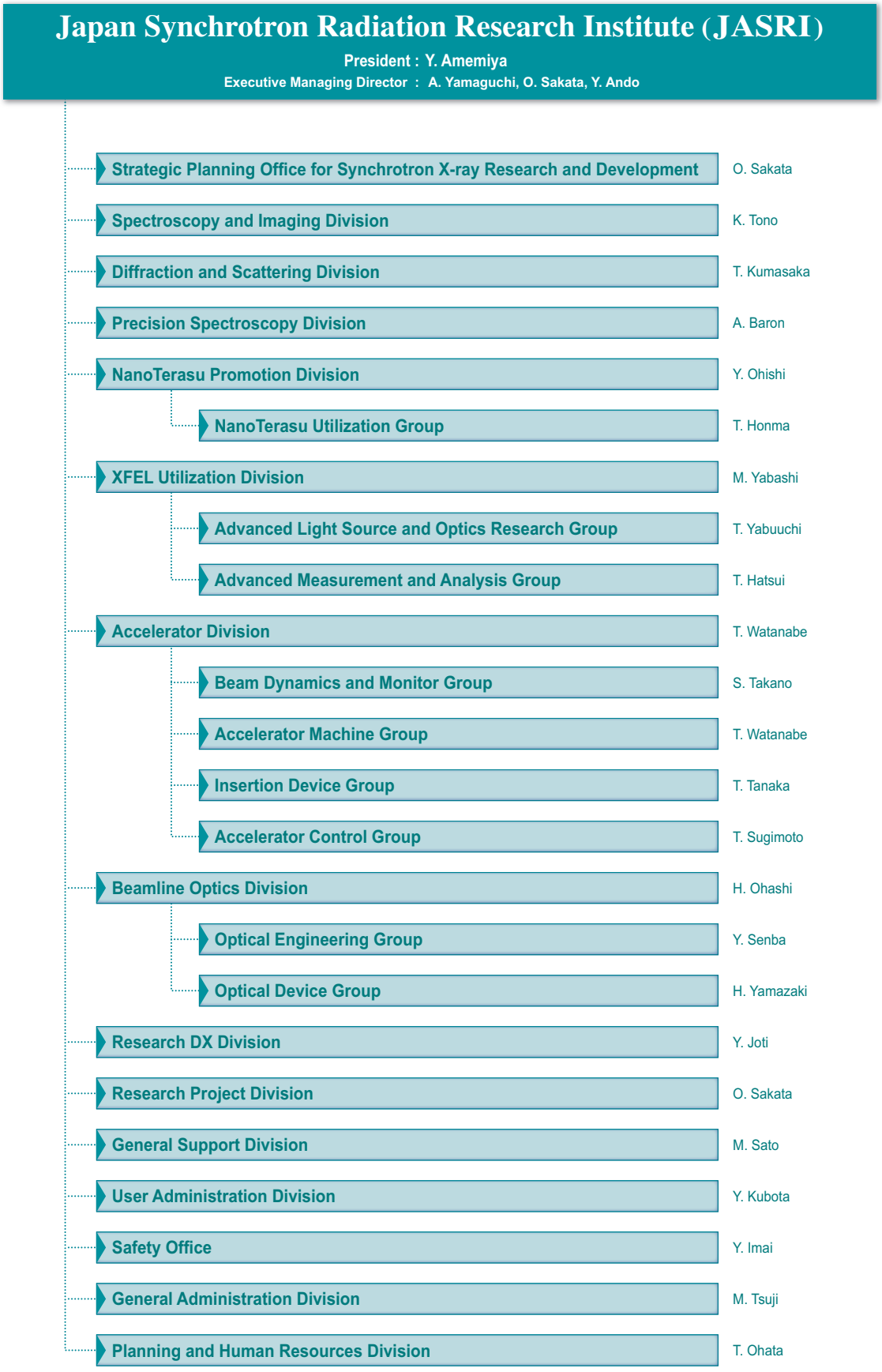

Fig. 15. JASRI chart as of April 2025.

VI. Specific Synchrotron Radiation Facility Users Community (SpRUC)

Chair Akihiko Fujiwara
Kwansei Gakuin University
Editorial Secretary Hiroyuki Asakura
Kindai University

The Specific Synchrotron Radiation Facility Users Community (SpRUC) was established on March 1, 2025, through the merger of the SPring-8 Users Community (SPRUC) and the NanoTerasu Users Community (NTUC). SpRUC comprises all users of SPring-8, SACLA, and NanoTerasu, and includes not only individual members but also representative organizations from 25 institutions, including major universities, national and international research institutes, industrial entities, and beamline consortiums. These members collaborate to discuss strategic directions and future perspectives for advancing the utilization of these facilities.

The SPring-8 Symposium is a significant annual event originally organized by SPRUC. The 2024 symposium was co-hosted by Kyushu University, RIKEN, and JASRI and took place on September 5–6 at Centennial Hall, Kyushu University School of Medicine, with additional live streaming online. The event saw 61 in-person attendees and 143 participants online. The theme of the symposium, "Synchrotron Radiation and FEL for SDGs," aimed to envision the future of next-generation synchrotron radiation and free electron laser science in the context of the Sustainable Development Goals (SDGs). Presentations focused on multi-scale advanced analysis of cutting-edge materials and devices, including semiconductors, catalysts for a hydrogen-based society, and recyclable plastics.

The symposium also featured the 13th SPRUC Young Scientist Award ceremony. This year's recipients were Dr. Kiyofumi Takaba from the University of Vienna, Dr. Yoshifumi Hashikawa from Kyoto University, and Dr. Takumi Nishikubo from the Kanagawa Institute of Industrial Science and Technology. The next SpRUC Symposium is scheduled to be held in Sendai in 2025.

SPRUC supported the "SPring-8 Summer School," held from July 7 to 10, to enhance users' research competencies, and co-hosted the "SPring-8 Autumn School," held from September 1 to 4, in collaboration with JASRI. The SPring-8 Summer School is centered around the practical use of SPring-8 and comprises lectures and hands-on training primarily aimed at master's course graduate students. In contrast, the SPring-8 Autumn School targets a broader audience, including third- and fourth-year undergraduate students, graduate students, and corporate researchers. Notably, it is open to participants who are not registered as radiation workers. SPRUC research groups contributed to the planning and organization of

The 13th SPRUC Young Scientist Award
Prof. A. Nakagawa, Dr. K. Takaba, Dr. Y. Hashikawa, Dr. T. Nishikubo, and Prof. A. Fujiwara

SPring-8 Symposium 2024

lectures for the Autumn School. This year, 67 participants attended the program and engaged in simulated practical training at SPring-8.

SpRUC also hosted the 7th Workshop on Beamlines Upgrade on March 1–2, in collaboration with RIKEN, QST, and JASRI, as in previous years. During the workshop, the teams responsible for beamlines BL04B2, BL39XU, and BL40XU—recently upgraded—shared their current status and presented feedback on their progress. This was followed by in-depth discussions regarding the upcoming SPring-8-II upgrade, focusing on the conceptual design, construction schedule, and the beamline portfolio, including soft and hard X-ray spectroscopy as well as high-energy scattering/diffraction beamlines. The latest developments in ongoing beamline upgrades, equipment innovations, and methodological advances were also shared. Additionally, the current status of NanoTerasu was presented, alongside discussions on its utilization and future prospects.

The seventh-term SPRUC research groups were self-organized within individual research fields, comprising a total of 37 groups. These groups actively convened to exchange ideas and assess the specific needs for beamline upgrades in their respective areas. Notably, most meetings this year were conducted in person rather than online.

Joint general assembly of SPring-8 Users Community (SPRUC) and NanoTerasu Users Community (NTUC)

VII. Outreach Activities

To reach new users in unexplored application fields, SPring-8 holds various serialized seminars named "Workshop on Advanced Techniques and Applications at SPring-8." Representative examples are as follows:

- 105th: Current Status and Future of Protein Structural Biology Research at SPring-8
  September 9, 2024 • Osaka University

- 11th: Joint Workshop for Collaborative Use of Synchrotron Radiation and Neutron Beam
  November 19, 2024 • SPring-8 / February 2, 2025 • J-PARC MLF

- 103rd: Current Status of Silicon Semiconductor Devices and Materials Supporting Their Production and the Use of Synchrotron Radiation
  November 20, 2024 • Meeting Space AP Shinagawa

SACLA

I. Machine Operation & Beamlines

Our twelfth year of operations proceeded without any significant issues. Operation statistics are summarized in Table 1. The ratio of downtime to user time was kept below 3%, a reasonably low rate for linac-based light sources.

Table 1. Operation Statistics for FY2024

		Time (h)
Total operation time		5694
User time		
	BL1	1428
	BL2	1920
	BL3	2848
Facility tuning time		696
Downtime		145.8

In 2012, two beamlines, BL3 for XFEL and BL1 for broadband spontaneous light, were opened for users, while all experiments were conducted at BL3. As the newest beamline, construction of BL2 was completed during the summer shutdown of 2014, and first laser amplification was achieved on October 21. An upgraded beamline for soft X-ray FEL, BL1, which combines the prototype accelerator of SACLA (SCSS), started operation in 2016. Parallel user operation of BL2 and BL3 started in 2018.

II. User Program and Statistics

SACLA normally calls for public user proposals twice per year. Moreover, SACLA Feasibility Study Program has started since 2021A to provide an opportunity to experience the use on a trial basis for the purpose of dissemination and enlightenment.

In FY2016, JASRI introduced the proprietary research of General Proposals and the Proprietary Time-Designated Proposals. The project leaders of these proprietary proposals are not required to publish their research results, but required to pay each beamtime fee. In addition, to apply for the proprietary research the project leaders should be affiliated with corporate enterprises or academic research institutions, which are located and registered in Japan.

Figures 1 and 2, and Table 2 provide statistics on proposals, users, and beamtime.

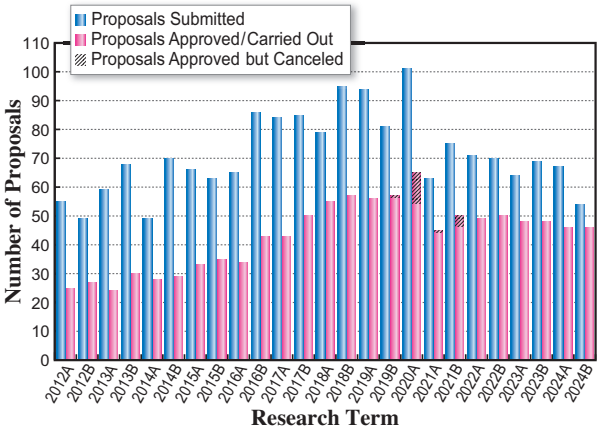

Fig. 1

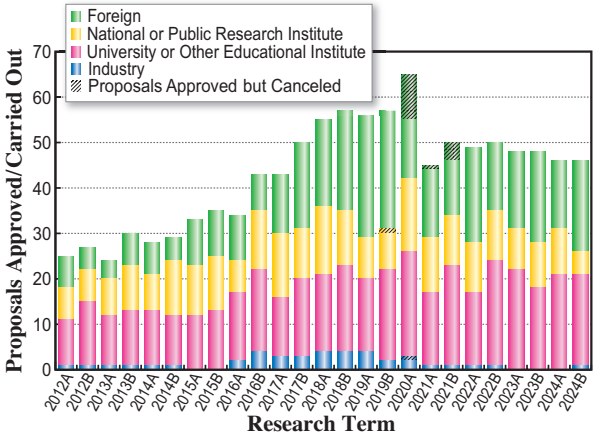

Fig. 2

Table 2. Number of proposals submitted, proposals approved/carried out, cumulative users, and beamtime available by research term

Half-year Research Term	Proposals Submitted	Proposals Approved / Carried Out					Cumulative Users	Beamtime Carried Out (Shifts)
			Priority Strategy Proposals	Non-proprietary	Proprietary			
				General Proposals	General Proposals	Time-Designated Proposals		
2012A	55	25	(12)	(13)	–	–	297	126
2012B	49	27	(19)	(8)	–	–	461	154
2013A	59	24	(15)	(9)	–	–	268	117
2013B	68	30	(19)	(11)	–	–	410	139
2014A	49	28	(20)	(8)	–	–	400	147
2014B	70	29	(17)	(12)	–	–	430	140
2015A	66	33	(23)	(10)	–	–	527	144
2015B	63	35	(23)	(12)	–	–	552	152
2016A	65	34	(21)	(12)	(1)	–	538	158
2016B	86	43	(21)	(20)	(1)	(1)	650	197
2017A	84	43	–	(43)	(0)	(0)	577	210
2017B	85	50	–	(50)	(0)	(0)	642	244
2018A	79	55	–	(55)	(0)	(0)	643	257
2018B	95	57	–	(56)	(0)	(1)	653	264
2019A	94	56	–	(55)	(0)	(1)	564	259
2019B	81	57	–	(56)	(0)	(0)	650	266
2020A	101	65	–	(54)	(0)	(0)	461	276
2021A	63	45	–	(44)	(0)	(0)	465	248
2021B	75	50	–	(46)	(0)	(0)	468	254
2022A	71	49	–	(49)	(0)	(0)	570	249
2022B	70	50	–	(50)	(0)	(0)	588	259
2023A	64	48	–	(48)	(0)	(0)	519	248
2023B	69	48	–	(48)	(0)	(0)	560	269
2024A	67	46	–	(45)	(0)	(0)	457	246
2024B	54	46	–	(45)	(1)	(0)	498	266

One shift = 12 hours at SACLA beamlines

SPring-8/SACLA

Budget and Personnel

When SPring-8 started operations in 1997, it was jointly managed by RIKEN, JAERI (now JAEA), and JASRI. However, JAEA withdrew from the management of SPring-8 on September 30, 2005. Currently, SPring-8 is collaboratively administered by RIKEN and JASRI.

RIKEN established specific synchrotron radiation facilities (i.e., SPring-8 and SACLA) and is responsible for their operation and maintenance. JASRI selects and supports users of these facilities under the "Act on the Promotion of Public Utilization of the Specific Advanced Large Research Facilities."

Figure 1 shows government subsidy for SPring-8 and SACLA. Figure 2 shows the manpower of RIKEN and JASRI.

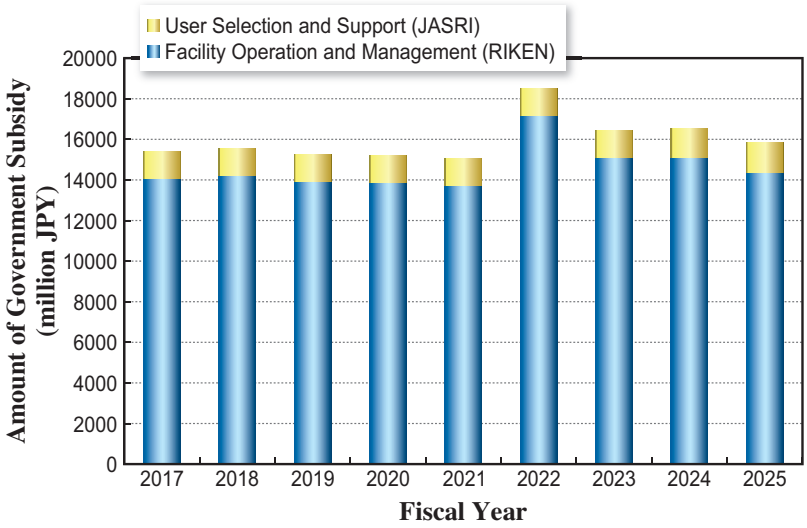

Fig. 1. Government subsidy (SPring-8 and SACLA).

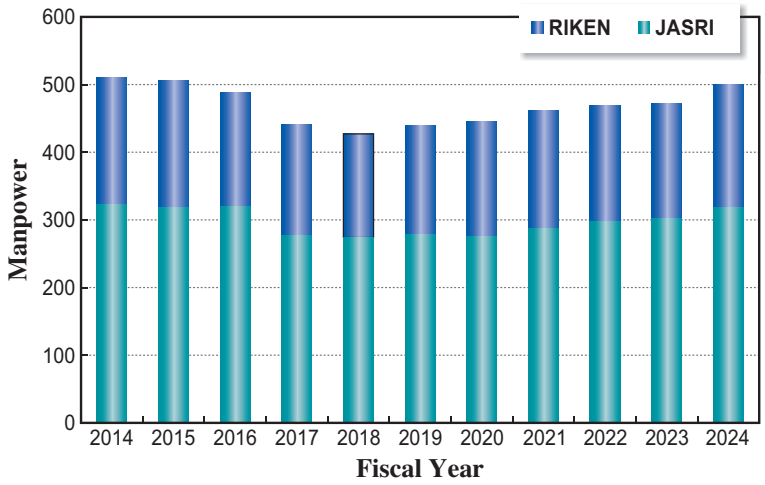

Fig. 2. Manpower at SPring-8: RIKEN and JASRI.

SPring-8 SACLA
Research Frontiers 2024

Editor

Toyohiko Kinoshita
Japan Synchrotron Radiation Research Institute (JASRI)

Secretariat

Tomoko Aoki
Marcia M. Obuti-Daté
Japan Synchrotron Radiation Research Institute (JASRI)

Printing
Hokuoh Printing Co.

JASRI
Information & Outreach Section
Users Administration Division

1-1-1 Kouto, Sayo-cho, Sayo-gun
Hyogo 679-5198 • JAPAN
Tel: +81-(0)791-58-2785

Email: frontiers@spring8.or.jp
http://www.spring8.or.jp/

August 2025

SPring-8 SACLA

http://www.spring8.or.jp

Japan Synchrotron Radiation Research Institute (JASRI)
1-1-1 Kouto, Sayo-cho, Sayo-gun, Hyogo 679-5198, Japan